



THE UNIVERSITY OF QUEENSLAND
A U S T R A L I A

Radiation in low density hypervelocity flows

Carolyn Jacobs

*A thesis submitted for the degree of Doctor of Philosophy at
The University of Queensland in August 2011
School of Mechanical and Mining Engineering*

in Cotutelle with Ecole Centrale Paris
Laboratoire d'Énergétique Moléculaire et Macroscopique,
Combustion (EM2C), CNRS UPR288

Declaration by author

This thesis is composed of my original work, and contains no material previously published or written by another person except where due reference has been made in the text. I have clearly stated the contribution by others to jointly-authored works that I have included in my thesis. I have clearly stated the contribution of others to my thesis as a whole, including statistical assistance, survey design, data analysis, significant technical procedures, professional editorial advice, and any other original research work used or reported in my thesis. The content of my thesis is the result of work I have carried out since the commencement of my research higher degree candidature and does not include a substantial part of work that has been submitted to qualify for the award of any other degree or diploma in any university or other tertiary institution. I have clearly stated which parts of my thesis, if any, have been submitted to qualify for another award.

I acknowledge that an electronic copy of my thesis must be lodged with the University Library and, subject to the General Award Rules of The University of Queensland, immediately made available for research and study in accordance with the *Copyright Act 1968*.

I acknowledge that copyright of all material contained in my thesis resides with the copyright holder(s) of that material.

Statement of Contributions to Jointly Authored Works Contained in the Thesis

- C. Jacobs and C. Laux (2009). Collisional-Radiative Model for Air and Titan. *Published as the majority of European Space Agency Contract Report AMOD-ECP-TN-033.*
 - Laux was responsible for 40% of the drafting and writing.
 - Jacobs was responsible for 60% of the drafting and writing.
- C. Jacobs, T. Eichmann, R. Morgan, M. McGilvray, T. McIntyre and A. Brandis (2008). Calibration procedures for emission spectroscopy measurements in shock and expansion tubes. *European Space Agency Contract Report AMOD-UQ-TN-012.*
 - Eichmann was responsible for 40% of the design of the optical setup and the spectral calibration, and 40% of the drafting and writing.
 - Morgan was responsible for 10% of the drafting and writing.
 - McGilvray was responsible for figures 16 and 17.
 - McIntyre was responsible for 20% of the design of the optical setup and the spectral calibration.
 - Jacobs was responsible for 40% of the design of the optical setup and the spectral calibration, and 50% of the drafting and writing.
- C. Jacobs, R. Morgan, T. Eichmann and T. McIntyre (2011). Radiative heat transfer measurements in a nonreflected shock tube at low pressures. *28th International Symposium on Shock Waves, Manchester.*
 - Morgan was responsible for 10% of the drafting and writing.
 - Brandis was responsible for 10% of the design of the optical setup and the spectral calibration.
 - Eichmann was responsible for 40% of the design of the optical setup and the spectral calibration.
 - McIntyre was responsible for 10% of the design of the optical setup and the spectral calibration, and 10% of the drafting and writing.
 - Jacobs was responsible for 40% of the design of the optical setup and the spectral calibration, and 80% of the drafting and writing.
- C. Jacobs and R. Morgan (2009). Radiation measurements in rarefied Titan atmospheres. *47th AIAA Aerospace Sciences Meeting, Orlando.*

- Morgan was responsible for 10% of the drafting and writing.
- Jacobs was responsible for 90% of the drafting and writing.

Statement of Contributions by Others to the Thesis as a Whole

The optical layout design and the calibration codes presented in Appendix D were developed with substantial contributions from Troy Eichmann and extended on the work of Aaron Brandis.

Statement of Parts of the Thesis Submitted to Qualify for the Award of Another Degree

None.

Published Works by the Author Incorporated into the Thesis

- C. Jacobs and C. Laux (2009). Collisional-Radiative Model for Air and Titan. *Published as the majority of European Space Agency Contract Report AMOD-ECP-TN-033.* - Incorporated as Chapter 2.
- C. Jacobs, T. Eichmann, R. Morgan, M. McGilvray, T. McIntyre and A. Brandis (2008). Calibration procedures for emission spectroscopy measurements in shock and expansion tubes. *European Space Agency Contract Report AMOD-UQ-TN-012.* - Incorporated as Chapter 3.
- C. Jacobs, R. Morgan, T. Eichmann and T. McIntyre (2011). Radiative heat transfer measurements in a nonreflected shock tube at low pressures. *28th International Symposium on Shock Waves, Manchester.* - Incorporated as Chapter 6.
- C. Jacobs and R. Morgan (2009). Radiation measurements in rarefied Titan atmospheres. *47th AIAA Aerospace Sciences Meeting, Orlando.* - Incorporated as Chapter 6.

Additional Published Works by the Author Relevant to the Thesis but not Forming Part of it

- T. McIntyre, T. Eichmann, C. Jacobs, D. Potter, M. McGilvray, P. Jacobs and R. Morgan (2010). Shock tube and expansion tunnel measurements of high temperature radiating flows. *4th International Workshop on Radiation of High Temperature Gases in Atmospheric Entr*, Lausanne.
- M. McGilvray, P. Jacobs, R. Morgan, R. Gollan and C. Jacobs (2009). Helmholtz resonance of Pitot pressure measurements in impulsive hypersonic test facilities. *AIAA Journal* 47(10) pp. 2430-2439.
- R. Gollan, C. Jacobs, P. Jacobs, R. Morgan, T. McIntyre, M. Macrossan, D. Buttsworth, T. Eichmann and D. Potter (2007). A simulation technique for radiating shock tube flows. *26th International Symposium on Shock Waves*, Göttingen.
- R. Morgan, T. McIntyre, D. Buttsworth, P. Jacobs, D. Potter, A. Brandis, R. Gollan, C. Jacobs, B. Capra, M. McGilvray and T. Eichmann (2008). Impulse facilities for the simulation of hypersonic radiating flows. *38th AIAA Fluid Dynamics Conference and Exhibit*, Seattle.



THESE

présentée par

Carolyn Jacobs

pour l'obtention du grade de

DOCTEUR de l'ECOLE CENTRALE PARIS

en cotutelle avec l'Université de Queensland

Spécialité: Energétique

Étude du rayonnement d'un écoulement hypersonique à basse densité

Laboratoire d'accueil : Laboratoire d'Énergétique Moléculaire
et Macroscopique, Combustion (EM2C), CNRS UPR288

Laboratoire partenaire : The Centre for Hypersonics
School of Mechanical and Mining Engineering
The University of Queensland, Australia

Soutenue le 20 Octobre 2011 devant le jury composé de:

Prof Richard Morgan	Directeur de thèse	The University of Queensland
Prof Christophe Laux	Directeur de thèse	Ecole Centrale Paris
Dr Timothy McIntyre	Coencadrant	The University of Queensland
Dr Vincent Wheatley	Président	The University of Queensland
Dr Lionel Marraffa	Rapporteur	ESA/ESTEC
Prof Douglas Fletcher	Rapporteur	The University of Vermont
Prof Penelope Sanderson	Convenor	The University of Queensland

Acknowledgements

A very big thank you must go to a variety of people who have helped me over the course of this thesis. In particular, my three supervisors: Richard Morgan, Christophe Laux, and Tim McIntyre. You have all given me a great deal of support and so many exciting opportunities over the last few years and I appreciate all of your efforts and advice.

A large part of this project involved experimental work in the Xlab facility at the University of Queensland. Successful experimental campaigns were achieved only with long hours of assistance from all of the X2 operators: Troy Eichmann, Daniel Potter, Fabian Zander, Mary D'Souza, David Gildfind, Andrew Dann, Hadas Porat, and Umar Sheikh. Troy's extensive work with me trying to improve all of the optical measurements is also greatly appreciated.

No experiments would ever take place without the dedicated work of our workshop staff, Brian Loughrey, Frans De Beurs, and Keith Hitchcock. They keep the tunnels running even when it seems impossible.

To all of my fellow cluster administrators (past and present) - Rowan Gollan, Andrew Denman, Daniel Potter, Wilson Chan, Rainer Kirchhartz, and Carlos Ventura - thank you very much for all of the support with the problems that cropped up during the CFD work involved in this thesis.

David Green and the rest of the HPCU crew. Thank you. You went above and beyond to fast track some last minute simulations, and it is greatly appreciated.

I would also like to recognise the assistance of a number of other people who spent hours proofreading, suggesting, and improving this document, and keeping me sane and

on target - all of my supervisors, Mum, Dad, Sandy Thirty, Delphine Finet, Clare Holmes, Nicole Smith, and Leigh Dacey.

Finally, to everyone at the EM2C laboratory at École Centrale Paris - your warm welcome and fantastic atmosphere made my year of exchange extremely enjoyable.

The project was supported by an Australian Postgraduate Award with a University of Queensland Engineering Top Up in Australia, and an Eiffel Scholarship for the cotutelle exchange to France.

Résumé

Cette thèse étudie le transfert de chaleur par rayonnement observé dans les conditions d'écoulement raréfié, en régime hypersonique qui seraient rencontrés au cours d'une mission d'aérocapture dans l'atmosphère de Titan.

Des estimations précises du rayonnement hors-équilibre dans des écoulements à grande vitesse tels que ceux autour des corps de re-entrée, sont indispensables pour la conception de systèmes de protection thermique plus efficace. Parce que la masse du système de protection thermique est une fraction importante de la masse totale du véhicule, il ya un grand intérêt dans la conception de systèmes plus légers et plus efficaces. Les expériences en vol sont coûteuses et contraignantes, c'est pourquoi l'essai en laboratoire dans des installations capables de produire des écoulements hypersoniques est nécessaire. Malheureusement, les échelles de longueur généralement impliquées dans les expériences en vol sont trop grandes pour être testées dans des installations expérimentales et donc des modèles réduits de véhicules "aeroshells" sont généralement testés. Les tubes d'expansion de l'université de Queensland - X1, X2 et X3 - ont été largement utilisés pour la modélisation à l'échelle réduite des écoulements hypersoniques (Morgan 2001).

Pour les installations d'essais au sol telle que la soufflerie X2, une mise à l'échelle binaire est utilisée pour tester des modèles à échelle réduite de véhicules de vol, ce qui constitue le paramètre le plus important à respecter afin de reproduire un vol à haute vitesse. La mise à l'échelle binaire, appelé aussi 'mise à l'échelle $\rho L'$ ', exige que le produit de la densité et de la longueur caractéristique du véhicule soit conservé entre le vol et les conditions expérimentales. Toutefois, le transfert de chaleur par rayonnement ne suit pas cette même loi de mise à l'échelle, et la similitude n'est pas créée pour les cas en vol où le transfert de chaleur par rayonnement et par convection sont fortement couplés. Cela peut

entraîner d'importantes erreurs dans les estimations des propriétés d'écoulement associée et l'estimation du transfert de chaleur due au rayonnement.

L'installation X2 a été modifiée en 2006 pour permettre l'expérimentation à basse pression en mode tube à choc non-réfléchi. L'utilisation d'un tube à choc non-réfléchi a permis la mesure du transfert de chaleur par rayonnement à la densité réelle en vol et supprimé les problèmes d'échelle liés à la mesure des rayonnements sur les véhicules en modèle réduit, au moins pour une partie de l'écoulement. Des mesures ont été effectuées dans la région immédiatement située derrière le choc et le long de la ligne médiane de l'écoulement de base, où le choc reste plan. Les écoulements externes, tels que ceux entourant une capsule de re-entrée, n'ont pas été reproduits. La limite de basse pression d'exploitation était d'environ 10 Pa, limitée par la croissance de la couche limite sur les murs.

Afin d'élargir la gamme de l'installation à des conditions de pression plus faible, le tube à choc a été remplacé par une section de plus grand diamètre. Ces modifications ont abouti à la réalisation d'essais d'écoulement à des pressions aussi faibles que 1 Pa dans l'air et 4 Pa dans un mélange atmosphérique de Titan - environ un tiers de la pression précédente, correspond à la limite basse de l'installation (Brandis 2009a). Cette gamme de pression correspond à un vol jusqu'à 90 km d'altitude dans l'air et 360 km d'altitude dans l'atmosphère de Titan (Yelle et al. 1997). À ces altitudes, le transfert de chaleur par rayonnement est suffisant pour constituer une importante question d'ingénierie et est compliquée par les effets de dynamique des gaz raréfié et en dés-équilibre, caractéristique de la région à faible densité de haute atmosphère.

Dans le travail expérimental, les conditions d'écoulement produites ont été étudiées et analysées afin d'identifier et de minimiser tous les effets de contamination de la matière du tube, du gaz conducteur et des diaphragmes. Des expériences ont été menées pour étudier le transfert radiatif en dés-équilibre dans un gaz d'essai Titan (98 % N₂, 2 % CH₄) à des pressions de 13, 8, et 4 Pa et le choc des vitesses de 6.4, 6.2, et 9.0 km/s respectivement.

Les données recueillies comprennent des mesures de pression statique, des mesures de pression pitot, des spectres d'émission, et des films haute-vitesse. Les résultats spectraux montrent que le rayonnement présent est principalement due aux bandes violettes CN. Une comparaison quantitative et qualitative des résultats spectraux a été faite avec les données précédentes, y compris les résultats expérimentaux recueillis par Brandis (2009a) et Bose et al. (2005) à des conditions similaires, et les résultats de calcul à partir d'une mise en œuvre du modèle radiatif collisionnel Mutation (Magin et al. 2006).

Il a été constaté que le pic de transfert thermique radiatif non-équilibre derrière le choc a été cohérent pour les conditions 13 et 8 Pa. Les résultats spectraux ont montré

que par rapport à ces précédents résultats, l'installation modifiée a permis une amélioration significative de la puissance du signal ainsi que de la durée d'essai disponibles dans ces conditions de basse pression, ce qui permet une résolution spectrale plus fine et la possibilité, si nécessaire, d'étendre la résolution spatiale. L'installation est validée pour l'étude des flux d'entrée à haute vitesse, à des conditions correspondantes à un vol à haute altitude.

Pour les conditions à 4 Pa, les résultats expérimentaux ont été obtenus avec succès et fournissent des informations à propos du pic de non-équilibre et le taux de chute de l'échauffement radiatif derrière l'onde de choc. Les résultats ont montré la cohérence et la répétabilité des nouvelles conditions basse pression, ainsi qu'un temps d'essai et des quantités de gaz suffisants pour permettre la capture d'images spectrale à haute résolution en utilisant une grille de 1800 traits/mm.

Abstract

This thesis investigates the radiative heat transfer encountered in rarefied, hypervelocity flow conditions such as would be experienced during an aerocapture mission to Titan.

Accurate estimates of the nonequilibrium radiation involved in high speed operations such as reentry are essential in order to design these thermal protection systems more efficiently. Because the mass of the thermal protection system is a large fraction of the overall vehicle mass, there is great interest in designing lighter and more efficient systems. Flight experiments are expensive and restrictive, hence laboratory testing is needed in facilities that are capable of producing hypervelocity flow. Unfortunately, as the size of a typical flight vehicle is too large to reasonably test in experimental facilities, subscale models of the aeroshell vehicles are generally tested. The University of Queensland's expansion tube facilities - X1, X2 and X3 - have been widely used for subscale modelling of hypersonic flowfields (Morgan 2001).

Ground testing facilities such as the X2 facility take advantage of binary scaling to test small scale models of flight vehicles, which is the most important parameter to match in order to correctly reproduce the phenomena involved in high speed flight, such as boundary layer growth, heat transfer, and binary chemical processes. Binary scaling, also called ' ρL ' scaling, requires that the product of density and the characteristic length of the vehicle be conserved between flight and experimental conditions. However, radiative heat transfer does not follow this same scaling factor, and true similarity with flight is not created for flows where the radiative and convective heat transfer are strongly coupled. The high pressure involved in conducting scaled laboratory tests fundamentally changes the effect of radiation on the flow. This can result in significant errors in the estimates of the associated flow properties and the estimation of the heat transfer due to radiation.

The X2 facility was modified in 2006 to allow experimentation at low pressures in nonreflected shock tube mode. Nonreflected shock tube operation allowed the taking of true-flight density measurements of the radiative heat transfer and removed the scaling problems involved in radiation measurements for model vehicles, at least for part of the flowfield. Measurements were made in the region immediately behind the shock along the centreline of the core flow, where the shock remained planar. External flow fields, such as those surrounding a reentry capsule, were not reproduced. The low density operating limit was approximately 10 Pa, limited by boundary layer growth on the walls.

In order to extend the range of the facility to lower density conditions for this study, the shock tube was replaced with a tube of larger diameter. The modification resulted in the achievement of test flow at pressures as low as 1 Pa in air and 4 Pa in simulated Titan atmospheric mixtures - approximately one third of the pressure previously marking the lower limit of the facility (Brandis 2009a). This density represents flight at up to 90 km altitude in air and 360 km altitude in the Titan atmosphere (Yelle et al. 1997). At these altitudes, the radiation heat transfer is sufficient to be an important engineering issue and is complicated by the nonequilibrium, rarefied gas dynamic effects characteristic of the low density upper atmosphere region.

In the experimental work, the flow conditions produced were investigated and analysed to identify and minimise any contamination effects from the tube material, driver gas and diaphragms. Experiments were completed to investigate the nonequilibrium radiative heat transfer in a Titan test gas (98% N₂, 2% CH₄) at pressures of 13, 8, and 4 Pa and shock speeds of 6.4, 6.2, and 9.0 km/s respectively.

The collected data included static pressure measurements, pitot pressure measurements, calibrated emission spectroscopy images, and high speed camera videos. The spectral results show that the radiation present is predominantly due to the CN violet bands. A quantitative and qualitative comparison of the spectral results was made with previous data, including experimental results collected by Brandis (2009a) and Bose et al. (2005) at similar conditions, and computational results from an implementation of the Mutation collisional radiative model (Magin et al. 2006).

It was found that the peak nonequilibrium radiative heat transfer level behind the shock was consistent for the 13 and 8 Pa conditions. The spectral results showed that in comparison to these previous results, the modified facility resulted in a significant improvement in signal strength and increase in the length of test flow available at such low pressure conditions, allowing finer spectral resolution and the potential, if needed, for further spatial resolution. The facility is validated for the study of high speed entry flows, at conditions corresponding to high altitude flight.

For the 4 Pa condition, experimental results were successfully gathered to provide information about the nonequilibrium peak and fall-off rate of the radiative heating behind the shock wave. The results showed consistency and repeatability in the new low pressure condition, and sufficient test time and test gas was available to allow the capture of high resolution spectral images using an 1800 lines/mm grating.

The facility is now validated as a tool to further investigate high speed, high altitude radiative phenomena for any gas composition of interest, such as simulated atmospheres of Mars, Venus, and the gas giants.

Keywords

nonequilibrium radiation, Titan, cyanogen, collisional-radiative models, nonreflected shock tube.

Australian and New Zealand Standard Research Classifications (ANZSRC)

020503	Nonlinear Optics and Spectroscopy	40%
090107	Hypersonic Propulsion and Hypersonic Aerodynamics	40%
091501	Computational Fluid Dynamics	20%

Contents

Résumé	xi
Abstract	xv
Introduction Générale	1
Introduction	5
1 Literature Review	9
1.1 Hypersonic facilities	9
1.2 Titan atmospheric entry investigations	14
1.3 Summary	21
2 Nonequilibrium Modelling Review	23
2.1 Review of existing collisional-radiative models	25
2.2 Recommended collisional-radiative models	30
2.3 Experimental validation	47
2.4 Summary	54

3 Experimental Considerations	55
3.1 Facility modifications	55
3.2 Test conditions	65
3.3 Optical diagnostics	65
3.4 Emission spectroscopy calibration	69
3.5 Summary	75
4 Computational Considerations	77
4.1 Quasi-one-dimensional calculations	77
4.2 Two-dimensional axisymmetric calculations	79
4.3 Radiative heat transfer calculations	80
4.4 Summary	84
5 Facility Analysis	87
5.1 Validation of flow quality: 13 Pa test condition (altitude 302 km)	88
5.2 Low pressure test condition development	95
5.3 Summary of developed conditions for Titan simulated atmospheres	111
5.4 Summary	112
6 Emission Spectroscopy Analysis	115
6.1 13 Pa condition	115
6.2 8 Pa condition	126
6.3 4 Pa condition	130
6.4 A note on shot-to-shot consistency	136
6.5 Further discussion and summary of results	137
Summary and Conclusions	143
References	149

A Spectrometry Notes	165
A.1 Alignment procedure	165
A.2 Non-linear response of the spectrometer	167
B Uncertainty Analysis	171
B.1 Flow condition	171
B.2 Spectral measurements	173
C Simulation Scripts	179
C.1 L1d3 simulations	179
C.2 Eilmer3 simulations	183
D Calibration Code for Emission Spectroscopy	191
D.1 Main code	191
D.2 Main function	192
D.3 Other functions	206
D.4 Calibration lamp data file	209
E Experimental Summary	211
F Calibrated Spectral Data	213

List of Figures

1	Freestream pressure vs altitude for Titan.	7
1.1	Flow in a shock tube.	10
1.2	Expansion tube mode schematic and space-time diagram for the X2 facility.	11
1.3	Schematics of the two modes of operation for the X2 facility.	13
1.4	Nonreflected shock tube mode schematic and space-time diagram for the X2 facility.	14
1.5	Radiating shock layer during a blunt body entry.	15
1.6	Outline of an aerocapture entry trajectory.	16
1.7	Comparisons of modelling and experimental profiles of CN(Violet) intensities at four different conditions.	19
2.1	Description of the collisional-radiative modelling process	24
2.2	A sample of simulated CEV stagnation point radiation spectrum and spectral coverage in different EAST shots.	37
2.3	Contribution of individual species to the total radiative flux for the Post-Ta(B) trajectory.	38
2.4	Comparison of rise times and fall off rates between ViSpeN and the collisional-radiative model by Magin et al. at 98 % N ₂ and 2 % CH ₄ , 5.7 km/s.	46

2.5	Computed and measured CN violet intensities integrated over the spectral range 400-430 nm in the post shock region.	47
2.6	Spectra of individual species for the Post-Ta(B) trajectory point at 191 s. .	48
2.7	Shock tube conditions investigated for air.	50
2.8	Shock tube conditions investigated for Titan mixtures.	50
2.9	Spectrum fitting with $V_s = 12.4 \text{ km/s}$, $L = 2.3 \text{ mm}$, N_2 ($T_r = 3500 \text{ K}$, $T_v = 5000 \text{ K}$, N_2^+ ($T_r = 17500 \text{ K}$, $T_v = 9000 \text{ K}$).	51
2.10	Temperature distribution for a) shock propagation velocity of 12.4 km/s in the case of air, and b) shock propagation velocity of 11.9 km/s in the case of pure nitrogen.	52
2.11	Spectra fitting of NASA Ames data.	53
3.1	Schematic of the nonreflected shock tube mode of operation.	57
3.2	Stagnation line radiative heating profile during entry showing the region of the flow which is captured by the shock tunnel facility in nonreflected shock tube mode.	58
3.3	Sketch of the flow behind the shock wave in a shock tube operating at a low initial pressure.	58
3.4	The advantages of a compound driver.	60
3.5	Photograph of the modified X2 facility in NRST-Al mode.	61
3.6	NRST-Al mode schematic and space-time diagram.	62
3.7	Schematic of the radiation collection methodology.	67
3.8	Schematic of the final optical layout used in the NRST-Al experiments. .	68
3.9	Operating mode of the periscope.	69
3.10	Calibration data and the spline fit of the spectral irradiance of the calibration lamp over the wavelengths examined (200-450 nm).	73
3.11	Schematic of the calibration setup for the external optical components. .	76
4.1	Computational domain for the L1d3 simulations of the partial facility. . .	79
4.2	Computational domain for the Eilmer3 simulations of the modified facility.	81

4.3	Computational domain for the <i>Eilmer3</i> simulations of the original X2 facility.	82
5.1	Shock speed variation down the tube for the 13 Pa condition experiments.	90
5.2	High speed camera footage for the 13 Pa freestream condition from 0 - 7 μ s.	91
5.3	High speed camera footage for the 13 Pa freestream condition from 8 - 15 μ s.	92
5.4	Transverse and temporal variation of Pitot pressure 30 mm downstream of the shock tube exit for the 13 Pa Titan condition.	94
5.5	Contour plot of temperature demonstrating the flow structures at the area change for the X2-NRST-Al facility.	96
5.6	Contour plot of temperature demonstrating the flow structures at the area change for the X2-NRST-Al facility.	97
5.7	Contour plot of temperature demonstrating the flow structures at the shock tube exit for the X2-NRST-Al facility.	98
5.8	Contour plot of temperature demonstrating the flow structures at the shock tube exit for the X2-NRST facility.	99
5.9	Shock speed variation down the tube for the 8 Pa condition experiments.	101
5.10	High speed camera footage for the 8 Pa freestream condition from 0 - 7 μ s.	102
5.11	High speed camera footage for the 8 Pa freestream condition from 8 - 15 μ s.	103
5.12	Transverse and temporal variation of Pitot pressure 30 mm downstream of the shock tube exit for the 8 Pa Titan condition.	104
5.13	Shock speed variation down the tube for the 4 Pa condition experiments.	105
5.14	High speed camera footage for the 4 Pa freestream condition from 0 - 7 μ s.	107
5.15	Transverse and temporal variation of Pitot pressure 30 mm downstream of the shock tube exit for the 4 Pa Titan condition.	108
5.16	Shock speed variation down the tube for the 1 Pa air condition experiments.	109
5.17	Transverse and temporal variation of Pitot pressure 30 mm downstream of the shock tube exit for the 1 Pa air condition.	110
6.1	An axial profile of the power density as the shock exited the shock tube at a freestream pressure of 13 Pa.	117

6.2 An axial profile of the power density as the shock exited the shock tube at a freestream pressure of 13 Pa.	118
6.3 NRST-Al spectral power density and its cumulative integration for the 13 Pa condition with important species indicated.	119
6.4 NRST-Al spectral power density and its cumulative integration for the 13 Pa condition.	120
6.5 A comparison of spectral power density and its cumulative integration for the 13 Pa condition.	122
6.6 An axial profile of the power density as the shock exited the shock tube at a freestream pressure of 13 Pa.	123
6.7 NRST-Al spectral power density and its cumulative integration for the 13 Pa condition with important species indicated.	124
6.8 NRST-Al spectral power density and its cumulative integration for the 13 Pa condition.	125
6.9 A comparison of spectral power density and its cumulative integration for the 13 Pa condition.	127
6.10 An axial profile of the power density as the shock exited the shock tube at a freestream pressure of 8 Pa.	129
6.11 NRST-Al spectral power density and its cumulative integration for the 8 Pa condition with important species indicated.	130
6.12 NRST-Al spectral power density and its cumulative integration for the 8 Pa condition.	131
6.13 A comparison of spectral power density and its cumulative integration for the 8 Pa condition.	132
6.14 An axial profile of the power density as the shock exited the shock tube at a freestream pressure of 4 Pa.	133
6.15 NRST-Al spectral power density and its cumulative integration for the 4 Pa condition with important species indicated.	134
6.16 NRST-Al spectral power density and its cumulative integration for a freestream pressure of 4 Pa.	135

6.17 A comparison of spectral power density and its cumulative integration for a freestream pressure of 4 Pa.	136
6.18 Shot-to-shot variation of the integrated power density for the 13 Pa condition.	138
6.19 Shot-to-shot variation of the integrated power density for the 8 Pa condition.	139
6.20 Shot-to-shot variation of the integrated power density for the 4 Pa condition.	139
A.1 Photograph of the final optical layout used in the nonreflected shock tube experiments.	166
A.2 Photograph of the alignment tool used for locating the laser diode on the centreline of the tube.	166
A.3 Photograph of the alignment tool set up with the slats.	167
A.4 Spectral image of the alignment tool taken with a fluorescent light.	167
A.5 Variation of camera response with exposure time.	169
F.1 Raw and calibrated data for x2s1475.	214
F.2 Raw and calibrated data for x2s1476.	215
F.3 Raw and calibrated data for x2s1460.	216
F.4 Raw and calibrated data for x2s1463.	217
F.5 Raw and calibrated data for x2s1465.	218
F.6 Raw and calibrated data for x2s1468.	219
F.7 Raw and calibrated data for x2s1469.	220
F.8 Raw and calibrated data for x2s1470.	221
F.9 Raw and calibrated data for x2s1471.	222
F.10 Raw and calibrated data for x2s1472.	223
F.11 Raw and calibrated data for x2s1473.	224
F.12 Raw and calibrated data for x2s1474.	225
F.13 Raw and calibrated data for x2s1493.	226
F.14 Raw and calibrated data for x2s1494.	227

F.15 Raw and calibrated data for x2s1495.	228
F.16 Raw and calibrated data for x2s1498.	229
F.17 Raw and calibrated data for x2s1477.	230
F.18 Raw and calibrated data for x2s1499.	231
F.19 Raw and calibrated data for x2s1500.	232
F.20 Raw and calibrated data for x2s1501.	233
F.21 Raw and calibrated data for x2s1503.	234
F.22 Raw and calibrated data for x2s1504.	235
F.23 Raw and calibrated data for x2s1505.	236
F.24 Raw and calibrated data for x2s1513.	237
F.25 Raw and calibrated data for x2s1514.	238
F.26 Raw and calibrated data for x2s1528.	239
F.27 Raw and calibrated data for x2s1529.	240
F.28 Raw and calibrated data for x2s1530.	241
F.29 Raw and calibrated data for x2s1509.	242
F.30 Raw and calibrated data for x2s1510.	243
F.31 Raw and calibrated data for x2s1511.	244
F.32 Raw and calibrated data for x2s1517.	245
F.33 Raw and calibrated data for x2s1518.	246
F.34 Raw and calibrated data for x2s1519.	247
F.35 Raw and calibrated data for x2s1520.	248
F.36 Raw and calibrated data for x2s1521.	249
F.37 Raw and calibrated data for x2s1522.	250
F.38 Raw and calibrated data for x2s1523.	251
F.39 Raw and calibrated data for x2s1524.	252
F.40 Raw and calibrated data for x2s1527.	253

F.41 Raw and calibrated data for x2s1531.	254
F.42 Raw and calibrated data for x2s1532.	255
F.43 Raw and calibrated data for x2s1533.	256
F.44 Raw and calibrated data for x2s1534.	257
F.45 Raw and calibrated data for x2s1535.	258
F.46 Raw and calibrated data for x2s1536.	259
F.47 Raw and calibrated data for x2s1538.	260
F.48 Raw and calibrated data for x2s1539.	261
F.49 Raw and calibrated data for x2s1540.	262
F.50 Raw and calibrated data for x2s1541.	263
F.51 Raw and calibrated data for x2s1542.	264
F.52 Raw and calibrated data for x2s1543.	265
F.53 Raw and calibrated data for x2s1544.	266
F.54 Raw and calibrated data for x2s1545.	267
F.55 Raw and calibrated data for x2s1546.	268
F.56 Raw and calibrated data for x2s1547.	269

List of Tables

2.1	General comparison of the two recommended collisional-radiative models for air.	31
2.2	Comparison of energy levels models for atomic nitrogen.	34
2.3	Comparison of energy levels models for atomic oxygen.	35
2.4	Radiative transitions of CN and N ₂ electronic states	39
2.5	Forward and reverse reaction rates: Titan collisional-radiative model	40
2.6	Excitation energy: N ₂	41
2.7	Dissociation energy: Titan molecules	41
2.8	Thermal nonequilibrium chemistry model	42
2.9	Reaction rate constants for Titan atmospheric entry	43
3.1	Axial locations of transducers and diaphragms in the X2 NRST-Al configuration.	64
3.2	Experimental fill conditions for the modified X2 NRST-Al facility.	66
4.1	Molecular transitions modelled in Specair with their (very) approximate spectral location.	83
5.1	Experimental fill conditions for the 1 Pa condition.	111

5.2	Summary of the developed Titan conditions.	113
A.1	Measured scaling factor for converting the $10\ \mu\text{s}$ calibration exposures to the experimental exposure time.	168
B.1	The percentage uncertainty in the measurement of the location of the shock arrival.	172
E.1	Summary of the fill pressures and shock speeds calculated at all transducer locations down the tube for all experiments.	212

Nomenclature

δ	Shock stand-off distance
ϵ	Optical component efficiency
ρ_∞	Free stream density
$a(x, y)$	Unprocessed spectral image
$b(x, y)$	Background component of spectral image
$E(\lambda, z)$	Spectral irradiance of measured image
$E_c(\lambda)$	Spectral irradiance of calibration lamp
E_s	Total energy emitted by the gas in all directions per second per unit volume immediately behind the shock
$f(x, y), f(\lambda, z)$	Measured image
$f_c(x, y), f_c(\lambda, z)$	Calibration image
$g_c(\lambda, z)$	Scaling map
M	Magnification of the optical system
$n(x, y)$	Noise component of spectral image
t	Exposure time of measured image
t_c	Exposure time of calibration image

V_∞	Free stream velocity
A	Radiative lifetime
f_J	Population of rotational internal energy levels
f_v	Population of vibrational internal energy levels
f_{el}	Population of electronic internal energy levels
L	Characteristic length scale of a vehicle
n_s	Concentration of species, s

Introduction générale

Définition du problème

Depuis que le premier satellite artificiel, Sputnik 1, a été lancé avec succès en 1957, il y a eu un grand intérêt dans le monde entier pour l'exploration et la recherche spatiale, tant pour les missions vers la lune que pour mieux comprendre d'autres corps planétaires. Les missions d'entrée atmosphérique pour explorer et améliorer notre connaissance des autres corps planétaires ont été, et continuent d'être, développées. Pour la réussite de ces missions, il est essentiel que les matériaux de protection thermique installés à la surface du véhicule suffisent à le protéger des flux thermiques, convectifs et radiatifs, à la surface au cours de la re-entrée. Toutefois, puisque le poids total est fortement limité par le coût de lancement d'un tel véhicule, la conception efficace du véhicule nécessite des prédictions précises de ces conditions aero-thermiques.

Afin d'atteindre cet objectif, un certain nombre d'études théoriques et expérimentales, pour une variété de véhicules et d'atmosphères, ont été accomplies. Les missions relatives à l'entrée dans l'atmosphère de Titan, telles que la mission Huygens et les études aérocaptures de la NASA, sont d'un intérêt particulier pour ce projet. Il a été constaté que, pour des trajectoires aérocapture avec des vitesses d'entrée entre 6 et 10 km/s, l'échauffement radiatif domine le transfert de chaleur à la surface du véhicule et que le flux de chaleur radiatif maximum est d'environ quatre fois supérieur au flux convectif (Olejniczak et al. 2003; Takashima et al. 2003; Witasse et al. 2006). Au pic de flux de chaleur de la trajectoire, le radical CN, formé par la dissociation du méthane et de l'azote, produit la majeure portion du rayonnement dans la région après le choc pour l'entrée dans une atmosphère de Titan. La dynamique de la chimie hors équilibre a une importance particulière pour l'entrée dans l'atmosphère de Titan, ce qui cause une augmentation significative des

niveaux électroniques exictés de CN par rapport aux valeurs d'équilibre, produisant des niveaux élevés de rayonnement. Des effets similaires ont été démontrés pour la sonde Huygens (Baillion et al. 1997).

Puisqu'il a été démontré que le flux de déséquilibre radiatif a une telle importance pour les missions Titan (Olejniczak et al. 2004), de nombreuses recherches expérimentales ont été menées pour mesurer précisément ce paramètre. En particulier, les expériences de Bose et al. (2005) et Brandis (2009a) ont fourni des données de spectroscopie d'émission calibrés sur le transfert de chaleur radiatif pour un certain domaine de la trajectoire d'entrée du véhicule. Toutefois, ces mesures ne couvrent pas toute la trajectoire d'entrée car elles sont limités à la région de plus haute pression (et, par conséquent, de plus basse altitude).

Ayant ceci à l'esprit, il est souhaitable que ces études soient étendues aux mesures expérimentales dans des conditions de basse pression en appliquant des techniques de spectroscopie d'émission, pour étendre les mesures de Bose et al. (2005) et Brandis (2009a).

Par conséquent, l'objectif principal de ce projet est de démontrer qu'il est possible de produire des mesures de transfert de chaleur radiatif calibré dans la région de déséquilibre d'une onde de choc à des pressions inférieures à 13 Pa (ie. pour des altitudes supérieures à 302 km).

Objectifs de la thèse

Cette thèse étudie le transfert de chaleur radiatif rencontré dans les conditions d'écoulement hypersonique raréfié qui seraient rencontrées au cours d'une mission d'aérocapTURE dans l'atmosphère de Titan. L'objectif principal de ce projet est de produire des mesures calibrées de transfert de chaleur radiatif à des pressions aussi faibles que 4 Pa pour une atmosphère de Titan, correspondant à une partie importante de la trajectoire de vol où les effets radiatifs et de déséquilibre sont importants (une altitude de 359 km, Yelle et al. 1997).

En résumé, les objectifs spécifiques du projet sont les suivants:

1. Modifier l'installation X2 pour permettre l'expérimentation à basse pression en mode tube à choc nonréfléchi.

2. Étudier et analyser les conditions d'écoulements et identifier (et minimiser) les effets de la contamination par la matière du tube, le gaz vecteur, et les diaphragmes.
3. Effectuer des mesures à basse pression du transfert de chaleur radiatif en utilisant la spectroscopie d'émission et interpréter les données spectrales par rapport aux derniers modèles de rayonnement.

Introduction

Problem definition

Ever since the first artificial satellite, Sputnik 1, was launched successfully in 1957, there has been a strong, worldwide interest in space exploration and investigation, both for missions to the moon and to better understand other planetary bodies. Atmospheric entry missions to explore and improve our knowledge of other planetary bodies have been (and continue to be) developed. In order for these missions to be successful, it is essential that the thermal protection layers installed on the vehicle bodies be sufficient to protect the craft from the convective and radiative heat transfer experienced on the surface during the entry procedure. However, as the total mass is heavily restricted by the expense of launching such a vehicle, efficient design of the vehicle requires accurate predictions of these heat loads.

In order to achieve this, a number of computational and experimental studies for a variety of vehicles and atmospheres have been completed. Of particular interest for this project, are those missions relating to atmospheric entry to Titan, such as the Huygens mission and the NASA aerocapture studies. It has been found that for aerocapture trajectories with entry speeds between 6 and 10 km/s, the radiative heating dominates the heat transfer to the surface of the vehicle and the peak radiative heat flux is approximately four times that of the convective (Olejniczak et al. 2003; Takashima et al. 2003; Witasse et al. 2006). However, there is a significant level of disagreement between the models, which creates a need for the collection of further data.

At the peak heating point of the trajectory, the formation of the CN radical by the dissociation of the atmospheric methane and nitrogen is the dominant radiator in the

post-shock region for Titan atmospheric entry. Of special importance to Titan entry is the interesting dynamics of the nonequilibrium chemistry, which causes CN levels to increase significantly over equilibrium values, resulting in high levels of radiation. Similar effects were discovered for the Huygens probe (Baillion et al. 1997).

Therefore, as the nonequilibrium radiative heat flux has been shown to be of such importance for Titan missions (Olejniczak et al. 2004), a number of experimental investigations to accurately measure this parameter have been completed. In particular, the experiments of Bose et al. (2005) and Brandis (2009a) provide emission spectroscopy data giving the calibrated radiative heat transfer at a variety of entry conditions. However, these measurements do not encompass the entire entry trajectory followed by a vehicle, and are focussed on the higher pressure (and, therefore, lower altitude) region.

With this in mind, it is desired that these studies be extended to include experimental measurements at conditions of lower freestream pressure by applying emission spectroscopy techniques, continuing the measurements of Bose et al. (2005) and Brandis (2009a).

Therefore, the primary aim of this project is to demonstrate that it is possible to produce calibrated measurements of radiative heat transfer in the nonequilibrium region behind a shock wave at pressures lower than 13 Pa for a simulated Titan atmosphere (i.e. for altitudes greater than 302 km; see Figure 1).

Project objectives

This thesis investigates the radiative heat transfer encountered in rarefied, hypervelocity flow conditions such as would be experienced during an aerocapture mission to Titan. The primary aim of this project is to produce calibrated measurements of radiative heat transfer at pressures as low as 4 Pa for a Titan atmosphere, corresponding to an important part of the flight path (altitude of 359 km, Yelle et al. 1997) where the nonequilibrium radiative effects are important.

In summary, the specific aims of the project are as follows:

1. To modify the X2 facility to allow experimentation at low pressures in nonreflected shock tube mode.
2. To investigate and analyse the flow conditions produced and identify and minimise any contamination effects from the tube material, driver gas, and diaphragms.

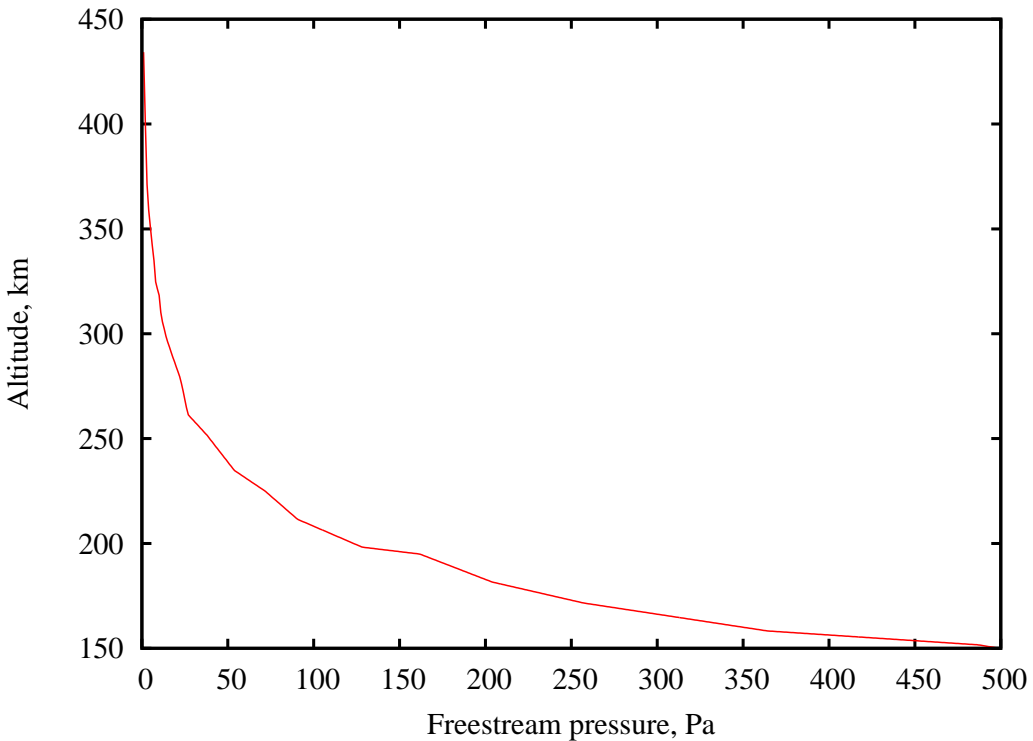


Figure 1 : Freestream pressure vs altitude for Titan. Adapted from Yelle et al. (1997).

3. To perform radiative heat transfer measurements at low pressures using emission spectroscopy and interpret the spectral data with reference to the latest radiation models.

Outline of thesis

Chapter 1 contains background information on hypersonic test facilities and the basic theory of experimental work in a free-piston nonreflected shock tube facility. A short summary of the recent investigations into both experimental and computational measurements of Titan entry flows is then conducted.

Chapter 2 outlines the collisional radiative modelling technique and highlights the modifications recommended for future work.

Chapter 3 details the experimental setup used for the experiments presented in later chapters. The X2 facility in its standard expansion tube form is briefly outlined compared with the modified experimental setup. The modified facility is described in detail, including the location of all instrumentation and the equipment used for taking all experimental readings. A table is given to provide all information on the three test conditions

investigated, including all section fill pressures and gas mixtures. The layout of the emission spectroscopy measurements and the details of the optical instrumentation is also presented - including all experimental settings used.

Chapter 4 reviews the computational codes used to analyse the shock tube flow, the chemistry behind the shock, and the radiative transfer behind the shock. The aim of this chapter is to provide all of the information relevant to reproducing the computational work.

Chapter 5 demonstrates the success of the facility modifications through details of the condition development and an investigation of the flow quality. The 13 Pa condition is chosen as a reference condition (approximate shock speed of 7 km/s) as it overlaps with data available from previous experimental studies Bose, Wright, and Bogdanoff (2005, Brandis (2009a). The validation of this condition includes comparisons of the experimental shock speed, test time and core flow diameter with those calculated with the computational codes described in the chapter. Particular attention is given to an analysis of the effect of the area change in the shock tube.

Chapter 6 presents the spectral data obtained over the course of the project. These results include a brief investigation into the quality of the results from the emission spectroscopy work and a comparison to the computational flow predictions, but focusses on the analysis of the spectral data. A comparison of all aspects of the 13 Pa condition is compared with the work of Bose et al. (2005) and Brandis (2009a) to provide a reference condition for this new facility.

CHAPTER 1

Literature Review

The design of hypersonic flight vehicles is a complex task, involving many interacting multidisciplinary phenomena. Not all of the processes are completely understood at the moment, and the integration of data from ground-based test facilities, computational fluid dynamics calculations, and flight tests is essential. Flight tests are an essential part of the process of the validation and certification of flight vehicles. However, these flight tests must be supported and preceded by ground-based experimental studies in order to define the fundamental issues involved. There are many reasons for conducting ground-based experimental work, including the validation and calibration of the results generated using computational methods and for the understanding of the fundamental physical processes governing the aerothermodynamics.

1.1 Hypersonic facilities

In the hypersonic regime, flows behave very differently than even at low supersonic Mach numbers. Important factors for hypersonic flight include molecular dissociation, ionization, chemical and thermal nonequilibrium, rarefied gas dynamics at high altitudes, radiation heat transfer, and ablation. These effects produce specific design constraints which must be met in order to produce a successful hypersonic mission. It has been widely recognised that, “at best, hypersonic facilities currently available are partial simulation

facilities" (Neumann 1989), and a variety of facilities are used in order to investigate the different aspects and uncertainties of hypersonic flight.

One important type of hypersonic facility is the wind tunnel, which can be divided into a number of different categories based on the duration of the test time. These range from continuous and blow-down-type intermittent wind tunnels, which can achieve test times ranging from hours to minutes or even seconds, to electric arc and combustion-heated facilities, which can reach much higher enthalpies and can produce minutes of test time. Pulsed facilities include shock tunnels, which are capable of producing flows beyond Mach 20 but are limited to milliseconds of test time. For investigations into high-temperature phenomena, a large primary shock speed is necessary. This can be achieved in a variety of ways, however the effect of such high shock velocities is to limit the achievable test time to the order of hundreds of microseconds.

Two types of impulse facility are primarily used for hypersonic testing - shock tubes (or tunnels) and expansion tubes (or tunnels).

Initial conditions

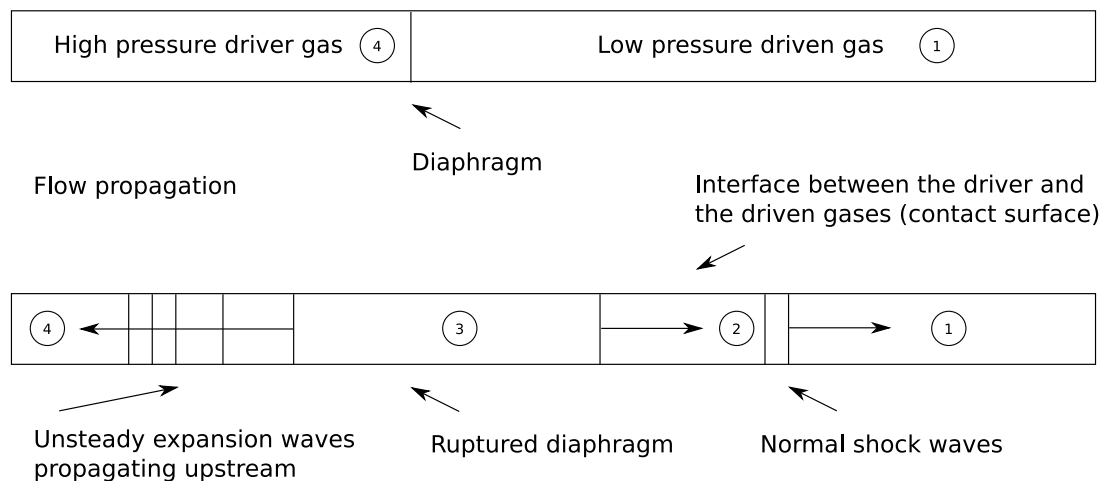


Figure 1.1 : Flow in a shock tube. (Scott 2006)

A basic shock tube is shown in Figure 1.1. High pressure driver gas (section 4) is initially separated from low pressure gas (section 1) by a diaphragm. These gases can be at different temperatures and have different molecular compositions. When the diaphragm bursts, the low pressure gas is processed by the shock wave that propagates into that region and an expansion wave propagates upstream into the driver gas. As the shock wave propagates downstream, the pressure of the processed gas in section 2 is increased, and a mass motion is induced. The interface between the driver and driven gases is called the contact surface. Energy is added to the driver gas in the form of thermal and chemical

enthalpy and kinetic energy. The balance between the energy storage modes depends on the shock Mach number and on the overall pressure and length scales involved.

A shock tunnel expands on this concept by using a reflected shock to stagnate the test gas. The expansion of this test gas through a nozzle produces the final experimental flow. Expansion tubes, however, do not stagnate the flow and are therefore not required to contain gas at the very high stagnation pressures and temperatures involved.

1.1.1 The X2 facility

The University of Queensland currently has three tunnel facilities capable of producing hypervelocity flows. The X2 facility at the University of Queensland is typically used as an expansion tunnel, with a layout as shown in Figure 1.2.

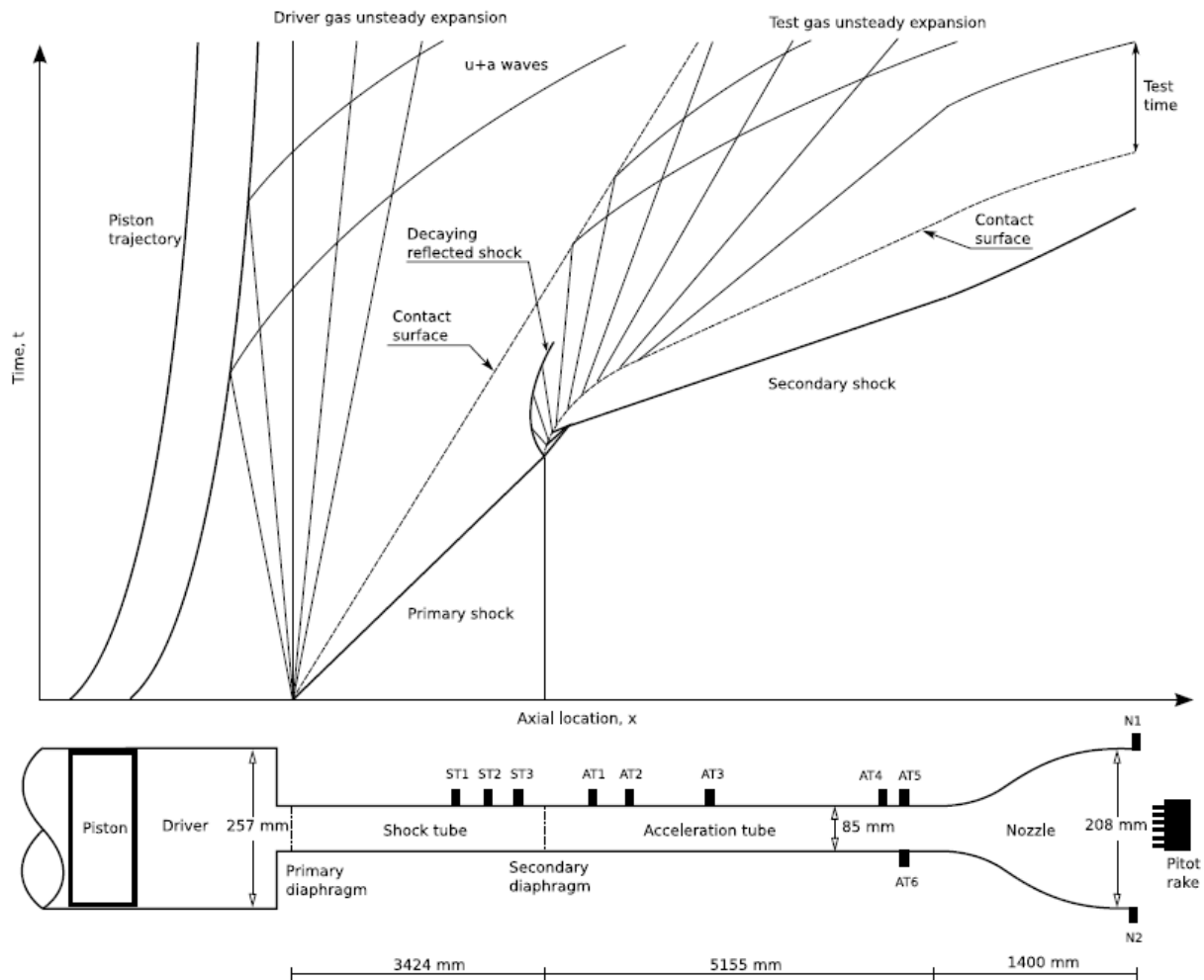


Figure 1.2 : Expansion tube mode schematic and space-time diagram for the X2 facility. (Potter et al. 2008)

It consists of a reservoir, a piston launch station, a compression tube, a shock tube, an acceleration tube and a dump tank. In its standard configuration, X2 is approximately 20 m long, with a bore diameter of 85 mm in the shock and acceleration tubes. Under normal expansion tube conditions, a primary diaphragm is located between the compression and the shock tubes and a secondary diaphragm between the shock and acceleration tubes.

The X2 facility uses high pressure gas in the reservoir ($\approx 1.15 \text{ MPa}$) to accelerate the single-stage, free-moving piston and compress the gas (usually a mixture of argon and helium) in the compression tube. When the piston is released, the high pressure of the reservoir gas behind it pushes downstream and compresses the driver gas until the diaphragm bursts and a shock wave propagates downstream. The primary diaphragm ($\approx 1.2 \text{ mm thickness}$) bursts when the pressure in the compression tube reaches approximately 15.5 MPa and the gas expands into the shock tube, compressing the test gas and bursting the secondary diaphragm. With the rupture of the light secondary diaphragm at the arrival of the shock wave, a shock wave of greatly increased speed propagates into the low density acceleration gas. The resultant change in velocity between the two adjacent shock heated regions then causes an unsteady u-a expansion wave to propagate back into the test gas. This creates a significant increase in the stagnation pressure and temperature of the test gas and because it is in a supersonic region, the expansion wave is swept downstream. In an expansion tunnel, a hypersonic nozzle is then used to expand the accelerated test gas into the test section. Figure 1.2 shows the simplified workings of the X2 facility in expansion tunnel mode.

Primarily, experimental work conducted in expansion tunnel facilities such as X2 involve the testing of subscale models of hypersonic craft or other geometries. This is demonstrated in Figure 1.3(a), where the test gas produces a steady bow shock ahead of a small model in the test section. However, the use of subscale models in the facilities requires that the test flow conditions are also suitably scaled, such that similarity between flight and experiment is maintained. For a constant test gas velocity between flight and experiment, binary scaling is used. Binary scaling, also called ' ρL ' scaling, requires that the product of density and the characteristic length, L , of the vehicle be conserved between flight and experimental conditions. However, in a test flow in which the radiative heat transfer is a significant proportion of the total heat transfer, similarity with flight is not maintained with binary scaling. The scaling of the model results in a corresponding scaling of the total convective heat transfer component, proportional to $1/L$, while the radiative heat transfer component remains constant (Capra and Morgan 2006; Capra 2007). When the flow is scaled, the convective losses remain constant as a percentage of the total enthalpy flux. For radiating flows, the similarity in the radiative losses is not

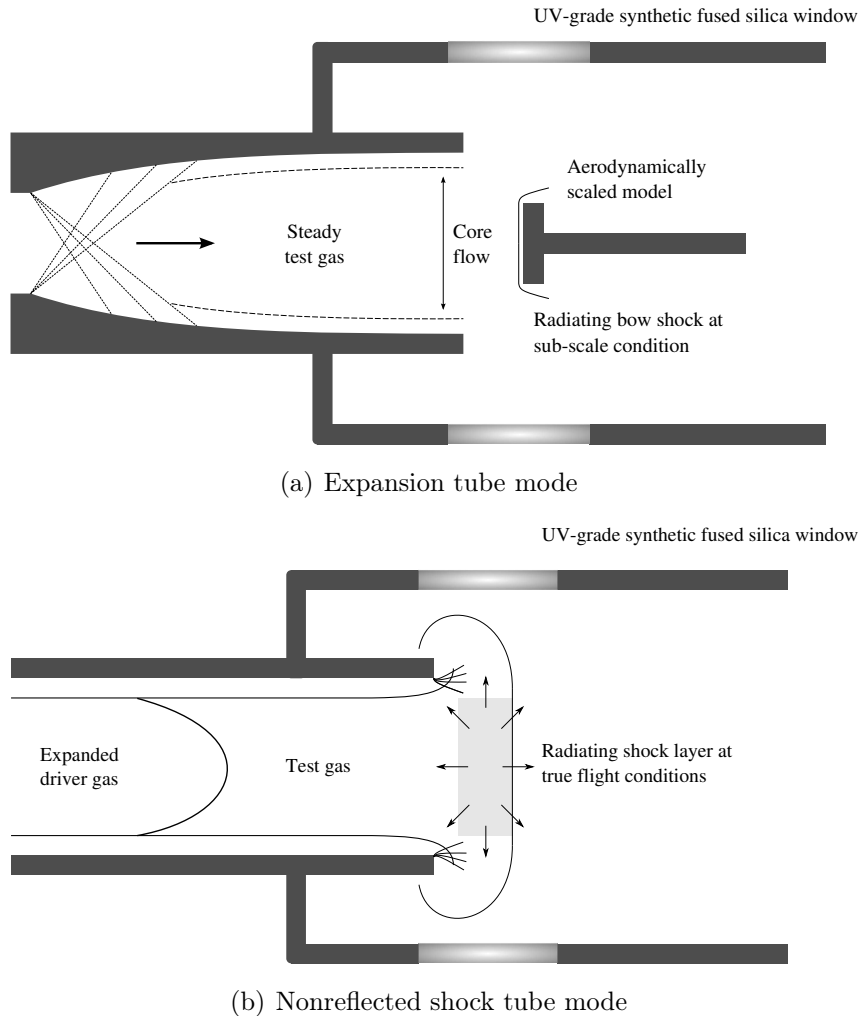


Figure 1.3 : *Schematics of the two modes of operation for the X2 facility. The first diagram outlines the expansion tunnel mode and the second the nonreflected shock tube experiments.*

maintained between the subscale model and flight vehicle.

The direct simulation of the flight conditions is, therefore, desired for radiating flows. This is achieved in the X2 facility by modifying the operating in nonreflected shock tube mode. Figure 1.3 outlines the difference between the expansion tunnel mode and the non-reflected shock tube mode. In nonreflected shock tube mode, no model is placed in the test section. Rather, the test section contains the stationary test gas and the region of interest is the processed gas immediately behind the shock wave.

The operation of the X2 facility in nonreflected shock tube mode is shown in Figure 1.4. Prior to the rupture of the primary diaphragm, the operation of the facility in expansion tube mode and nonreflected shock tube mode remains unmodified. In nonreflected shock tube mode, however, the secondary diaphragm is removed from the facility and the test gas is contained in both the shock tube and the test section, with a direct connection

between the shock tube and the test section.

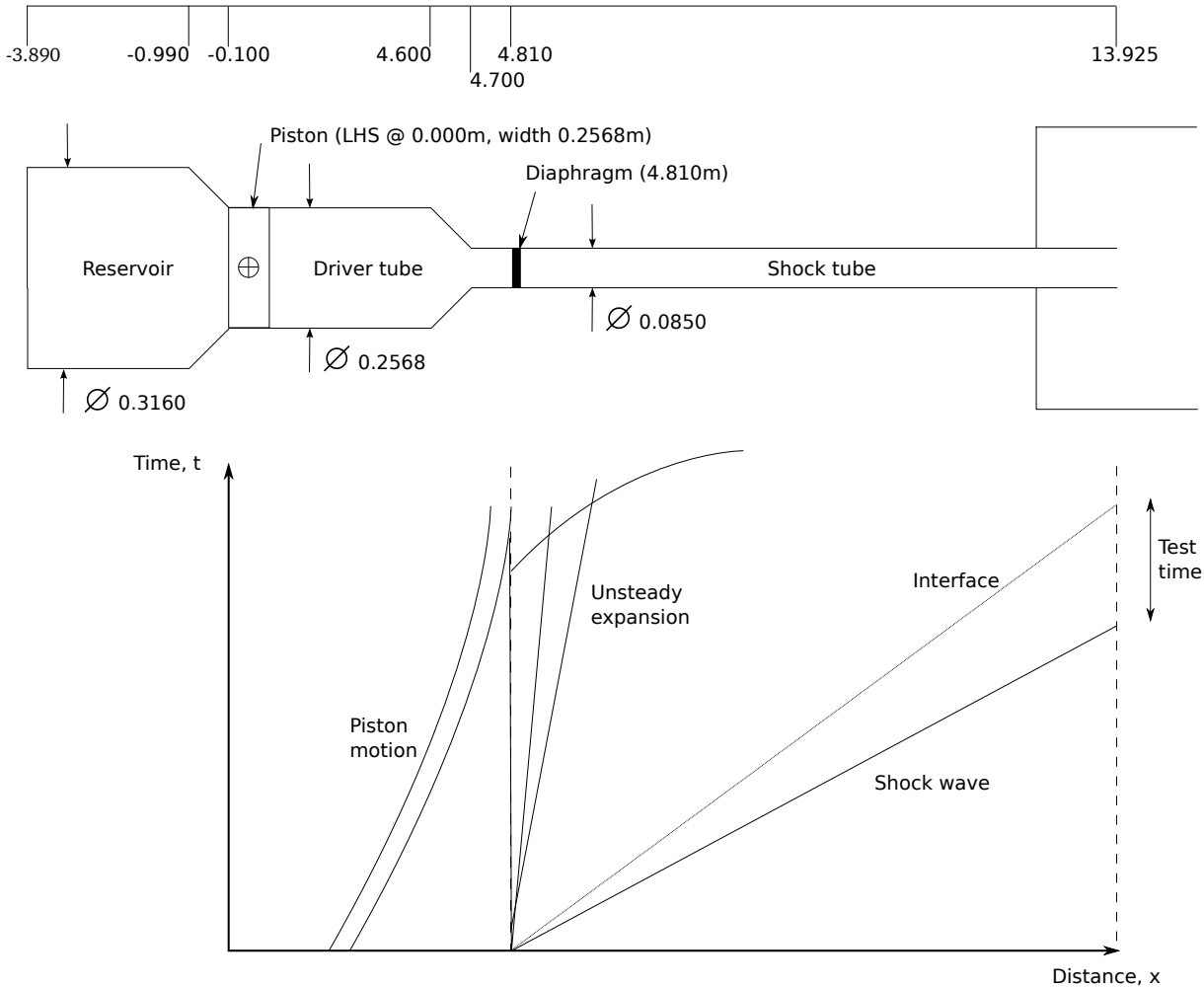


Figure 1.4 : Nonreflected shock tube mode schematic and space-time diagram for the X2 facility.

1.2 Titan atmospheric entry investigations

In the Introduction, the primary aim of this thesis was defined as the gathering of calibrated measurements of radiative heat transfer in the nonequilibrium region behind a shock wave at pressures lower than 13 Pa for a simulated Titan atmosphere (i.e. for altitudes greater than 302 km). This statement leads to a number of questions:

1. Why investigate a simulated Titan atmosphere?
2. Why measure radiative heat transfer?
3. Why focus on altitudes greater than 302 km?

The answer to the first of these questions is quite straightforward - as the only planetary body in our solar system other than the Earth with a thick nitrogen atmosphere, Titan is of considerable scientific interest. In fact, the Voyager 1 mission, launched in September 1977, deviated from its original course in order to take a closer look at Titan. Unable to see through the thick haze surrounding Titan, the Huygens mission was developed to land on the surface of Titan and record a variety of information during its 2.5 hour descent to the surface. The results of this mission revealed “the uniqueness of Titan in the Solar System as a planetary-scale laboratory for studying pre-biotic chemistry, which confirms the astro-biological interest of Saturn’s largest moon” (Lebreton et al. 2005).

The second question - *Why measure radiative heat transfer?* - requires further explanation.

During atmospheric entry, a bow shock is formed ahead of the vehicle. The convective and radiative heating loads on the vehicle, produced by this shock-heated region, can be quite high. Immediately behind the shock wave, the gas particles are in an excited state, and the relaxation of energy to local equilibrium conditions occurs over a finite distance through the collision of particles. This nonequilibrium region and the relaxation towards equilibrium is highlighted in Figure 1.5.

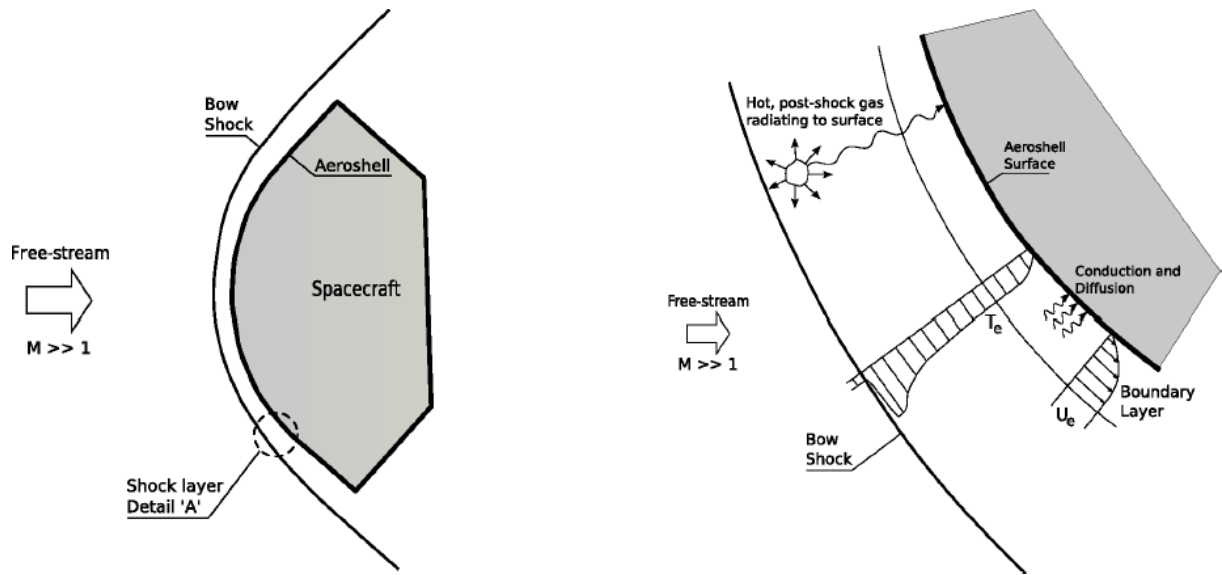


Figure 1.5 : Radiating shock layer during a blunt body entry. Courtesy of Peter Jacobs.

Analyses by Takashima et al. (2003) have shown that the non-equilibrium shock layer that forms in Titan’s atmosphere results in significant amounts of CN radiation due to the presence of methane in Titan’s predominantly nitrogen atmosphere. This is driven by a special feature of the nonequilibrium chemistry of the N₂-CH₄ mixture, which allows

CN concentrations many times larger than equilibrium to develop. It is caused by the $C + N_2 \rightarrow CN + N$ reaction, which overshoots CN equilibrium levels due to the low N concentration immediately behind the shock.

As a follow-on to the Cassini-Huygens mission, an aerocapture mission to Titan is being developed (Bailey et al. 2003; Way et al. 2003; Olejniczak et al. 2004). Aerocapture uses the drag produced by the spacecraft's movement through the upper atmosphere to decelerate the vehicle so that it settles into the desired orbit in a single pass, as shown in Figure 1.6. For a Titan entry, aerocapture has been shown (Takashima et al. 2003) to lead to a potential overall mass saving of up to 66 %, making a Titan aerocapture mission a crucial further step in the development of spacecraft.

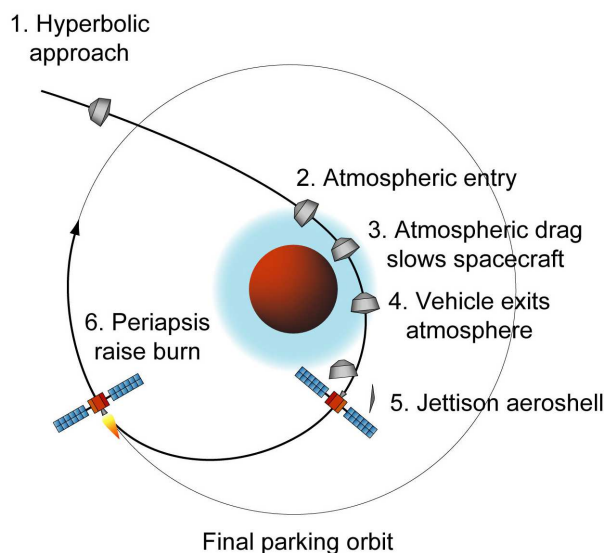


Figure 1.6 : Outline of an aerocapture entry trajectory. Courtesy of Troy Eichmann.

The aerocapture technique allows for the transport of greater payloads, as the braking manoeuvre is completed without the requirement for an onboard retrobraking rocket system and the associated fuel load. In order to successfully achieve aerocapture, accurate predictions of the lift and drag forces on the vehicle are required. It is also necessary to have reliable estimates of the conductive and radiative heat transfer between the vehicle and the gases for the purpose of designing a working craft. The Titan Explorer mission has been investigated closely by NASA for some years now, and it has been shown by Bailey et al. (2003) that the concept of Titan aerocapture is feasible.

The body of the aeroshell for Titan aerocapture used in a preliminary aeroheating analysis was based on the Mars Smart Lander design, scaled to a diameter of 3.75 m,

with a 70 degree sphere cone body and a bi-conic afterbody. The structure had an overall length of 2.096 m. The nominal entry velocity was 6.5 km/s and the angle of attack was 16 degrees. Takashima et al. (2003) used an atmospheric composition of 95 % N₂ and 5 % CH₄ by volume for the entire trajectory. Simulations were completed using the Langley Aerothermodynamic Upwind Relaxation Algorithm (LAURA) and Data Parallel Line Relaxation (DPLR) programs, solving the three-dimensional Navier-Stokes equations with finite rate chemistry. It was found that the convective heat transfer rates were sensitive to the diffusion model used and the chemical species chosen, while the radiative heat transfer results depended on the shock stand off distance and the post shock temperature profile.

Radiative heat transfer for the Titan aerocapture system was investigated in detail by Olejniczak et al. (2003) using uncoupled flowfield-radiation simulations. Again, DPLR and LAURA were the two CFD solvers used for the simulations, with the radiation modelling conducted using the two codes NEQAIR96 and LORAN. It was found that more than 90 % of the radiative heating occurring was from the CN violet band and that the peak radiative heating rate was found to be five times the convective heating rate.

The radiative loss parameter or Goulard number (Anderson 1989; Wright et al. 2004), $\Gamma = 2q_R/\frac{1}{2}\rho_\infty V_\infty^3 = E_s\delta/\frac{1}{2}\rho_\infty V_\infty^3$, provides an indication of the degree of coupling between the convective and radiative heat transfer. Significant levels of radiative heat transfer remove energy from the flow and change the flowfield in the shock layer, as total enthalpy is not conserved along streamlines. Accurate modelling of the effect requires a complex ‘coupled’ analysis. The Goulard number provides a simple preliminary estimate of the magnitude of this effect, giving the ratio of radiative heat loss to convective enthalpy flux. As a rule of thumb, coupling of the radiative and convective heat transfer is considered to have a significant effect for conditions where $\Gamma > 0.01$. For the Titan conditions investigated by Olejniczak et al. (2003) and Wright et al. (2004), the radiative loss parameter was calculated to have a value of more than 0.04, indicating that coupling is significant for Titan aerocapture modelling and future work should consider this. In the conditions investigated in this work, the radiative loss parameter was found to vary between values of 0.01 and 0.02.

Olejniczak et al. (2004) and Wright et al. (2004) continued the investigation into the modelling of the radiative heat transfer for the Titan aerocapture. Three-dimensional calculations were completed with coupled radiation, investigating the aeroshell afterbody in more detail, and non-adiabatic radiative cooling effects were added to the simulations. It was found that the convective heating was significantly affected by the radiative cooling effects that were not included in the previous work. The optically thin nature of the CN radiation allows the calculations to be well coupled with the flow field calculation by a simple procedure. It also made it possible to use a view-factor approach to compute the

radiative heating at each location rather than the tangent-slab approximation which is used in NEQAIR. In this method, the total heat flux at each surface point is calculated from the radiation intensity emitted from each computational volume and the view factor which determines the amount of the radiation from the flowfield cell which reaches the surface cell.

These studies (Takashima et al. 2003; Olejniczak et al. 2003; Olejniczak et al. 2004; Wright et al. 2004) of the Titan entry trajectory show that the heat flux transmitted to the surface of the vehicle is dominated by the radiation generated in the post-shock region. In fact, Wright et al. (2004) found that in some cases, the predicted peak radiative heat flux was as much as four times the level of the peak convective heat flux. Therefore, for the design of suitable thermal protection systems for a Titan entry vehicle, it becomes necessary to model accurately the nonequilibrium radiative heat transfer, as this portion of the heat flux becomes critical to the design (Laub 2003).

At NASA Ames, Bose et al. (2005) conducted a series of experiments using the EAST facility. This facility is a 10.16 cm diameter shock tube that uses an electric arc-heated driver. In these experiments, five different premixed N₂-CH₄-Ar gas mixtures, simulating the Titan atmosphere, were used at fill pressures of 13.3 and 133.3 Pa. Emission spectroscopy was used behind the shock to interrogate flows between 5 and 9 km/s in the CN violet and CN red bands. Absolute measurements of the intensity were achieved through calibration using a tungsten ribbon lamp. The primary purpose of these experiments was to provide comparative spectral and temporal radiative heat transfer intensity data for assessing the suitability of various nonequilibrium thermochemical models. The level of radiation is driven by the nonequilibrium chemical composition in the post-shock flow and by the nonequilibrium thermal and electronic excitation of the associated species. This is a very significant effect, and this comparison showed that using the assumption of a Boltzmann distribution for the CN electronic states overpredicted the intensity by a factor of 3-7. A nonlocal collisional radiative model using the rates of Zalogin et al. (2001) was developed from a simplified master equation. Two different collisional radiative models were tested; both with and without accounting for the non-local absorption in the shock tube. Figure 1.7 presents a comparison of the AMES experimental and computational data at four different conditions. Although the collisional radiative model developed significantly improved the prediction of the intensity of the radiation, it failed to predict the decay of the intensity behind the shock accurately.

Mazoué and Marrappa (2005a, Mazoué et al. (2005)) investigated computationally the entry heat flux conditions for the Huygens probe using the codes TINA and PARADE, to calculate the flowfield and radiative heat fluxes respectively. When these calculations were coupled, it was found that there was a reduction of between 8 and 27 % in the

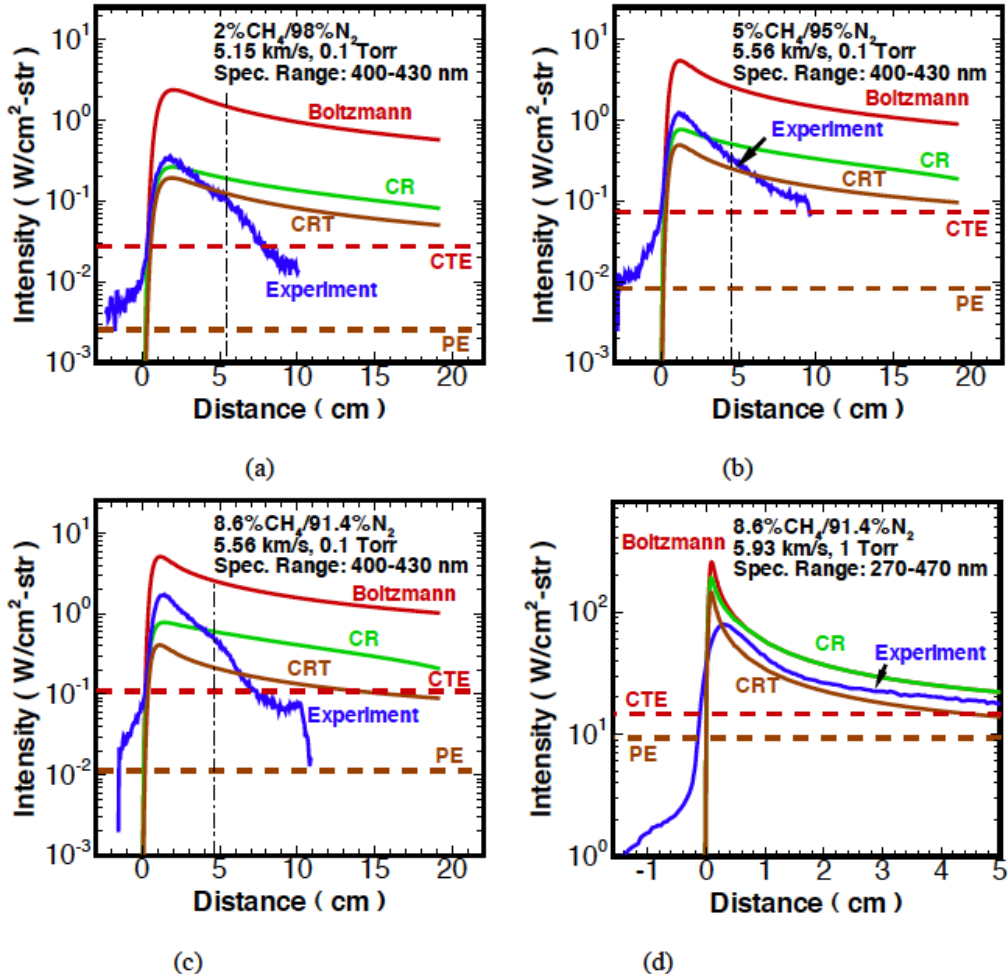


Figure 1.7 : Comparisons of modeling and experimental profiles of CN(Violet) intensities at 4 different conditions. ‘Boltzmann’ model assumes that the CN excited states are populated in a Boltzmann distribution governed by the gas vibrational temperature. ‘CR’ is the non-local collisional radiative model. ‘CRT’ is the local collisional radiative model that ignores the absorption term. The horizontal lines represent the complete thermodynamic equilibrium (CTE) and partial equilibrium (PE) values. The vertical line represents the estimated arrival of driver gas contamination beyond which the experimental data is not considered useful. Taken from Bose et al. (2005).

convective heat transfer and a reduction of between 6 and 32 % in the radiative heat transfer. The addition of absorption calculations to these simulations was also found to be significant, reducing the radiative heat flux by as much as 30 % for an uncoupled simulation. These results indicated the importance of considering the effects of both absorption and flowfield-radiation coupling for Titan entry calculations.

Caillault et al. (2006) found during a computational investigation of the Huygens entry that the radiation of the CN (red and violet) formed in the nonequilibrium shock layer was responsible for a significant portion of the total heat flux at the surface of the craft. These calculations of the radiative heating were conducted using SPECAIR (Laux 1993; Laux 2002) assuming a Boltzmann distribution of the electronic excited levels, with inputs from the flow solver LORE (Walpot et al. 2006) accounting for thermal nonequilibrium and finite-rate chemistry. Radiation was not coupled to the flowfield.

At the Université de Provence in Marseille, shock tube experiments were undertaken to investigate flow conditions relating to the Huygens mission (Rond et al. 2007). A free piston shock tube, TCM2, was used to generate spectral radiative heat flux data for CN Violet, C₂ Swan and CN Red band emissions at pressures of 40, 200 and 1100 Pa and shock speeds of 5.5 km/s. As the purpose of these experiments was to measure the radiative flux during a Huygens-like entry into a Titan atmosphere, a streak camera was used to obtain temporally resolved radiative intensity measurements at the wavelengths of interest. Spectral analysis of only the main radiative system, that of the CN violet system, provided good general agreement with computational results. However, spectral data was taken only once every microsecond in the nonequilibrium region behind the shock and once every three microseconds in the equilibrium region. It was clear that finer resolution of the nonequilibrium peak was desired in order to accurately capture the relevant details of the spectra. Numerical simulations were also conducted to reproduce the post-shock thermochemical and radiative processes in the experimental work (Rond and Boubert 2009). An uncoupled approach was used for the calculation of the radiative heat transfer; a one-dimensional two-temperature chemical kinetic code and a line-by-line radiative code (PARADE) (Smith et al. 1996). The computational results were found to be sensitive to the chemical and physical models used and the assumption of a Boltzmann distribution for the excited electronic levels of CN produced the same overprediction of the radiative intensity found by Bose et al. (2005). All of this led to the conclusion that radiative heating predictions for Titan entry would be improved through the use of a collisional radiative model.

A series of experiments was completed at the University of Queensland in the X2 facility (configured to a nonreflected shock tube mode) with the aim of producing a comprehensive set of benchmark data for Titan entry (Brandis 2009a). These experiments

were completed in a nonreflected shock tube for freestream pressures between 6 and 1000 Pa and shock speeds ranging between 4 and 10.3 km/s. A comparison of the radiation intensity between these experiments and those conducted in the EAST facility (Bose et al. 2005) showed excellent agreement. As will be described in the following chapter, a collisional radiative model was developed which included vibrationally specific energy exchanges for a selection of reactions. The model was able to predict the rise time of the nonequilibrium peak radiation behind the shock front and the decay rate of the relaxation towards equilibrium, but there remained discrepancies in the comparison of the absolute level of the radiation intensity.

This leads us to the answer to the third question raised by the global project aim - *Why focus on altitudes greater than 302 km?*. The experimental campaigns of Bose et al. (2005) and Brandis (2009a) provided a large dataset for conditions with freestream pressures greater than 6 Pa, although the signal strength below approximately 10 Pa was poor. At higher altitudes, where the freestream density is relatively low, nonequilibrium effects become very significant as there may not be sufficient collisions between particles for the gas to reach an equilibrium state. This longer region of nonequilibrium can result in the radiative heating being a very significant portion of the total heating load on the vehicle. Thus, we desire to obtain calibrated data at low freestream density conditions to extend the range of experimental data available beyond what has been previously measured and to provide some comparative data with an improved signal strength.

1.3 Summary

As was stated earlier, the combination of ground testing, computational modelling, and flight data is necessary in order to further our understanding of the fundamental processes involved in planetary entry. The literature describes numerous examples of computational and experimental work that has been conducted for Titan entry conditions.

A summary of the major findings is as follows:

- The predominant source of radiative heating in Titan entry flows comes from the CN violet band, with significant contributions from the CN red band.
- The peak radiative heating could be significantly larger than the convective heating rate for some trajectory points.
- The radiative loss parameter indicates that for Titan entry flows, radiation modelling should be coupled to the flowfield.

- The heat flux transmitted to the surface of the vehicle is dominated by the radiation generated in the post-shock region.
- Collisional radiative modelling provides improved radiative heating predictions.
- The inclusion of certain vibrationally specific reactions to an electronically specific collisional radiative model improved the calculation of the nonequilibrium peak rise time and the decay rate of the peak.

Large variations exist in computational predictions of radiation levels, generating a need for experimental data with which to validate the models. The experimental work of Bose et al. (2005), Brandis (2009a), and Rond et al. (2007, Rond and Boubert (2009)) provide a large database of experimental radiation measurements. It is the aim of this work to develop a facility capable of producing calibrated spectral data at conditions which extend on the trajectory range previously investigated experimentally.

CHAPTER 2

Nonequilibrium Modelling Review

Radiation simulations of nonequilibrium plasmas require the knowledge of the concentration of all radiating species, of their distribution over internal energy states, and of the intensity of the radiation emitted by these species.

In a standard computational package such as the well known NEQAIR (Park 1985; Whiting et al. 1996), the species concentrations, n_s , are given by the flowfield module, and the radiative intensity, formally noted A here, is given by the radiation module. The calculation of the population distributions over the internal energy states (f_{el} for electronic, f_v for vibrational and f_J for rotational states) is completed by a collisional-radiative model, also called a quasi-steady state (QSS) or excitation model.

Chemical kinetics models consider reactions between the various species and thus give no information on the internal energy level distribution, but are driven by the associated temperature levels. The rotational, vibrational, and electronic temperatures (T_r , T_v , and T_{el} respectively) may be modelled independently or set to be equal to the translational temperature, T_t , depending on the application. The simplest excitation model assumes that the internal energy levels have a Boltzmann population distribution at the electronic, T_{el} , vibrational, T_v , and rotational, T_r , temperatures. While these temperatures do not physically exist, they provide a compact method for representing Boltzmann populations of the particles among the different internal energy levels. The next level of complexity

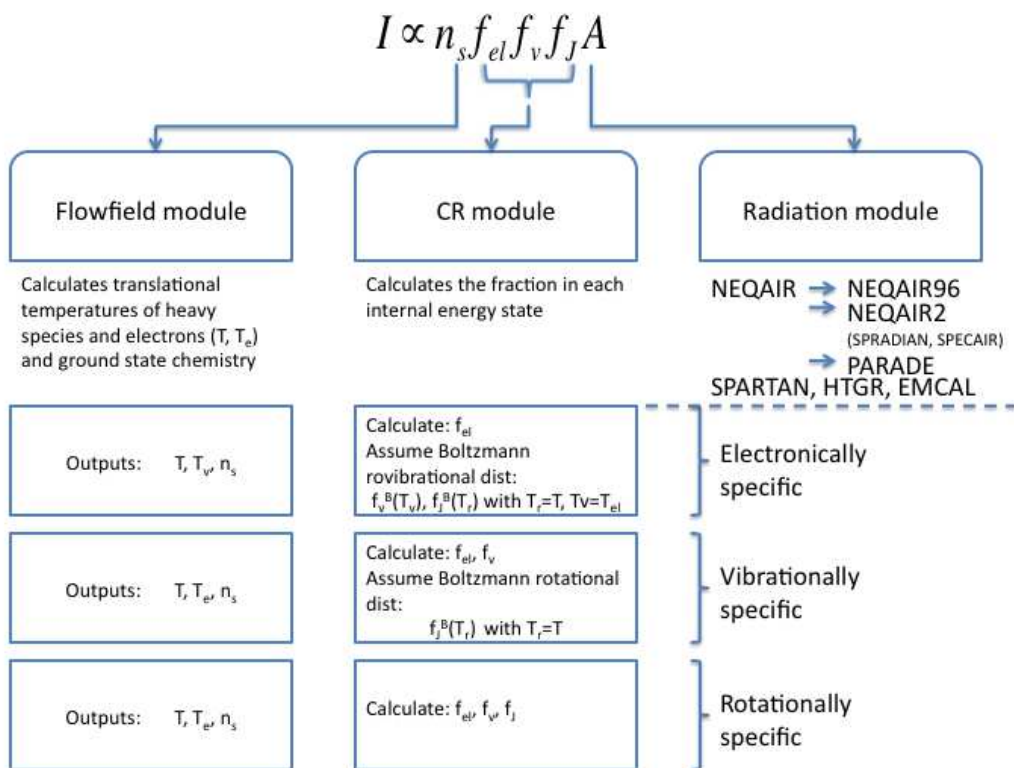


Figure 2.1 : Description of the collisional-radiative modelling process

is to account for non-Boltzmann populations of the internal energy levels (collisional-radiative models).

Three possibilities exist for collisional-radiative models. The first, electronically specific, considers transitions only between electronic states and assumes that the rovibrational levels in molecules have a Boltzmann population at temperatures T_v and T_r . The second, vibrationally specific, adds the transitions between the molecular vibronic levels but still assumes a Boltzmann distribution at temperature T_r for the rotational levels.

To date, most collisional-radiative models developed for air or Titan are electronically specific¹. Vibrationally specific models, also called state-to-state models, have been developed in recent years for nitrogen and air by Pierrot, Chauveau, and Capitelli². However, no collisional-radiative models include the rotational transitions.

This is for two main reasons. Firstly, there is no information available for all rates of rotational transitions; secondly, the computational time required for such a model is extremely expensive. For an electronically specific model, there could be 10-20 species and 100 reactions. In vibrationally specific cases, there could be 100-500 species and 10000 reactions. For rotationally specific models, this can extend to thousands of species and millions of reactions.

2.1 Review of existing collisional-radiative models

This section summarizes the existing collisional-radiative models for air and methane/nitrogen mixtures. We first describe the electronically specific models, then the more advanced vibrationally specific ones.

2.1.1 Electronically specific models for air

The NEQAIR code (Park 1985; Whiting et al. 1996) was developed at the NASA Ames Research Centre and combines a line-by-line radiation model with a collisional-radiative model to predict the nonequilibrium populations of excited bound electronic states of air species. It was developed in order to provide realistic estimates of the spectra emitted in both equilibrium and nonequilibrium conditions encountered in various conditions including in the bow shock wave forming ahead of a planetary entry vehicle. The populations of

¹Park 1985; Whiting et al. 1996; Fujita and Abe 1997; Fujita and Abe 2003; Magin et al. 2006; Johnston 2006; Johnston et al. 2006; Bultel et al. 2006; Sarrette et al. 1995a; Sarrette et al. 1995b; Teulet et al. 2001; Panesi et al. 2008; Johnston et al. 2008c; Johnston et al. 2008a; Johnston et al. 2008b

²Capitelli et al. 2000; Chauveau et al. 2002; Chauveau et al. 2003; Pierrot 1999; Pierrot et al. 1998; Pierrot et al. 1999; Capitelli et al. 2002

the electronic energy states within the atoms and diatomic molecules are found by either assuming a Boltzmann approximation or by using a quasi-steady-state collisional-radiative model.

In preparation for the MUSES-C launch of 2002, the Institute of Space and Astronautical Science developed a computer code for radiation analysis, SPRADIAN (Fujita and Abe 1997; Fujita and Abe 2003). SPRADIAN was designed to be applicable up to a temperature of 100 000 K, with a variety of gas species and ablation products. The package included a collisional-radiative module capable of modeling electronic transitions including bound-bound, bound-free and free-free transitions or atomic species and electronic-vibrational-rotational transitions for diatomic species.

In the early 1990s, following earlier work at CPAT³ in Toulouse, Sarrette et al. (1995a) proposed an electronically specific collisional-radiative model describing a homogeneous and stationary air plasma at a fixed pressure and for temperatures ranging from 2000 to 13 000 K. Multiply-charged ions, triatomic molecules and argon were neglected at these conditions. The chemical species considered in the model were the free-electrons: the neutral molecules N₂, O₂, and NO; their positive ions N₂⁺, O₂⁺, and NO⁺ and the neutral atoms N, O (in both ground and excited energy states). The negative molecular ion O₂⁻ and atomic ions N⁺, O⁺ and O⁻ were assumed to be in their ground state only. Over 100 species were considered in the model. The reaction rate coefficients were calculated using the assumption of Boltzmann energy distribution functions for all species and grouped energy levels to reduce the computational effort.

Two models were developed in order to cover the entire temperature range: CR1E (Sarrette et al. 1995a) included only inelastic collisional processes between electrons and heavy particles; CR1H (Sarrette et al. 1995b) extended this to lower temperatures by the addition of mechanisms between heavy particles (charge exchange, dissociation, dissociative attachment). Some discrepancies were noted when compared to experimental data, thus Teulet et al. (2001) developed the two-temperature model CR2. This model included updated reaction rate coefficients and extended the number of reaction processes, using as complete a set of collisional interactions as possible. Comparison of the updated model to experimental data showed an improvement over the CR1 model and that the nonequilibrium effects due to radiative losses are limited and between 8000 and 12 000 K.

More recently, Bultel et al. (2006) extended the work of Teulet by proposing a new collisional-radiative model for air as a mixture of N₂ and O₂. The model is a two-temperature model designed for pressures between 1 kPa and atmospheric pressure and

³Bacri and Gomes 1978; Gomes 1983; Bacri et al. 1982; Gomes et al. 1990.

applications including Earth atmospheric entry. It consists of 131 different internal energy levels involving 13 species: N_2 ; O_2 ; N; O; NO; N_2^+ ; O_2^+ ; N^+ ; O^+ ; NO^+ ; O_2^- and O^- . Although most reactions are electronic specific only, some degree of vibrational specificity is introduced in the model for certain electron impact reactions: namely, the dissociative recombination of NO^+ that was calculated (with a mono-quantum approach) for each excited vibrational level between $v=0$ and $v=14$.

Johnston et al. (Johnston 2006; Johnston et al. 2008a) present an electronically specific collisional-radiative model for air that includes electron impact, heavy-particle impact and radiative processes. In this model, only two atomic species, N and O, and one molecular species N_2^+ were considered. NO and O_2 were assumed to be populated in a Boltzmann distribution because their nonequilibrium contribution was found to be small. An approximate collisional-radiative model was developed following a review of the most suitable reaction rates for each species. Three main approximations were used: firstly, a curve-fit method was used for the non-Boltzmann population of the radiating atomic and molecular states as a function of the electronic temperature and electron number density; secondly, closely spaced atomic states were assumed to be in a Boltzmann distribution with each other and thirdly, the three lowest atomic states were assumed to be populated by a Boltzmann distribution.

Following the work of Johnston (Johnston 2006), Panesi et al. (2008) developed an electronically specific collisional-radiative model for air plasmas that was coupled to a one dimensional shock tube flow solver in order to compare with shock tube results for three points on the trajectory of the FIRE II flight experiment. The model assumed an air mixture with 116 species including 46 electronic energy levels of atomic nitrogen, 40 levels of atomic oxygen and 21 levels for molecules. Vibrational populations of molecules N_2 , O_2 and NO were assumed to follow Boltzmann distributions at temperature T_{v,N_2} , T_{v,O_2} and $T_{v,NO}$, with all other molecules at T_{v,N_2} . Rotational energy level populations were assumed to follow Boltzmann distributions at the gas temperature, T. Electronic energy level populations of N^+ and O^+ were assumed to follow Boltzmann distributions at the free-electron temperature T_e .

2.1.2 Vibrationally specific models for air

The nonequilibrium populations of internal energy states can be determined by solving the coupled state-specific rate equations using a collisional-radiative model. Many collisional-radiative models (Bultel et al. 2006; Sarrette et al. 1995a; Bacri and Medani 1982; Park 1990) use the simplifying assumption that the rotational and vibrational energy levels of molecules are populated according to Boltzmann distributions at temperatures T_r and

T_v respectively. In these models, the master equation is solved for electronic levels only, with rates obtained by averaging state-specific rates over the rovibrational states of each electronic level.

These approaches implicitly assume that departures from Boltzmann distributions of the populations of rovibrational states are small. Experiments conducted at Stanford University (Gessman et al. 1997) with a nitrogen/argon plasma forced to recombine within 250 μ s from a state of equilibrium at a temperature of 7200 K to a state of chemical non-equilibrium at 4720 K have shown that the vibrational levels of most electronic states, in particular the C₃ Π and B₃ Π of N₂, can strongly depart from a Boltzmann distribution when the concentration of atomic nitrogen is higher than its local thermal equilibrium (LTE) value.

In the mid-1990s, the Stanford group (Pierrot 1999; Pierrot et al. 1998; Pierrot et al. 1999) proposed the first detailed vibrationally specific collisional-radiative model to predict the radiation emitted by nonequilibrium nitrogen plasmas. The model included electronic excitation and ionisation, dissociation, heavy-particle excitation, ionisation and dissociation, radiation and predissociation reactions and was tested against the measurements of Gessman (Gessman et al. 1997) for a nonequilibrium recombining plasma. Excellent agreement was reached and it was found in particular that through predissociation the vibrational level v=13 of N₂(B) is fully coupled with ground state N atoms, allowing spectroscopic measurements of N concentration through the N₂(B-A) system.

Chauveau et al. (Chauveau et al. 2002; Chauveau et al. 2003) extended the nitrogen collisional-radiative model to include oxygen species. This model considered electron-impact vibrational excitation, V-T and V-V vibrational relaxation, electron and heavy particle impact dissociation, dissociative recombination, electron impact ionisation, Zeldovich and charge exchange reactions. For oxygen, only the ground electronic state was considered.

2.1.3 Collisional-radiative models for methane/nitrogen plasmas

A first electronically specific collisional-radiative model for Titan mixtures was proposed by EADS in the early 1990s (Hamma and Sacilotto 1992). This model emphasized electron-impact reactions for the formation of excited CN. This was justified by the assumption that the Titan atmosphere included a significant amount of argon - an easily ionized species in comparison with nitrogen or methane, thus electron-impact reactions would be dominant for Huygens entry conditions. However, it was later found that the Titan atmosphere contains a negligible percentage of argon. Therefore, this earlier model was revisited in 2004 as described below.

Magin et al. (2006) in collaboration with NASA Ames, ESTEC (Mazoué et al. 2005; Mazoué and Marrappa 2005b; Mazoué and Marrappa 2005a), and EADS developed an electronically specific collisional-radiative model for the prediction of nonequilibrium populations in a Titan mixture for the Huygens atmospheric entry conditions. The model involved the electronic states CN(A,B) and N₂(A,B,C). Rotational and vibrational energy levels were assumed to have Boltzmann population distributions at the gas temperature, T = T_r and electron temperature, T_v = T_e, respectively.

A non-local collisional-radiative model was developed by Bose et al. (2006). This model used the rate constants given by Zalogin et al. (2001). It modelled the collisional (de)excitation of CN, electron and heavy-particle impact ionization, electron recombination, and radiative processes. Using this model, the prediction of the peak radiation heat transfer overpredicted the measured data by less than a factor of 2 (where models using Boltzmann distributions for electronic level populations overpredicted the peak by a factor of 3-7).

When comparisons were completed between the collisional-radiative model developed by Magin et al. (2006), the Titan radiation measurements by emission spectroscopy in a shock tube at NASA Ames (Bose et al. 2006), and the measurements at the University of Queensland (Brandis 2009a), discrepancies were noted between the experimental and computational post-shock decay rates. This disparity was also noticed in the calculations completed by Bose et al. (2006).

This led to the modification of the Titan collisional-radiative model by Brandis (2009a) to more accurately model nitrogen dissociation, using the vibrationally specific approach of Pierrot (Pierrot 1999; Pierrot et al. 1998; Pierrot et al. 1999). A mono-quantum vibrationally specific model for nitrogen excitation and de-excitation reactions was incorporated into the electronically specific model of Magin et al. (2006). The ViSpeN model predicts the decay rates, rise time and overall trends of the experimental data quite well, although issues remain as to the absolute level of the intensity predicted. ViSpeN is being currently extended to replace the mono-quantum reactions and rates of Pierrot with the more representative multi-quantum approach of Capitelli et al. (2004) (Brandis 2009b).

Johnston (2006) developed an electronically specific collisional-radiative model for investigations into the radiative heating experienced by the Huygens probe. This model used 14 species, neglecting ionization. In an examination of the reactions contributing significantly to the CN(B) population, Johnston discovered that the use of the Gökçen reaction rates (Gökçen 2004), rather than the Nelson rates (Nelson et al. 1991) used by Magin et al. (2006), led to a lower predicted electron number density. Johnston also found that the use of the collisional-radiative model reduced the radiative heat transfer by up to 70 % over simulations assuming a Boltzmann distribution.

A series of papers was prepared by Park, in which an updated set of rate parameters and reference cross-sections were presented for the collisional excitation of electronic states in N₂, O₂, NO, CO, CN and N₂⁺ (Park 2008a; Park 2008b; Park 2008c). Experimental data from the literature was collated for transitions from the ground electronic states, and theoretical data was gathered for transitions between excited states. The reaction rates for the electronic transitions were calculated using the weighted cross-section method and were fitted to an Arrhenius equation; These updated rate coefficients were used in calculations of the CN radiation behind a shock wave in the code SPRADIAN07. SPRADIAN07 computes Boltzmann and non-Boltzmann radiation profiles, using temperature and species number densities as inputs. In the case of non-Boltzmann distributions of excited energy levels, the QSS model was used.

Calculations of CN radiation were compared to experimental results for Titan entry (Bose et al. 2006; Rond et al. 2007) and Mars entry (Lee et al. 2007). SPRADIAN07 successfully reproduced the experimental data for the CN Violet radiation profiles, including both the absolute intensity level and the decay rate from the nonequilibrium peak. However, it was found that the radiative loss parameter required an adjustment due to the effects of the vacuum-ultra-violet (VUV) emission of CN and that the CN Red radiation profile was overpredicted by as much as a factor of 10. The spatial smearing of the experimental data resulted in a difference in the peak intensity profile compared to the computational results.

2.2 Recommended collisional-radiative models

2.2.1 Collisional-radiative model for Earth entry

The development of a collisional-radiative model for Earth entry should focus on the modelling of the most important radiators, namely atomic lines of oxygen and nitrogen, and of the singlet states of molecular nitrogen that produce the intense VUV radiation estimated to be responsible for about half of the total heating in high speed entry at velocities above 10 km/s.

The reaction rates proposed by Johnston (Johnston 2006; Johnston et al. 2008a) or Panesi (2006, Panesi et al. (2008) are recommended for atomic species modelling. These two models are compared in Table 2.1, although the rates used are not tabulated here directly. Tables 2.2 and 2.3 compare the energy levels of atomic nitrogen and oxygen respectively between the two models. For the VUV system, a vibrationally specific approach should be pursued, with reaction rates computed following the state-specific approach of Pierrot et al. (Pierrot 1999; Pierrot et al. 1998; Pierrot et al. 1999).

Table 2.1 : General comparison of the two recommended collisional-radiative models for air.

	Johnston (Johnston 2006; Johnston et al. 2008a)	Panesi (Panesi 2006; Panesi et al. 2008)
Species considered	<p>N, O and N_2^+ are considered in detail</p> <p>NO and O_2 are considered to have Boltzmann population distributions</p> <p>35 electronic levels of atomic nitrogen</p> <p>32 electronic levels of atomic oxygen</p> <p>The first 25 levels are ungrouped; the remaining are grouped</p>	<p>116 species, including:</p> <ul style="list-style-type: none"> - 46 electronic levels of atomic nitrogen - 40 electronic levels of atomic oxygen - 21 electronic levels of molecules
Electron-Impact Excitation	<p>For N,</p> <p>The rates of Frost et al. (1998) are used for the lowest three levels to the first 21 levels</p> <p>Remaining allowed transitions to a level above the 22nd use van Regemorter's (van Regemorter 1962) formula</p> <p>Remaining forbidden transitions to a level above the 22nd use Allen's (Allen 1962) formula</p> <p>All remaining transitions use Gryzinski's (Gryzinski 1959) formula</p> <p>For O,</p>	<p>For the first three states of N and O, the rate coefficients of Bultel et al. (2006) are used</p> <p>Otherwise, for atomic processes, Drawin's (Drawin 1967) formula is used</p> <p>For molecular species, the rate coefficients of Teulet (Teulet et al. 1999) are used</p>

Continued on next page...

Table 2.1 – Continued

	Johnston (Johnston 2006; Johnston et al. 2008a)	Panesi (Panesi 2006; Panesi et al. 2008)
Zatsarinny and Tayal (Zatsarinny and Tayal 2003)	rates are used for the first three levels to the second through 21, where available	Bhatia and Kastner (Bhatia and Kastner 1995) for the remaining rates with final level less than 10, where available
Gordillo-Vazques and Kunc (Gordillo-Vazquez and Kunc 1995) for remaining rates with final level less than 7	Remaining allowed transitions with final level greater than 22 use van Regemorter's (van Regemorter 1962) formula, where available	Remaining forbidden transitions with final level greater than 22 use Allen's (Allen 1962) formula
All remaining transitions use Gryzinski's (Gryzinski 1959) formula		
Electron-Impact Ionization	From excited levels, calculated from Drawin's (Drawin 1967) formula From the lowest two states of O and N, use the rate coefficients from Kunc and Soon (Kunc and Soon 1989) and Soon and Kunc (Soon and Kunc 1990)	For the first three states of N and O, the rate coefficients of Bultel et al. (2006) are used Otherwise, for atomic processes, Drawin's (Drawin 1967) formula is used

Continued on next page...

Table 2.1 – Continued

	Johnston (Johnston 2006; Johnston et al. 2008a)	Panesi (Panesi 2006; Panesi et al. 2008)
		For molecular species, the rate coefficients of Teulet (Teulet et al. 1999) are used
Heavy-Particle-Impact Excitation		For the first three states of N and O, the rate coefficients of Bultel et al. (2006) are used Otherwise, for atomic processes, Drawin's (Drawin 1967) formula is used
		Except where experimental data exists, the excitation of molecular species is described by Lotz (Lotz 1968). Experimental data is taken from Teulet (Teulet et al. 2001), Capitelli (Capitelli et al. 2000) and Kossyi (Kossyi et al. 1992)
Heavy-Particle-Impact Ionization		For the first three states of N and O, the rate coefficients of Bultel et al. (2006) are used Otherwise, for atomic processes, Drawin's (Drawin 1967) formula is used
Spontaneous Emission	Bound-bound transitions use NIST database and the selected atomic lines for N and O are presented in Johnston et al. (2008c) Only optically allowed radiative transitions are considered Bound-free transitions use Drawin (Drawin 1967)	45 spontaneous emission lines for N 40 spontaneous emission lines for O Tabulated in Panesi <i>et al.</i> (Panesi et al. 2007)

Table 2.2 : Comparison of energy levels models for atomic nitrogen.

Johnston's model (Johnston 2006)							Panesi's model (Panesi 2006)				
Index	Energy (eV)	g	n	l	x	S	L	Index	Energy (eV)	g	l
1	0.0	4	2	1	3	2	0	1	0.0	4	1
2	2.383962	10	2	1	3	1	2	2	2.384	10	1
3	3.575602	6	2	1	3	1	1	3	3.576	6	1
4	10.332297	12	3	0	1	2	1	4	10.332	12	0
5	10.686543	6	3	0	2	2	2	5	20.687	6	0
6	10.927030	12	2	1	4	2	1	6	10.927	12	1
7	11.602633	2	3	1	1	1	0	7	11.603	2	1
8	11.758386	20	3	1	1	2	2	8	11.759	20	1
9	11.841712	12	3	1	1	2	1	9	11.842	12	1
10	11.995575	4	3	1	1	2	0	10	11.996	4	1
11	12.005823	10	3	1	1	1	2	11	12.006	10	1
12	12.124906	6	3	1	1	1	1	12	12.125	6	1
13	12.356713	10	3	0	1	1	2	13	12.257	10	0
14	12.856402	12	4	0	1	2	1	14	12.856	12	0
15	12.918660	6	4	0	1	1	1	15	12.919	6	0
16	12.972258	6	3	2	1	1	1	16	12.972	6	2
17	12.983572	28	3	2	1	2	3	17	12.984	28	2
18	12.999657	14	3	2	1	1	3	18	13.000	26	2
19	12.999948	12	3	2	1	2	1	19	13.020	20	2
20	13.019245	20	3	2	1	2	2	20	13.035	10	2
21	13.034976	10	3	2	1	1	2	21	13.202	2	1
22	13.201564	2	4	1	1	1	0	22	13.245	20	1
23	13.244404	20	4	1	1	2	2	23	13.268	12	1
24	13.268039	12	4	1	1	2	1	24	13.294	10	1
25	13.294202	10	4	1	1	1	2	25	13.322	4	1
26	13.321559	4	4	1	1	2	0	26	13.343	6	1
27	13.342560	6	4	1	1	1	1	27	13.624	12	0
28	13.676543	90	4	-	-	-	-	28	13.648	6	0
29	13.697743	126	4	-	-	-	-	29	13.679	90	2
30	13.960947	450	5	-	-	-	-	30	13.693	126	3
31	14.170345	648	6	-	-	-	-	31	13.717	24	1
32	14.270642	822	7	-	-	-	-	32	13.770	2	1
33	14.335606	1152	8	-	-	-	-	33	13.792	38	1
34	14.380238	1458	9	-	-	-	-	34	13.824	4	1

Continued on next page...

Table 2.2 – Continued

Johnston's model								Panesi's model			
Index	Energy (eV)	g	n	l	x	S	L	Index	Energy (eV)	g	l
35	14.412100	1800	10	-	-	-	-	35	13.872	10	1
								36	13.925	6	1
								37	13.969	18	0
								38	13.988	60	2
								39	13.999	126	3
								40	14.054	32	1
								41	14.149	18	0
								42	14.160	90	2
								43	14.164	126	3
								44	14.202	20	1
								45	14.260	108	0
								46	14.316	18	0

Table 2.3 : Comparison of energy levels models for atomic oxygen.

Johnston's model (Johnston 2006)								Panesi's model (Panesi 2006)			
Index	Energy (eV)	g	n	l	x	S	L	Index	Energy (eV)	g	l
1	0.009668	9	2	1	4	1	1	1	0.0	9	1
2	1.967364	5	2	1	4	0	2	2	1.970	5	1
3	4.189746	1	2	1	4	0	0	3	4.410	1	1
4	9.146091	5	3	0	1	2	0	4	9.146	5	0
5	9.521363	3	3	0	1	1	0	5	9.521	3	0
6	10.74064	15	3	1	1	2	1	6	10.740	15	1
7	10.98884	9	3	1	1	1	1	7	10.990	9	1
8	11.83761	5	4	0	1	2	0	8	11.838	5	0
9	11.93039	3	4	0	1	1	0	9	11.930	3	0
10	12.07863	25	3	2	1	2	2	10	12.090	25	2
11	12.08703	15	3	2	1	1	2	11	12.100	15	2
12	12.28610	15	4	1	1	2	1	12	12.300	15	1
13	12.35887	9	4	1	1	1	1	13	12.370	9	1
14	12.54019	15	3	0	1	1	2	14	12.550	15	0
15	12.66086	5	5	0	1	2	0	15	12.670	5	0
16	12.69747	3	5	0	1	1	0	16	12.710	3	0

Continued on next page...

Table 2.3 – Continued

Johnston's model (Johnston 2006)							Panesi's model (Panesi 2006)				
Index	Energy (eV)	g	n	l	x	S	L	Index	Energy (eV)	g	l
17	12.72847	5	3	0	1	0	2	17	12.740	5	0
18	12.75370	25	4	2	1	2	2	18	12.760	25	2
19	12.75902	15	4	2	1	1	2	19	12.770	15	2
20	12.76644	35	4	3	1	2	3	20	12.780	56	3
21	12.76645	21	4	3	1	1	3	21	12.860	15	1
22	12.84802	15	5	1	1	2	1	22	12.890	9	1
23	12.87824	9	5	1	1	1	1	23	13.030	5	0
24	13.06612	25	5	2	1	2	2	24	13.050	3	0
25	13.06905	15	5	2	1	1	2	25	13.080	40	2
26	13.07310	35	5	3	1	2	3	26	13.087	56	3
27	13.07311	21	5	3	1	1	3	27	13.130	15	1
28	13.220803	288	6	-	-	-	-	28	13.140	9	1
29	13.337837	392	7	-	-	-	-	29	13.220	5	0
30	13.404041	512	8	-	-	-	-	30	13.230	3	0
31	13.448797	648	9	-	-	-	-	31	13.250	168	2
32	13.480535	800	10	-	-	-	-	32	13.330	5	0
								33	13.340	3	0
								34	13.353	96	2
								35	13.412	8	0
								36	13.418	40	2
								37	13.459	8	0
								38	13.464	40	2
								39	13.493	8	0
								40	13.496	40	2

In addition, it is important to consider other transitions such as N₂ first and second positive. Even though these transitions produce a negligible amount of radiation, their detection is useful to provide information on the thermodynamic state of the plasma. For example, as discussed in the previous section, the first positive system contains information on the fraction of atomic nitrogen in the flow. The mechanism proposed by Pierrot et al. (Pierrot 1999; Pierrot et al. 1998; Pierrot et al. 1999) can be readily used to model the population of these species.

Figure 2.2 is taken from the paper of Bose et al. (2009). It presents spectral emissions measured in the EAST facility in the equilibrium region behind a shock wave passing

through air. The broad spectral range shows clearly the importance of modelling both atomic and molecular species in order to capture the essential structure of the emissions.

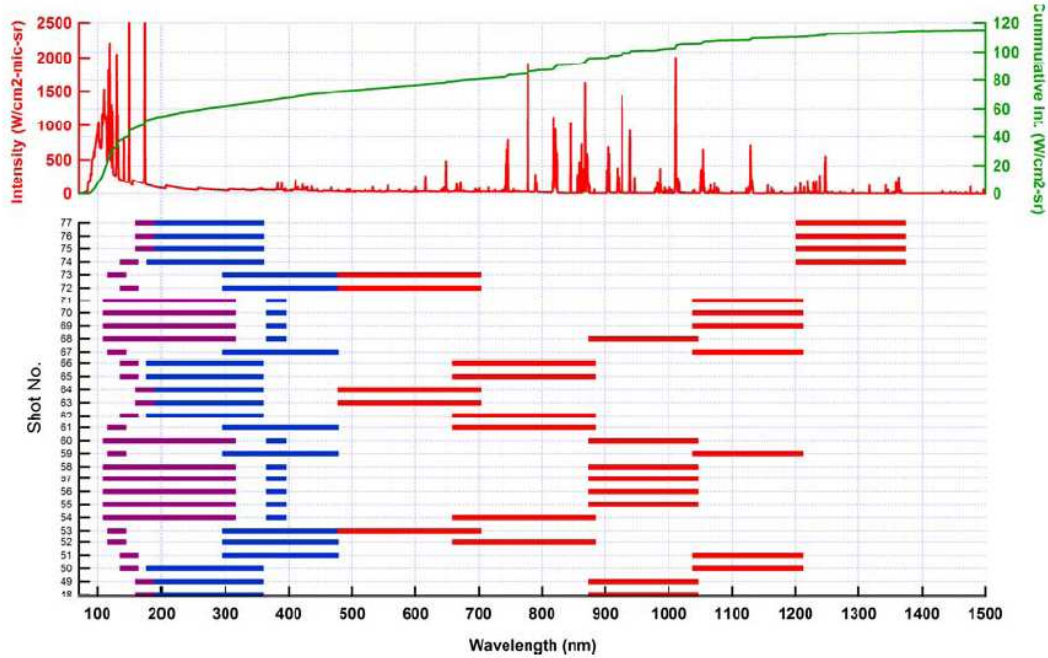


Figure 2.2 : A sample of simulated CEV stagnation point radiation spectrum and spectral coverage in different EAST shots. The colour of the bars represent different cameras. Red camera covers visible and infrared regions. Blue camera covers the ultraviolet regions. VUV camera coverage is represented by purple bars. Taken from Bose et al. (2009).

2.2.2 Collisional-radiative models for Titan entry

For Titan entry conditions, Figure 2.3 shows the contributions of the main radiators to the total radiative heat flux for the trajectory in a calculation by Caillault et al. (2006). Initially, the first and second positive N₂ systems are quite significant, but then these become negligible and the CN become dominant. The CN violet contribution is by far the largest. In this calculation, the populations of the electronic excited energy levels were assumed to follow a Boltzmann distribution. This assumption was considered to be overly conservative, and a collisional-radiative model is necessary to describe the contribution of individual species more accurately over the entire trajectory.

The reaction rates and chemical reaction database for the collisional-radiative model of Magin et al. (2006) are presented here.

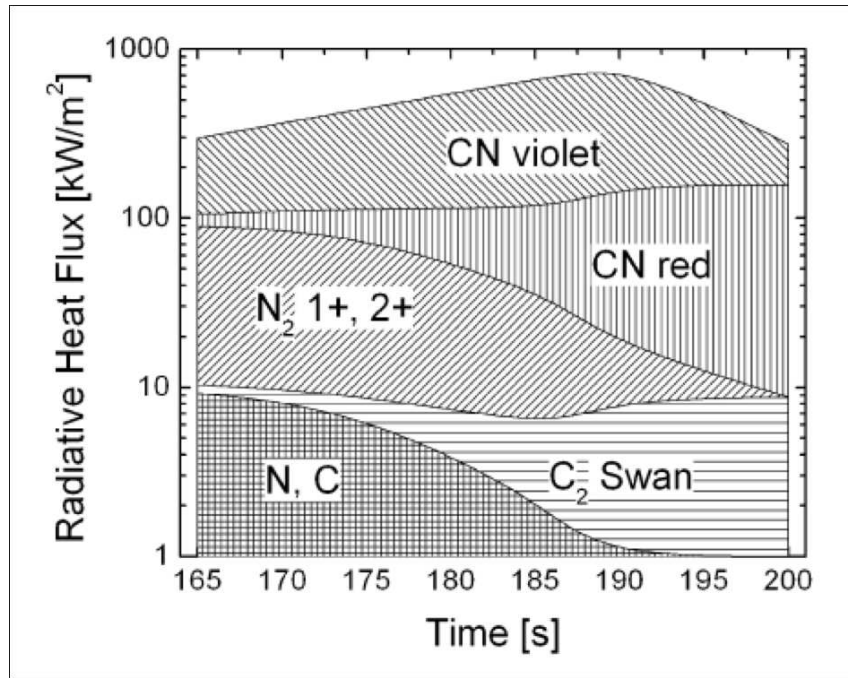
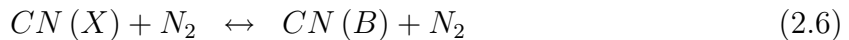


Figure 2.3 : Contribution of individual species to the total radiative flux for the Post-Ta(B) trajectory. (Caillault et al. 2006)

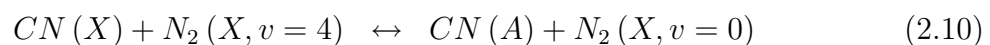
Spontaneous emission



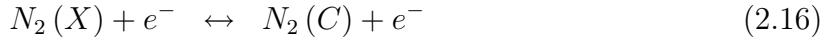
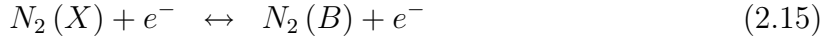
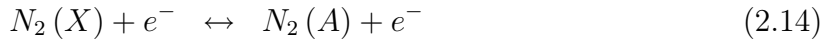
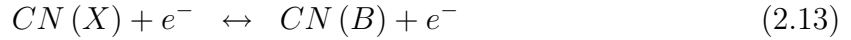
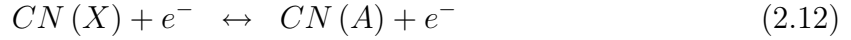
Collisional (de)excitation with nitrogen



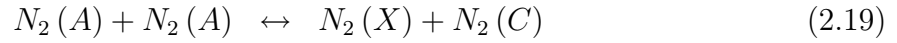
Resonant collisional (de)excitation with nitrogen



Electron-impact (de)excitation



Pooling



Quenching

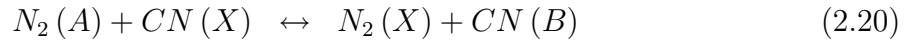


Table 2.4 contains the transition lifetimes for the spontaneous emission of reactions 2.1-2.4. In this model, radiation from the $N_2(A)$ excited state is neglected because the transition to the ground state is spectroscopically forbidden (ie. weak). The reaction rates for the excitation and de-excitation reactions for CN and N_2 (reactions 2.5-2.20) are presented in Table 2.5 for thermal nonequilibrium. The reaction rates are computed on the basis of the translational and vibrational temperatures. As proposed by Park (1988), an average temperature, $T_a = \sqrt{TT_v}$ is used to compute rates where vibrational excitation is favourable for molecular impact. For electron-impact, the rates are calculated with the vibrational temperature. The reverse processes are calculated based on the principle of detailed balance.

Table 2.4 : Radiative transitions of CN and N_2 electronic states (Magin et al. 2006)

	Transition Name	Spectroscopic Notation	Energy, eV	Ref	Lifetime,s	Ref
1.	CN red	$CN(A^2\Pi_i) \rightarrow CN(X^2\Sigma^+)$	1.15	a ¹	1.54×10^{-5}	b ²
2.	CN violet	$CN(B^2\Sigma_i) \rightarrow CN(X^2\Sigma^+)$	3.19	a ¹	6.55×10^{-8}	b ²
3.	N_2 first positive	$N_2(B^3\Pi_g) \rightarrow N_2(A^3\Sigma_u^+)$	1.17	a ¹	7.00×10^{-6}	b ²
4.	N_2 second positive	$N_2(C^3\Pi_u) \rightarrow N_2(B^3\Pi_g)$	3.66	a ¹	3.65×10^{-8}	c ³

¹ Huber and Herzberg (1979)

² Cherniy and Losev (1999)

³ Guerra and Loureiro (1997)

Table 2.5 : Forward and reverse reaction rates: Titan collisional-radiative model (Magin et al. 2006)

	Reaction	Rate (mol/cm ³ /s)	Source
5.	$CN(X) + N_2 \leftrightarrow CN(A) + N_2$	$k_f(T_a) = 1.5 \times 10^{11} T_a^{0.5} \exp(-13300/T_a)$ $k_b(T) = k_f(T)/K_{eq}(T)$	¹ a
6.	$CN(X) + N_2 \leftrightarrow CN(B) + N_2$	$k_f(T_a) = 1.8 \times 10^{11} T_a^{0.5} \exp(-37000/T_a)$ $k_b(T) = k_f(T)/K_{eq}(T)$	¹ a
7.	$N_2(X) + N_2 \leftrightarrow N_2(A) + N_2$	$k_f(T_a) = 10^{12} T_a^{-0.5} \exp(-71610/T_a)$ $k_b(T) = k_f(T)/K_{eq}(T)$	¹ a
8.	$N_2(A) + N_2 \leftrightarrow N_2(B) + N_2$	$k_f(T_a) = 1.2 \times 10^{13} T_a^{0.5} \exp(-13495/T_a)$ $k_b(T) = k_f(T)/K_{eq}(T)$	¹ a
9.	$N_2(B) + N_2 \leftrightarrow N_2(C) + N_2$	$k_f(T_a) = K_{eq}(T_a) k_b$ $k_b = 5.1 \times 10^{13}$	² b
10.	$CN(X) + N_2(X, v=4) \leftrightarrow CN(A) + N_2(X, v=0)$	$k_f = 6.0 \times 10^{13}$ $k_b(T) = k_f(T)/K_{eq}(T)$	¹ a
11.	$CN(X) + N_2(X, v=11) \leftrightarrow CN(B) + N_2(X, v=0)$	$k_f = 6.0 \times 10^{13}$ $k_b(T) = k_f(T)/K_{eq}(T)$	¹ a
12.	$CN(X) + e^- \leftrightarrow CN(A) + e^-$	$k_f(T_v) = 6.0 \times 10^{14} T_v^{0.5} \exp(-13300/T_v)$ $k_b(T_v) = k_f(T_v)/K_{eq}(T_v)$	¹ a
13.	$CN(X) + e^- \leftrightarrow CN(B) + e^-$	$k_f(T_v) = 6.3 \times 10^{14} T_v^{0.5} \exp(-37000/T_v)$ $k_b(T_v) = k_f(T_v)/K_{eq}(T_v)$	¹ a
14.	$N_2(X) + e^- \leftrightarrow N_2(A) + e^-$	$k_f(T_v) = 2.4 \times 10^{15} T_v^{0.5} \exp(-71610/T_v)$ $k_b(T_v) = k_f(T_v)/K_{eq}(T_v)$	¹ a
15.	$N_2(X) + e^- \leftrightarrow N_2(B) + e^-$	$k_f(T_v) = 2.8 \times 10^{16} T_v^{0.5} \exp(-85740/T_v)$ $k_b(T_v) = k_f(T_v)/K_{eq}(T_v)$	¹ a
16.	$N_2(X) + e^- \leftrightarrow N_2(C) + e^-$	$k_f(T_v) = 2.3 \times 10^{15} T_v^{0.5} \exp(-127900/T_v)$ $k_b(T_v) = k_f(T_v)/K_{eq}(T_v)$	³ c
17.	$N_2(A) + e^- \leftrightarrow N_2(B) + e^-$	$k_f(T_v) = 3.0 \times 10^{15} T_v^{0.5} \exp(-13495/T_v)$ $k_b(T_v) = k_f(T_v)/K_{eq}(T_v)$	¹ a
18.	$N_2(A) + N_2(A) \leftrightarrow N_2(X) + N_2(B)$	$k_f = 1.8 \times 10^{14}$ $k_b(T) = k_f/K_{eq}(T)$	³ c
19.	$N_2(A) + N_2(A) \leftrightarrow N_2(X) + N_2(C)$	$k_f = 9.0 \times 10^{13}$ $k_b(T) = k_f/K_{eq}(T)$	³ c
20.	$N_2(A) + CN(X) \leftrightarrow N_2(X) + CN(B)$	$k_f = 4.2 \times 10^{12} T^{0.5}$ $k_b(T_a) = k_f(T_a)/K_{eq}(T_a)$	⁴ d

¹ Cherniy and Losev (1999)

² Fresnet et al. (2002)

³ Capitelli et al. (2000)

⁴ Pintassilgo et al. (2001)

For the resonant molecular impact reactions (reactions 2.10, 2.11), the vibrational population of $N_2(X)$ is assumed to follow a Boltzmann distribution. Most rates are taken from the database of Cherniy and Losev (1999) that was mainly developed for Martian entries. The forward rate of reaction 2.20, measured by Pintassilgo et al. (2001) at 300 K, is extrapolated to higher temperatures by assuming a square root temperature dependence of the rate.

Caillault et al. (2006) have shown, assuming Boltzmann populations in thermochemical nonequilibrium, that the excited states of N_2 can have a significant contribution to the total radiative heat flux, especially at early times of the Huygens trajectories defined by ESA.

Therefore, in this collisional-radiative model, it must be checked that the excited states of N_2 are not depleted by a quenching mechanism such as reaction 2.20. An additional quenching process results in the dissociation of a molecule colliding with the $N_2(A,B,C)$ states. This reaction is likely to occur if the energy released during the transition of the $N_2(A,B,C)$ states to a lower state is higher than the dissociation energy of the collision

partner. Transition energies of N₂ electronic states to the ground state and dissociation energies of major molecules present in Titan's atmosphere are given in Table 2.6 and Table 2.7.

Table 2.6 : *Excitation energy of N₂ electronic states (Magin et al. 2006)*

Process	Energy, eV	Reference
$N_2 (X^1\Sigma_g^+) \rightarrow N_2 (C^3\Pi_u)$	11.05	a ¹
$N_2 (X^1\Sigma_g^+) \rightarrow N_2 (B^3\Pi_g)$	7.39	a ¹
$N_2 (X^1\Sigma_g^+) \rightarrow N_2 (A^3\Sigma_u^+)$	6.22	a ¹

¹ Huber and Herzberg (1979)

Table 2.7 : *Dissociation energy of major molecules in Titan's atmosphere (Magin et al. 2006)*

Process	Energy, eV	Reference
$N_2 \leftrightarrow N + N$	9.76	a ¹
$CN \leftrightarrow C + N$	7.76	a ¹
$C_2 \leftrightarrow C + C$	6.21	a ¹
$CH_3 \leftrightarrow CH_2 + H$	5.16	b ²
$CH_4 \leftrightarrow CH_3 + H$	4.64	b ²
$CH_2 \leftrightarrow CH + H$	4.60	b ²
$H_2 \leftrightarrow H + H$	4.56	a ¹
$CH \leftrightarrow C + H$	3.69	b ²
$NH \leftrightarrow N + H$	3.47	a ¹

¹ Huber and Herzberg (1979)

² Wang and Mak (1995)

For Earth entries, it may be argued that the N₂ excited states are quenched by O₂ (leading to dissociated O₂ molecules) and therefore that N₂ radiation is negligible. For Titan entries, quenching of the N₂(C) state by dissociation of N₂ or CN is a possible reaction not accounted for in this model.

Finally, the CN(A,B) excited states cannot be quenched efficiently by dissociation of any molecule present in the gas, given the low transition energy of CN(A,B) to the ground state (see Table 2.4). 19 species are used to form the Titan mixture for the electronically specific model: C; H; N; C₂; CH₄; CH₃; CH₂; CH; CN; H₂; HCN; N₂; NH; C⁺; H⁺; N⁺; CN⁺; N₂⁺ and e⁻. 47 vibrational states of ground state nitrogen are included in the

vibrationally-specific model as separate species. The temperatures involved in calculating the various reaction rates are specified in Table 2.8.

Table 2.8 : *Thermal nonequilibrium chemistry model (Magin et al. 2006)*

Process	k_f	k_b
Dissociation, M = heavy particle	T_a	T
Dissociation, M = electron	T_v	T_v
Radical reaction	T	T
Associative ionization	T	T_v
Electron impact ionization	T_v	T_v
Charge transfer	T	T

The reduced chemical reaction set developed by Gökçen (2004) and used by Magin et al. (2006) and Brandis (2009a) as a basis for the collisional-radiative chemistry reaction set is presented in Table 2.9. In this model, as per the derived model used by Magin et al., Park's (Park 1988) two-temperature model is used. For dissociation reactions, the rates are assumed to be governed by an average temperature, $T_a = \sqrt{TT_v}$, exchange reactions by T, and ionization reactions by T_v . Again, the reverse processes are calculated based on the principle of microreversibility. This reduced chemistry model contains 21 species and 35 reactions.

For completeness, the Ar ionisation reaction is included in the table, although both Magin et al. and Brandis exclude the species Ar and Ar^+ from their collisional-radiative models.

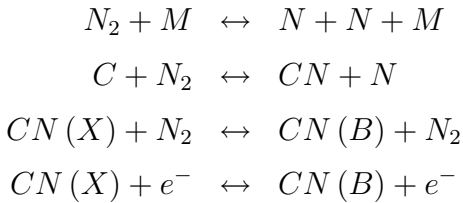
For both Tables 2.5 and 2.9, the sensitivity factor, F, is defined such that the value of k_f is bounded by the multiplication and division of k_f by the uncertainty factor. This is recommended as a lower bound of the uncertainty (Gökçen 2004).

A comparison of the results of the collisional-radiative model developed by Magin et al. for Titan and experimental results found that although the prediction of the peak radiation level was significantly improved, discrepancies in the post-shock decay rates remained. Brandis completed a sensitivity analysis of the reaction schemes of both Magin et al. and Gökçen. The four most influential reactions were determined to be:

Table 2.9 : Reaction rate constants for Titan atmospheric entry (Gökçen 2004)

	$k_f = AT^n e^{-T_a/T}$	A (cc/mol/s)	n	T _a (K)	Uncertainty ⁴	Source
A. Dissociation Reactions						
1.	$N_2 + M \leftrightarrow N + N + M$ enhanced rate for $M = N, C, H$ enhanced rate for $M = e^-$	$7.00E + 21$ $3.00E + 22$ $3.00E + 24$	-1.60 -1.60 -1.60	113200	F = 3.0	Park et al. (2001)
2.	$CH_4 + M \leftrightarrow CH_3 + H + M$	$4.70E + 21$	-8.20	113200	F = 5.0	Park et al. (2001)
3.	$CH_3 + M \leftrightarrow CH_2 + H + M$	$1.02E + 21$	0.00	59200	F = 2.0	Baulch et al. (1994)
4.	$CH_3 + M \leftrightarrow CH + H_2 + M$	$5.00E + 15$	0.00	45600	F = 1.26 - 3.2	Baulch et al. (1994)
5.	$CH_2 + M \leftrightarrow CH + H + M$	$4.00E + 15$	0.00	42800	F = 1.26 - 2.0	Dean and Hanson (1992)
6.	$CH_2 + M \leftrightarrow C + H_2 + M$	$1.30E + 14$	0.00	41800	F = 1.26 - 2.0	Dean and Hanson (1992)
7.	$CH + M \leftrightarrow C + H + M$	$1.90E + 14$	0.00	29700	F = 1.26 - 2.0	Dean and Hanson (1992)
8.	$C_2 + M \leftrightarrow C + C + M$	$1.50E + 16$	0.00	33700	F = 1.26 - 2.0	Dean and Hanson (1992)
9.	$H_2 + M \leftrightarrow H + H + M$	$2.23E + 14$	0.00	71600	F = 1.26 - 2.0	Kruse and Roth (1997)
10.	$CN + M \leftrightarrow C + N + M$	$2.53E + 14$	0.00	48350	F = 1.26 - 2.0	Baulch et al. (1992, Baulch et al. (1994))
11.	$NH + M \leftrightarrow N + H + M$	$1.80E + 14$	0.00	71000	F = 1.5 - 2.0	Park et al. (1994, Tsang (1992))
12.	$HCN + M \leftrightarrow CN + H + M$	$3.57E + 14$	-2.60	37600	F = 1.26 - 2.0	NIST (2003)
				62845	F = 1.5 - 2.0	Tsang and Herron (1991)
B. Radical Reactions						
13.	$CH_3 + N \leftrightarrow HCN + H + H$	$7.00E + 13$	0.00	0	F = 10.0	Dean et al. (1990)
14.	$CH_3 + H \leftrightarrow CH_2 + H_2$	$6.03E + 13$	0.00	7600	F = 10.0	Baulch et al. (1992)
15.	$CH_2 + N_2 \leftrightarrow HCN + NH$	$4.82E + 12$	0.00	18000	F = 10.0	NIST (2003)
16.	$CH_2 + N \leftrightarrow HCN + H$	$5.00E + 13$	0.00	0	F = 10.0	Dean et al. (1990)
17.	$CH_2 + H \leftrightarrow CH + H_2$	$6.03E + 12$	0.00	-900	F = 5.0 - 10.0	NIST (2003)
18.	$CH + N_2 \leftrightarrow HCN + N$	$4.40E + 12$	0.00	11060	F = 1.5 - 3.2	Dean et al. (1990)
19.	$CH + C \leftrightarrow C_2 + H$	$2.00E + 12$	0.00	0	F = 10.0	Dean and Hanson (1992)
20.	$C_2 + N_2 \leftrightarrow CN + CN$	$1.50E + 13$	0.00	21000	F = 1.26 - 2.0	Sommer et al. (1997)
21.	$CN + H_2 \leftrightarrow HCN + H$	$2.95E + 05$	0.00	1130	F = 3.2 - 5.0	Wooldridge et al. (1996)
22.	$CN + C \leftrightarrow C_2 + N$	$5.00E + 13$	0.00	13000	F = 2.0 - 5.0	Park et al. (2001)
23.	$N + H_2 \leftrightarrow NH + H$	$1.60E + 14$	0.00	12650	F = 1.26 - 2.0	Davidson and Hanson (1990)
24.	$C + N_2 \leftrightarrow CN + N$	$5.24E + 13$	0.00	22600	F = 1.6 - 2.0	Baulch et al. (1994)
25.	$C + H_2 \leftrightarrow CH + H$	$4.00E + 14$	0.00	11700	F = 1.6 - 2.0	Dean et al. (1991)
26.	$H + N_2 \leftrightarrow NH + N$	$3.00E + 12$	0.50	71400	F = 2.0 - 3.2	Roose et al. (1978)
27.	$H + CH_4 \leftrightarrow CH_3 + H_2$	$1.32E + 04$	3.00	4045	F = 1.6 - 2.0	Baulch et al. (1992, Baulch et al. (1994))
C. Ionization Reactions						
28.	$N + N \leftrightarrow N_2^+ + e^-$	$4.40E + 07$	1.50	67500	F = 10.0	Park et al. (2001)
29.	$C + N \leftrightarrow CN^+ + e^-$	$1.00E + 15$	1.50	164400	F ≥ 10.0	Nelson et al. (1991)
30.	$N + e^- \leftrightarrow N^+ + e^- + e^-$	$2.50E + 34$	-3.82	168600	F = 10.0	Park et al. (2001)
31.	$C + e^- \leftrightarrow C^+ + e^- + e^-$	$3.70E + 31$	-3.00	130720	F = 10.0	Park et al. (2001)
32.	$H + e^- \leftrightarrow H^+ + e^- + e^-$	$2.20E + 30$	-2.80	157800	F ≥ 10.0	Park et al. (2001)
33.	$Ar + e^- \leftrightarrow Ar^+ + e^- + e^-$	$2.50E + 34$	-3.82	181700	F ≥ 10.0	Nelson et al. (1991)
34.	$CN^+ + N \leftrightarrow CN + N^+$	$9.80E + 12$	0.00	40700	F ≥ 10.0	Nelson et al. (1991)
35.	$C^+ + N_2 \leftrightarrow N_2^+ + C$	$1.11E + 14$	-0.11	50000	F ≥ 10.0	Nelson et al. (1991)

*The range of values for k_f is bounded by the multiplication and division of k_f by F (as a lower limit)



It was found that the relatively slower dissociation of the N_2 molecules compared to CH_4 behind the shock led to an over-population of CN molecules through the coupling of the first two reactions. Also, the second reaction has a significant effect on the post-shock radiation decay rate. The final two reactions influence the absolute intensity of the radiation due to the formation of $CN(B)$.

These results highlighted the importance of correctly modelling atomic and molecular nitrogen behind the shock. Therefore, a vibrationally specific subroutine was implemented in order to simulate the dissociation and vibrational (de-)excitation reactions of all of the ground electronic state vibrational levels of nitrogen.

The current ViSpeN model of Brandis is a modified version of the code of Magin et al. and works in the following way. For each time step for the solution of the electronic states, a subroutine evaluates the vibrationally specific dissociation and excitation/de-excitation of molecular nitrogen as presented by Pierrot (Pierrot 1999; Pierrot et al. 1998; Pierrot et al. 1999). This means that the reaction $N_2 + M \leftrightarrow N + N + M$ (for $M = N_2, N, N^+, N_2^+, e^-$) uses the Schwartz-Slawsky-Herzfield (SSH) theory (Schwartz et al. 1952) rather than the global rate of Gökçen for the calculation of the rate. 47 vibrational states of nitrogen are included in the model as separate species.

For the mono-quantum vibrationally-specific subroutine included in ViSpeN by Brandis, the rate of the excitation reaction of the nitrogen molecule in the ground state to the first vibrational state is analytically calculated and the other reaction rates are scaled from this value.

The V-T reaction rates for vibrationally-specific nitrogen are calculated as per Brandis:

$$k_{1,0} = AT_g^n \exp \left(-\frac{B}{T_g^{1/3}} + \frac{C}{T_g^m} \right) \left[1 - D \exp \left(-\frac{E_{10}}{T_g} \right) \right]^{-1} \quad (2.21)$$

$$k_{v+1,v} = k_{1,0} G(v+1) \quad (2.22)$$

SSH theory (Schwartz et al. 1952) and some approximations for the Morse oscillator model gives $G(v + 1)$ as:

$$G(v + 1) = \frac{(v + 1)(1 - x_e)}{1 - x_e(v + 1)} \frac{F(y_{v+1,v})}{F(y_{1,0})} \quad (2.23)$$

$$y_{v+1,v} = 0.32E_{v=1,v}L\sqrt{\frac{\mu}{T_g}} \quad (2.24)$$

$$F(y) = \frac{1}{2} \left[3 - \exp\left(\frac{-2y}{3}\right) \right] \exp\left(\frac{-2y}{3}\right) \quad \text{for } 0 \leq y \leq 20 \quad (2.25)$$

$$F(y) = 8\left(\frac{\pi}{3}\right)^{1/3} y^{7/3} \exp(-3y^{2/3}) \quad \text{for } y > 20 \quad (2.26)$$

The ViSpeN model has been shown to predict the fall-off rates, rise time and overall trends of the experimental data quite well. Figure 2.4 shows this improvement for a number of experiments completed in the X2 facility at the University of Queensland.

Figure 2.5 allows a comparison between the QSS model used by Bose et al. (2006), the collisional-radiative model of Magin et al. (2006) and the ViSpen model (Brandis 2009a). The experimental condition being compared is that of Figure 1.7(a). For both the collisional-radiative models of Bose et al. and Magin et al., the value and location of the maximum intensity provide a good agreement with the experimental data. However, it can be seen that there is a significant improvement in the modelling of the intensity drop off with the ViSpeN model.

The SSH theory has two main limitations. Firstly, the theory assumes that multi-quantum jumps in vibrational mode are negligible; and secondly, the validated temperature range of the model is limited. Therefore, for high speed planetary entry problems, the implementation of a multi-quantum model such as developed by Macheret and Adamovich (2000) and Adamovich et al. (1998) or Esposito and Capitelli (2005) and Capitelli et al. (2004) is recommended in the future. Currently, this modification to the ViSpeN code is underway using the method presented by Capitelli (Brandis).

In order to get the most appropriate balance between accuracy and computational efficiency, as well as to allow for the limited knowledge of reaction rates for rotational transitions, the most suitable collisional-radiative model for a Huygens entry would be a multi-quantum hybrid vibronic/electronic-specific model that extends the work of Magin et al. and Brandis, with only those species for which the vibrational modelling is critical extended into a vibrationally specific model.

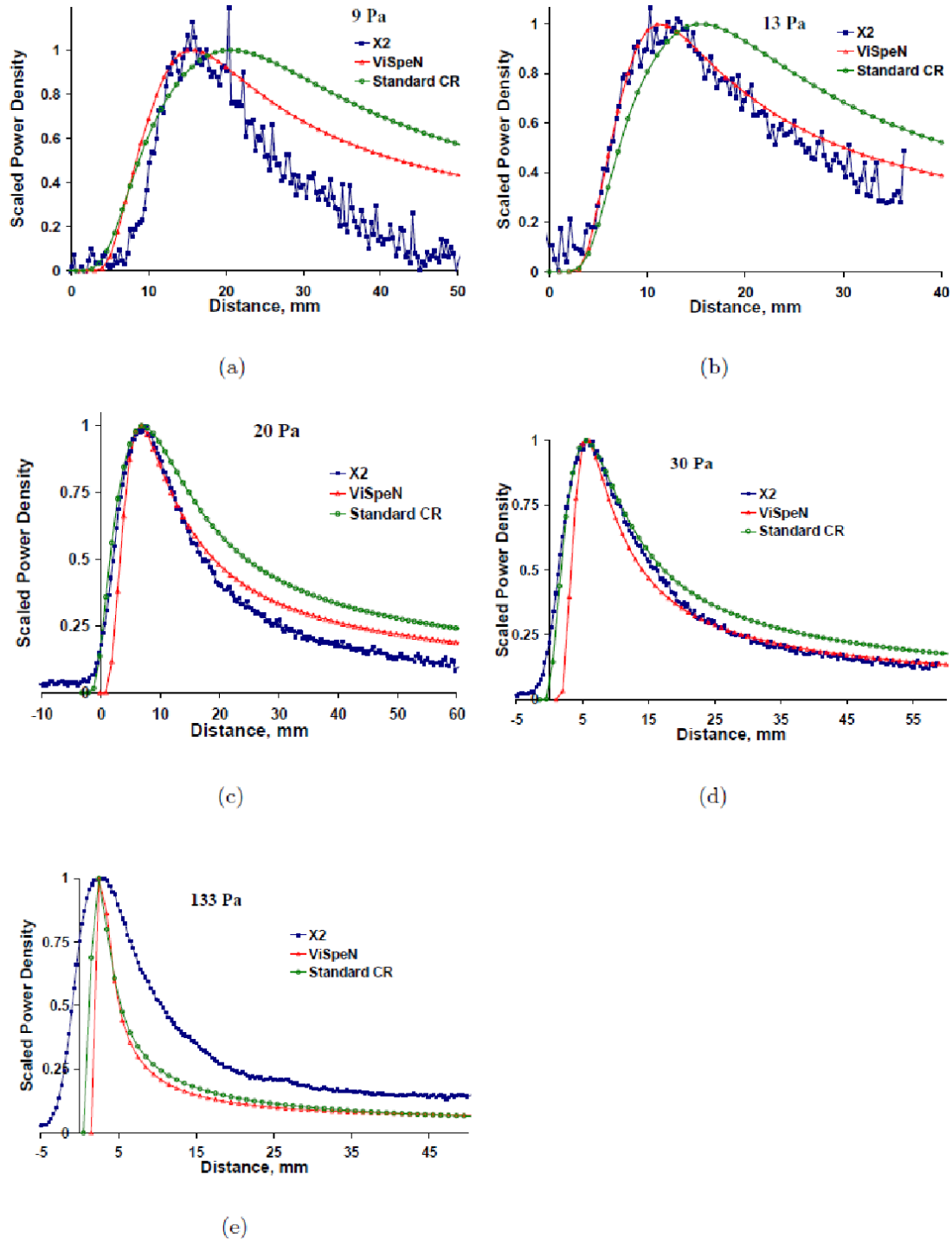


Figure 2.4 : Comparison of rise times and fall off rates between ViSpeN and the collisional-radiative model by Magin et al. at 98 % N_2 and 2 % CH_4 , 5.7 km/s. (Brandis 2009a).

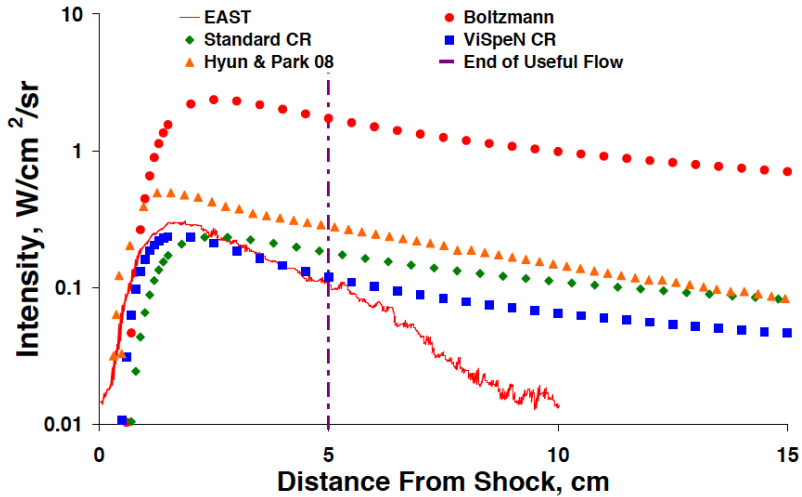
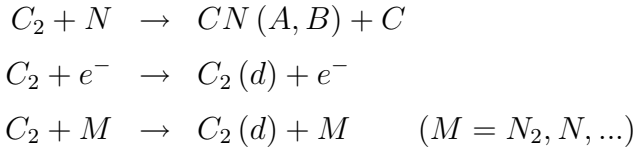


Figure 2.5 : Computed and measured CN violet intensities integrated over the spectral range 400-430 nm in the post shock region. (Brandis 2009a)

It is also desirable to continue exploring the important reaction channels for the formation of radiating species. *Ab initio* chemistry studies and/or carefully designed experiments would be useful to investigate the importance of reactions such as, in particular, those involving C₂.



In Figure 2.6, the individual radiative contributions of various species over a broad spectral range have been presented by Caillault et al. (2006). Although these simulations were completed using the Boltzmann assumption, the importance of including molecular and atomic species in the collisional-radiative model is clear.

2.3 Experimental validation

2.3.1 Existing validation data

This section aims to provide a very brief summary of the experimental data currently published and useful for the validation of a collisional-radiative model. Here, the data sources are simply cited, but a detailed description of all of these data is given in Winter and Laux (2008).

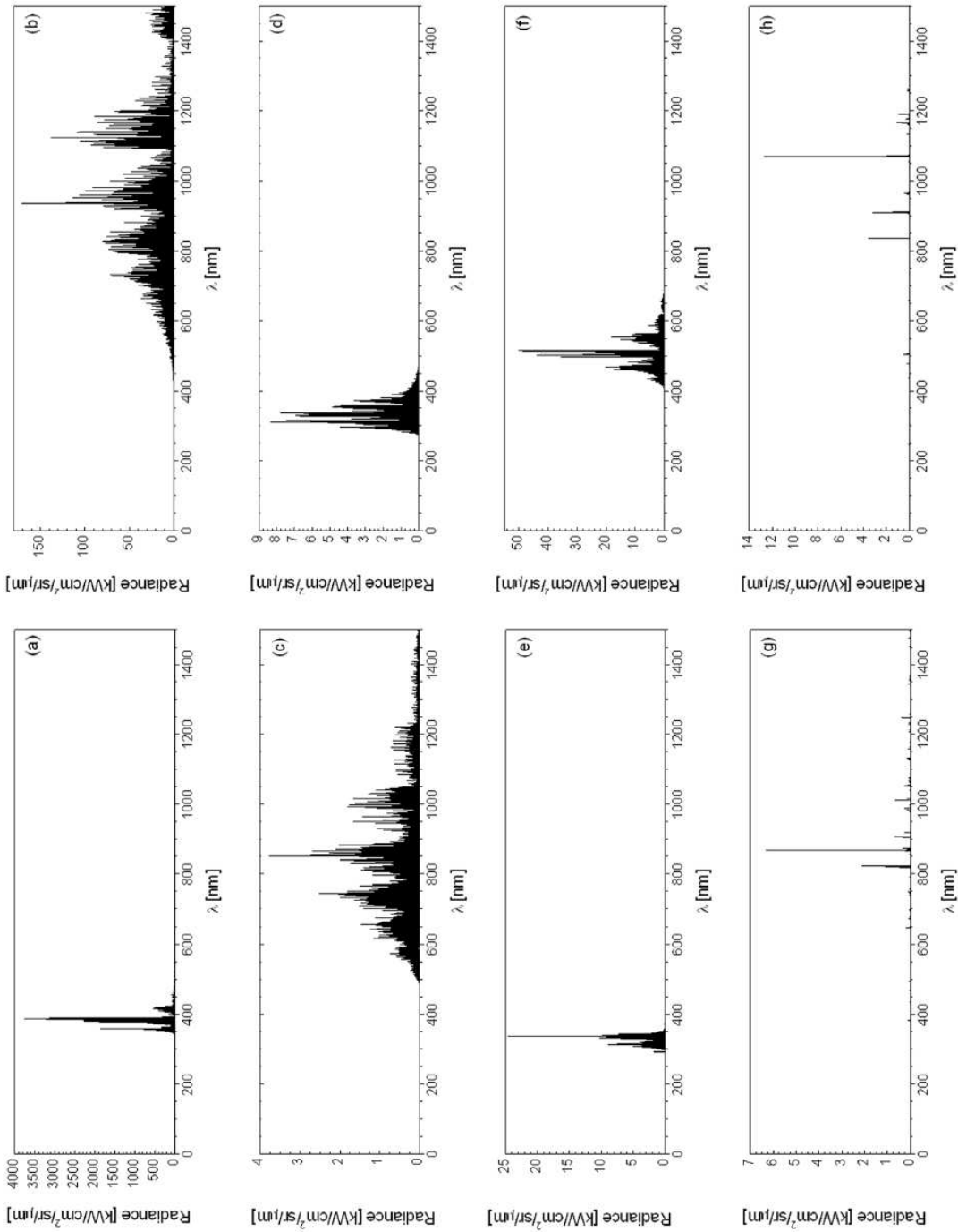


Figure 2.6 : Spectra of individual species for the Post-Ta(B) trajectory point at 191 s. The systems considered are (a) CN violet (B-X), (b) CN red (A-X), (c) first positive of N_2 (B-A), (d) second positive of N_2 (C-B), (e) NH (A-X), (f) C_2 Swan (d-a) and atomic lines (g) of N and (h) of C. (Caillault et al. 2006)

A number of flight experiments producing data useful to the validation of the computational codes required here have been completed over the years. These include:

- the FIRE II experiment, flown in March 1965 (Panesi et al. 2008; Park 2004; Fertig et al. 2008; Cauchon et al. 1967)
- the APOLLO 4 flight in November 1967 (Park 2004; Balakrishnan et al. 1986; Ried et al. 1972; Curry and Stephens 1970; Bartlett et al. 1970; Sutton 1984)
- the Bow Shock UV II experiment launched in February 1991 (Candler et al. 1993; Erdman et al. 1993; Erdman et al. 1993; Erdman et al. 1994; Levin et al. 1993; Levin et al. 1994; Levin et al. 1994)
- the HUYGENS probe, entering Titan's atmosphere in January 2005 (Magin et al. 2006; Wright et al. 2006; Caillault et al. 2006; Lorentz et al. 2006; Witasse et al. 2006; Walpot et al. 2006)
- the STARDUST return in January 2006 (Jenniskens et al. 2006; Jenniskens 2008; Trumble et al. 2008; Dean et al. 2008; Boyd et al. 2007; Boyd et al. 2008; Stackpoole et al. 2008; Winter and Herdrich 2008)

Shock tube experiments represent the most accurate method to rebuild flight conditions in ground test facilities and are a suitable tool for examining the flow field in the shock and in the post shock layer. Spectral data have been obtained: in the NASA Ames EAST facility (Bose et al. 2005; Sharma and Gillespie 1991; Grinstead et al. 2008); in the University of Queensland X2/X3 facilities in Australia (Brandis 2009a; Jacobs and Morgan 2009; Jacobs et al. 2011); in the TCM2 Wind Tunnel and Shock Tube facility at the University of Provence in Marseilles (Rond et al. 2007; Ramjaun et al. 1999); in the MIPT shock tube in Russia (of Physics and Technology 2009a; of Physics and Technology 2009b; Kosarev et al.); in a double-diaphragm free-piston shock tube at the University of Chiba, Japan (Koreeda et al. 1998; Morioka et al. 2000) and in an ISAS/JAXA facility in Japan (Matsuda et al. 2002; Matsuda et al. 2004; Matsuda et al. 2005). A summary of the conditions examined in these shock tube facilities for air mixtures is given in Figure 2.7 and for Titan mixtures in Figure 2.8.

2.3.2 Required validation data

A number of recent investigations have raised questions regarding the validity of assuming that the rotational temperatures can be described by a Boltzmann distribution and equal to the translational temperatures.

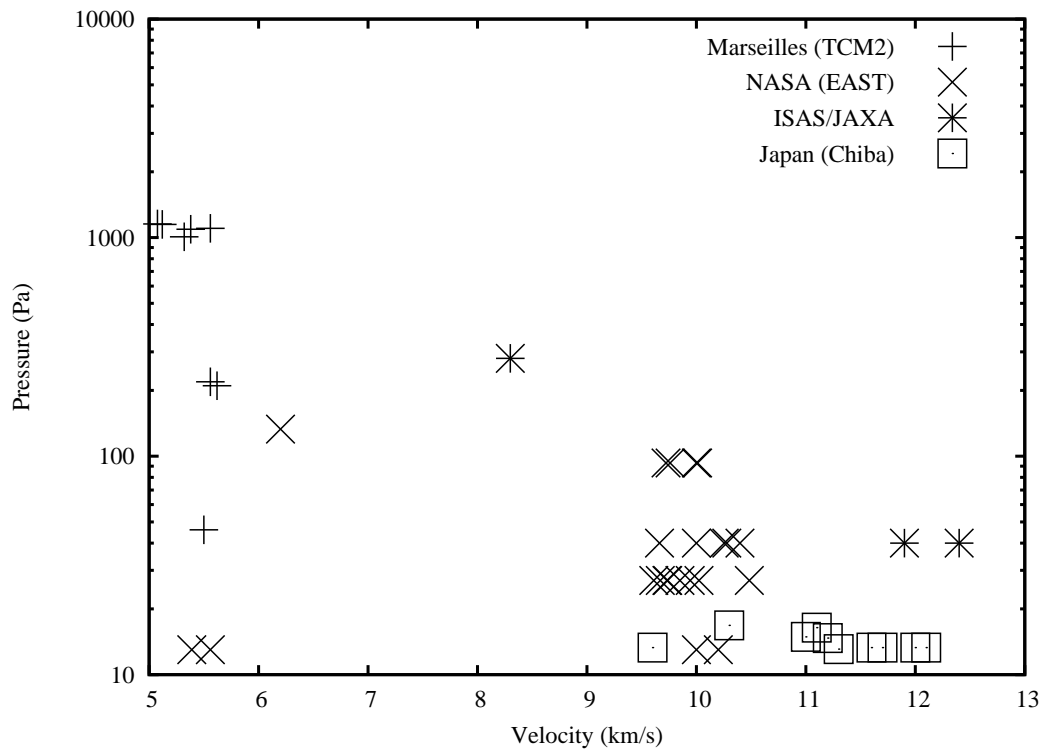


Figure 2.7 : Shock tube conditions investigated for air.

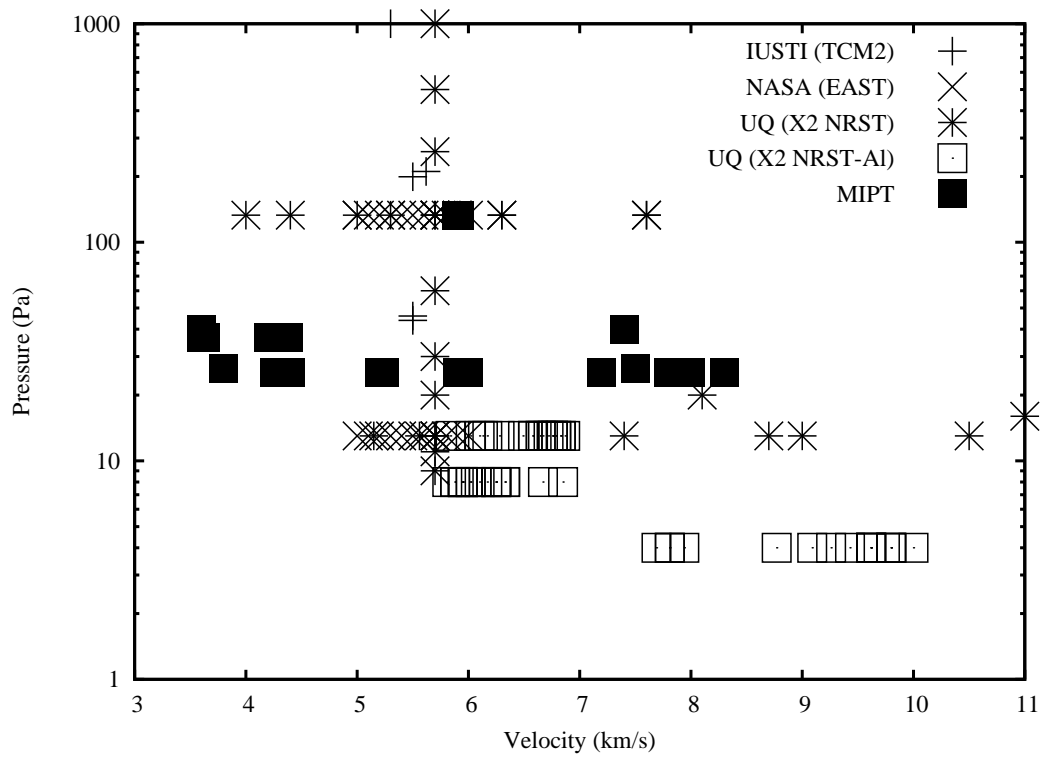


Figure 2.8 : Shock tube conditions investigated for Titan mixtures.

In 2002, Matsuda et al. (Matsuda et al. 2002; Matsuda et al. 2004) conducted shock tube experiments at the Institute of Space and Astronautical Science in Japan at shock velocities of 8 and 12 km/s (with test pressures of 2.1 and 0.3 torr respectively). Spectra in the wavelength range of 260-500 nm were measured and used to determine the rotational and vibrational temperatures of N_2 and N_2^+ using the spectrum fitting method. An example of the spectra fitting and measurements is given in Figure 2.9, where below 400 nm, there is a good agreement between the numerical (produced using the radiation code SPRADIAN (Fujita and Abe 1997)) and experimental spectra.

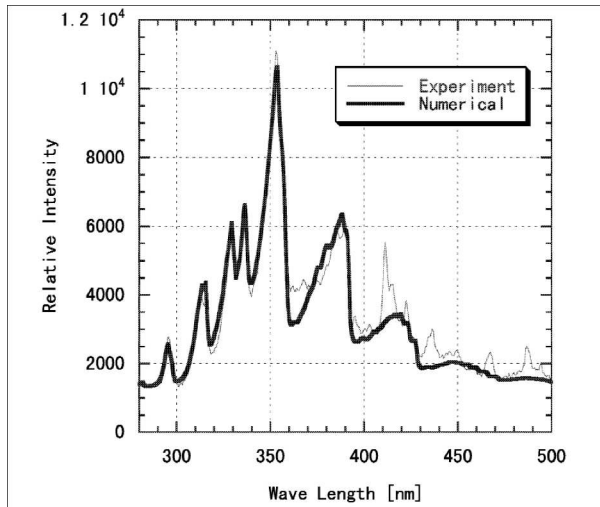


Figure 2.9 : Spectrum fitting with $V_s = 12.4 \text{ km/s}$, $L = 2.3 \text{ mm}$, N_2 ($T_r = 3500 \text{ K}$, $T_v = 5000 \text{ K}$, N_2^+ ($T_r = 17500 \text{ K}$, $T_v = 9000 \text{ K}$). (Matsuda et al. 2004)

The rotational and vibrational temperatures of N_2 were found to be 3500 K and 5000 K respectively. For N_2^+ , however, these values were determined to be 17500 K and 9000 K.

Figure 2.10(a) presents the temperature distributions behind a shock wave of velocity 12.4 km/s in air, and Figure 2.10(b) shows those same temperature distributions for a velocity of 11.9 km/s in pure nitrogen. The measured rotational temperatures did not match the numerical predictions (where $T_r=T_t$, and it was also found that the rotational temperatures calculated from the spectra for N_2 and N_2^+ were not in equilibrium).

In an analysis of the experimental work conducted at the NASA Ames Research Centre, Laux (Laux 2006) used the SPECAIR program (Laux 2002) to fit numerical spectra to those measured in the EAST facility. In Figure 2.11, a numerical spectra was fit to data from a shock with velocity 10.46 km/s through air at a pressure of 0.1 torr. This data was taken from the equilibrium region behind the shock, where thermal equilibrium is assumed. In order to generate the best numerical fit for the data, the $N_2(2+)$, $N_2^+(1-)$, CN violet, and NH(A-X) species were found to have temperatures at an equilibrium

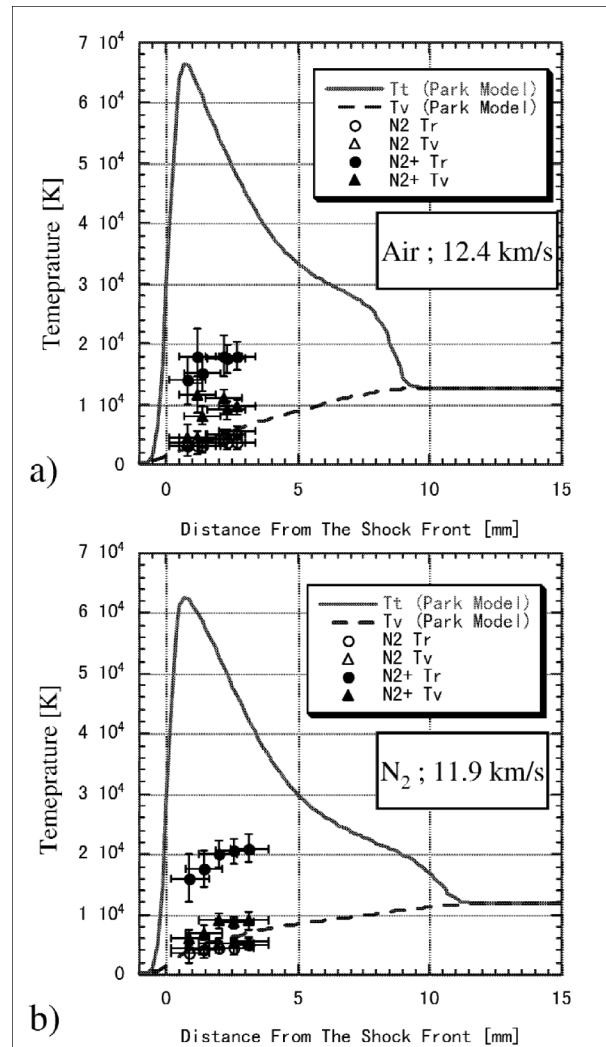


Figure 2.10 : Temperature distribution for a) shock propagation velocity of 12.4 km/s in the case of air, and b) shock propagation velocity of 11.9 km/s in the case of pure nitrogen. (Matsuda et al. 2004)

value of 12000 m/s. For N and O atomic species, however, T_{el} was found to be 8600 K, showing that the equilibrium region is underpopulated. This has been well confirmed in the simulations of Johnston et al. (Johnston et al. 2008c; Johnston et al. 2008a). From this result, it is clear that a collisional-radiative model is necessary for the atomic lines.

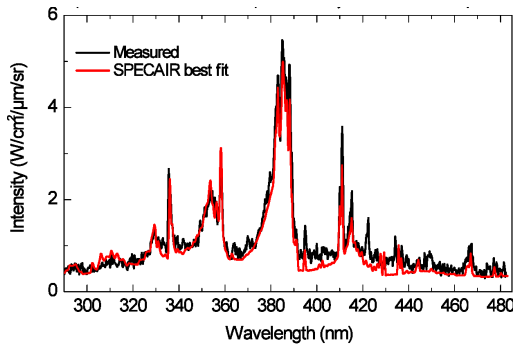


Figure 2.11 : Spectra fitting of NASA Ames data. (Laux 2006)

In an analysis of the nonequilibrium region behind the shock, for the same conditions, Laux found higher rovibrational temperatures for $N_2^+(B)$ and CN(B) than for N₂(C): $T_v = T_r = 16000 \pm 2000$ K and 8000 ± 1000 K respectively. This result was consistent with the observations of Matsuda et al. (Matsuda et al. 2002; Matsuda et al. 2004).

This result indicates that it will be necessary to develop a rotationally specific collisional-radiative model for air mixtures, and it is necessary to conduct further investigations into this phenomenon before conducting detailed collisional-radiative model developments. Repeating these experiments in air and nitrogen test gases at a pressure of 0.3 torr and shock velocity of 12 km/s with spectral measurements between 260 and 500 nm will be necessary in both the nonequilibrium and 'equilibrium' regions. In the original measurements by Matsuda et al. (Matsuda et al. 2002; Matsuda et al. 2004), the spectral resolution was not sufficient to determine the rotational temperature from the ratio of each rotational spectrum. Therefore, it is desirable to conduct these validation measurements at a resolution which allows the calculation of the rotational temperatures directly - resolutions of 0.1 nm or better.

Also, in order to investigate the atomic lines and the N₂(1+) system in more detail (as this allows the determination of the ground state atomic nitrogen concentration (Laux et al. 2001)), measurements and analysis should also be extended to 900 nm.

2.4 Summary

A review of existing models for nonequilibrium radiation in high speed Earth reentry and Titan entry has been presented. Recommendations were made for selecting the most appropriate models, and directions for improvement of these models were discussed. There is, however, still a clear need for additional spectral measurements, especially in the VUV region ($\leq 200\text{nm}$). Further investigations of the rotational population distributions of the important molecular species present in the spectra are also warranted.

CHAPTER 3

Experimental Considerations

The overall objective of this project, as highlighted in the Introduction, is to further the knowledge of the radiative heating environment for Titan entry applications - specifically at low density conditions where nonequilibrium effects are most pronounced. In order to do this experimentally, the X2 expansion tube facility was modified to have a large diameter shock tube, and experiments were completed using various diagnostic techniques.

In this chapter, the X2 facility and its modifications are described. Detailed information is given as to the instrumentation of the facility and the setup of the optical measurements presented in Chapter 6 and Appendix F. Although detailed results are left to Chapters 5 and 6, an example of the results obtained in the final facility is given in the conclusion of this chapter.

3.1 Facility modifications

To allow for experimental investigation into radiative heat transfer for low density Titan entry conditions, the X2 facility was modified in a number of ways. These modifications and the reasoning behind each are summarised in the following sections.

Briefly, these modifications were:

1. The X2 expansion tube facility was modified to run in nonreflected shock tube mode.
2. The shock tube bore diameter was increased.
3. A secondary driver section was added to the facility.
4. Aluminium was selected as the material of the shock tube walls.

3.1.1 Nonreflected shock tube mode

Modification 1 *The expansion tube facility was modified to run in nonreflected shock tube mode.*

Ground testing facilities such as the X2 facility take advantage of binary scaling to test small scale models of flight vehicles, which is the most important parameter to match in order to reproduce most of the phenomena occurring in high speed flight. The process of binary scaling for hypersonic models is described in detail in the literature (Hall et al. 1962; Hornung 1988; Hornung and Belanger 1990; Anderson 1989; Stalker 1989) and, therefore, will only be briefly outlined here.

Binary scaling, also called ‘ ρL ’ scaling, requires that the product of density and the characteristic length of the vehicle must be conserved between flight and experimental conditions, *i.e.*

$$\rho_{\infty, \text{flight}} L_{\text{flight}} = \rho_{\infty, \text{experiment}} L_{\text{experiment}}$$

The convective heat transfer at the stagnation point of a entry vehicle typically scales as (Anderson 1989)

$$\dot{q}_c \propto \sqrt{\frac{\rho}{L}} U_{\infty}^3 \propto \frac{\sqrt{\rho L}}{L} U_{\infty}^3 \quad (3.1)$$

Following the derivation contained in Capra (2007), the ratio of convective heat transfer between experimental and flight models is given as

$$\frac{(\dot{q}_c)_{\text{flight}}}{(\dot{q}_c)_{\text{experiment}}} = \frac{L_{\text{experiment}}}{L_{\text{flight}}} \quad (3.2)$$

When the total amount of convective heating is normalised by the kinetic energy flux past the vehicle, it is seen that the same amount of heat is removed from the flow per unit mass of gas in scaled testing and similarity with flight applies.

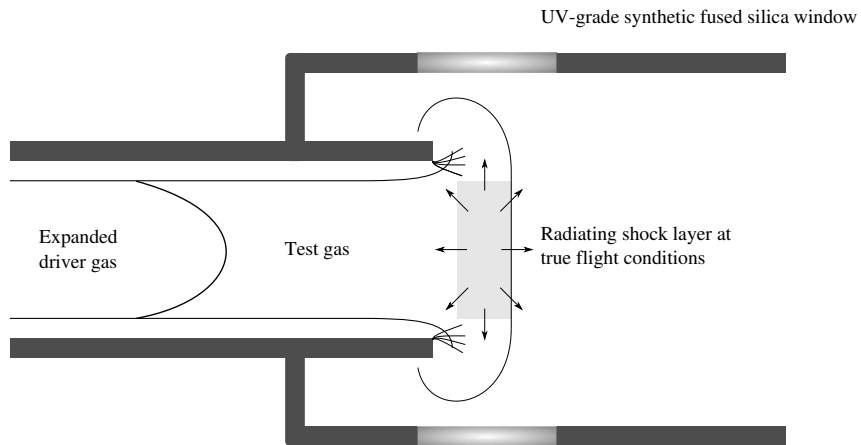


Figure 3.1 : Schematic of the nonreflected shock tube mode of operation.

However, it was shown (Capra 2007) that radiative heat transfer does not follow this same scaling factor, and true similarity with flight is not created for flows where the radiative and convective heat transfer are both significant. This can result in significant errors in the associated flow properties and the estimation of the heat transfer due to radiation.

To allow observation of a fully similar flow (with respect to flight), the first modification made to the X2 facility involved a conversion to nonreflected shock tube mode. A diagrammatic outline of this operation mode is given in Figure 3.1, in which the shock passes the observation point - as it would do for a vehicle flying by. This modification allowed experiments to be conducted at true flight densities, albeit for a small section of the full flow just behind the bow shock, avoiding the issue of radiation coupling to the flow. This was first implemented on X3 in 2005 (Morgan et al. 2006; Morgan et al. 2008a; Morgan et al. 2008b).

Using nonreflected shock tube mode enables the production of a normal shock, which recreates the aerothermochemical properties of the gas in the bow shock at a certain trajectory point. The tunnel conditions reproduce the flow properties along the vehicle's stagnation point in the region near the shock front, as illustrated in Figure 3.2.

3.1.2 Achievement of low pressure conditions

Modification 2 *The shock tube bore diameter was increased.*

Having modified the facility to allow for radiation heat transfer measurements, further modifications were required in order to allow the measurements to be taken at low density conditions. In an ideal case, the shock and contact surface would propagate down the

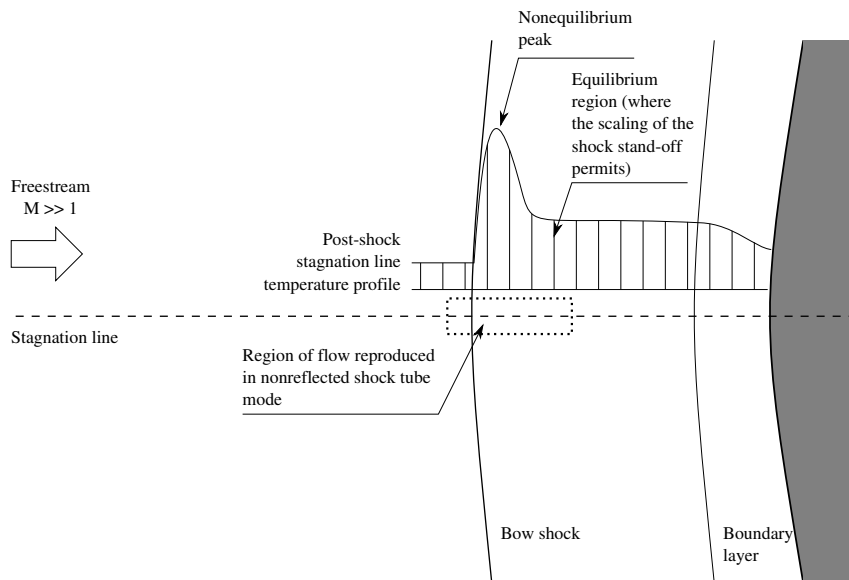


Figure 3.2 : Stagnation line radiative heating profile during entry showing the region of the flow which is captured by the shock tunnel facility in nonreflected shock tube mode.

shock tube at a constant velocity. However, the presence of the boundary layer at the wall of the shock tube creates a boundary layer entrainment effect as the shock propagates, removing mass from the gas between the shock and the contact surface (see Figure 3.3). As the length-to-diameter ratio of the tube is increased and the pressure reduced, the effect of the wall boundary layer entrainment becomes more significant.

This has been modelled by the analysis of Mirels (1963) and Roshko (1960), and the effect of the process is to limit the separation between the shock and the interface, reducing the test time available for radiation measurements (and, therefore, the achievable conditions).

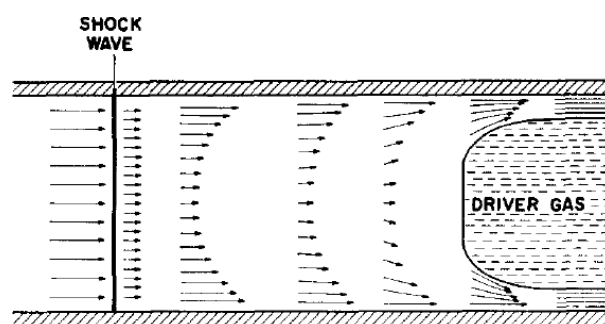


Figure 3.3 : Sketch of the flow behind the shock wave in a shock tube operating at a low initial pressure from a frame of reference in which the shock wave and contact surface are at rest. The arrows represent the fluid velocity; and the density of the flow is indicated qualitatively by the concentration of the arrows. (Duff 1959)

The length of usable test gas in laminar flows has been shown to scale with the square of diameter of the tube, as $D^2\rho/u$ (Mirels 1963). For this reason, the standard shock tube (diameter 85 mm) of the X2 facility was replaced with a section of larger diameter (155 mm). This modification allowed for measurements to be taken at initial fill pressures as low as 1 Pa in the shock tube and dump tank, however contamination of the test gas restricted this to a practical limit of 4 Pa in gases other than air.

3.1.3 Flow quality at low pressure conditions

Modification 3 *A secondary driver section was added.*

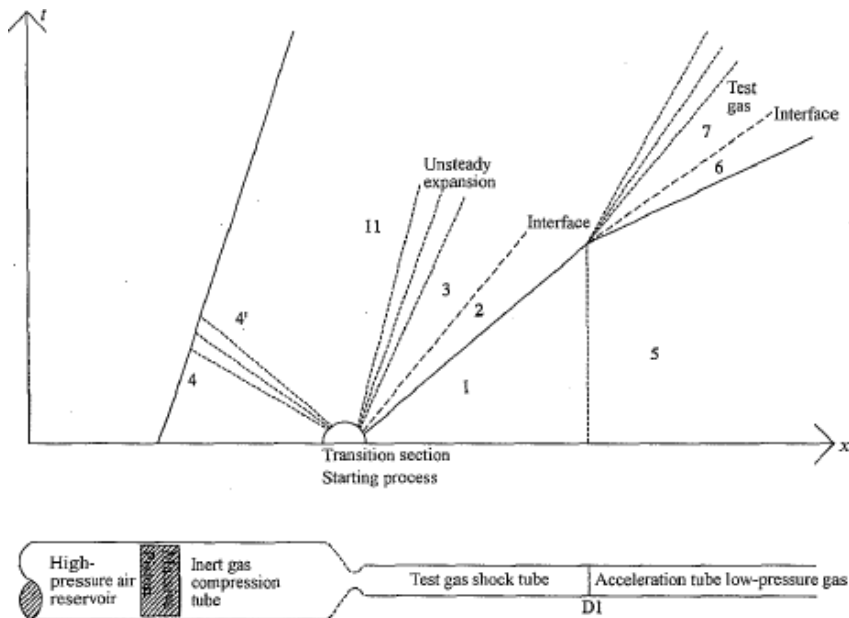
The speed of the shock wave exiting the shock tube is limited by the temperature of the driver gas. The addition of a so-called secondary driver section allows for the production of faster shock waves in the test section by providing a shock-heated driver which can reach much higher temperatures.

Theoretical and experimental investigations into multiple-diaphragm shock tubes (Henshall 1956; Bernstein 1953; Stalker and Plumb 1968) found that the use of an intermediate stage between the free-piston driver and the test gas significantly increased the shock Mach number. Figure 3.4 from Morgan (2001) further highlights the advantages of the compound driver¹. Using the nomenclature from Figure 3.4(a), the flow equivalent Mach number, M_7^* , is the flow speed behind the secondary shock normalised by the speed of sound in the primary driver (u_7/a_4). This value represents the primary factor that determines the advantages of using a secondary driver. In Figure 3.4(b), three different driver types are compared using this factor: single; combustion and compound. There is a clear improvement in the ratio of the gas pressure behind the secondary shock to the primary driver fill pressure (p_6/p_4) for a secondary driver at flow equivalent Mach numbers greater than 2.

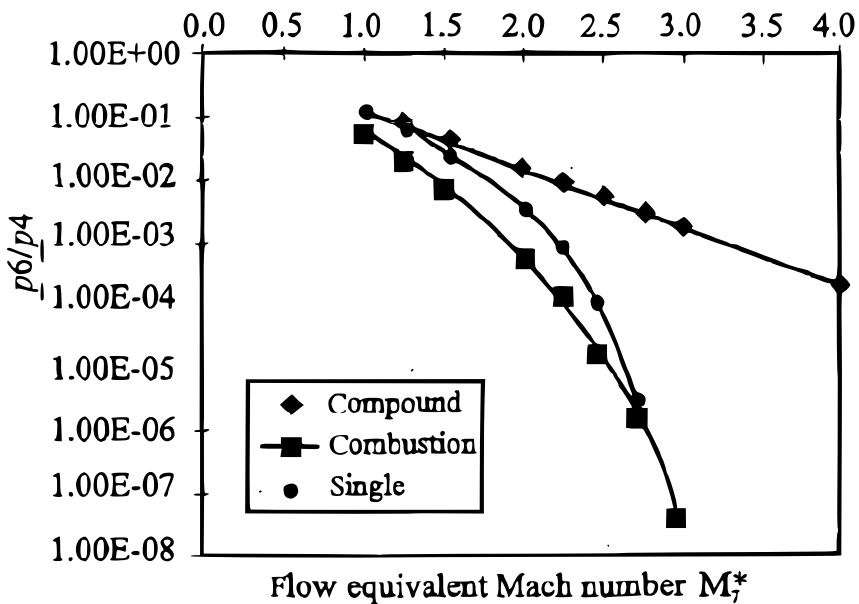
To enhance the performance of the facility, a secondary driver stage was placed between the compression tube and shock tube. This secondary driver was separated from the test gas by a very thin mylar diaphragm, designed to break quickly such that the reflection of the shock at the secondary diaphragm did not have a significant impact on the flow properties.

Modification 4 *Aluminium was selected as the material of the shock tube walls.*

¹A variety of nomenclature is used to describe the secondary driver: compound driver; double-diaphragm shock tube; multiple-diaphragm shock tube and secondary driver. Here, secondary driver has been chosen, and it will be used in all future discussions.



(a) Schematic illustration of a generic expansion tube with a corresponding x-t diagram.



(b) Comparison of driver options.

Figure 3.4 : The advantages of a compound driver. (Morgan 2001)

Bose et al. (2009) found that even in a synthetic air mixture containing only oxygen and nitrogen there were spectral lines corresponding to C, CN, and H. One possible cause considered for this phenomenon was that the flow down the tube swept up particles from the steel wall of the shock tube as it propagated downstream.

In an attempt to remove any possible contamination from the tube walls, a final modification was made to the facility. The modified shock tube was, therefore, constructed from aluminium rather than steel.

This modification was designed to allow an investigation into the effects of outgassing and other contamination on the spectral data in comparison with data from the previous steel tube.

3.1.4 Final facility description

Figure 3.5 shows the modified X2 facility from the start of the aluminium section downstream to the dump tank, and Figure 3.6 provides a schematic of the modified X2 facility and a space-time diagram of the NRST-Al flow.



Figure 3.5 : Photograph of the modified X2 facility in NRST-Al mode. Image shows the aluminium shock tube and the dump tank with the optical systems in place.

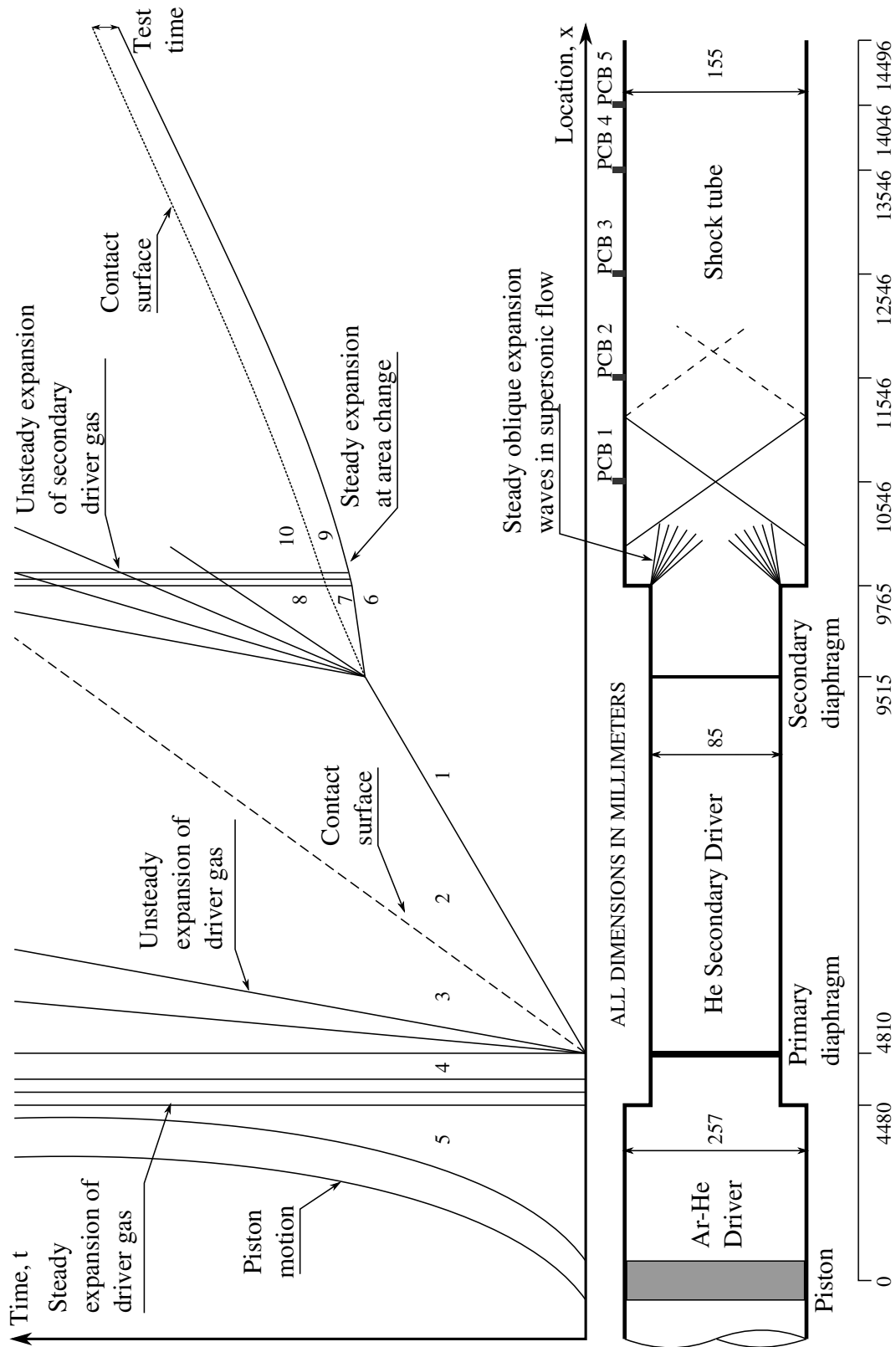


Figure 3.6 : NRST-Al mode schematic and space-time diagram. Not drawn to scale.

The modified facility uses a reservoir filled with compressed air at a pressure of 1.15 MPa to accelerate a free, single stage piston. The argon-helium primary driver mixture in the compression tube is compressed until the primary diaphragm (1.2 mm scored cold-rolled steel) bursts at a pressure of approximately 15.5 MPa, propagating a normal shock downstream. Within the primary driver, there is an area change where the diameter decreases from 257 mm to 85 mm. When the primary diaphragm bursts and the driver gas expands unsteadily and supersonically into the driver gas, there is also a steady expansion of driver gas at the change in diameter. Ideally, the conditions at this throat are sonic (Mach 1), resulting in a conservation of total pressure across this subsonic steady expansion.

The helium gas in the secondary driver is then compressed by the shock wave ahead of the expanding driver gas, bursting the secondary diaphragm ($12.5 \mu\text{m}$ mylar) and allowing the flow to expand into the larger diameter shock tube. Again, the bursting diaphragm produces an unsteady expansion of the driver gas into the test gas. However, at this point, the unsteady expansion is supersonic. In order to get any benefit from the compound driver setup, it is necessary to ensure that the operating conditions are overdriven. In this case, the post-shock speed of sound in the secondary driver gas (a_2 in Figure 3.6) is required to be greater than the speed of sound in the expanding primary driver gas (a_3), preventing any propagation of any acoustic effects ahead of the contact surface.

The shock propagates down the length of the shock tube into the dump tank, where measurements are taken at the exit of the tube. The bore diameter in this aluminium shock tube section is 155 mm and the tube extends 4.731 m downstream of the area change in the aluminium tube. This area change introduces another steady expansion wave into the flow. At this sudden area change, a complex wave pattern will be introduced into the flow with the potential to introduce oscillations into the core flow. It is found, however, that these oscillations are restricted to the expanding driver gas and do not corrupt the useful flow. This is investigated in Chapter 5. Across this sudden area change, the steady expansion will also result in a loss in total pressure. As discussed earlier, an increase in area ratio of approximately 3.3 results in an increased length of test gas being produced at the exit of the shock tube. With this gain, the losses are deemed to be acceptable.

Five PCB pressure transducers were mounted along the wall of the aluminium shock tube section as shown in Figure 3.6. An additional six PCB pressure transducers were mounted along the secondary driver tube section. The details of all transducer and diaphragm locations are given in Table 3.1. A rake containing nine PCB transducers was also placed in the dump tank to record the Pitot pressures for each shot. For experiments in which emission spectroscopy was performed, these Pitot pressure transducers were removed from the facility so as not to interfere with the optical measurements.

The data recording system, the high speed camera and the spectrometer, when used, were all triggered off the same system. This triggering system used the static pressure traces from *al4* and *al5* as inputs to a microcontroller-based delay generator (Jacobs 2011). The shock speed was calculated using the time taken for the shock to propagate between the two transducers 0.5 m apart. This shock speed was used to estimate the time at which the shock reached the desired measurement point (nominally 70 mm from the shock tube exit; 0.52 m from *al5*) and a TTL trigger pulse was output from the system.

Feature	Axial location (m)
Start of reservoir	-3.890
Piston centre before launch	0.000
Buffer (halting piston)	4.4795
Primary diaphragm	4.810
Transducer st1	7.381
Transducer st2	7.614
Transducer st3	7.845
Transducer at1	8.755
Transducer at2	9.005
Transducer at3	9.255
Secondary diaphragm	9.515
Transducer al1	10.546
Transducer al2	11.546
Transducer al3	12.546
Transducer al4	13.546
Transducer al5	14.046
End of shock tube	14.496

Table 3.1 : Axial locations of transducers and diaphragms in the X2 NRST-Al configuration.

The databox used was a National Instruments device constructed from the following components

- 1× NI PXI-1042Q 8 slot 3U PXI chassis
- 1× NI PXI-8196 embedded controller
- 4× NI PXI-6133 S Series Multifunction DAQ cards

The PXI-8196 embedded controller is a high-performance Pentium M 760 based controller, and for these experiments it was used in conjunction with the four PXI-6133

S Series Multifunction DAQ cards. These cards had eight analog inputs, 14 bit input resolution and a 1×10^6 samples/s per channel sampling rate.

3.2 Test conditions

Table 3.2 presents the final experimental fill conditions and details. Three Titan conditions were examined with shock speeds between 6 and 9 km/s. The first of these conditions, the 13 Pa condition, was designed to allow a comparison between the NRST-Al setup of the X2 facility and the work of Brandis (2009a). Additionally, a number of computational simulations were completed at the 13 Pa condition to demonstrate the improved flow quality and success of the modified facility. The improved test flow gave radiative heat transfer signals with reduced noise when compared to the previous facility, and also extended the measurements into the equilibrium region following the shock by producing a longer test flow.

In order to demonstrate the ability of the X2 NRST-Al facility to provide emission spectroscopy data for Titan entry conditions at very low freestream pressures, two further conditions (8 Pa and 4 Pa) were also completed.

3.3 Optical diagnostics

Imaging of the spectroscopic data was achieved using an intensified CCD camera (Princeton Instruments PI-MAX) coupled to the output of a Czerny Turner spectrometer (Acton Research Spectra Pro SP2300i). The PI-MAX ICCD array has a resolution of 1024 pixels in the horizontal axis (wavelength) and 256 pixels in the vertical axis (position). The system used for these experiments was capable of imaging over the wavelength range of 200-600 nm, with an optimal range of 280-500 nm. The images obtained with this system consist of a two-dimensional distribution of intensity which is the sum of a series of monochromatic images of the entrance slit, each one corresponding to a different wavelength. The resultant image records intensity variations with wavelength along one dimension, while the other dimension yields spatial variations in intensity as viewed along the long axis of the entrance slit of the spectrometer. Figure 3.7 outlines the manner in which the external optics form a real image of the object plane on the spectrometer slit.

For all experimental work completed in this project, a region approximately 100 mm long by 1 mm high was imaged onto the entrance slit of the spectrometer. A magnification factor of 0.063 was measured for these experiments between the centreline of the shock tube exit and the image plane on the spectrometer's entrance slit. Resolution was controlled by varying the width of the entrance slit to the spectrometer and by the choice

	13 Pa Condition	8 Pa Condition	4 Pa Condition
Reservoir gas mixture	Air	Air	Air
Reservoir fill pressure	1.15 MPa	1.15 MPa	1.15 MPa
Primary driver gas mixture	85 % He - 15 % Ar	80 % He - 20 % Ar	100 % He
Primary driver fill pressure	30 kPa	30 kPa	30 kPa
Primary diaphragm	1.2 mm steel; 0.2 mm scoring	1.2 mm steel; 0.2 mm scoring	1.2 mm steel; 0.2 mm scoring
Primary diaphragm burst pressure	15.5 MPa	15.5 MPa	15.5 MPa
Secondary driver gas mixture	100 % He	100 % He	100 % He
Secondary driver fill pressure	30 kPa	30 kPa	10 kPa
Secondary diaphragm	1/2 thou Mylar	1/2 thou Mylar	1/2 thou Mylar
Secondary diaphragm burst pressure	75 kPa	75 kPa	75 kPa
Test gas mixture	98 % N ₂ - 2 % CH ₄	98 % N ₂ - 2 % CH ₄	98 % N ₂ - 2 % CH ₄
Test gas fill pressure	13 Pa	8 Pa	4 Pa
Nominal average shock speed	6.41 km/s	6.19 km/s	9.04 km/s

Table 3.2 : Experimental fill conditions for the modified X2 NRST-Al facility.

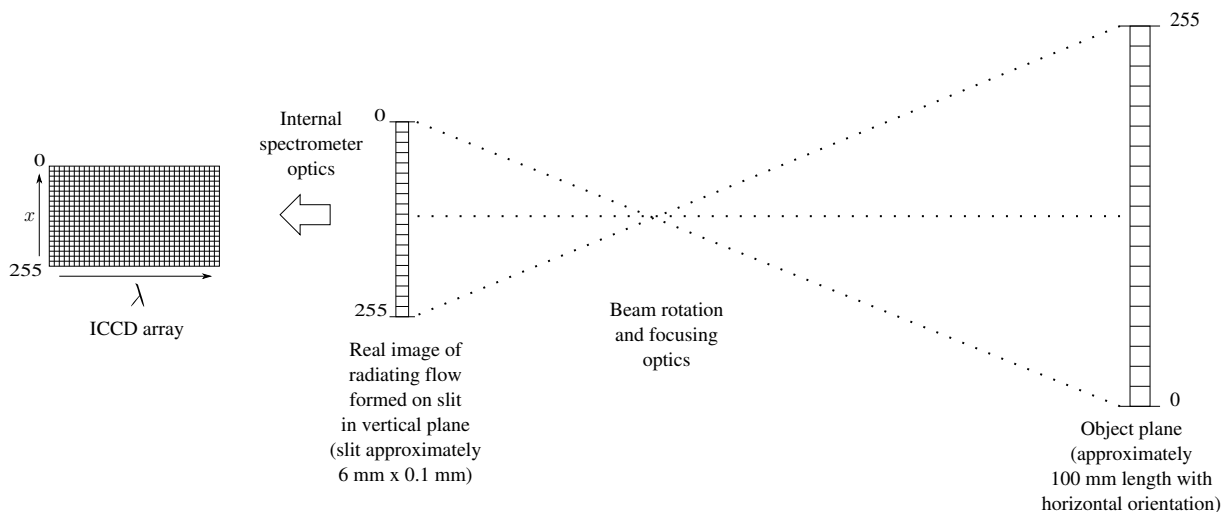


Figure 3.7 : Schematic of the radiation collection methodology.

of which of the three interchangeable diffraction gratings was used. Each grating has a different dispersion, yielding single shot wavelength ranges across the 1024 pixels of the camera of approximately 40 nm, 120 nm and 480 nm. The sensing elements of the ICCD camera were 16 bit. Data was gathered for all conditions using each of the three gratings to provide the most detailed information possible within signal strength constraints.

The sensitivity of the system was dependent on the size of the area imaged, the spectral resolution, and the magnifying optics utilised in the imaging. Figure 3.8 provides an overall schematic view of the optical setup using a spherical curved mirror to focus the beam onto the spectrometer slit. The iris diameter was 15 mm, located 1458 mm from the plane of the centreline at the shock tube exit.

The spectrometer can only function with a vertical slit orientation, but for the purposes of these experiments, a horizontal scan in the shock tube test section was required in order to obtain axial profiles of radiance. As shown in Figure 3.9, two UV enhanced aluminium mirrors affixed to the optical table, on which the spectrometer rests, were used as a combined beam rotator and periscope to turn the image of the horizontal flow 90 degrees to match the vertical entrance slit of the spectrometer and to lower the optical path from the height of the windows and test section to one in line with the entrance slit and internal optics of the spectrometer. The image is then focussed with an $f=100$ mm aluminium spherical mirror before a small turning mirror directs it normal to the entrance slit.

The periscope introduced a vertical offset to the optical path, which must be included in the physical design of the apparatus when calculating the magnification. It also added two additional optical components whose reflectivity had to be included in the calibration

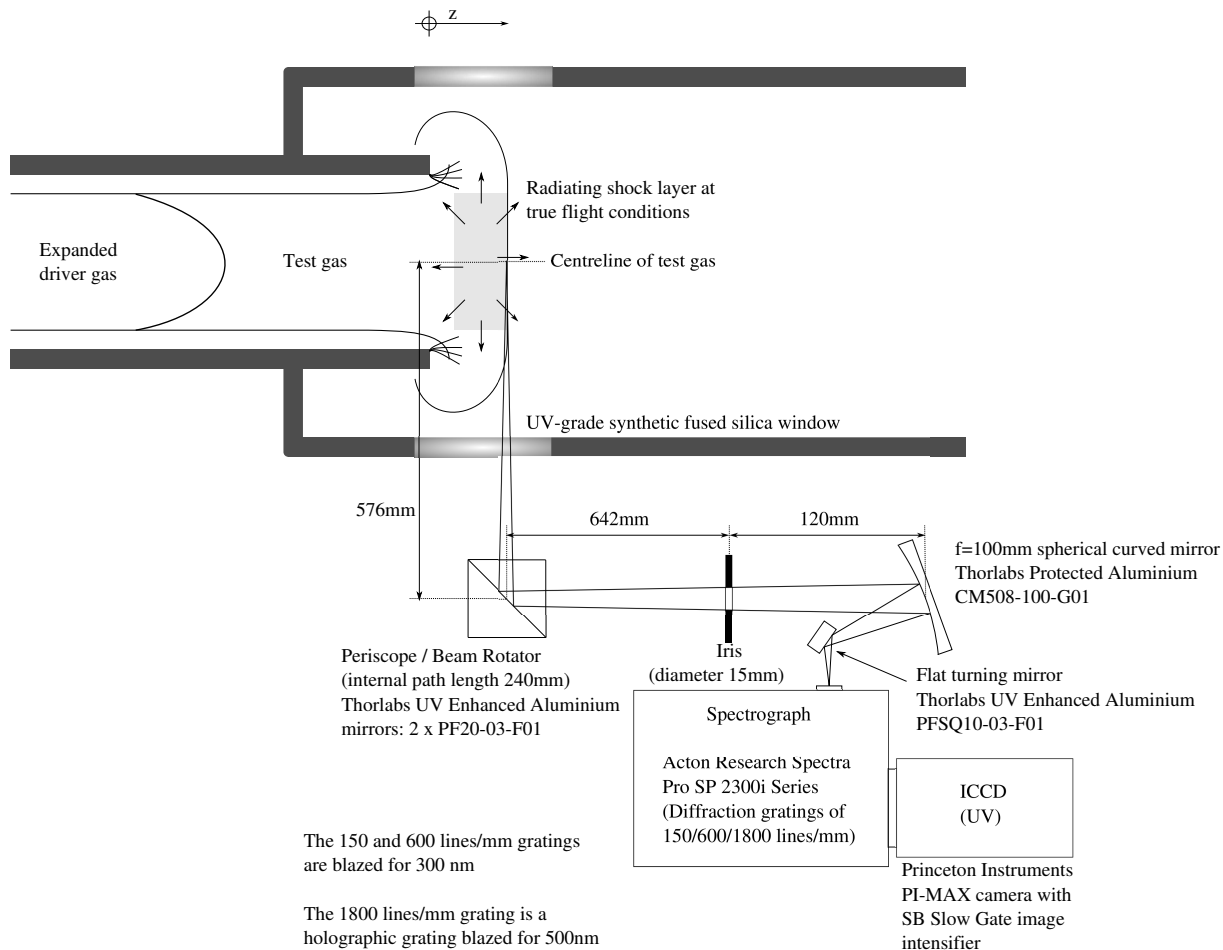


Figure 3.8 : Schematic of the final optical layout used in the NRST-Al experiments.

process.

The spectrometer and camera settings used during the experiments were as follows:

- Gate mode, with a nominal gate width of 100 ns.
- Slit width of 20, 50, 100, or 200 μm (details tabulated in Appendix F).
- Intensifier gain of 240.
- Bracket pulsing of the intensifier microchannel plate to reduce charge smearing.

A high speed camera (Shimazdu HPV-1) was also used for optical diagnostics of these conditions. Video of the flow exiting the shock tube was captured using a 1 MHz frame rate.

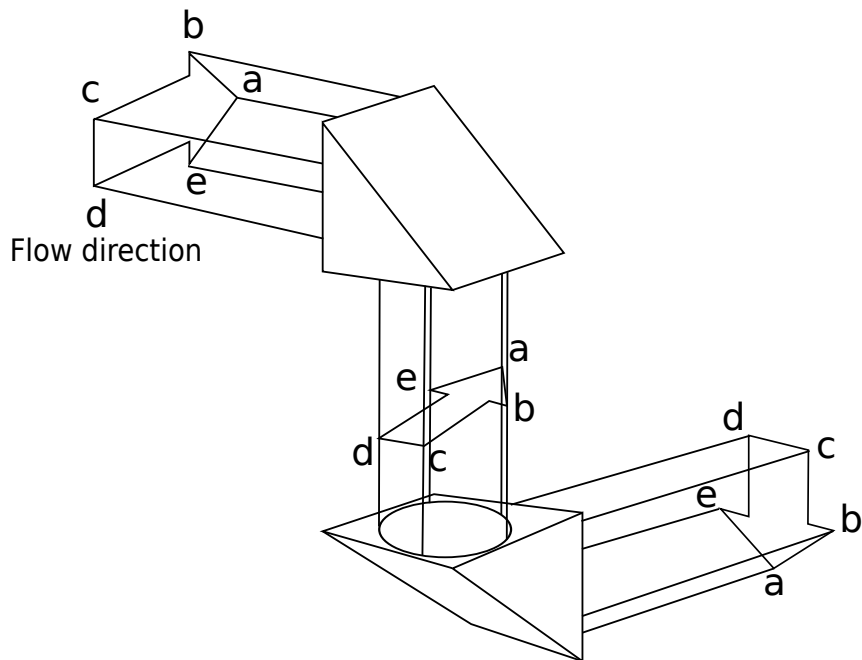


Figure 3.9 : Operating mode of the periscope.

3.4 Emission spectroscopy calibration

Calibration of all spectral data was used to convert the intensity measurements to spectral radiance ($\text{Wcm}^{-2}\text{nm}^{-1}\text{sr}^{-1}$) and spectral power density ($\text{Wcm}^{-3}\text{nm}^{-1}\text{sr}^{-1}$). To obtain absolute values, it is necessary to calibrate each pixel of the ICCD array for the appropriate wavelength it will be recording. As the wavelength seen by each pixel changes with spectrometer setup, it is necessary to recalibrate the system using an invariant calibration

source for each configuration used. The calibration lamp used was an Optronics Laboratories OL-200M tungsten-halogen spectral lamp, which has an element approximately 25 mm long, with an effective radiating area of approximately 20 mm × 5 mm. This lamp is not a point source, but at distances of 500 mm or more from the spectrometer slit, the radiance scales with $1/d^2$ and it may be used to give accurate absolute levels of calibration. At a distance of 500 mm, the light radiating from the extreme ends of the lamp source has an included angle of approximately 3 degrees, which is less than the capture angle of the spectrometer. Therefore, the lamp will provide a valid calibration of the spectrometer and ICCD.

The calibration codes are included in Appendix D, and the calibrated data for all experiments are included in Appendix F.

3.4.1 Calibration image acquisition

While it is desirable to ensure that the spectrometer settings for the calibration images remain as close as possible to those for the experimental images, some deviation was necessary. During the experiments, the nominal exposure time is 100 ns. Unfortunately, a single 100 ns exposure image of the calibration lamp would not provide sufficient intensity for a calibration. The software which drives the spectrometer allows the user to capture multiple instances with a certain exposure time and build these into a single accumulated image. This image could then be scaled down linearly to a 100 ns equivalent. Using an accumulated image, the signal-to-noise ratio of the image is improved.

However, at 100 ns the signal strength of the calibration image on the ICCD array was so small as to cause numerical problems in the calibration procedure, and the very low intensity of the calibration after the removal of the background noise introduced significant levels of noise in the calibrated data. Therefore, it is necessary to capture calibration images at a larger exposure time and to scale these images appropriately. The difficulty then becomes adding an appropriate scaling factor to convert the calibration image back to the equivalent of 100 ns. Ideally, this would be a linear relationship, but it was found that this did not hold for the very small exposure times used in these experiments (see Appendix A for details). The calculated scaling factor to convert a 10 μ s calibration exposure to a 100 ns equivalent exposure was found to be 144.54 rather than the originally expected value of 100.

The final calibration images were taken over two frames, each comprising of 100 accumulations with an exposure time of 10 μ s. During the calibration process, the entrance slit of the spectrometer was shielded from the calibration lamp between images so as to prevent any charge build-up. This shielding was removed during the capture of the first

frame. Therefore, during the calculations, the first frame was discarded, and the scaled second frame was used as the calibration image.

3.4.2 Image processing

The recorded signal may be expressed as

$$a(x, y) = f(x, y) + b(x, y) + n(x, y) \quad (3.3)$$

where $f(x, y)$ is the response of the ICCD to each image of the slit corresponding to individual wavelengths of the emitted radiation, $b(x, y)$ is the background due to the thermal noise present in the CCD array, and $n(x, y)$ represents noise in the image due to shot noise, hot pixels and, occasionally, cosmic rays.

3.4.2.1 Dark current removal

Thermal noise, or dark current, is the result of the random thermal generation of electrons and holes within the depleted region of the charged-coupled device even when there are no incident photons. The simplest method of reducing dark current is to reduce the operating temperature of the CCD array. Nominally, the temperature of the array in the PI-MAX ICCD was reduced to 253 K using a Peltier cooler.

For each experimental and calibration image, a background level of intensity was subtracted from the data. In each case, this background level was taken from a pixel region known to be outside of the capture area of the image intensifier array.

3.4.2.2 Hot pixel and cosmic ray removal

Hot pixel noise was then removed from the images by using the gradient in the vertical axis to locate pixels that are significantly brighter than those surrounding. Hot pixels are elements of the CCD array which have an above average rate of charge leakage. They appear as small (usually single pixel) bright spots in an image and grow progressively brighter with a longer exposure time. A simple average of the adjacent cells was used to replace the value of the hot pixel.

3.4.2.3 Noise filtering

Other than the hot pixel removal, no noise filtering was added to the calibration code. This is primarily due to the fact that with such short exposure times, the signal-to-noise ratio is fairly small in these experiments and filtering techniques would result in the loss of significant data. The addition of smoothing techniques to the calibration methodology would also result in an undesirable loss of resolution.

3.4.2.4 Calculation of the scaling map

At each location in $f(x, y)$ there is a 16-bit integer determined by the number of photons detected by each element of the CCD array. The spectral radiance due to the flow can be determined by comparison with a calibration image $f_c(x, y)$ from a source of known spectral irradiance by taking into account the solid angle of detection. The coordinate frame of the CCD image may be re-expressed in terms of wavelength, λ , and position past the expansion tube exit, z .

$$f(x, y) \equiv f(\lambda, z) \quad (3.4)$$

$$f_c(x, y) \equiv f_c(\lambda, z) \quad (3.5)$$

The spectral irradiance of the calibration lamp is a known quantity and varies as a function of wavelength, $E_c(\lambda)$. The calibration data for the various calibration lamps are included in Appendix D. The calibration allowed a determination of the energy per unit count for each pixel. A tunnel measurement records the number of counts for light emitted into a solid angle, Ω , which is determined by the aperture size of the iris (15 mm; see Figure 3.8). A scaling map can thus be formed which converts the counts recorded in a tunnel measurement to a spectral radiance.

Dividing this known spectral irradiance function on a point by point basis by the measured signal strength of the calibration image and allowing for any disparity in the exposure time between the calibration, t_c , and measurement image, t , yields a scaling map;

$$g_c(\lambda, z) = M^2 \epsilon \frac{E_c(\lambda)}{\Omega} \frac{1}{f_c(\lambda, z)} \frac{t_c}{t} \quad (3.6)$$

where ϵ represents the efficiency of the optical system due to components such as windows and mirrors and M is the magnification of the system.

The spectral irradiance of the measured image is therefore;

$$E(\lambda, z) = g_c(\lambda, z) f(\lambda, z) \quad (3.7)$$

Figure 3.10 shows the spline fit for the calibration standard. In order to account for the oxygen absorption that occurs in the laboratory environment at wavelengths below approximately 200 nm, an additional data point was added to the calibration data provided with the lamp to ensure that the spline fit used remains at a value of zero below this wavelength limit.

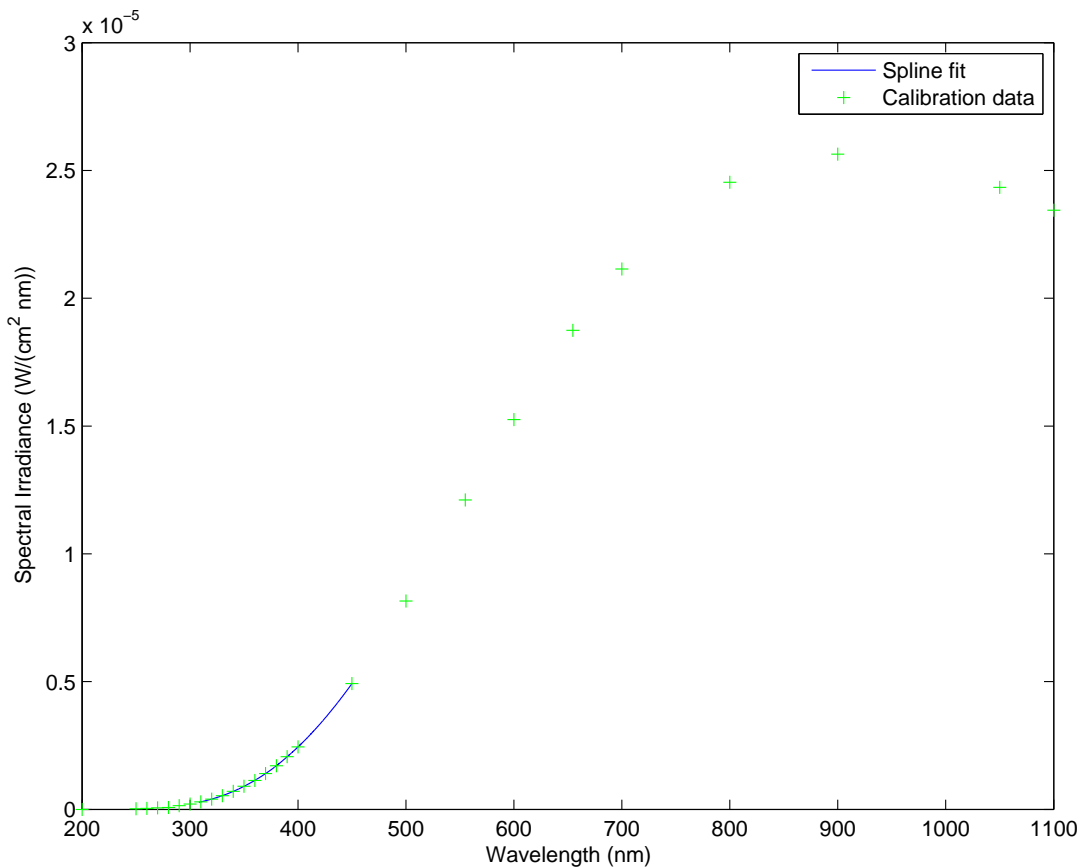


Figure 3.10 : Calibration data and the spline fit of the spectral inrradiance of the calibration lamp over the wavelengths examined (200-450 nm).

3.4.3 Image uncertainties

The object plane of the external optics may be considered to consist of a one-dimensional array of virtual pixels, each of which maps down onto a single row of pixels on the ICCD, giving the wavelength dependency of the source at that physical location. During the exposure of the ICCD, the shock wave moves approximately 0.6 mm for the 13 Pa and 8 Pa conditions and 0.9 mm for the 4 Pa condition, resulting in spatial averaging. The magnification of the external optics was 0.063, resulting in a physical size of each virtual pixel in the test section on the order of 0.35 mm. In addition, the geometry of the optics and the width of the radiating region (approximately 155 mm) means that the light recorded at each spatial location is, in fact, an average signal accumulated along a line of sight passing through the test flow at an angle and not along a line of uniform properties. The effect of this will change with offset from the optical axis of the focussing mirror. For on-axis pixels, the effect will be at a minimum and is set by the aperture of the iris to be the equivalent of 2.3 mm of axial flow, or approximately 7 pixels. For pixels at the extremes of the field of view, the line of sight passes through approximately 5 mm of axial distance, meaning that the signal is effectively averaged over roughly 14 pixel lengths. This means that the signal attributed to each single pixel may include contributions from 13 other pixels. This is accounted for in the uncertainty analysis of the emission spectroscopy measurements discussed in Appendix B.

In the measurement situation, each pixel receives an integrated amount of radiation along its line of sight, and a direct measurement of $\text{Wcm}^{-2}\text{nm}^{-1}\text{sr}^{-1}$ is obtained for the total radiation along that line of sight. To enable quantitative measurements of source radiation (in terms of $\text{Wcm}^{-3}\text{nm}^{-1}\text{sr}^{-1}$), a knowledge of the uniformity and extent of the radiating zone is needed. If the flow is completely uniform and of known transverse length, then this is obtained by dividing the direct measurement ($\text{Wcm}^{-2}\text{nm}^{-1}\text{sr}^{-1}$) by that length. This procedure is complicated by the presence of the boundary layers, which form on the tube walls, and the expansion at the tube exit, which leads to the formation of a slightly curved shock. The line of sight for each pixel passes through all of these regions, with varying levels of significance depending on axial location. When interrogating the flow near the tube exit, the normal region of the shock dominates, the boundary layer thickness is small, and the radiating layer can be considered to extend across the full width of the duct. Further downstream, the core flow decreases and a smaller slug of radiating gas is examined. In practice, data measurements are focussed in the region near the tube exit, and repeated exposures of the same flow condition with the shock at different locations have shown only minor variations, indicating that these effects are second order for this configuration (Brandis 2009a).

Because the lamp has a certified absolute calibration, the overall calibration of the spectrograph system can be obtained to good accuracy. Losses are incurred in the external optics, including the window of the tunnel, mirrors in the periscope, the focussing mirror and the planar turning mirror used to bend the final beam onto the spectrometer slit. These losses may be accounted for independently, and the absolute calibration is obtained by chaining all of the transmittance factors together to calculate the overall collection efficiency, ϵ . For the planar mirror surfaces and the windows, the same calibration source was used to measure the relative magnitude of the signal received at each pixel, with and without the reflecting or transmitting surface in the path. The effective optical path length was maintained at 500 mm for all cases and the wavelength dependency of reflectivity was quantified. For the focussing mirrors, the light source was placed two focal lengths away from the mirror, so as to form a full size real image of the lamp, also two focal lengths away from the mirror. The relative signal strengths were then obtained by locating the spectrometer slit 500 mm from both the lamp and its real image. Figure 3.11 shows the setup of all optical efficiency measurements conducted.

This uncertainty is described in further detail in Appendix B. The results of the calibration quantify the response of the overall system collected from the test section by each pixel, that is, it is a pixel-by-pixel calibration.

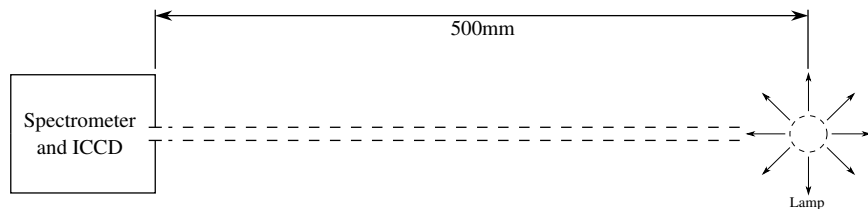
3.5 Summary

A number of modifications were made to the X2 facility. These were:

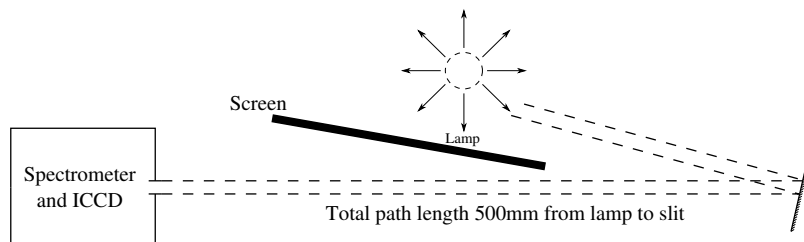
- The facility was altered to allow for operation in nonreflected shock tube mode.
- The shock tube bore diameter was increased.
- A secondary driver was added to the facility.
- The shock tube was constructed from aluminium.

These modifications allowed experiments to be conducted at very low freestream pressure conditions in a simulated Titan atmosphere. A variety of diagnostics were used during the experiments: static pressure measurements; Pitot pressure measurements; high speed camera videos and emission spectroscopy images. All measurements made are analysed in detail in Chapters 5 and 6. Raw and calibrated spectral data for all successful experiments are provided in Appendix F. The calibration scripts for processing the spectral data are provided in Appendix D. Further details on the uncertainty associated with the experimental measurements are given in Appendix B.

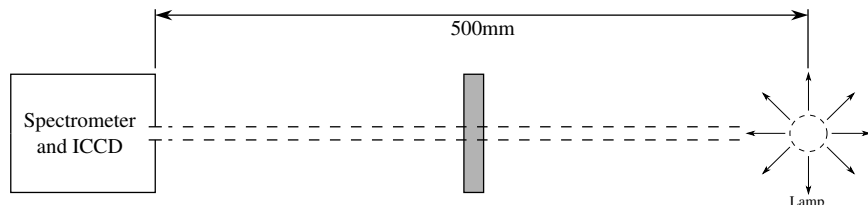
Direct calibration of ICCD



Calibration of planar mirrors



Calibration of planar window



Calibration of spherically curved mirror

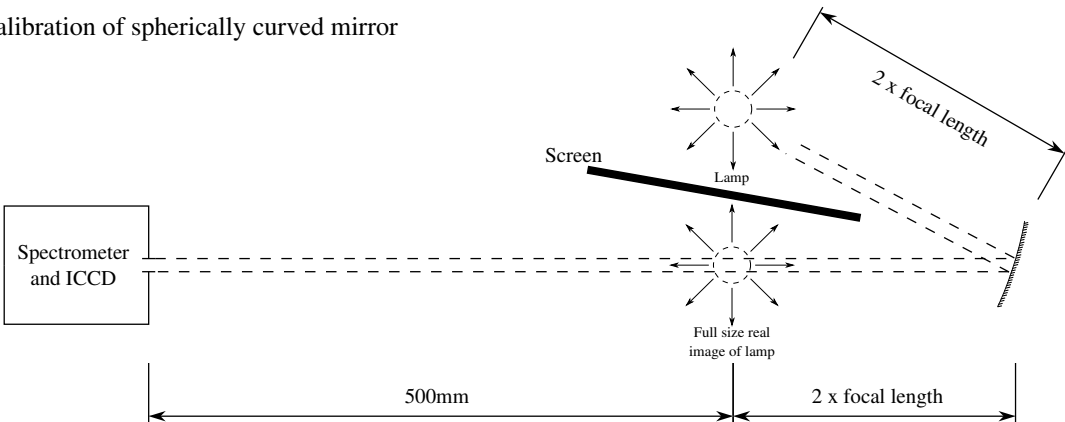


Figure 3.11 : Schematic of the calibration setup for the external optical components.

CHAPTER 4

Computational Considerations

Validation of the experimental results and definition of the flow conditions was achieved through comparisons of the data with computational models. Two flow models were used; the quasi-one-dimensional `L1d3` (Jacobs 1998b) code and the two-dimensional axisymmetric `Eilmer3` (Jacobs et al. 2010) code. Both of these codes were developed at the University of Queensland.

An equilibrium chemistry model for shock tube flows, `CEA2` (Gordon and McBride 1994; McBride and Gordon 1996) was used in conjunction with the radiative transfer code `Specair` (Laux 2002) (developed at École Centrale Paris) to produce comparisons to the spectral intensity data. Non-Boltzmann comparisons were also achieved through the use of the `Mutation` (Magin et al. 2006) code. These simulations were completed by Brandis (2011).

All of the computational models are briefly described in this chapter, including the generation of any geometries and grids. The aim of this chapter is to provide all of the information required to reproduce the simulation results.

4.1 Quasi-one-dimensional calculations

Quasi-one-dimensional simulations were completed using the `L1d3` code (Jacobs 1998b). The code provides viscous simulations of the gas flow in a variable-area duct and models

the piston dynamics. A number of gas slugs, pistons and diaphragms can be modelled in L1d3 using a Lagrangian formulation, with second order accuracy in both space and time. Flow in one dimension only is calculated and changes in duct area are assumed to be gradual. Boundary layers are approximated by the addition of wall shear stress to the momentum equation and heat transfer to the energy equation.

The L1d3 computational results are used primarily as an aid in developing the experimental operating conditions.

In the L1d3 simulations contained three slugs of gas: the primary driver gas; the secondary driver gas and the test gas. Separate calculations of the piston dynamics were used to provide the location of the piston and the temperature of the primary driver gas at the moment the pressure reached the burst pressure of the primary diaphragm.

This burst diaphragm was inserted as a gas interface 4.81 m downstream of the initial piston location. A secondary diaphragm, with burst pressure 75 kPa and rupture delay $5\ \mu\text{s}$, separated the secondary driver gas from the test gas in the shock tube. The piston upstream was modelled by a stationary wall at the calculated position, and the shock tube exit boundary condition was defined as a free end. The piston wall was at an axial location of 4.5645 m, the initial primary driver gas temperature was 3500 K, and the initial primary driver gas pressure was the burst pressure of 15.5 MPa.

A loss region, with a head loss coefficient of 0.35, was added at all locations where the tube diameter varied. The secondary driver tube bore was 0.085 m, and the diameter of the shock tube was 0.155 mm. The initial temperature of all gas slugs was 296 K. Equilibrium chemistry was used in the simulations as only a small region behind the shock wave was expected to be in thermochemical nonequilibrium, and the aim of these simulations was to investigate the flowfield properties and not the nonequilibrium region behind the shock front.

Figure 4.1 shows the computational domain used for the L1d3 simulations which did not include the piston dynamics.

An example setup file for the 13Pa Titan simulation - both with and without the piston dynamics - is provided in Appendix C. These files contain all information required for a reproduction of the geometry of the facility. 300 cells were used in each of the gas regions. A list of the physical locations of important geometry points may be found in Table 3.1.

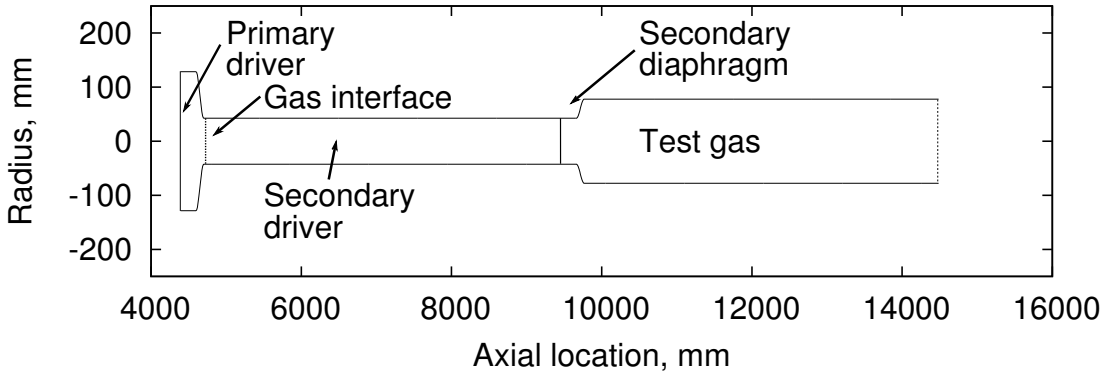


Figure 4.1 : Computational domain for the L1d3 simulations of the partial facility.

4.2 Two-dimensional axisymmetric calculations

While the L1d3 simulations provided reasonable estimates of the flow properties for condition development and comparison with experimental data, they did not allow investigation into the effect of the area change. This modification to the facility was significant and, therefore, it is essential to understand the effect of the addition of this expansion on the test gas.

A viscous two-dimensional axisymmetric simulation of the shock propagation through the shock tube and into the test section was conducted using the **Eilmer3** code (Jacobs et al. 2010). **Eilmer3** is a 2D/3D code developed at the University of Queensland that integrates the finite-volume form of the compressible Navier-Stokes equations with an explicit time-stepping scheme. For these simulations, the primary interest was on the effect of the area change. Therefore, the simulations were completed with an equilibrium chemistry model for Titan gas. The fundamental elements of the flow solver and equilibrium chemistry module were based on those used in the precursor code **MBCNS2** (Jacobs 1998a).

As for the quasi-one-dimensional simulations, the facility was simulated from the moment of primary diaphragm rupture. The computational domain is shown in Figure 4.2 for the modified facility, although the majority of the blocks shown were further divided in the simulation. A symmetry condition was used for the centreline of the tube, and the facility walls were considered to be fixed-temperature boundaries at 296 K. The upstream boundary condition was set to a stationary, fixed-temperature wall at 296 K, representing the piston. A secondary diaphragm was defined between the secondary driver and the aluminium shock tube section, with a burst pressure of 75 kPa. The downstream boundary condition was set as an outflow, as only the first section of the dump tank was included in the domain. The primary driver tube had a bore of 0.257 m, the secondary driver tube

bore was 0.085 m, and the diameter of the shock tube was 0.155 mm. A list of the physical locations of important geometry points may be found in Table 3.1.

The piston wall was at an axial location of 4.5645 m, the initial primary driver gas temperature was 3500 K, and the initial primary driver gas pressure was the burst pressure of 15.5 MPa. The blocks between the two diaphragm stations contained He gas at a fill pressure determined by the test condition. In all blocks representing the shock tube and dump tank (i.e. downstream of the secondary diaphragm station), the initial fill conditions used the Titan gas mixture (98 % N₂, 2 % CH₄) at a room temperature of 296 K and the desired test pressure.

Three blocks were used to describe the compressed primary driver geometry, and five blocks defined the secondary driver tube. The shock tube contained a single block upstream of the area change and then two rows of five blocks for the aluminium section of the shock tube. In the blocks describing the shock tube, the grid used 5000 cells axially and 50 cells vertically. For all other blocks, this was scaled to the length of each section (see Appendix C for the simulation script containing the scaling).

As the primary goal of the **Eilmer3** simulations was to provide information regarding the effect of the area change at the area change and at the exit of the shock tube, a simulation was also conducted for the unmodified facility geometry. This is shown in Figure 4.3. A similar block configuration was used for this simulation, however, as the shock tube length and diameter were smaller for this facility, the nominal number of cells in the axial and radial directions were 3000 and 30 respectively in the shock tube.

4.3 Radiative heat transfer calculations

4.3.1 Specair calculations

The air plasma radiation model, **Specair** (Laux 2002), was developed at Stanford university on the basis of the NASA code NEQAIR (Park 1985). The model includes: 33 electronic transitions (tabulated in Table 4.1); 1484 lines of atomic nitrogen from 86.523 nm to 54.83 μ m; 856 lines of atomic oxygen from 69.753 nm to 16.71 μ m and 1291 lines of atomic carbon from 94.519 nm to 12.28 μ m. In this case, the populations of emitting vibronic levels were calculated by the code **CEA2**. The rotational populations are always assumed to follow a Boltzmann distribution at T_{rot} . **Specair** solves the radiative transport equation along a line-of-sight using a one-dimensional tangent slab approach. This approximation assumes that the properties of the shock layer vary in a single direction, normal to the shock tube exit.

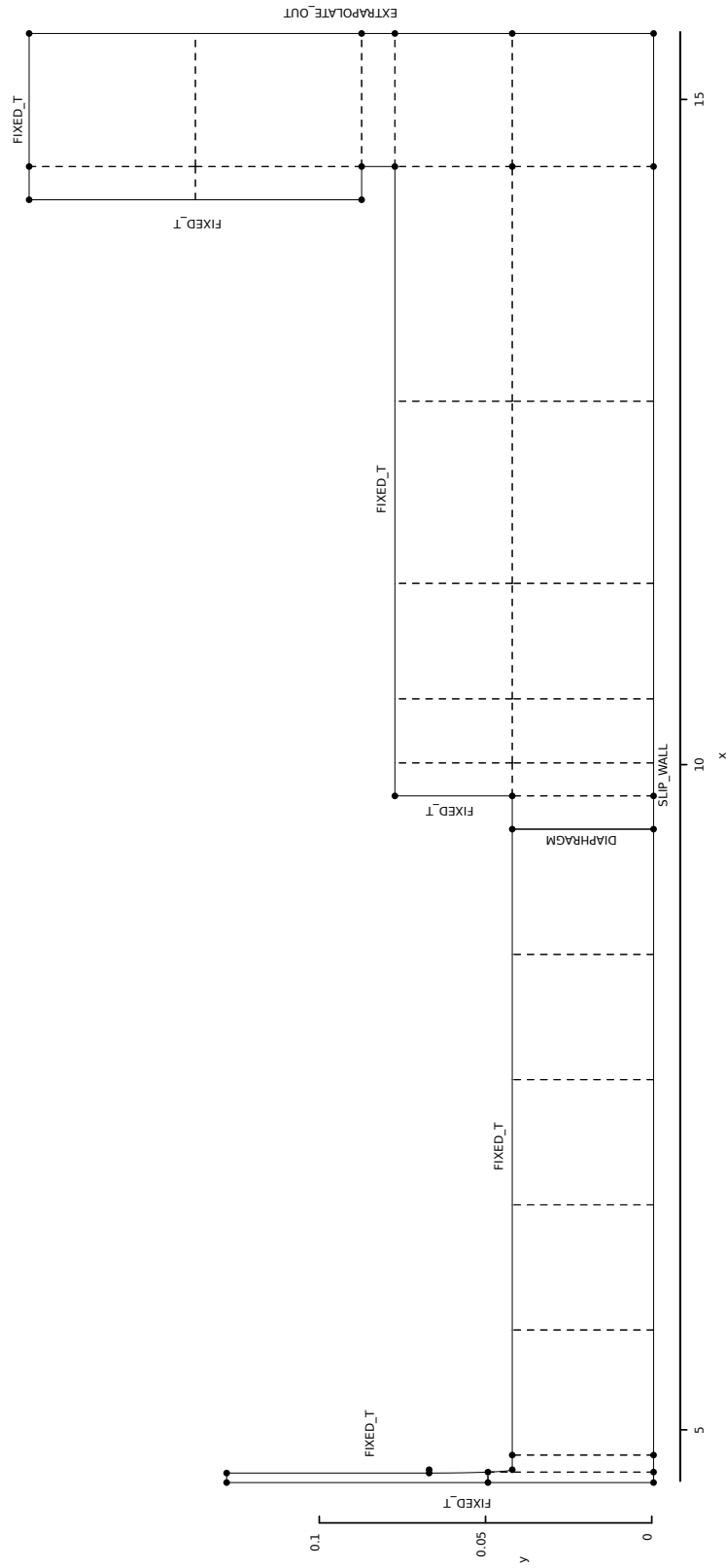


Figure 4.2 : Computational domain for the Eulmer3 simulations of the modified facility.

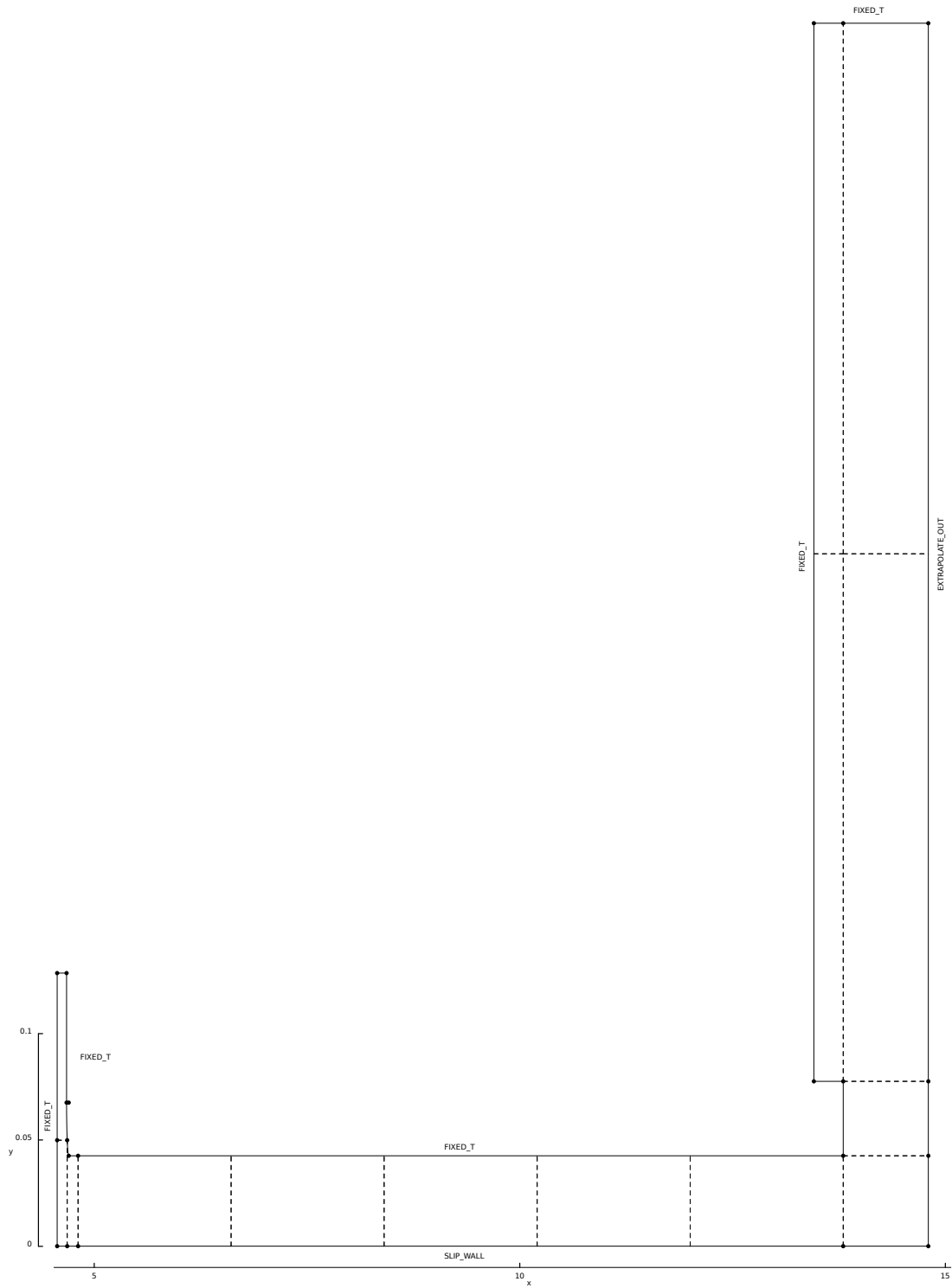


Figure 4.3 : Computational domain for the *Eilmer3* simulations of the original X2 facility.

VUV	UV	Visible	Near-IR	IR
80-200 nm	200-400 nm	400-800 nm	0.8-1.5 μm	1.5-6 μm
$\text{N}_2 \text{ b-X}$ (Birge-Hopfield 1)	$\text{O}_2 \text{ B-X}$ (Schumann-Runge)	$\text{N}_2 \text{ B-A}$ (First Positive)	$\text{N}_2^+ \text{ A-X}$ (Meinel)	NO X-X
$\text{N}_2 \text{ b'-X}$ (Birge-Hopfield 2)	$\text{N}_2 \text{ C-B}$ (Second Positive)	CN A-X (Red)	NO C-A	CO X-X
$\text{N}_2 \text{ c}^+_4\text{-X}$ (Carroll-Yoshino)	$\text{N}_2^+ \text{ B-X}$ (First Negative)		NO D-A	OH X-X
$\text{N}_2 \text{ c}_3'\text{-X}$ (Worley-Jenkins)	NO B-X (β)		NO F-C	
$\text{N}_2 \text{ o}_3\text{-X}$ (Worley)	NO A-X (γ)		NO E-C	
$\text{N}_2 \text{ e}^+\text{-X}$	NO C-X (δ)		NO E-D	
	NO D-X (ϵ)		NO H-C	
	$\text{NO B}'\text{-X}$ (β')		NO H-D	
	NO E-X (γ')		NO H' C	
	CN B-X (Violet)		NO H' D	
	OH (A-X)			
	NH (A-X)			

Table 4.1 : Molecular transitions modelled in *Specair* with their (very) approximate spectral location. (Lauw 2002)

Specair was used to produce a computational spectral comparison to the experimental results of Chapter 6. The temperature, pressure, and molar fraction information from the **CEA2** simulations was used as input into the spectral calculations. The computational spectra included N₂ B-A (First Positive), CN B-X (Violet), N₂ C-B (Second Positive), N₂⁺ B-X (First Negative), and NH (A-X) vibronic spectral bands over the wavelength range 310-450 nm. The atomic lines of N and C were also included. The CN B-X (Violet) spectral band system is calculated in Specair using the spectroscopic constants of Laux (1993). The computed spectra was convoluted with a Gaussian of full-width-half-maximum 0.54 nm to simulate the 600 lines/mm grating, and the resulting additional wavelengths were clipped from either end of the data.

A comparison by Caillault et al. (2006) of the spectroscopic constants used in Specair and those used by Playez (2006) found that there was a good agreement between the two models between 430 and 550 nm (C₂ Swan, CN Violet), but that discrepancies existed between 600 and 950 nm (CN Red). While the transition probabilities used in Playez (Knowles, Werner, Hay, and Cartwright 1988) are more recent than those used in Specair (Arnold and Nicholls 1972; Bauschlicher and Langhoff 1988) for the CN Red transitions, these probabilities are quoted as an upper bound, making it unclear, as yet, which is more appropriate to use.

4.3.2 Mutation calculations

As described in Chapter 2, collisional radiative modelling provides very detailed and reliable estimates of the radiative heat transfer in nonequilibrium flows. The **Mutation** code (Magin, Caillault, Bourdon, and Laux 2006) was originally an electronically-specific collisional radiative code which was adapted to include multi-quantum-level vibrational energy level exchanges in a manner similar to ViSpeN (Brandis 2009a).

The **Mutation** simulations calculated the temperature and species profiles axially across a normal shock using the electronically-specific collisional radiative model. The information was then passed to the **Specair** radiation solver and the spectra calculated (Brandis 2011). From this, the axial profile of the power density, integrated over a wavelength band was calculated and compared to the experimental spectra.

4.4 Summary

To complement and provide validation through comparison with the experimental work, a number of computational codes were used. **L1d3** provided a comparison of shock speed and pitot pressure with the experimental results. **Eilmer3**, being a 2D-axisymmetric simulation, provided shock speed and pitot pressure comparisons - including a vertical profile

of the pitot pressure. Of particular interest in the **Eilmer3** simulations was the effect of the area change. A combination of the **CEA2** and **Specair** codes allowed the generation of spectral comparisons for each test condition. Similarly, the **Mutation** collisional radiative code provided an axial profile of the radiative intensity over a wavelength range.

This chapter provided detail of the computational codes used and the parameters used in the calculation of results. All of these results will be investigated in Chapters 5 and 6.

CHAPTER 5

Facility Analysis

As the experimental work completed in this thesis involves two main components - the modification of the facility and the generation of spectral data - this chapter presents the analysis of the performance of the shock tube following the various modifications described in Section 3.1.

Pitot pressure data provide a means of determining the test time achieved in the facility and the width of the flow exiting the tube which corresponds to the usable test gas, and of validating the calculations of the core flow conditions. Static pressure measurements at various locations along the length of the tubes allow for the calculation of the speed of the propagating shock wave. These data may be compared with computational results from the various simulations.

A reference condition at 13 Pa freestream pressure in a Titan simulated atmosphere is used in order to provide a comparison - both experimentally and computationally - between the modified and original facility flow conditions. Of particular interest is the effect of the area change on the quality of the flow immediately downstream and at the exit of the tube, where the spectral measurements were conducted.

5.1 Validation of flow quality: 13 Pa test condition (altitude 302 km)

As the operating conditions in the tunnel were changed by these modifications, an investigation into the flow quality down the length of the shock tube is required before confidence can be placed in the results at the exit of the tube. A reference condition was selected from the results of Brandis (2009a) for a 13 Pa freestream pressure in a Titan simulated atmosphere. Comparisons were made at this condition between the old and new facilities.

5.1.1 Shock speed analysis

The shock speed was calculated by using an estimate of the time of arrival of the shock front at each static pressure transducer located in the wall of the facility. The uncertainty in each measurement was calculated using the method described in Appendix B. When quoting the shock speed for a given shot, the shock speed as the discontinuity passed the last transducer (*al5*; 450 mm upstream of the tube exit) was used.

For the 13 Pa condition, the average shock speed at the exit of the tube was found to be 6.41 km/s, with an experimental shot-to-shot variation of ± 0.53 km/s. The accuracy of each shock speed measurement was ± 0.1 km/s.

This category of shots was nominally referred to as the ‘13 Pa condition’, although, due to shot-to-shot variations, the individually calculated flow conditions from each shot may be accurately analysed for interpretation of the radiative data sets.

As was mentioned previously, PCB piezoelectric transducers were flush-mounted to the wall of the facility in order to measure the static pressure in a number of locations. From the static pressure measurements it is possible to extract the time at which the shock wave passed known locations and use time-of-flight calculations to estimate the shock speed.

Using all of the static pressure transducers in the facility, it was possible to calculate the shock speed decay over the length of the facility. Figures 5.1, 5.9, and 5.13 plot the decay of the shock speed in both the secondary driver and the aluminium shock tube sections for all three test conditions.

In these figures, all values of the shock speed calculated were assumed to be located at the midpoint between the two transducers used in the calculation. To ensure clarity in the figures, only one experimental measurement at each condition is presented with

errorbars indicating the estimated uncertainty in the measurement. This has been offset from the remainder of the measurements slightly. Also offset from the actual location is the mean value of the shock speed for each condition. This value was calculated from the experimental data and the errorbars indicate the overall spread of the values.

For the 13 Pa condition, Figure 5.1 shows that the shock speed decreases from an average value of 4.2 km/s to 3.6 km/s in the secondary driver tube, an average drop of 0.6 km/s. In the shock tube, the average shock speed decay was quite small - on the order of 0.1 km/s. These results indicate that there is a negligible shock attenuation observed in the shock tube for the 13 Pa condition - at least to the resolution of the instrumentation, as it is less than the uncertainty in the measurement (± 0.1 km/s). This, and other supportive data discussed in later sections, confirms that very high quality flow was produced in the modified facility.

As a further result of this lack of measurable attenuation, the application of the shock speed estimated between the final two transducers as the shock speed at the exit of the tube can be justified.

5.1.2 High speed camera footage

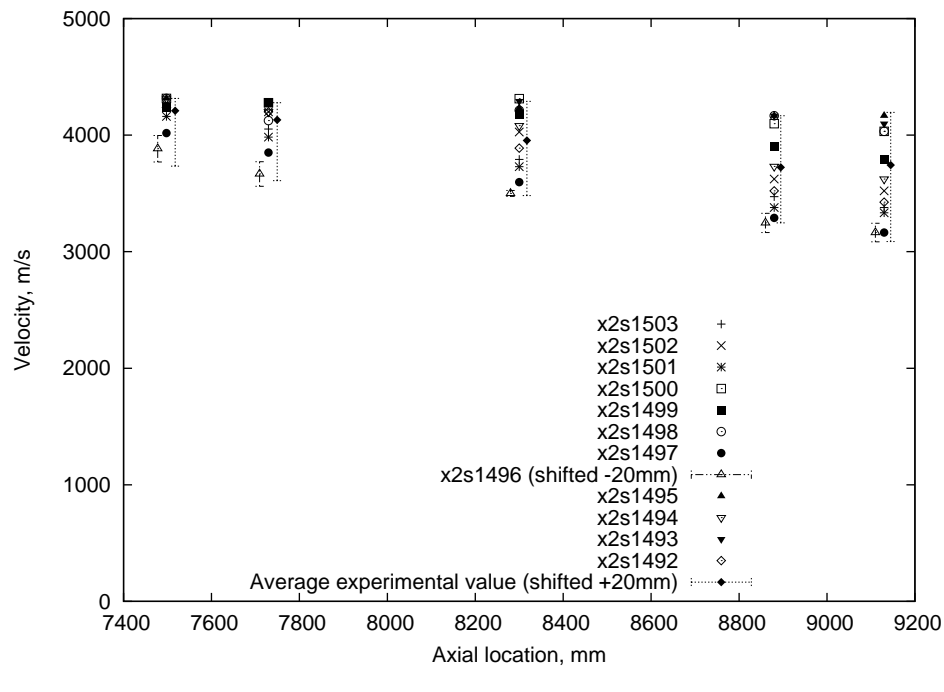
A visual interrogation of the flow exiting the tube was performed with a HPV-1 high speed camera. In Figures 5.2 and 5.3, a number of frames were extracted from the video of the flow exiting the tube for the 13 Pa condition. In this video, a frame was captured every $1\ \mu\text{s}$ with an exposure of $0.5\ \mu\text{s}$ and lens aperture of 11.

The series of images captures the shock exiting the shock tube and propagating downstream. In these images, the camera was slightly misaligned such that the shock front is on a slight angle. Despite this, it can be seen that the shock remained planar exiting the tube along the centreline of the tube, although the curvature of the edges of the shock due to the expansion as the flow exits the tube is visible. This planar shock is propagating at a uniform velocity into a uniform gas, and the flow immediately behind it must also be uniform.

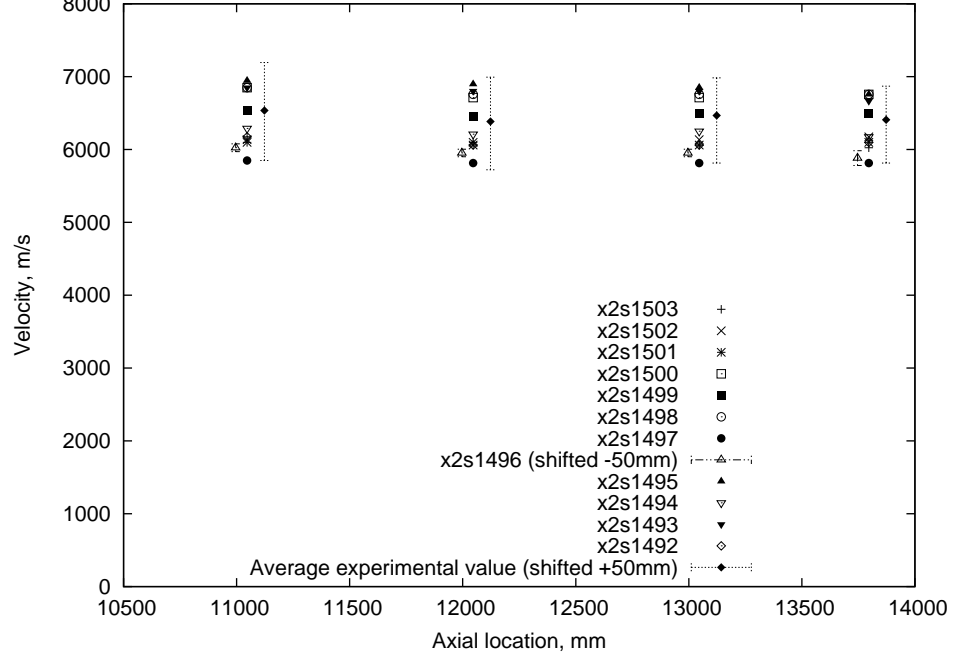
5.1.3 Pitot pressure analysis

A Pitot rake was placed 30 mm downstream of the exit of the shock tube, and the Pitot pressure traces were recorded along the centreline of the tube and at a number of points offset vertically from the centreline.

Due to the hazardous operating environment, it was necessary to protect the Pitot sensors from the direct impact and heating involved in stagnation measurements. The



(a) Secondary driver



(b) Shock tube

Figure 5.1 : Shock speed variation down the tube for the 13Pa condition experiments. The shock speed is calculated as a time of flight between the various transducers in each section. The location is then given as the midpoint between the two transducers. For one shot, the uncertainty in the calculated shock speed is shown. The average value of the experimental results is shown, with errorbars giving the overall spread of the values.

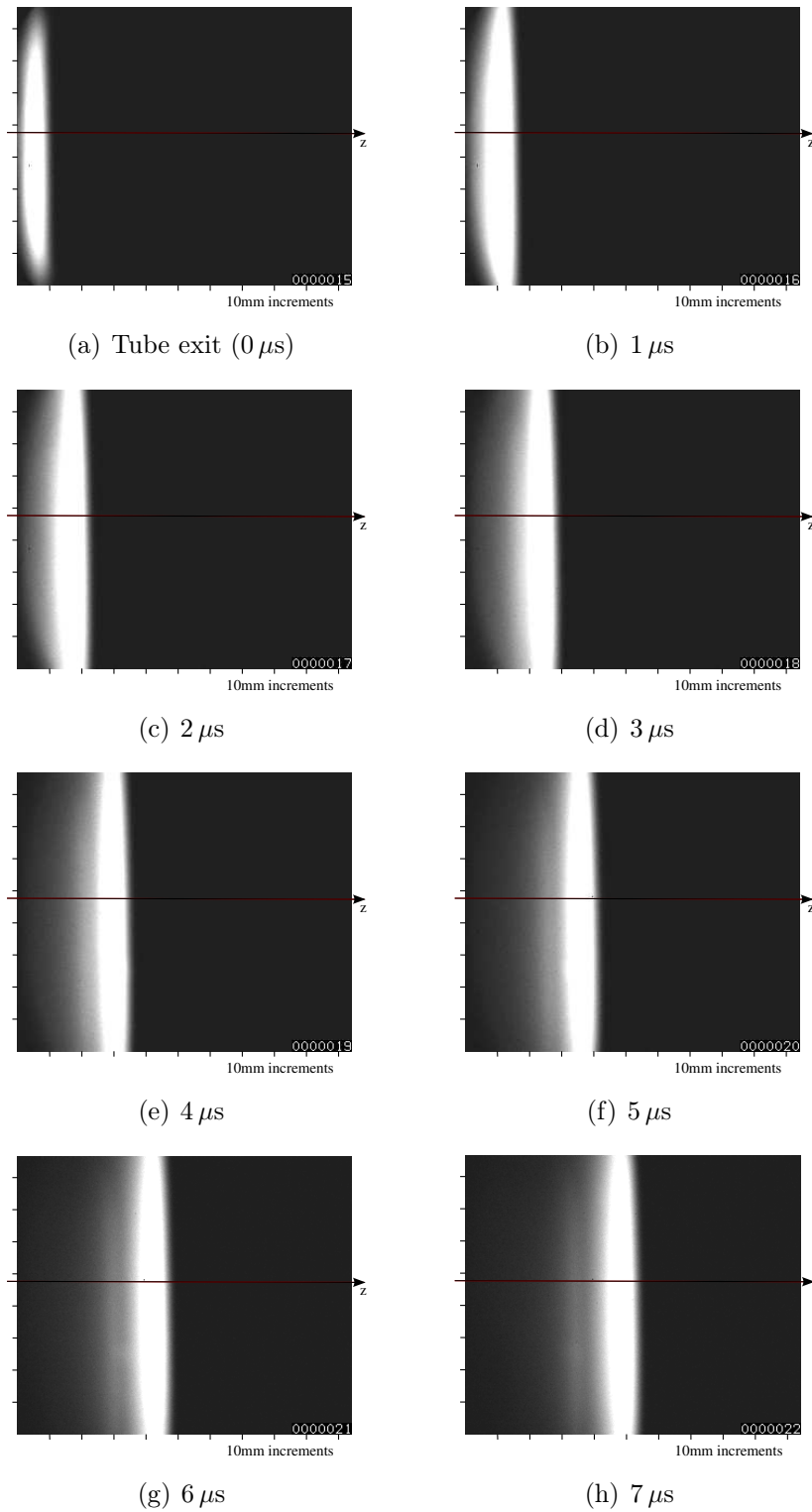


Figure 5.2 : High speed camera footage for the 13 Pa freestream condition from 0 - 7 μs . A frame rate of 1 MHz and exposure time of 0.5 μs was employed, with a lens aperture of 11. This data was taken from experiment x2s790.

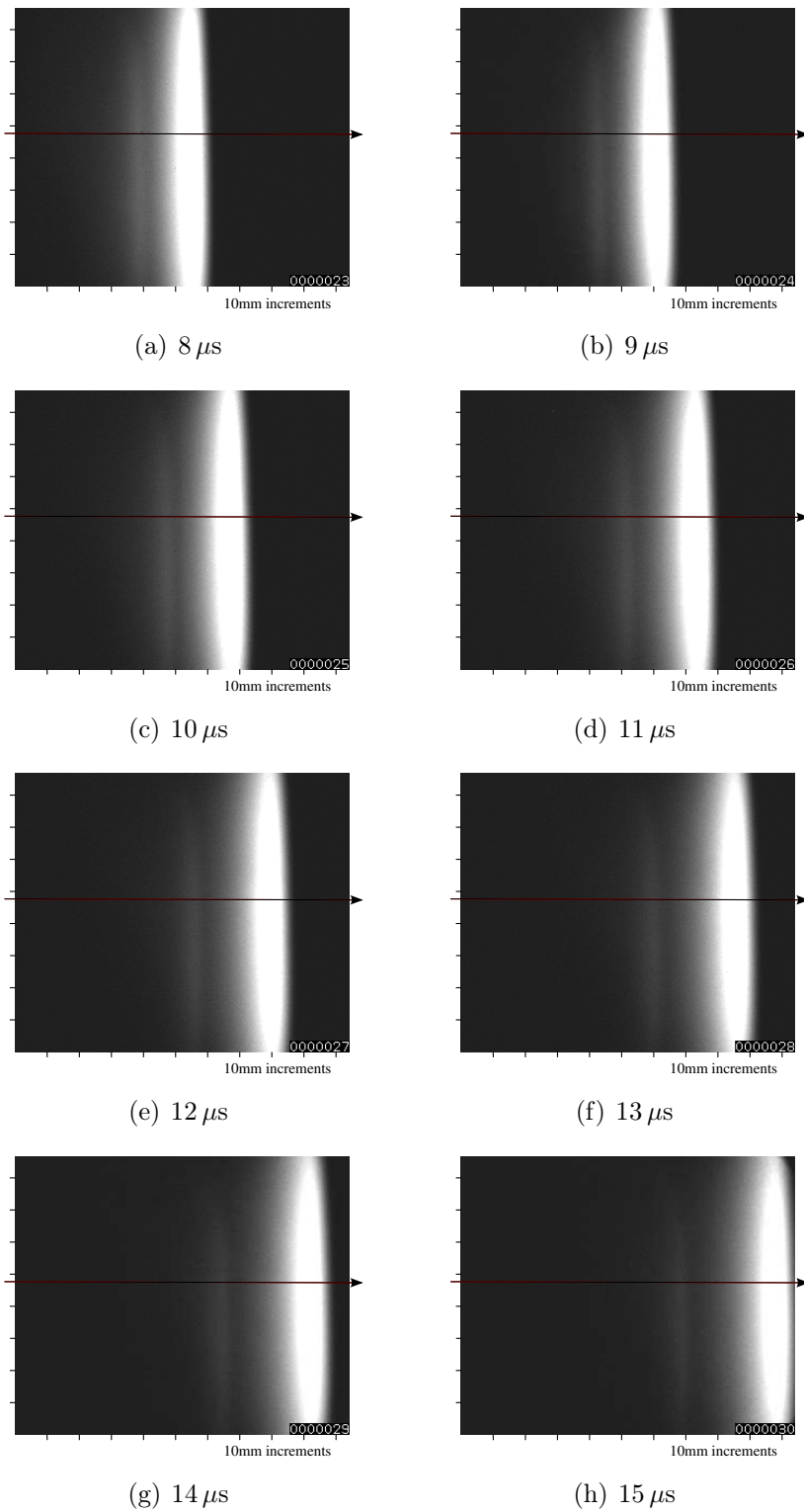


Figure 5.3 : High speed camera footage for the 13 Pa freestream condition from 8 - 15 μ s. A frame rate of 1 MHz and exposure time of 0.5 μ s was employed, with a lens aperture of 11. This data was taken from experiment x2s790.

probes were mounted in a housing which was fed through small orifices with no direct line of sight to the sensor diaphragms to prevent particle impact and to cool the gas in contact with the sensors. This resulted in a response time on the order of $20\ \mu\text{s}$, compared to the inherent sensor rise time of approximately $1\ \mu\text{s}$. Therefore, for the test times encountered in these experimental conditions (also on the order of $20\ \mu\text{s}$, as will be shown later), the pressure traces do not give a time accurate pressure history. They do, however, approximately asymptote to the correct values by the end of the test time.

The asymptotic values are plotted in Figure 5.4(a) to define the extent of the core flow. These measurements are supported by the high speed images in Figures 5.2 and 5.3. From this, the width of the core flow was calculated to be 85 mm. It was found that a large portion of the shock tube diameter contains core flow and that the Pitot pressure variation axially within the core flow was reasonably consistent. This indicated that the flow produced by the modified facility was producing a normal shock at the tube exit with uniform conditions in the test gas immediately following the shock.

The test time of the 13 Pa Titan condition was measured using the Pitot probe traces near the centreline of the flow. Estimates from the experimental data in Figure 5.4(b) indicate that the test time for this reference condition was $27\ \mu\text{s}$. The analytical asymptote calculated for this condition is also plotted in this Figure. For an average experimental shock speed of 6.41 km/s, this test time corresponds to a test gas slug of length 173 mm. Pitot pressure results from the EILMER3 simulations are also included in this figure. These results estimate a shorter test time, on the order of $20\ \mu\text{s}$, and a higher Pitot pressure than the analytical results indicate.

5.1.4 Effect of the area change

In order to produce flow conditions at lower freestream pressures, the shock tube was replaced by a section with a larger cross-sectional area, with an area ratio of 3.3. This area change produces a steady expansion fan pinned to the corner of the expanding section, when the driver gas flow is established. Because this expansion was not contoured, a quasi-steady train of shock waves is also created in the flow straightening region, whose presence may persist several diameters downstream. Unsteady expansion waves are also present, which establish the flow after the diaphragm rupture.

Therefore, computational and experimental comparisons between the old and modified geometry were necessary in order to determine if the modified facility behaved in a consistent manner. Simulations were completed with the two-dimensional axisymmetric code, EILMER3, for both tube configurations.

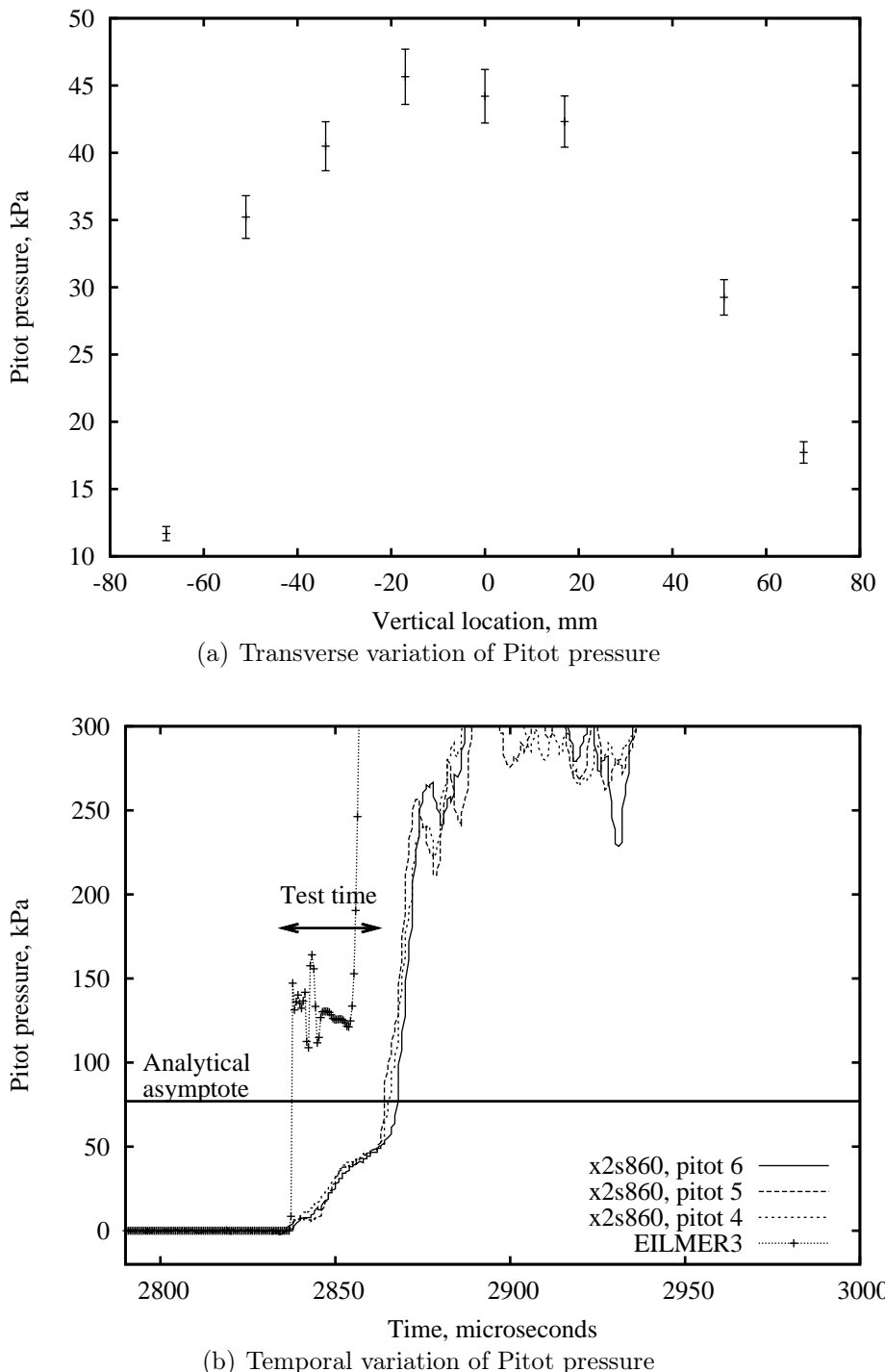


Figure 5.4 : Transverse and temporal variation of Pitot pressure 30 mm downstream of the shock tube exit for the 13 Pa Titan condition. Pitot 5 is on the centreline of the shock tube, while Pitots 4 and 6 are 17 mm above and below, respectively.

Figures 5.5 and 5.6 show a series of images from the EILMER3 simulations, focussed on the region near the area change in the shock tube. As the flow passes the area change and expands into the larger diameter, a shock train forms downstream of the expansion. These disturbances are seen to propagate for only a short distance downstream before they settle into a laboratory-stationary steady shock train, resulting in a high quality, undisturbed flow at the tube exit.

The unusual behaviour of the flow immediately behind the shock wave, where the driver gas has been pulled forward is thought to be produced by grid resolution problems, as no evidence of perturbed flow was visible at the shock tube exit in the high speed camera footage.¹ While this does not allow a direct comparison of the test length estimated by EILMER3 and the Pitot pressure signals, this region of the flow is believed to extend the length of what would be the test gas in a more resolved simulation. When used as a rough estimate, this region indicates that there is likely to be approximately 200 mm of test gas available, consistent with other estimates.²

Figures 5.7 and 5.8 compare the computational flow estimates at the exit of the tube for both facility geometries. It can be seen that a normal shock wave propagates down the shock tube in both facilities, with no disturbances from upstream affecting the exit flow quality. As the flow Mach number in a laboratory frame of reference is approximately 3.5, this normal shock wave expands out of the exit of the tube at an angle of approximately 16 degrees to the flow. This will cause the planar shock to sequentially transform into a curved wave from the outside of the tube as it propagates into the dump tank. In the absence of boundary layer effects, the curvature effects should reach the centerline of the flow at a distance on the order of 1.8 diameters downstream from the tube exit. This effect was visible in the EILMER3 simulation results. The spectral measurements were taken less than 120 mm downstream of the exit of the aluminium shock tube, a distance less than the tube diameter and a region where the shock remains planar. Therefore, spectral measurements are taken through a curved shock, but the shock remains planar along the centreline of the flow where the optical measurements are focussed.

5.2 Low pressure test condition development

5.2.1 8 Pa condition (325 km altitude)

For the 8 Pa condition, the average shock speed at the exit of the tube was found to be 6.19 km/s, with an experimental shot-to-shot variation of ± 0.52 km/s and a shock speed

²Simulations are currently in progress with a much finer mesh in order to establish this and resolve the issue. Simulations at the other conditions will be conducted once this issue has been resolved.

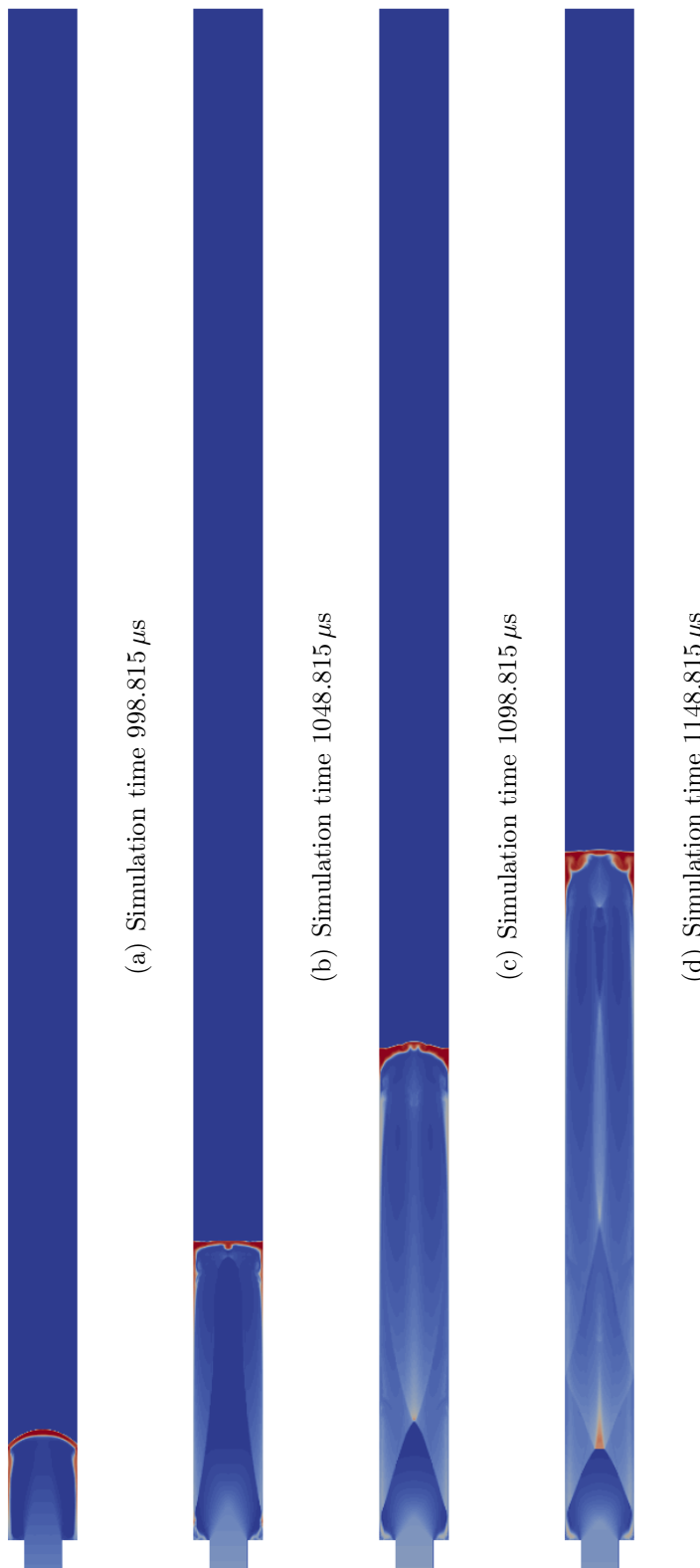


Figure 5.5 : Contour plot of temperature demonstrating the flow structures at the area change for the X_2-NRST_{Al} facility. This data was extracted from EILMER3 over an axial distance of 9.7 to 13.2 m.

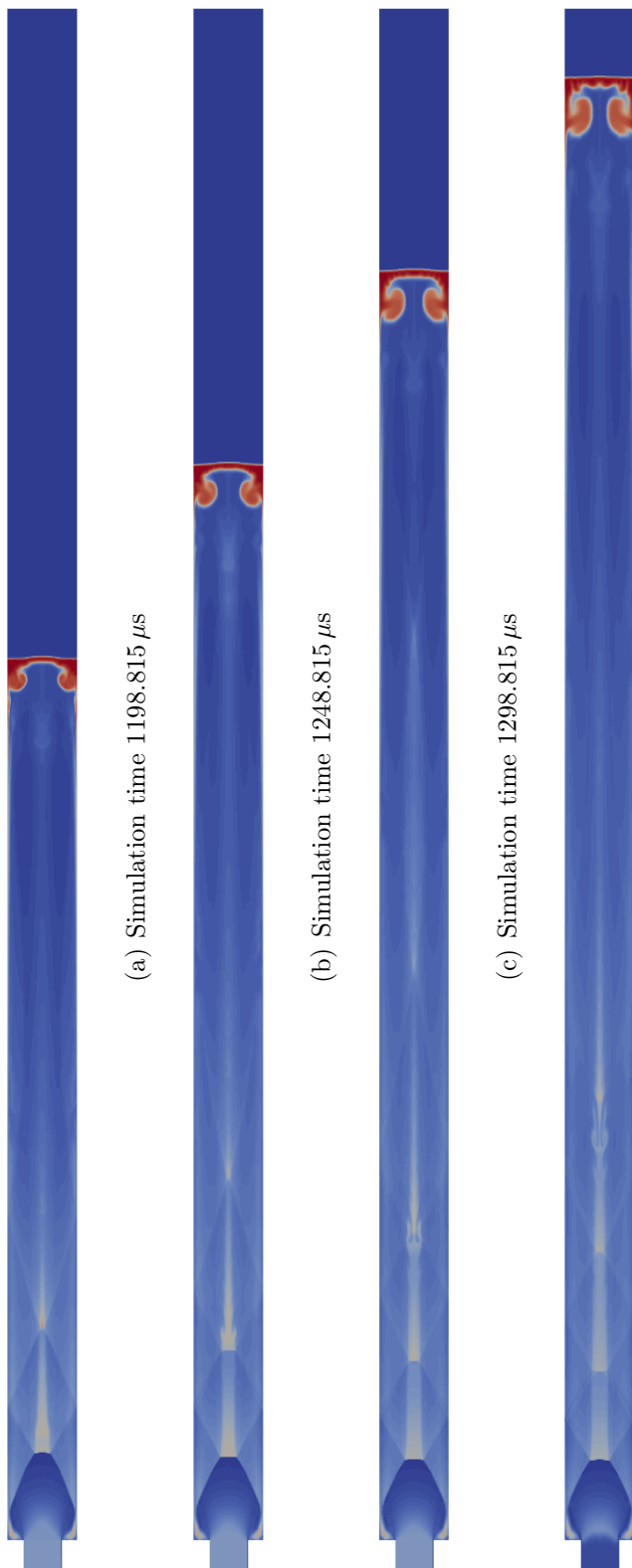


Figure 5.6 : Contour plot of temperature demonstrating the flow structures at the area change for the X^2 -NRST-Al facility. This data was extracted from ELMER3 over an axial distance of 9.7 to 13.2 m.

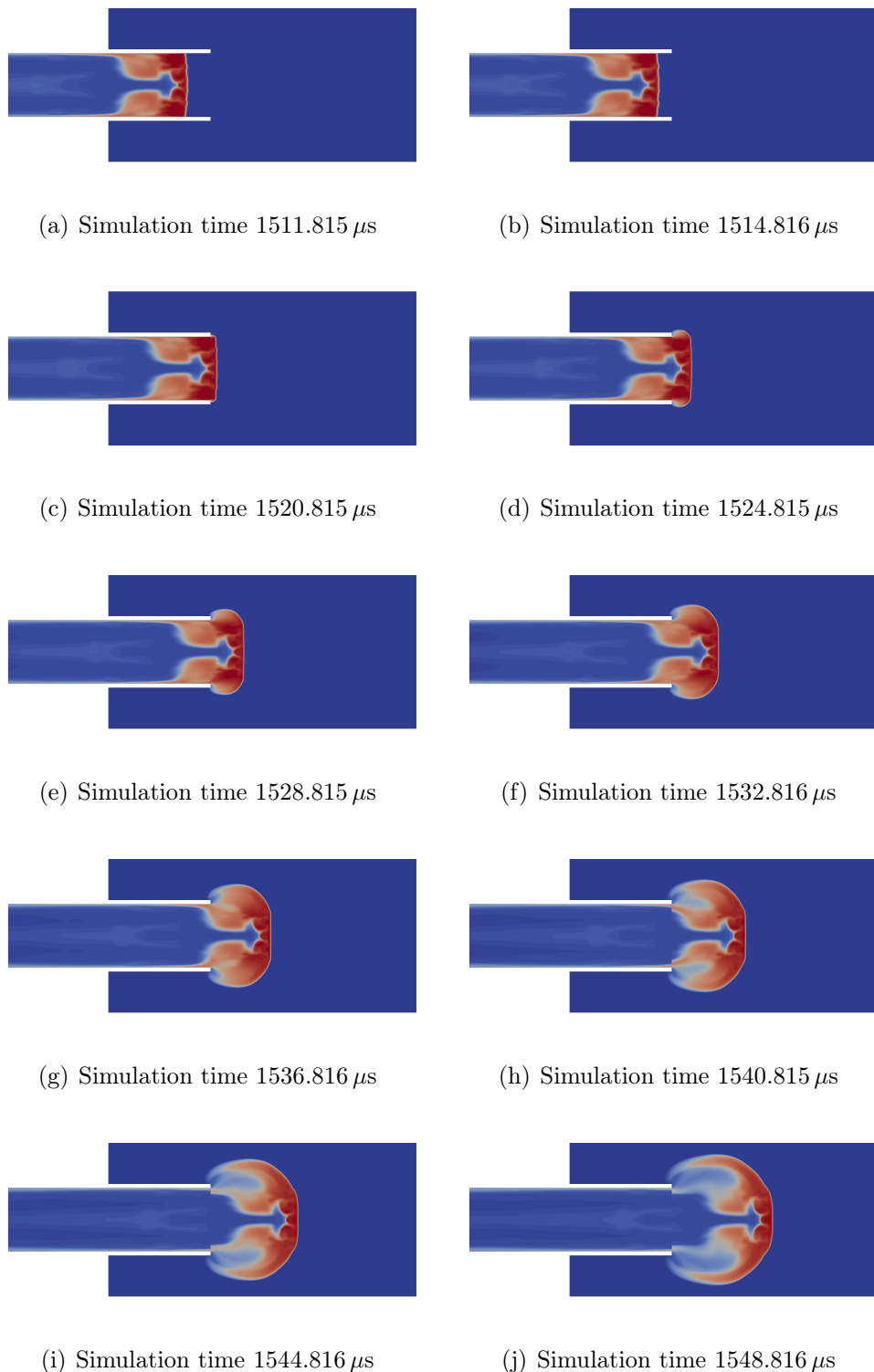


Figure 5.7 : Contour plot of temperature demonstrating the flow structures at the shock tube exit for the X2-NRST-Al facility. This data was extracted from EILMER3 over an axial distance of 14 to 15 m.

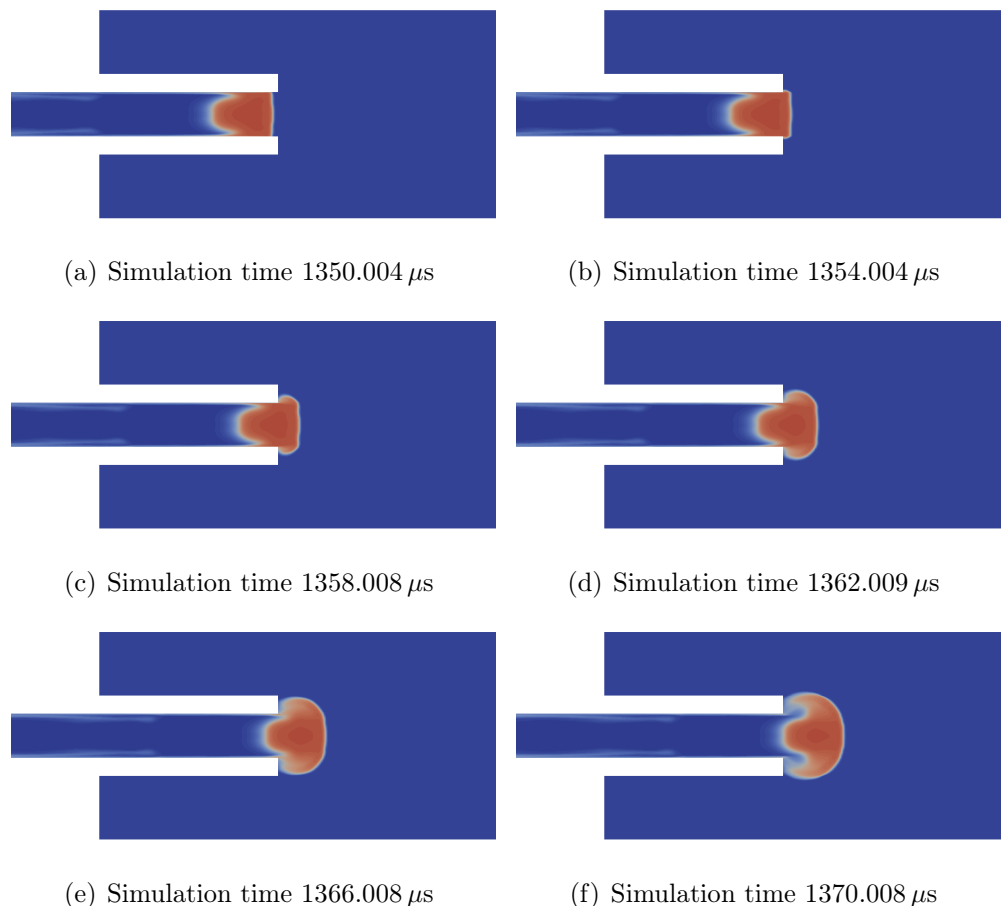


Figure 5.8 : Contour plot of temperature demonstrating the flow structures at the shock tube exit for the X2-NRST facility. This data was extracted from EILMER3 over an axial distance of 13.25 to 14.25 m.

measurement accuracy of $\pm 0.1 \text{ km/s}$.

From Figure 5.9 it can be seen that the shock speed attenuation over the length of the facility was also negligible for this condition. In the secondary driver tube, an average drop in shock speed of approximately 0.6 km/s occurred for the 8 Pa condition, while the drop in shock speed on average over the length of the shock tube was 0.1 km/s , right on the limit of the instrumentation accuracy.

In Figures 5.10 and 5.11, a number of frames were extracted from the video of the flow exiting the tube for the 8 Pa condition. In this video, a frame was captured every $1 \mu\text{s}$ with an exposure of $0.5 \mu\text{s}$ and lens aperture of 11. From these figures, it can be seen that, apart from shock curvature at the edges of the flow, the shock exiting the tube remained planar close to the centreline (where the spectral data was captured).

Figure 5.12(a) shows the variation of the Pitot pressure with distance from the centreline in the vertical axis. From this, the width of the core flow was estimated to be 80 mm , reduced from the core flow diameter achieved in the 13 Pa Titan condition.

Figure 5.12(b) indicates that the test time for this 8 Pa condition was $20 \mu\text{s}$. For an average experimental shock speed of 6.19 km/s , this test time corresponds to a test gas slug of length 124 mm . Once again, difficulties arise when attempting to estimate the test time available for this condition. The rise time of the Pitot pressure signal is of a similar order of magnitude to the overall test time, however, the rapid increase in Pitot pressure with the arrival of the driver gas is clearly indicated to within a few microseconds, so the test time estimation is considered to be reasonably good. In this nonreflected shock tube configuration, the test flow properties can be calculated accurately from known shock speeds and fill conditions.

5.2.2 4 Pa condition (359 km altitude)

For the 4 Pa condition, the average shock speed at the exit of the tube was found to be 9.04 km/s , with an experimental shot-to-shot variation of $\pm 1.15 \text{ km/s}$ and a shock speed measurement accuracy of $\pm 0.1 \text{ km/s}$.

From Figure 5.13 it can be seen that the shock speed drop over the length of the facility is more significant for the 4 Pa than for the 13 Pa condition. In the secondary driver tube, an average drop in shock speed of approximately 0.8 km/s occurred for the 4 Pa condition experiments, while the drop in shock speed on average over the length of the shock tube was 0.3 km/s . While this shock speed decay is not negligible, as for the higher pressure conditions, it still remains reasonably small.

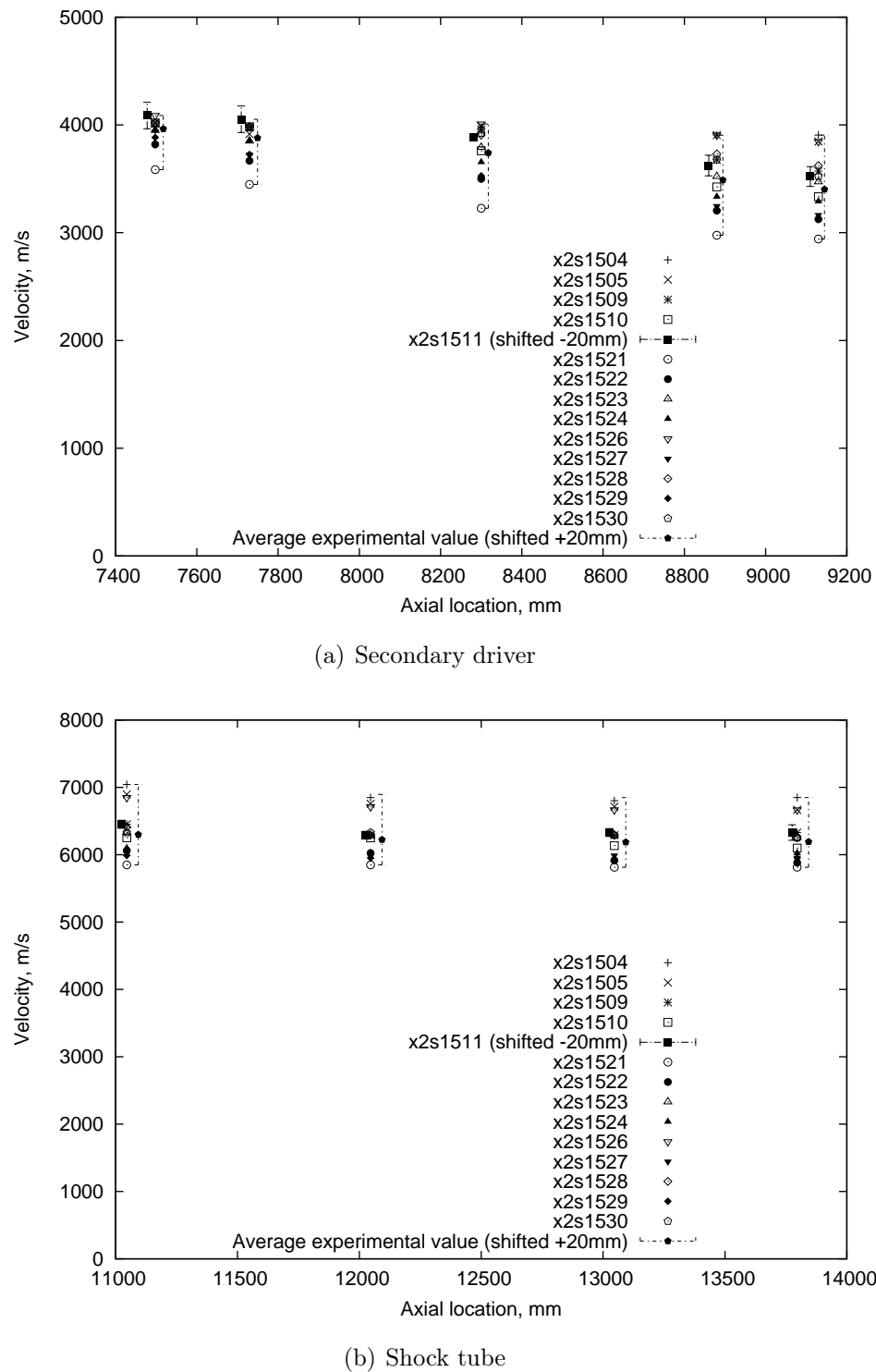


Figure 5.9 : Shock speed variation down the tube for the 8 Pa condition experiments. The shock speed is calculated as a time of flight between the various transducers in each section. The location is then given as the midpoint between the two transducers. For one shot, the uncertainty in the calculated shock speed is shown. The average value of the experimental results is shown, with errorbars giving the overall spread of the values.

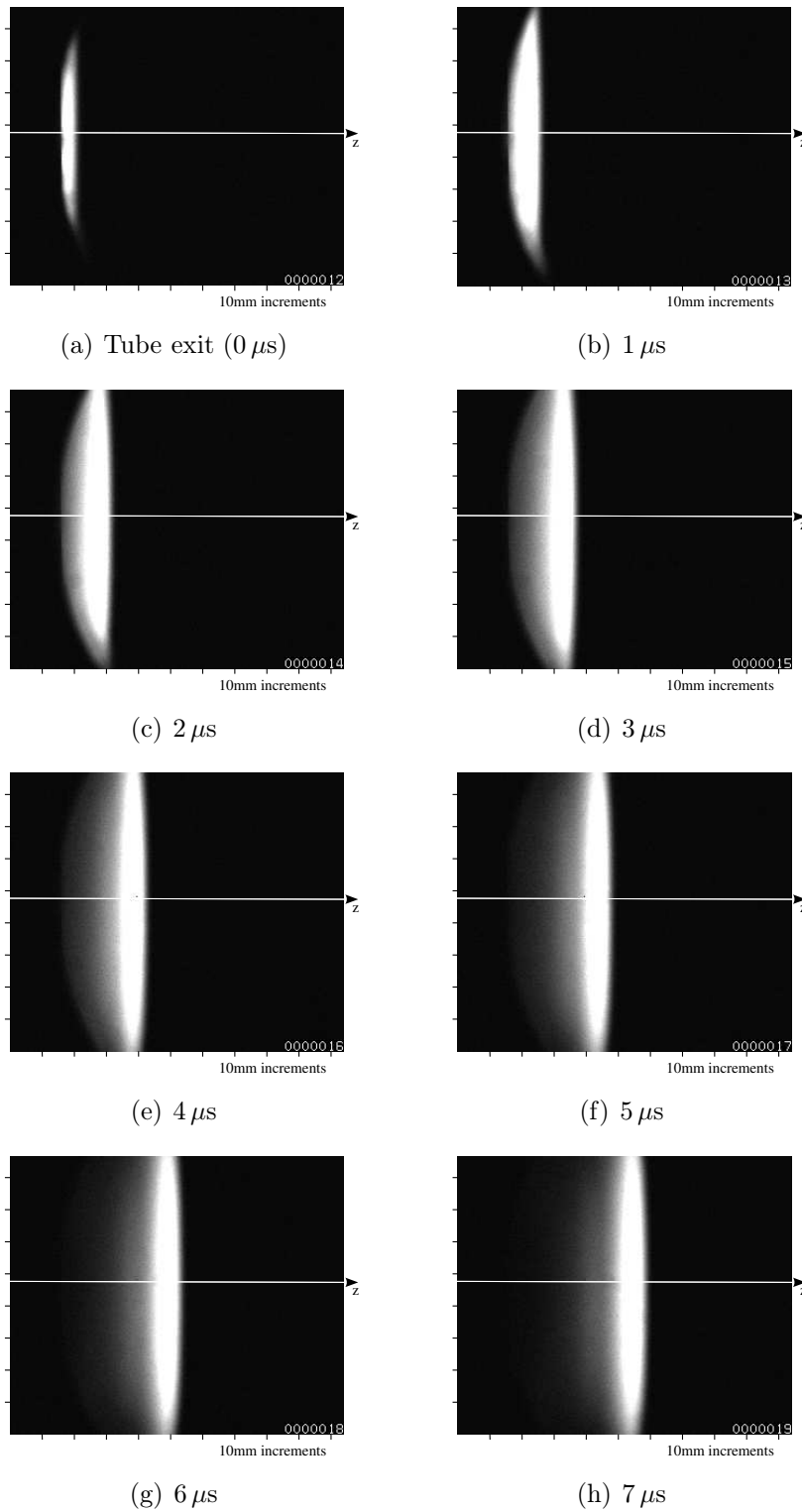


Figure 5.10 : High speed camera footage for the 8 Pa freestream condition from $0 - 7 \mu\text{s}$. A frame rate of 1 MHz and exposure time of $0.5 \mu\text{s}$ was employed, with a lens aperture of 11. This data was taken from experiment x2s797.

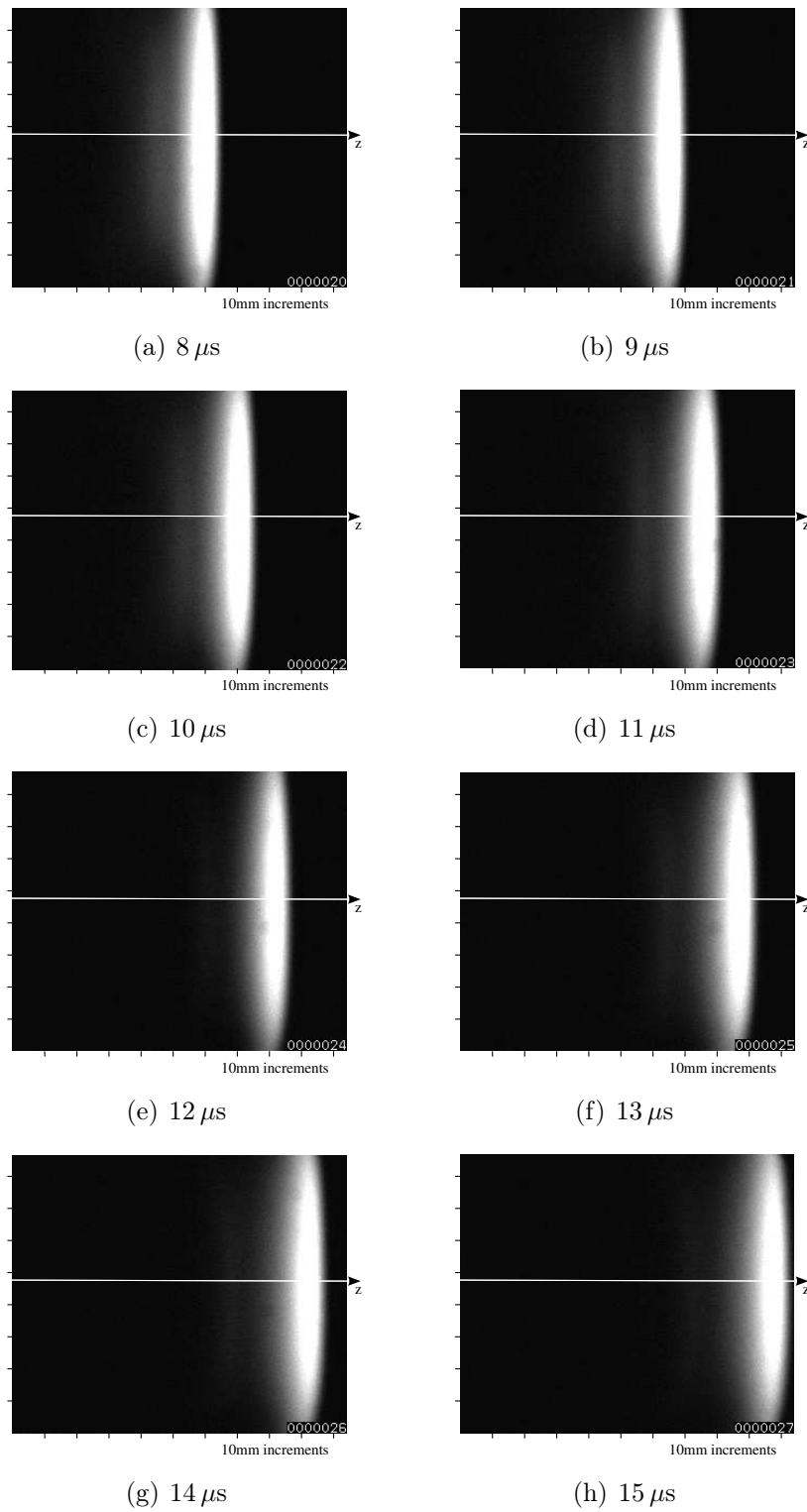


Figure 5.11 : High speed camera footage for the 8 Pa freestream condition from 8 - 15 μ s. A frame rate of 1 MHz and exposure time of 0.5 μ s was employed, with a lens aperture of 11. This data was taken from experiment x2s797.

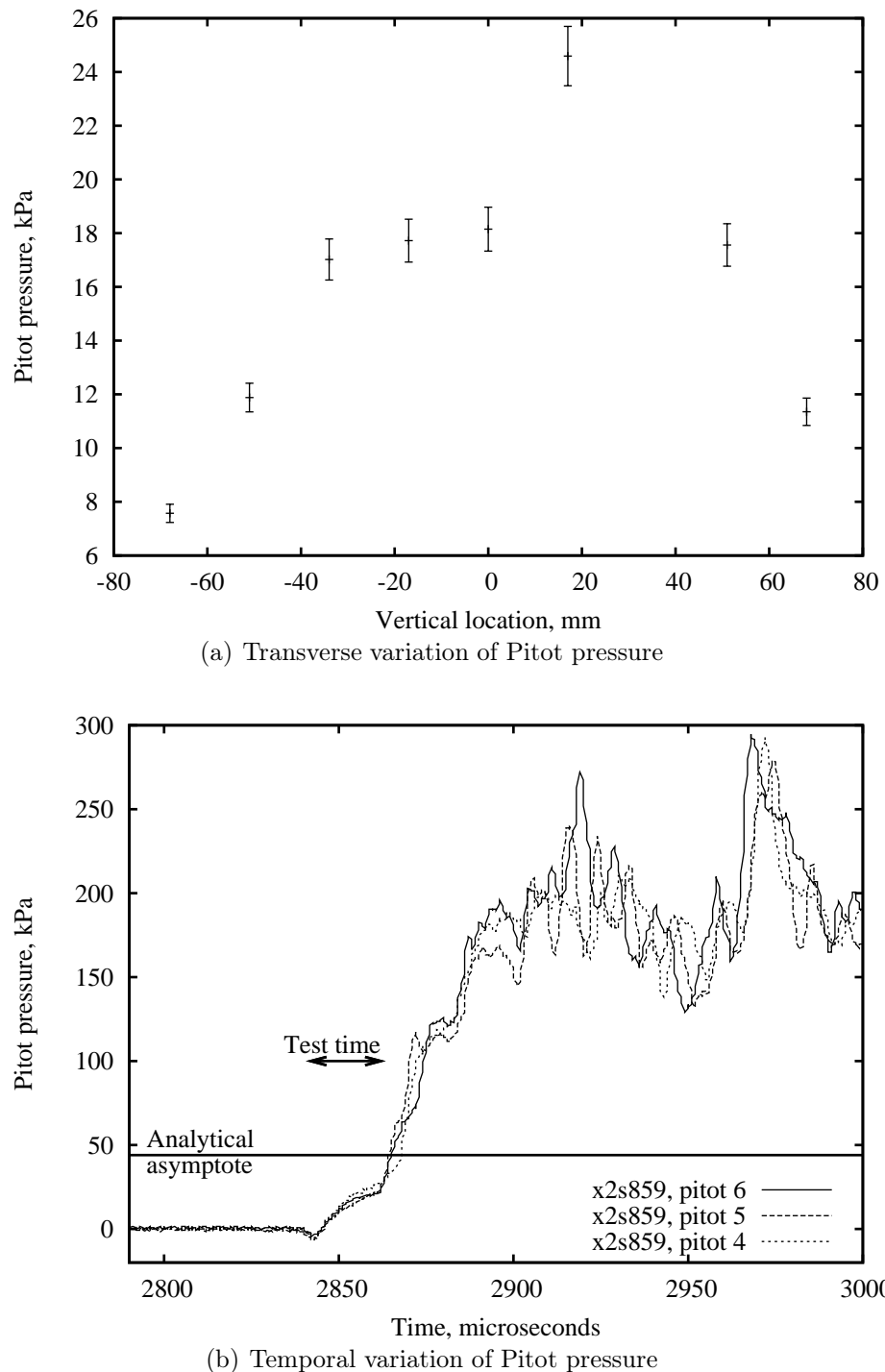


Figure 5.12 : Transverse and temporal variation of Pitot pressure 30 mm downstream of the shock tube exit for the 8 Pa Titan condition. Pitot 5 is on the centreline of the shock tube, while Pitots 4 and 6 are 17 mm above and below, respectively.

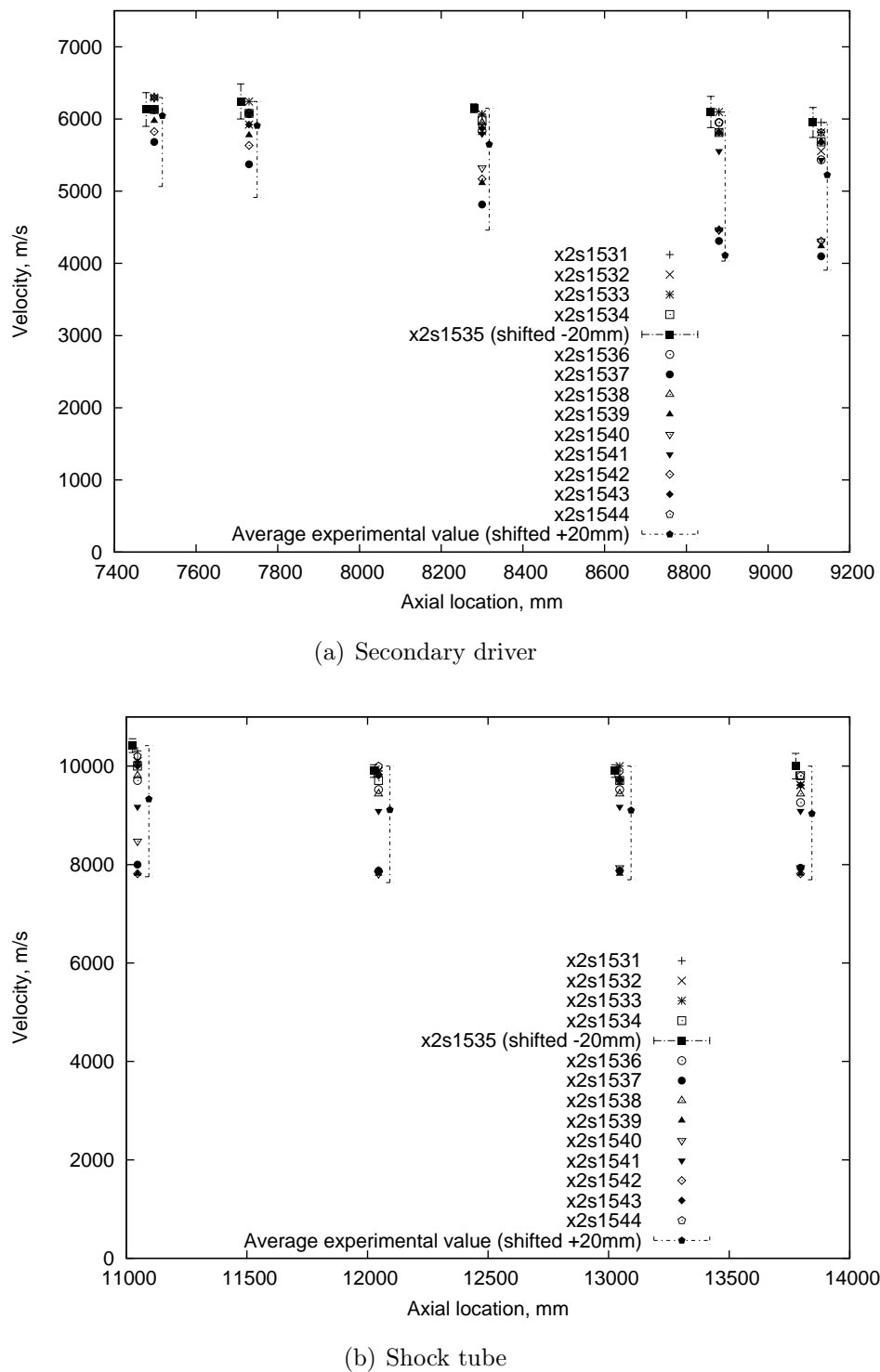


Figure 5.13 : Shock speed variation down the tube for the 4 Pa condition experiments. The shock speed is calculated as a time of flight between the various transducers in each section. The location is then given as the midpoint between the two transducers. For one shot, the uncertainty in the calculated shock speed is shown. The average value of the experimental results is shown, with errorbars giving the overall spread of the values.

In Figure 5.14, a number of frames were extracted from the video of the flow exiting the tube for the 4 Pa condition. In this video, a frame was captured every $1\ \mu\text{s}$ with an exposure of $0.5\ \mu\text{s}$ and lens aperture of 5.6. As for the previous two conditions, the shock remained planar near the centreline as it exited the shock tube. The combination of the small shock speed decay and the images showing the the shock exiting the shock tube is planar, indicate that high quality test gas is produced at this very low pressure condition.

Figure 5.15(a) shows the variation of the Pitot pressure with distance from the centreline in the vertical axis. From this, the width of the core flow was estimated to be 50 mm. It is expected that the core flow will become smaller as the freestream pressure is reduced, however, once again it is extremely difficult to extract the test flow from the signal response of the Pitot probes.

Figure 5.15(b) indicates that the test time for this 4 Pa condition was $13\ \mu\text{s}$. For an average experimental shock speed of $9.04\ \text{km/s}$, this test time corresponds to a test gas slug of length 118 mm.

5.2.3 1 Pa Air condition

Due to air contamination of the dump tank and the limits of the achievable vacuum in the facility, conditions below a freestream pressure of 4 Pa were not considered to be feasible for the X2 facility. It was expected, however, that the modifications to the facility would result in usable conditions to pressures as low as 1 Pa. In order to investigate this, a 1 Pa air condition was examined.

The fill conditions for this experimental condition are listed in Table 5.1

For the 1 Pa air condition, the average shock speed at the exit of the tube was found to be $10.31\ \text{km/s}$, with a shock speed measurement accuracy of $\pm 0.3\ \text{km/s}$. Figure 5.16 plots the change in the experimental shock speed down the secondary driver and shock tubes. In the secondary driver tube, it can be seen that the decay in the shock speed is on the order of $2.5\ \text{km/s}$.

Figure 5.17(a) shows the variation of the Pitot pressure with distance from the centreline in the vertical axis. From this, the width of the core flow was estimated to be 34 mm and Figure 5.17(b) indicates that the test time for this condition was $11\ \mu\text{s}$. For an average experimental shock speed of $10.3\ \text{km/s}$, this test time corresponds to a test gas slug of length 113 mm. No high speed camera footage was available to show the flow quality at the tube exit, and the measurements of test time are questionable, as the Pitot pressure traces do not indicate the arrival of the driver gas clearly. It is possible that there is no test gas available at this condition, therefore, this 1 Pa condition is not yet considered to be a usable condition.

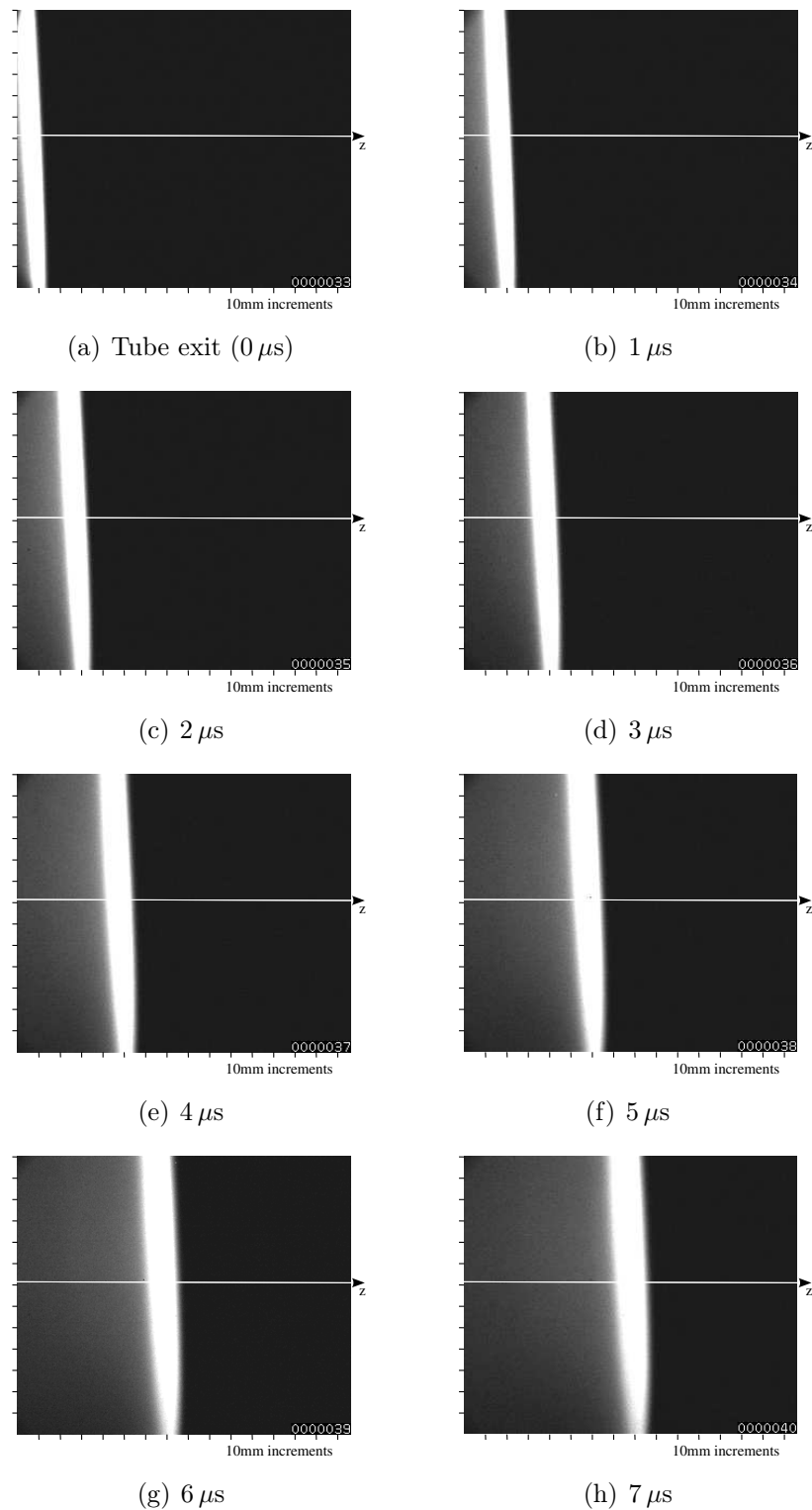


Figure 5.14 : High speed camera footage for the 4 Pa freestream condition from 0 - 7 μ s. A frame rate of 1 MHz and exposure time of 0.5 μ s was employed, with a lens aperture of 5.6. This data was taken from experiment x2s774.

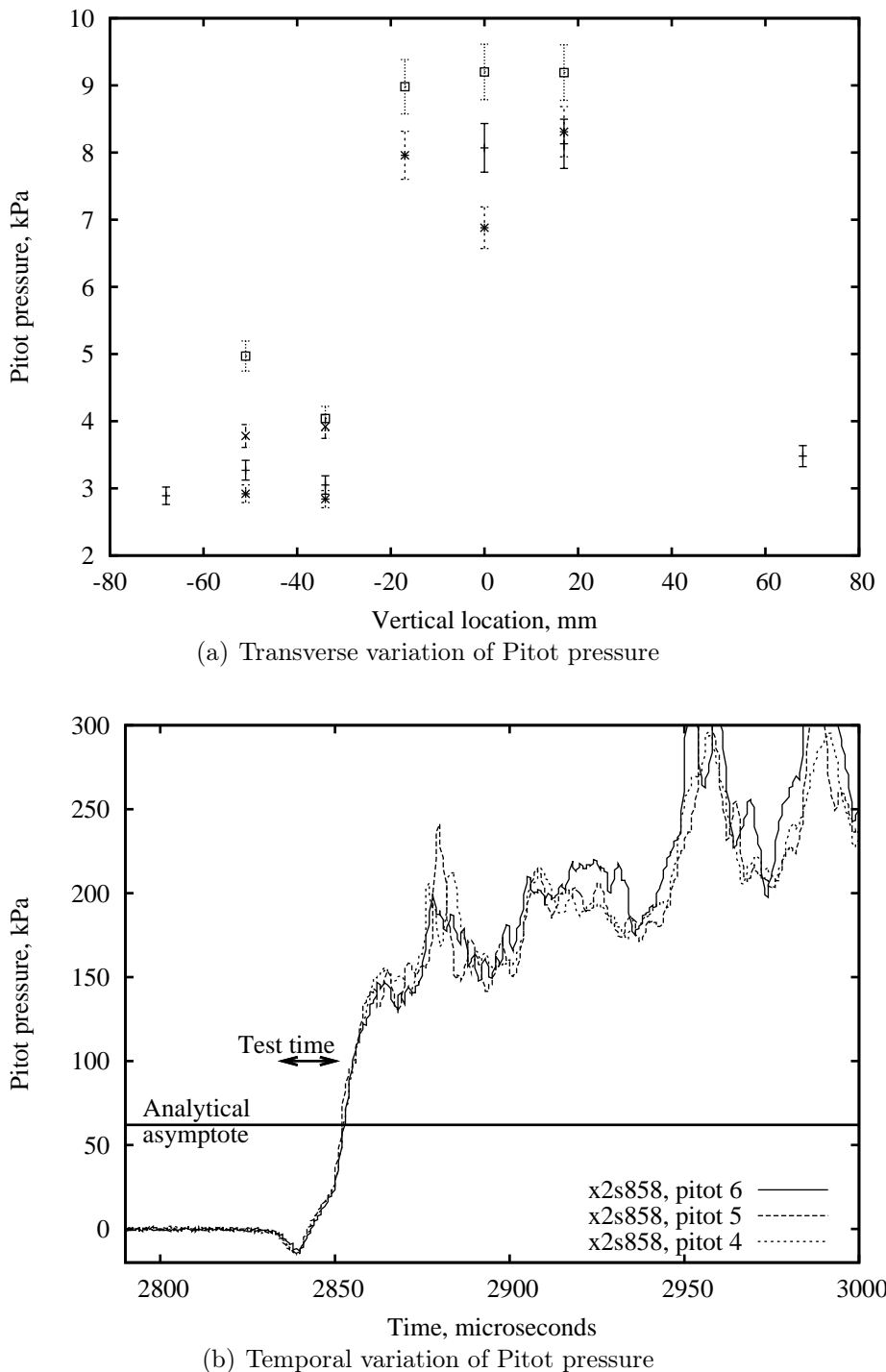


Figure 5.15 : Transverse and temporal variation of Pitot pressure 30 mm downstream of the shock tube exit for the 4 Pa Titan condition. Pitot 5 is on the centreline of the shock tube, while Pitots 4 and 6 are 17 mm above and below, respectively.

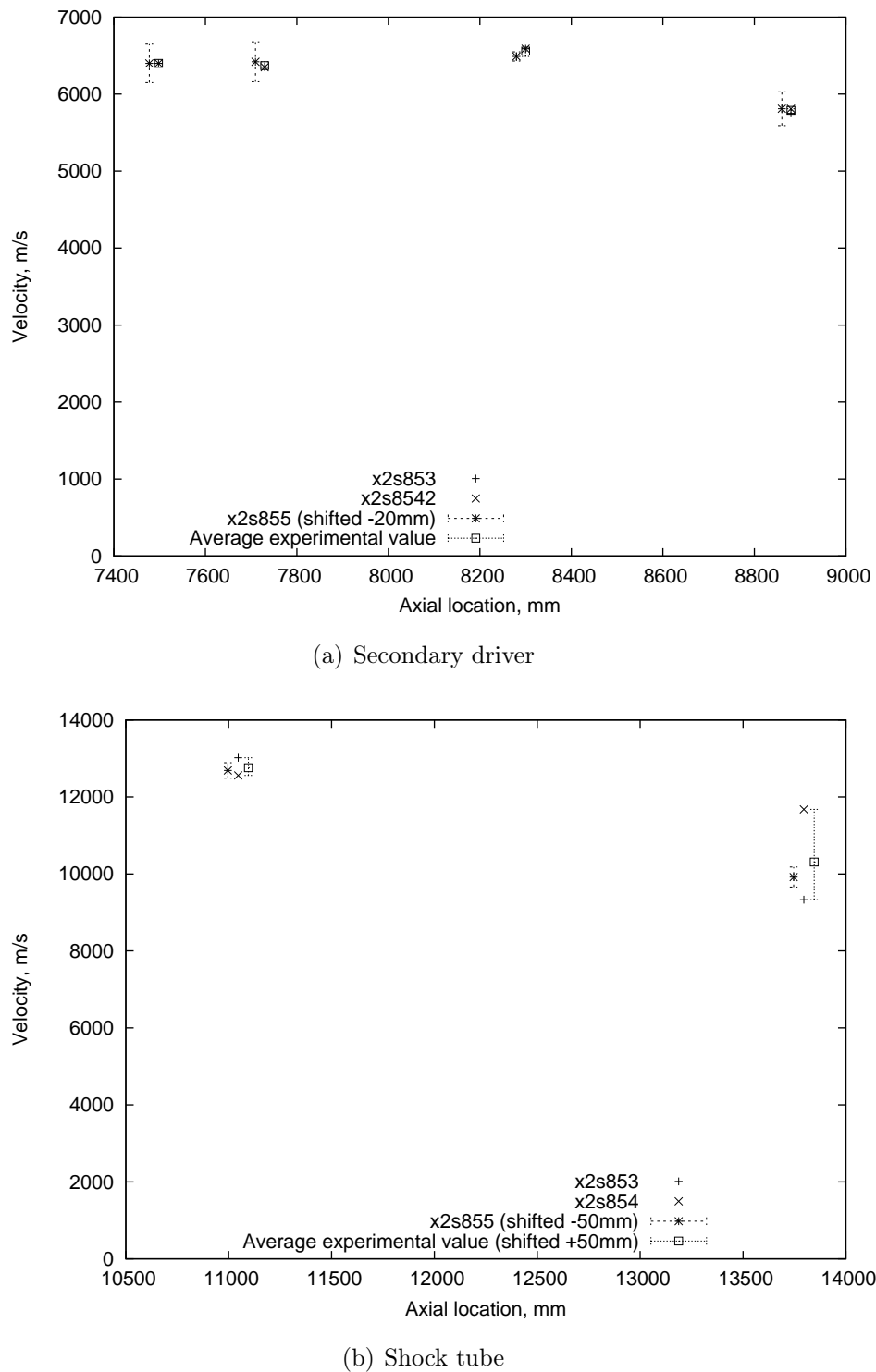


Figure 5.16 : Shock speed variation down the tube for the 1 Pa air condition experiments. The shock speed is calculated as a time of flight between the various transducers in each section. The location is then given as the midpoint between the two transducers. For one shot, the uncertainty in the calculated shock speed is shown. The average value of the experimental results is shown, with errorbars giving the overall spread of the values.

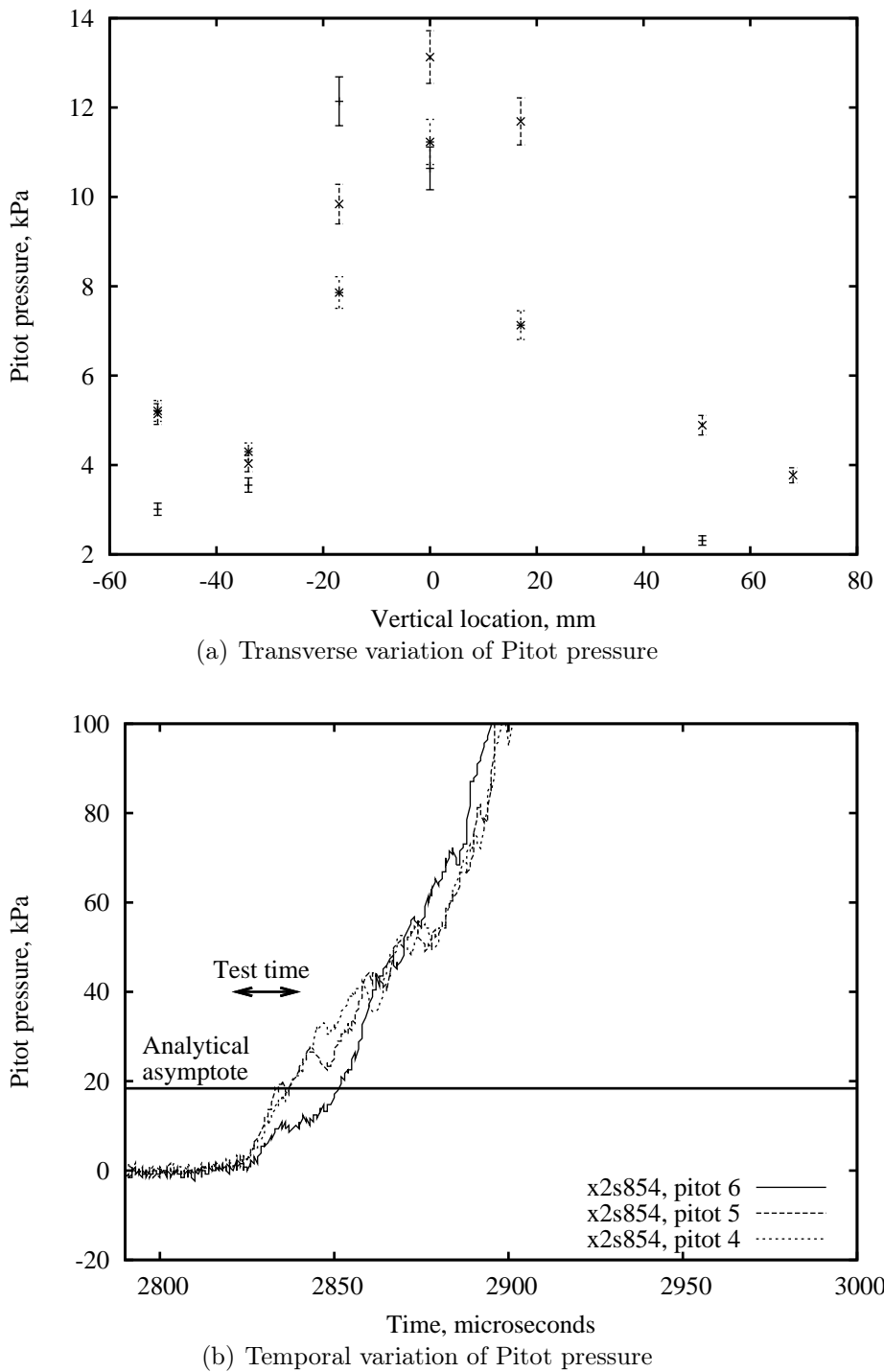


Figure 5.17 : Transverse and temporal variation of Pitot pressure 30 mm downstream of the shock tube exit for the 1 Pa air condition. Pitot 5 is on the centreline of the shock tube, while Pitots 4 and 6 are 17 mm above and below, respectively.

Reservoir gas mixture	Air
Reservoir fill pressure	1.15 MPa
Primary driver gas mixture	100 % He
Primary driver fill pressure	30 kPa
Primary diaphragm	1.2 mm steel; 0.2 mm scoring
Primary diaphragm burst pressure	15.5 MPa
Secondary driver gas mixture	100 % He
Secondary driver fill pressure	10 kPa
Secondary diaphragm	1/2 thou Mylar
Secondary diaphragm burst pressure	75 kPa
Test gas mixture	Air
Test gas fill pressure	1 Pa
Nominal average shock speed	10.30 km/s

Table 5.1 : Experimental fill conditions for the 1 Pa condition.

5.3 Summary of developed conditions for Titan simulated atmospheres

One of the primary aims of this work was to produce nonreflected shock tube test conditions at lower density freestream pressures. It is therefore desirable to measure the degree of rarefaction in the test flows. Continuum flows are characterised by Knudsen numbers, Kn , less than 0.01, where the Knudsen number is defined as the ratio of the mean free path of the gas particles, λ^3 , to the characteristic length scale, L . The transition from continuum to rarefied flows is generally considered to occur over the range $Kn = 0.01 - 1$.

$$Kn = \frac{\lambda}{L} \quad (5.1)$$

The mean free path of a gas is given by:

$$\lambda = \frac{2\mu}{\rho\sqrt{8RT/\pi}} \quad (5.2)$$

The mean free path in the test gas, both freestream and processed by the shock, is tabulated in Table 5.2. From the freestream value, the Knudsen number was calculated for each condition. This calculation was completed based on a number of different

³Not to be confused with wavelength. The mean free path directly referenced outside of this section, therefore all other references to λ refer to the wavelength dimension of the spectral data.

characteristic lengths: the diameter of the shock tube; the test length estimated from Mirels (1963) and the test length estimated from the experimental Pitot pressure traces. While the Knudsen number calculated based on the experimental test length remains in the continuum regime for the 13 Pa condition, the 8, 4, and 1 Pa conditions have transitional Knudsen numbers, indicating that continuum-based simulation methods may not be suitable for these conditions.

For the 13 and 8 Pa conditions, the shock speed attenuation in the shock tube was found to be of the same order as the accuracy of the instrumentation, and was therefore considered to be negligible in the context of the precision to which the operating conditions can be determined. For the 4 Pa condition, the decay in the shock speed was found to be more significant, but still small. Thus, the assumption that the shock speed measured by the last transducer in the shock tube approximates the shock speed at the exit of the tube is valid.

Table 5.2 presents a summary comparison of the three test conditions from both experimental and computational data which includes the calculated shock speeds and analytical results estimating the length of the test gas (based on the analysis of Mirels (1963)). The estimated mean free paths are also calculated for both the freestream and post-shock flows. These values are used to calculate the Knudsen number based on both the tube diameter and the estimated test length.

5.4 Summary

Prior to recording spectral data in the modified facility, it is necessary to show that the modifications did not produce any significant changes to the test flow. In order to investigate the flow quality, a reference condition at a freestream pressure of 13 Pa and experimental shock speed of 6.41 km/s was used.

Both the high speed camera images and the EILMER3 simulations showed that the shock exiting the aluminium tube remained planar near the centreline, where the spectral images were focussed. It was also found that the quasi-steady shock train introduced by the step increase in area in the shock tube settled well before the test gas reached the exit of the shock tube, and perturbations due to this were confined to a section of length approximately four times the diameter of the shock tube. Unfortunately, a potential problem in the grid resolution resulted in the driver gas being pulled along immediately behind the shock wave rather than establishing a length of test gas. It is expected that on a finer mesh, these anomalies would resolve themselves and the EILMER3 simulations would indicate a high quality, undisturbed flow at the tube exit of a similar length as

Test pressure (Pa)	Source	Shock speed (km/s)	λ pre-shock (mm)	λ post-shock (mm)	Test length Mirels (1963) (mm)	Test length measured (mm)	Kn_D (Mirels)	Kn_U (exp)	Core width (mm)
13.0	Experiment (mean)	6.41							
	Analysis		0.612	0.028	392.5	173	0.0039	0.0016	85
8.0	Experiment (mean)	6.19							
	Analysis		0.994	0.046	237.1	124	0.0064	0.0042	80
4.0	Experiment (mean)	9.04							
	Analysis		1.998	0.051	207.3	118	0.0128	0.0096	50
1.0	Experiment (mean)	10.30							
	Analysis		7.953	0.208	57.8	113	0.0513	0.1377	34

Table 5.2 : Summary of the developed Titan conditions. The Knudsen number is calculated based on both the shock tube diameter (155 mm) and the length of the test gas. The 1 Pa condition included here is for a test gas of air.

the anomalies. This would match well with the high speed camera footage and other estimates of the test gas slug length.

For the nonreflected shock tube mode, the freestream pressure and the shock speed are known. This leaves the total length of the test gas as the main unknown. As the response time of the Pitot pressure signals were of a similar order to the total available test time, the Pitot traces did not give a reliable time-accurate pressure record, but were able to provide an estimate of the available test gas. Therefore, analytical calculations across the shock wave, numerical calculations with L1d3 and EILMER3, and analytical results using the analysis of Mirels (1963) were used to provide additional information for comparison.

The Pitot pressure traces recorded in the modified facility provided information regarding the test time and core diameter of the usable test gas produced. For the three conditions simulating a Titan entry at 13, 8, and 4 Pa, the usable test gas was found to be 173, 124, and 118 mm respectively. At these conditions, spectral data was gathered for an axial length of less than 100 mm. Therefore, the spectral data recorded only test gas for each of these conditions.

The test gas was found to have a core diameter of 85 mm, 80 mm, and 50 mm for the 13, 8, and 4 Pa conditions respectively, just under half of the diameter of the shock tube.

Although it was not possible, due to air contamination of the test gas, to test at freestream pressures as low as 1 Pa in a Titan mixture, results were gathered for the NRST-Al facility at a 1 Pa air condition. It was found that for a condition with an average shock speed of 10.3 km/s, potentially 11 μ s of test gas was produced. This test gas had a core diameter of 34 mm, similar to the 4 Pa condition. However, at this 1 Pa pressure, it was not possible to clearly distinguish between the test gas and the driver gas in order to identify the interface from the Pitot measurements. This condition requires more study.

These results show that the modified facility produces flows of high quality and provides sufficient test gas for spectral data to be recorded, although further numerical simulation work is required. Test flow of a sufficient length and core diameter for recording spectral data across an axial distance of 100 mm along the centreline of the tube was produced for all three Titan conditions.

CHAPTER 6

Emission Spectroscopy Analysis

In this chapter, the calibrated data from the emission spectroscopy analysis are presented. These data are compared with results calculated with the `Specair` program (Laux 2002). Further comparisons for the 13 Pa condition are made against the data from Brandis (2009a). The optical system included a three dimensional radiating source in the test section, UV-grade synthetic fused silica windows to provide access to the evacuated chamber, external optics, and a spectrometer and ICCD camera as outlined in Figure 3.8

6.1 13 Pa condition

While the 13 Pa condition was investigated as a single nominal condition in Chapter 5, here it is convenient to separate the experimental data into two distinct sections: experiments with low shock speeds of approximately 6 km/s and experiments with faster shock speeds of approximately 6.6 km/s. This is done to allow further comparison to experimental data, as the work of Brandis (2009a) examined conditions with similar shock speeds at a freestream pressure of 13 Pa.

6.1.1 Low shock speed conditions: 6 km/s

Figure 6.1 presents a comparison of the power density at the shock front and shows the decay of the nonequilibrium peak behind the shock for the 13 Pa condition. In this figure,

results are presented for shot numbers x2s1475, x2s1469, and x2s691.

In Figure 6.1(a), the power density was integrated over a wavelength range of 310–450 nm and a spatial width equivalent to the tunnel width. This figure presents the results from two different experiments in the NRST-Al tube; the spectral results of x2s1475 were taken with a 150 lines/mm grating centred at 380 nm, while the data from x2s1469 used a 600 lines/mm grating, increasing the resolution of the wavelength domain. These experiments had shock speeds of 6.13 ± 0.11 and 5.84 ± 0.10 km/s respectively.

Figure 6.1(b) adds the results of an experiment completed by Brandis (2009a) in the unmodified facility, with a smaller slug (in both diameter and length) of radiating gas. This experiment, x2s691 used a 600 lines/mm grating centred at 380 nm and had a shock speed of 5.7 km/s. The spatial width used to calculate the power density in each case was the facility bore. For the NRST-Al facility, this was 155 mm, compared to 85 mm for the older facility. It can be seen that the peak power density level matches very well between the two facilities and there is a good agreement in the decay rate of this peak behind the shock front. This agreement between the two facilities - which have different dimensions, optical configurations, and independent calibrations - is an encouraging result for the modified facility.

The experiments conducted in the NRST-Al facility aimed not only to provide data consistent with the unmodified facility, but also to demonstrate that the modifications provided more usable test gas for measurements and improved the signal strength of those measurements. Figure 6.1(a) shows a sudden drop in signal at an axial location of approximately 90 mm which marks the end of the useful test gas in the spectral measurements. Physically, this is the location of the exit of the shock tube in the spectral image. As the length of the test gas calculated in Chapter 5 for this condition, 174 mm, is longer than the total axial distance captured by the spectral data, it is the loss of signal due to the presence of the shock tube, rather than the end of the test gas, which limits the axial length of the spectral data. In Figure 6.1(b), the sudden increase in noise at approximately 60 mm indicates the end of the useful test gas for the experiment x2s691 in the older facility, which is limited by the shorter slug length of test gas produced by the 85 mm bore facility. The improvement in the signal-to-noise ratio is also visible in this figure, demonstrated by the smoothness of the signal generated in the NRST-Al experiments in comparison to the unmodified facility. There is a visibly larger amplitude to the variations in the power density measurement due to noise for the NRST facility when compared to the NRST-Al measurements.

Figure 6.2 compares the power density of the same NRST-Al experiments with the computational results calculated by Brandis (2011) using the electronically specific collisional-radiative model **Mutation**. **Mutation** is described in further detail in Chapter 4. In this

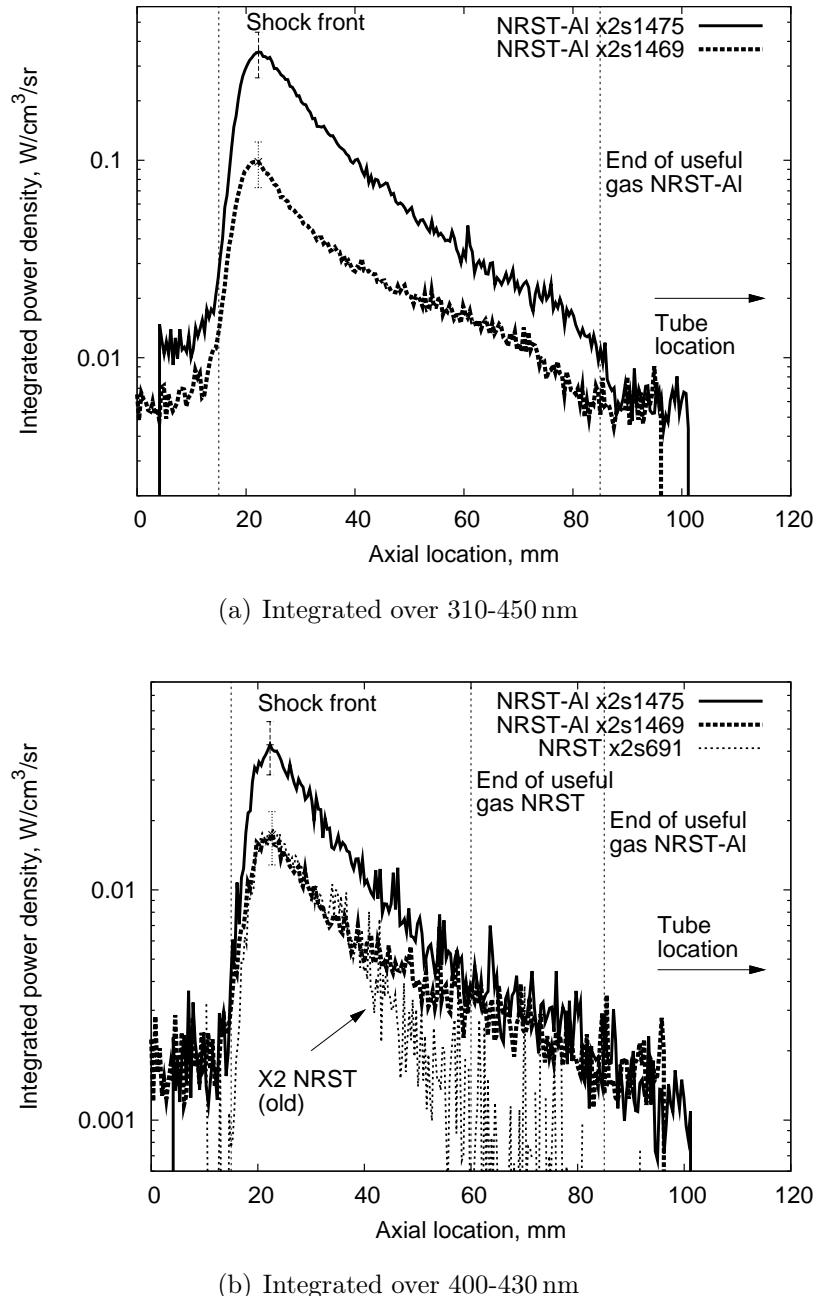


Figure 6.1 : An axial profile of the power density as the shock exited the shock tube at a freestream pressure of 13 Pa. The power densities are integrated over the wavelength ranges (a) 310-450 nm and (b) 400-430 nm. The data from shots x2s1475 and x2s1469 were taken in the modified facility, while x2s691 measurements were made in the older X2 facility by Brandis (2009a).

comparison, the power density is integrated over the wavelength range 310 - 470 nm and the shock speed for the **Mutation** simulation is 6.0 km/s. As for the comparison with the experimental data from the unmodified facility, there is a very good agreement between the datasets in the level of the nonequilibrium peak. However, there is a significant disagreement in the decay rate of the power density behind the peak.

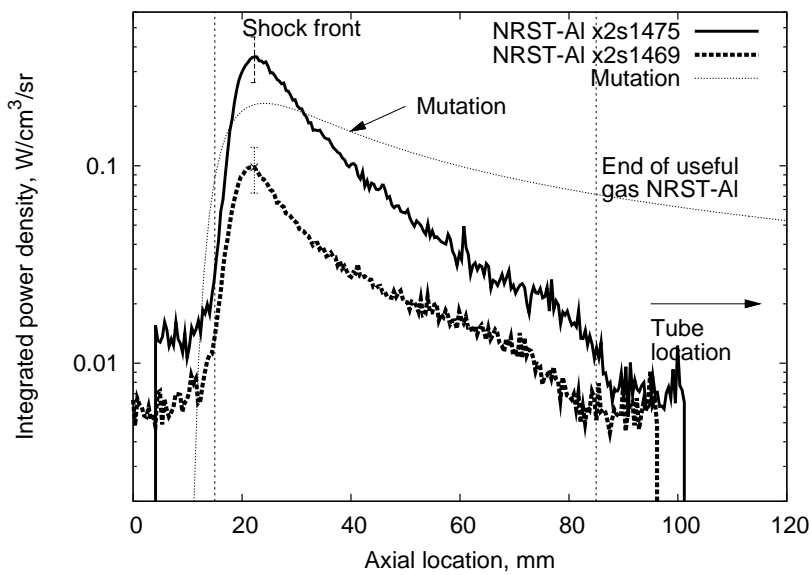


Figure 6.2 : An axial profile of the power density as the shock exited the shock tube at a freestream pressure of 13 Pa. The power densities are integrated over the wavelength range 310-470 nm. The data from shots x2s1476 and x2s1471 were taken in the modified facility, while **Mutation** results were calculated by Brandis (2011).

In Figure 6.3, the spectral power density is plotted across all wavelengths for the 600 lines/mm grating centred at 380 nm. This spectral power density is calculated at the axial location of the nonequilibrium peak value indicated in Figure 6.1. This spectra was recorded during shot x2s1469, at a shock speed of 5.84 km/s. The locations of rovibronic spectral bands for various species are labelled in this figure: CN(B-X); N₂⁺(B-X) and NH(A-X). The dominating species is the CN violet, across the three observable vibronic spectral bands ($\Delta v = -1, 0, +1$). There is also a considerable amount of NH present, producing a strong peak at approximately 335 nm.

Figure 6.4 presents three spectra typical of the 13 Pa condition at a shock speed of approximately 6 km/s. These figures demonstrate the range of spectral resolution which was achieved in the experiments and illustrate the level of detailed information which can be obtained with the finer gratings. As CN violet was found to be the primary radiating species present in the flow, the resolved images focussed on the CN(B-X) $\Delta v = 0$ band.

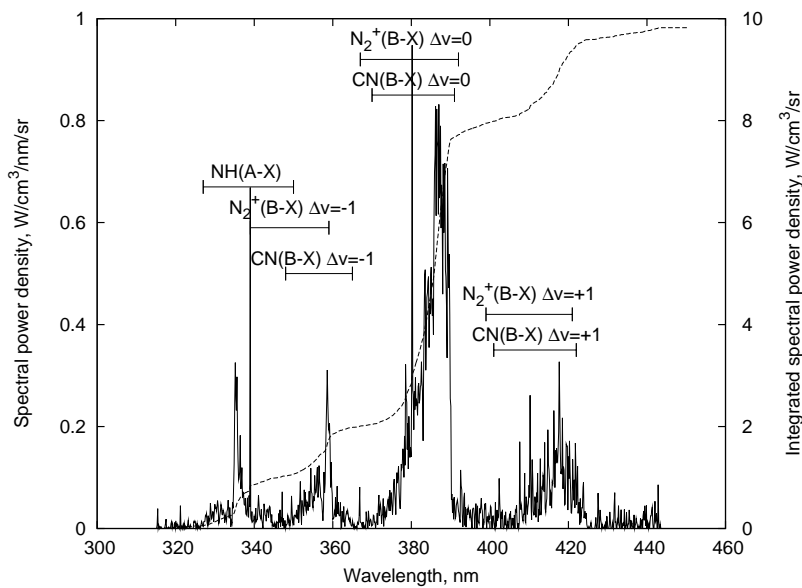


Figure 6.3 : NRST-Al spectral power density and its cumulative integration for shot x2s1469 at the axial location of the peak shown in Figure 6.1. Important species are indicated. The freestream pressure was 13 Pa and the 600 lines/mm grating was used.

As for the plots of the axial profile of power density, the spectral power density results were compared to experiments by Brandis (2009a). This comparison was completed using data gathered with the 600 lines/mm grating. It can be seen in Figure 6.5 that there is a significant difference in the spectral profiles gathered in the two facilities. In the NRST-Al results, the strength of the CN(B-X) $\Delta v=0$ spectral band is reduced and there is a corresponding increase in the strength of the NH(A-X) band. The most likely cause of this discrepancy is contamination of the test gas during the experimental setup. Prior to the experiments, the shock tube and dump tank were evacuated to a maximum value of 0.1 Pa. The sections were then flushed with the Titan atmospheric gas mixture to a value of 8 Pa. Following this, the test gas was added approximately 20 seconds prior to the completion of the experiment. The resulting drop methane concentration of the test gas was 1.85 % rather than the desired 2 %.

Figure 6.5(d) plots the results of the Specair simulations for the 13 Pa condition at a shock speed of 6.0 km/s. The computational spectra included N_2 B-A (First Positive), CN B-X (Violet), N_2 C-B (Second Positive), N_2^+ B-X (First Negative), and NH (A-X) vibronic spectral bands over the wavelength range 310-450 nm. The atomic lines of N and C were also included. The temperature, pressure, and species concentrations were extracted from the results of a CEA2 simulation, and thermal equilibrium was assumed for the Specair calculations. It can be seen that the results match very closely the experimental results of x2s691 (Brandis 2009a), however differences do occur in the estimation of the NH(A-X)

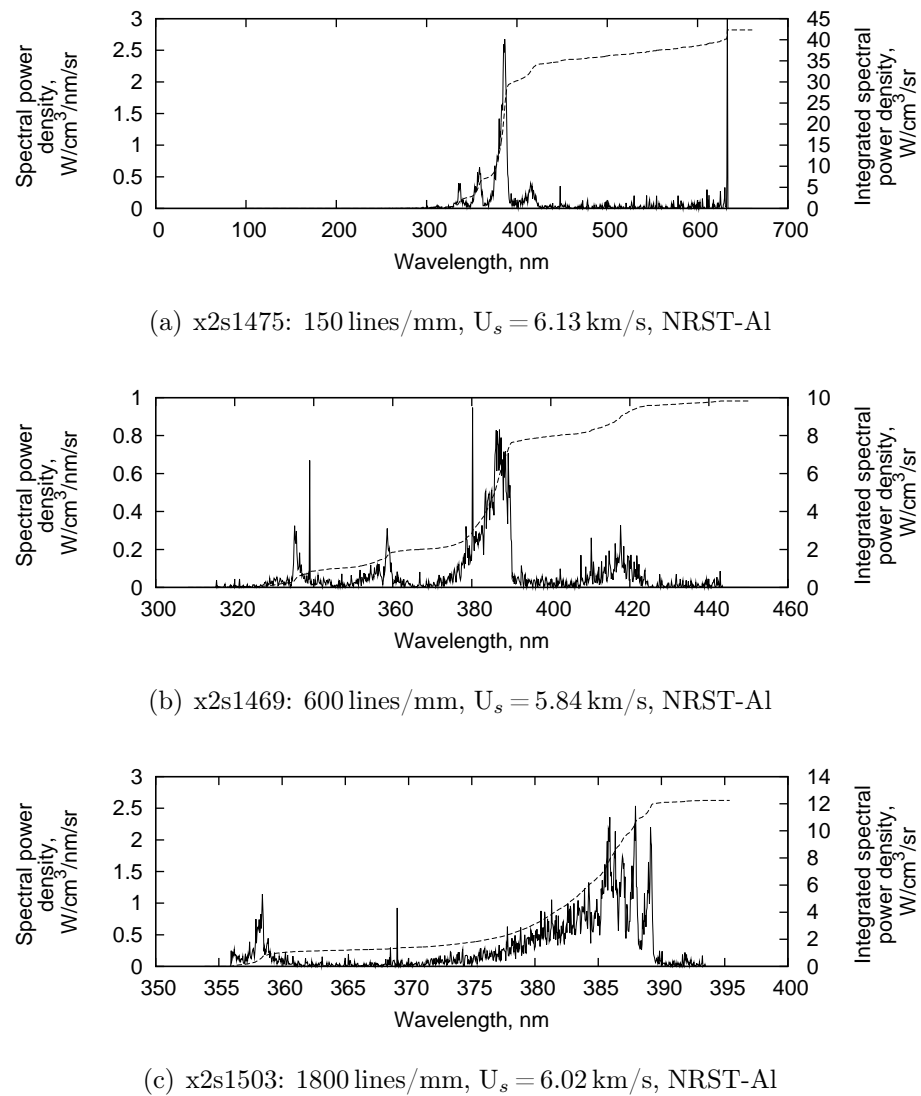


Figure 6.4 : NRST-Al spectral power density and its cumulative integration for shots x2s1475, x2s1469, and x2s1503 at the axial location of the peak shown in Figure 6.1. For all conditions, the freestream pressure was 13 Pa.

and N_2^+ (B-X) $\Delta v=+1$ vibronic spectral bands when compared to the NRST-Al results. This is most likely due to the CEA2 code calculating the equilibrium species concentrations, which have decayed from the concentrations expected near the nonequilibrium peak where the experimental data is extracted.

One of the aims of this thesis was to identify and minimise any contamination effects from the tube material, driver gas, and diaphragms. The spectral results indicate that there is no contamination present in the flow due to the tube material or diaphragms at the location of the nonequilibrium peak as there are no peaks corresponding to aluminium, iron, or calcium associated with mylar visible above the level of the noise. As indicated in the axial profiles of power density, the test length has been significantly increased over the previous conditions achievable in the X2 facility, removing any contamination effects due to the presence of the driver gas for the results in the region of the nonequilibrium peak.

6.1.2 High shock speed conditions: 6.6 km/s

Figure 6.6 presents a comparison of the power density at the shock front and shows the decay of the nonequilibrium peak behind the shock for shot numbers x2s1476, x2s1471, and x2s697. These experiments had shock speeds of 6.65 ± 0.13 , 6.58 ± 0.12 , and 7.40 km/s respectively and freestream pressures of 13 Pa. As for the 13 Pa condition results presented previously at lower shock speeds, the first two of these experiments were completed in the modified X2 facility, while x2s697 was an experiment completed by Brandis (2009a). The spectral results of x2s1476 were taken with a 150 lines/mm grating centred at 380 nm, while the data from x2s1471 and x2s697 used a 600 lines/mm grating. The power density was integrated over a wavelength range of 310-450 nm and a spatial width equivalent to the tunnel width.

As for the previous comparison, the experimental results in Figure 6.6(a) show the very good agreement in the level of the nonequilibrium peak radiation behind the shock wave, although there is some disagreement between the decay rate of this peak between the modified and older facility. Unfortunately, in the single comparable experiment of Brandis (2009a), the front of the shock has been cut off in the spectral image and therefore the rise time cannot be compared between the two experiments. Similar to Figure 6.1(b), the improvement in the signal strength and test time available may again be seen in Figure 6.6(a).

In Figure 6.6(b), the experimental power density of the NRST-Al facility - integrated over the wavelength range 310-470 nm - is compared to calculations of the stagnation line power density simulated with **Mutation** (Brandis 2011). The **Mutation** simulation

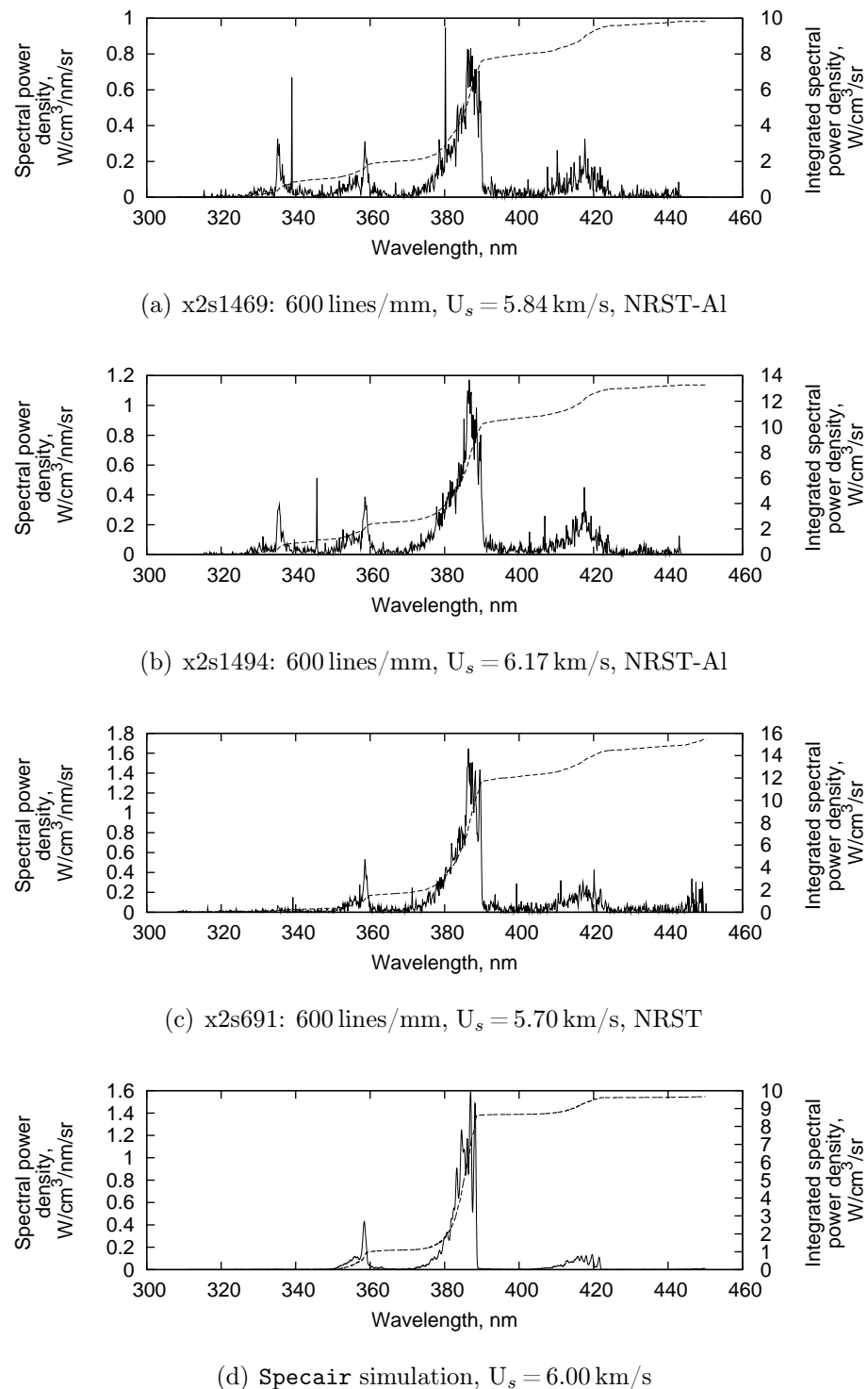


Figure 6.5 : A comparison of spectral power density and its cumulative integration for shots (a) x2s1469, (b) x2s1494, and (c) x2s691 at the axial location of the peak shown in Figure 6.1. The data from shots x2s1469 and x2s1494 were taken in the modified facility, while the x2s691 measurements were made in the older X2 facility. These data were taken by Brandis (2009a). A comparison with Specair is shown in (d). For all conditions, the freestream pressure was 13 Pa.

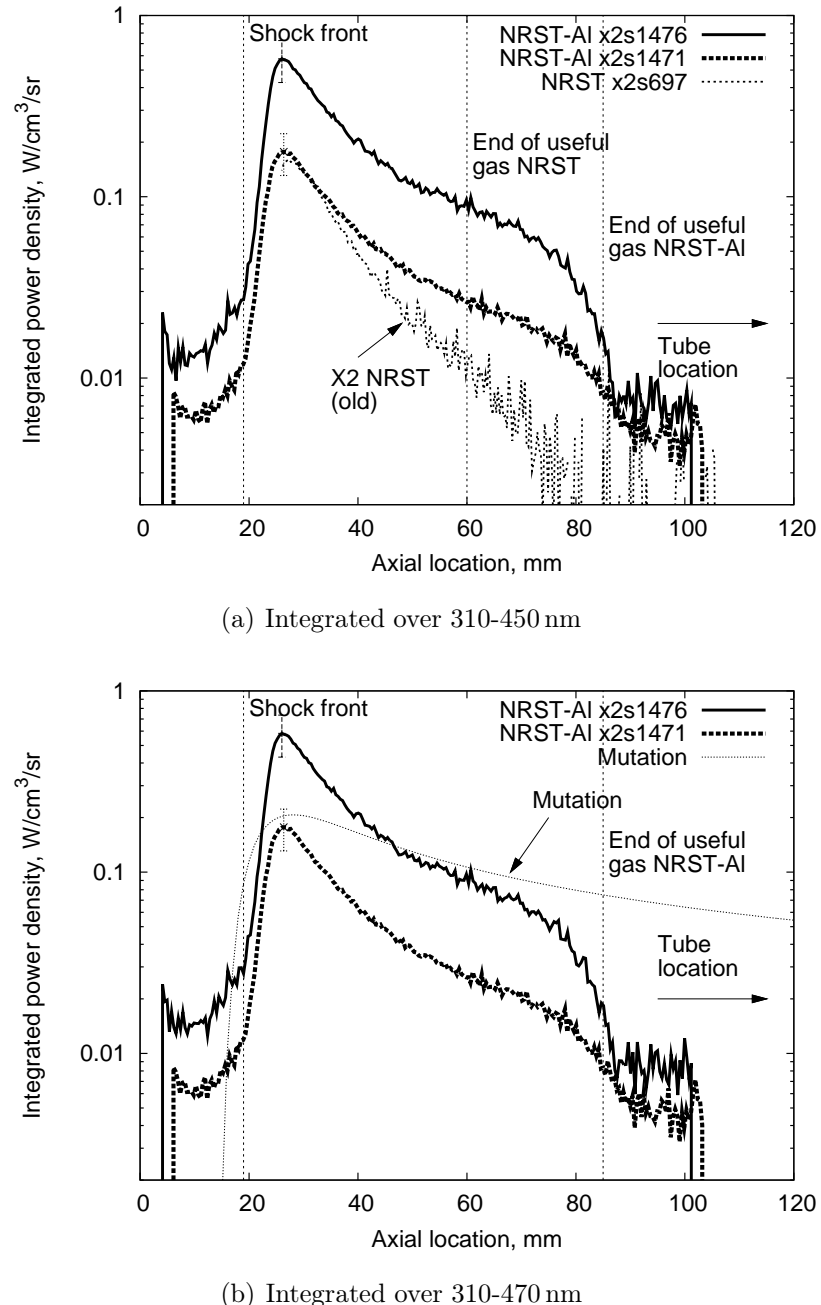


Figure 6.6 : An axial profile of the power density as the shock exited the shock tube at a freestream pressure of 13 Pa. The power densities are integrated over the wavelength ranges (a) 310-450 nm and (b) 310-470 nm. The data from shots x2s1476 and x2s1471 were taken in the modified facility, while x2s697 measurements were made in the older X2 facility by Brandis (2009a). Mutation results were calculated by Brandis (2011).

was completed at a freestream pressure of 13 Pa with a shock speed of 6.6 km/s. As for the previous comparisons, the nonequilibrium peak level of the power density compares well between collisional-radiative model and experimental data, but there is a significant discrepancy between the experimental and computational decay rates behind this peak.

As for the previous 13 Pa condition results, Figure 6.7 presents the spectral power density for the 600 lines/mm grating centred at 380 nm. Again, this spectral power density is calculated at the axial location of the nonequilibrium peak value indicated in Figure 6.6, and the results are consistent with those presented in Figure 6.3. These data were recorded during shot x2s1470, at a shock speed of 6.87 km/s. The locations of spectral bands for various species are labelled in this figure: CN(B-X); N₂⁺(B-X) and NH(A-X). The dominating species is the CN violet, across the three vibronic spectral bands ($\Delta v = -1, 0, +1$). There is also a considerable amount of NH present, producing a strong peak at approximately 335 nm.

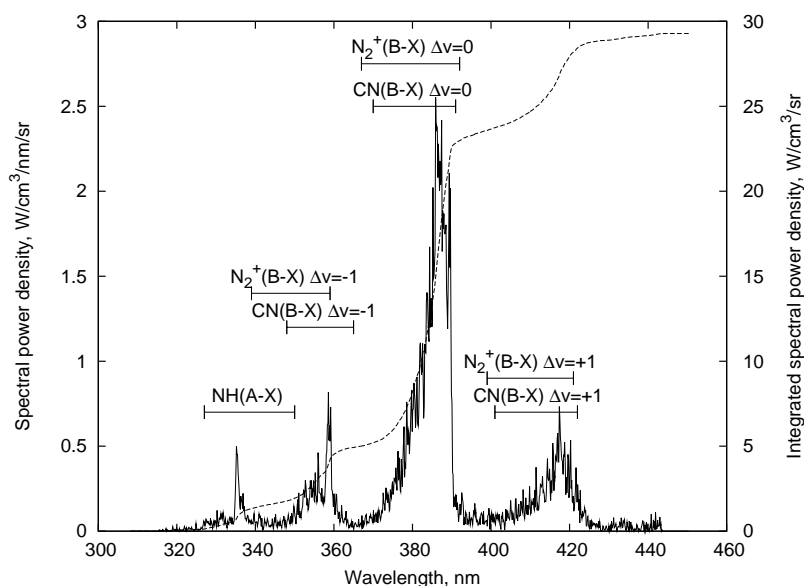


Figure 6.7 : NRST-Al spectral power density and its cumulative integration for shot x2s1470 at the axial location of the peak shown in Figure 6.6. Important species are indicated. The freestream pressure was 13 Pa and the 600 lines/mm grating was used.

Figure 6.8 presents three spectra typical of the 13 Pa condition at a shock speed of approximately 6.6 km/s. These figures demonstrate the range of spectral resolution which was achieved in the experiments and illustrate the level of detailed information which can be obtained with the finer gratings. As CN violet was found to be the primary radiating species present in the flow, the images focussed on the CN(B-X) $\Delta v = 0$ band.

Figure 6.9 allows for a comparison to be made between the spectral profiles pro-

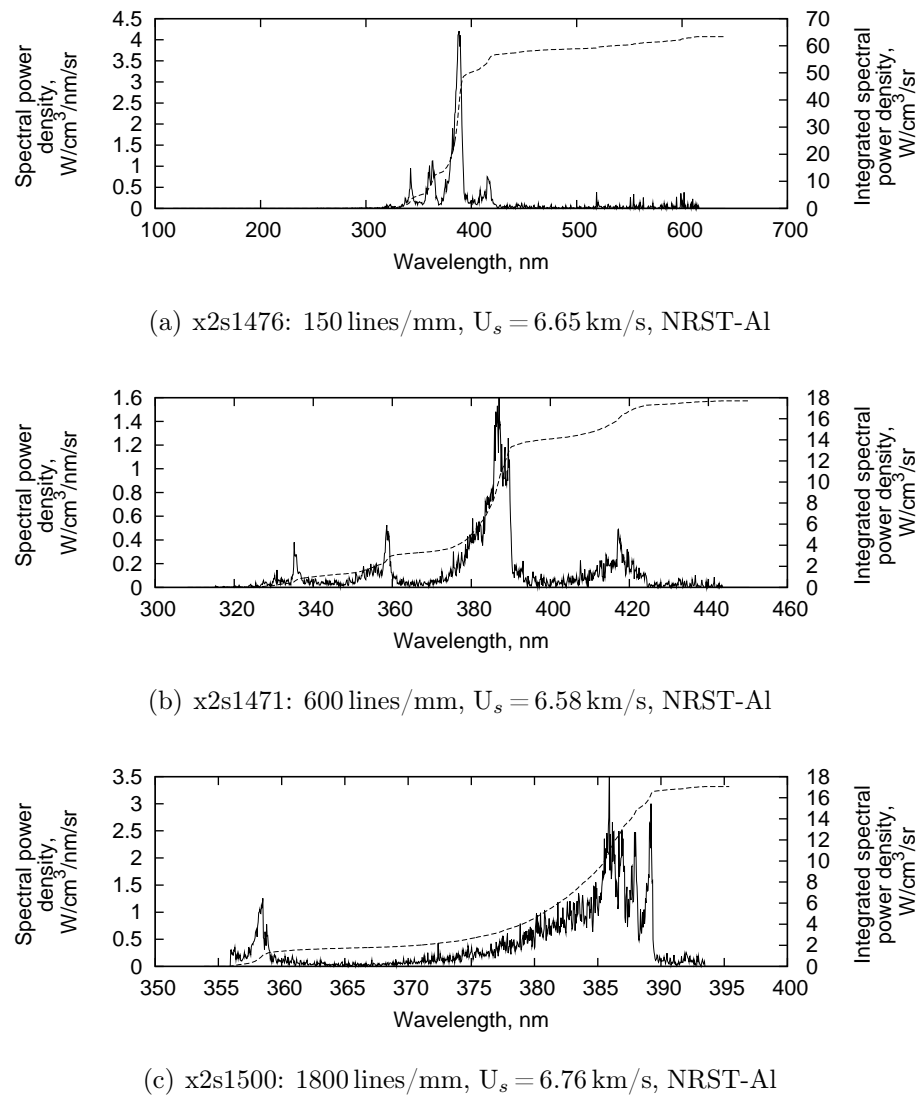


Figure 6.8 : NRST-Al spectral power density and its cumulative integration for shots x2s1476, x2s1471, and x2s1500 at the axial location of the peak shown in Figure 6.6. For all conditions, the freestream pressure was 13 Pa.

duced by the two experimental facilities and the computational profile simulated using **Specair**. This comparison was completed using experimental spectra captured with the 600 lines/mm grating. The trend observed in the results is consistent with that identified in Figure 6.5: potential air contamination of the NRST-Al facility has resulted in varying strengths of the CN(B-X) $\Delta v=0$ and NH(A-X) vibronic spectral bands. Unfortunately, the work of Brandis (2009a) provides only a single experiment for comparison at each condition. This makes it difficult to determine whether a similar trend occurred in the unmodified facility (as one would expect it to) and where the experimental data of Brandis would lie on a scale of this contamination.

Figure 6.9(d) plots the results of the **Specair** simulations for the 13 Pa condition at a shock speed of 6.6 km/s. It can be seen that the results match very closely the experimental results of x2s697 (Brandis 2009a) and x2s1471, however differences do occur in the estimation of the NH(A-X) and N₂⁺ (B-X) $\Delta v=+1$ vibronic spectral bands. This is most likely due to the CEA2 code calculating the equilibrium species concentrations, which have decayed from the concentrations expected near the nonequilibrium peak where the experimental data is extracted.

6.2 8 Pa condition

Figure 6.10 presents a comparison of the power density at the shock front and shows the decay of the nonequilibrium peak behind the shock for shot numbers x2s1529, x2s1521, and x2s545. These experiments had shock speeds of 5.95±0.10, 5.81±0.10, and 5.70 km/s and freestream pressures of 8, 8, and 9 Pa respectively. As for the comparison of the 13 Pa condition results above, the first two of these experiments were completed in the NRST-Al X2 facility, while x2s545 was an experiment completed by Brandis (2009a). The spectral results of x2s1529 were taken with a 150 lines/mm grating centred at 380 nm, while the data from x2s1521 and x2s545 used a 600 lines/mm grating.

The previous limit of the facility, and therefore the experiments of Brandis (2009a), was a freestream pressure of 9 Pa. While data was gathered for conditions with freestream pressures as low as 6 Pa, the poor signal-to-noise ratio of these results (due to the very small amount of gas) and very short test time limited the usable data to conditions of 9 Pa and above. Therefore, no data exists to provide a direct comparison between the results of the new facility at this condition and the previous tunnel. However, experiment x2s545 provides a reasonably close test condition and has been used here.

Figure 6.10(a) compares the NRST-Al results with the older facility. The power density was integrated over a wavelength range of 310 - 450 nm and a spatial width equivalent to the tunnel width (155 mm for NRST-Al and 85 mm for NRST). This comparison

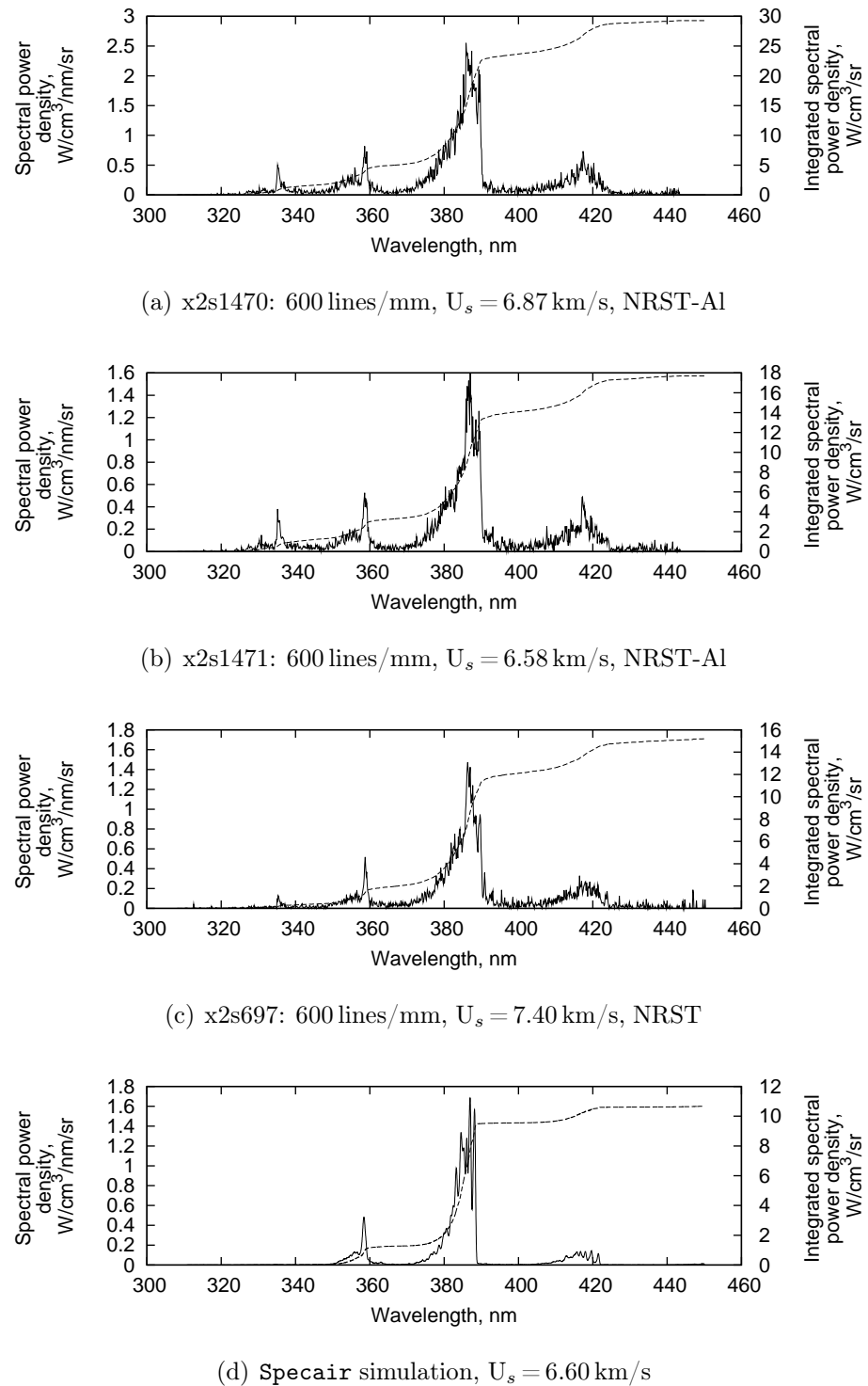


Figure 6.9 : A comparison of spectral power density and its cumulative integration for shots (a) x2s1470, (b) x2s1471, and (c) x2s697 at the axial location of the peak shown in Figure 6.6. The data from shots x2s1470 and x2s1471 were taken in the modified facility, while the x2s697 measurements were made in the older X2 facility. These data were taken by Brandis (2009a). A comparison with Specair is shown in (d). For all conditions, the freestream pressure was 13 Pa.

demonstrates the very strong agreement between the facilities in both the level of the nonequilibrium peak radiation behind the shock wave and the decay rate. The discretisation of the data in x2s545 indicates the low signal-to-noise ratio of the condition in the unmodified facility, and the improvement in the results from the NRST-Al facility can be clearly seen. The vertical lines representing the end of the useful test gas also show that there was a significant improvement in the test time with the larger diameter tube. As for the 13 Pa condition, the limit of the axial location in the NRST-Al results is due to the presence of the shock tube exit rather than the end of the test gas produced by the facility. The axial limit indicated for x2s545 in the unmodified facility is due to the limited test gas produced in the smaller bore facility.

In Figure 6.10(b), the power density for the NRST-Al integrated over the wavelength range of 310 - 470 nm is compared to a **Mutation** simulation completed by Brandis (2011). As for the 13 Pa conditions, this simulation used an electronically specific collisional-radiative model, with a freestream pressure of 8 Pa and a shock speed of 6 km/s. There is a significant discrepancy in the level of the nonequilibrium peak power density between the experimental and computational results, with the **Mutation** simulation overestimating the peak by a factor of 4. The collisional-radiative model was also unable to completely match the decay rate of the experimental data behind the peak.

As for the results from the 13 Pa condition, Figure 6.11 presents the spectral power density for the 600 lines/mm grating centred at 380 nm. This spectral power density is calculated at the axial location of the nonequilibrium peak value indicated in Figure 6.10, and the results are consistent with those presented in Figures 6.7 and 6.3. These data were recorded during shot x2s1521, at a shock speed of 5.81 km/s. The locations of spectral bands for various species are labelled in this figure: CN(B-X); N₂⁺(B-X) and NH(A-X). The dominating species is the CN violet, across the three vibronic spectral bands ($\Delta v = -1, 0, +1$). There is also a considerable amount of NH present, producing a strong peak at approximately 335 nm.

Figure 6.12 presents three spectra typical of the 8 Pa condition at a shock speed of approximately 5.95 km/s, demonstrating the range of spectral resolution which was achieved in the experiments. As CN violet was found to be the primary radiating species present in the flow, the images focussed on the CN(B-X) $\Delta v = 0$ band.

Figure 6.13 allows for a comparison to be made between the spectral profiles produced by the two experimental facilities and the computational profile simulated using **Specair**. This comparison was completed using experimental spectra captured with the 600 lines/mm grating. The trend observed in the results is consistent with that identified in Figures 6.5 and 6.9: potential air contamination of the NRST-Al facility has resulted

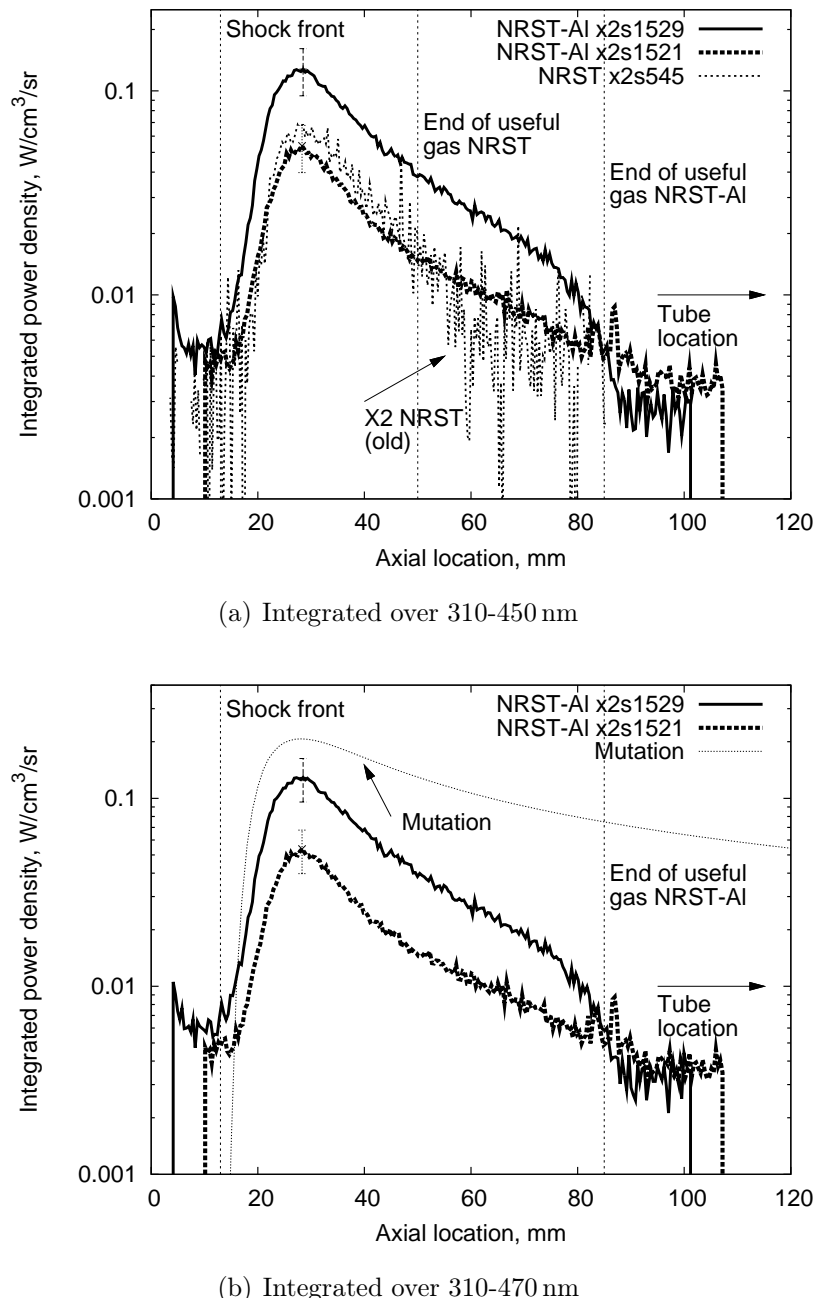


Figure 6.10 : An axial profile of the power density as the shock exited the shock tube at a freestream pressure of 8 Pa. The power densities are integrated over the wavelength ranges (a) 310-450 nm and (b) 310-470 nm. The data from shots x2s1529 and x2s1521 were taken in the modified facility, while x2s545 measurements were made in the older X2 facility by Brandis (2009a). The freestream pressures for x2s1529, x2s1521, and x2s545 were 8, 8, and 9 Pa respectively. Mutation results were calculated by Brandis (2011).

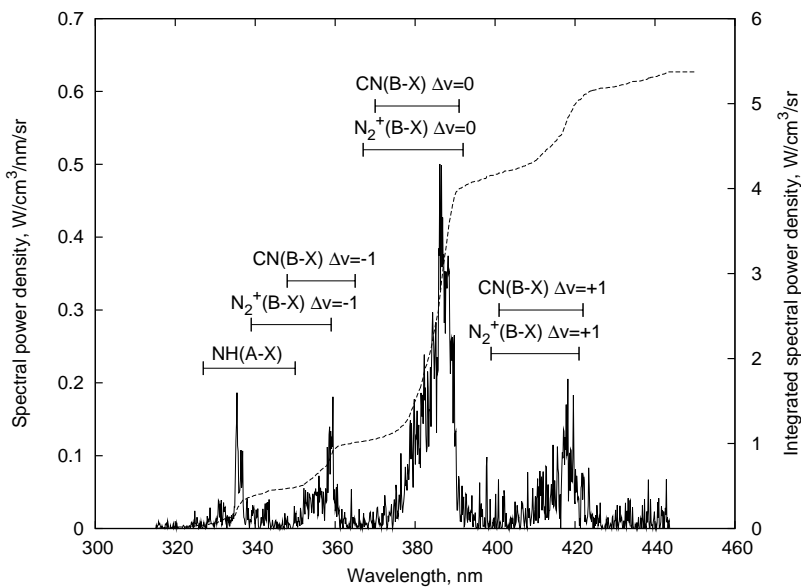


Figure 6.11 : NRST-Al spectral power density and its cumulative integration for shot x2s1521 at the axial location of the peak shown in Figure 6.10. Important species are indicated. The freestream pressure was 8 Pa and the 600 lines/mm grating was used.

in varying strengths of the CN(B-X) $\Delta v=0$ and NH(A-X) spectral bands. The estimated drop in the concentration of methane in the test gas due to leaks was 0.23 %.

Figure 6.13(c) plots the results of the **Specair** simulations for the 8 Pa condition at a shock speed of 6.19 km/s. The computational spectra included N_2 B-A (First Positive), CN B-X (Violet), N_2 C-B (Second Positive), N_2^+ B-X (First Negative), and NH (A-X) vibronic spectral bands over the wavelength range 310-450 nm. The atomic lines of N and C were also included. It can be seen that the results match very closely the experimental results of x2s545 (Brandis 2009a).

6.3 4 Pa condition

In Figure 6.14, a comparison of the power density at the shock front and the decay of the nonequilibrium peak is presented for two experiments at the 4 Pa condition in the modified facility. Unlike the 13 and 8 Pa conditions, no experimental data from other facilities exists with which to make a comparison. This freestream pressure was selected for investigation as it represented the lowest possible test pressure achievable in the NRST-Al facility (as discussed in Chapter 5).

Figure 6.14 presents data from shot numbers x2s1533 and x2s1544, with shock speeds of 9.62 ± 0.25 and 9.80 ± 0.25 km/s respectively. This shock speed is significantly higher

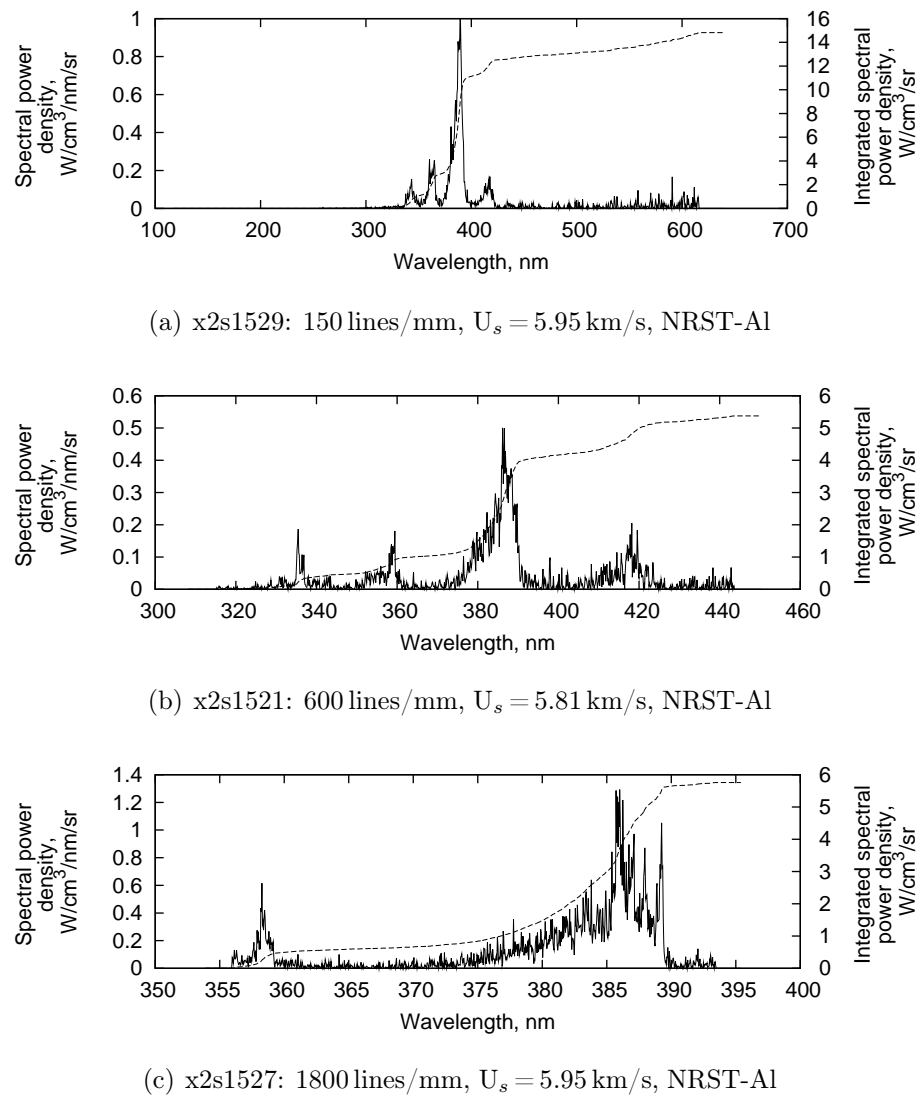


Figure 6.12 : NRST-Al spectral power density and its cumulative integration for shots x2s1529, x2s1521, and x2s1527 at the axial location of the peak shown in Figure 6.10. The freestream pressures for all conditions were 8 Pa.

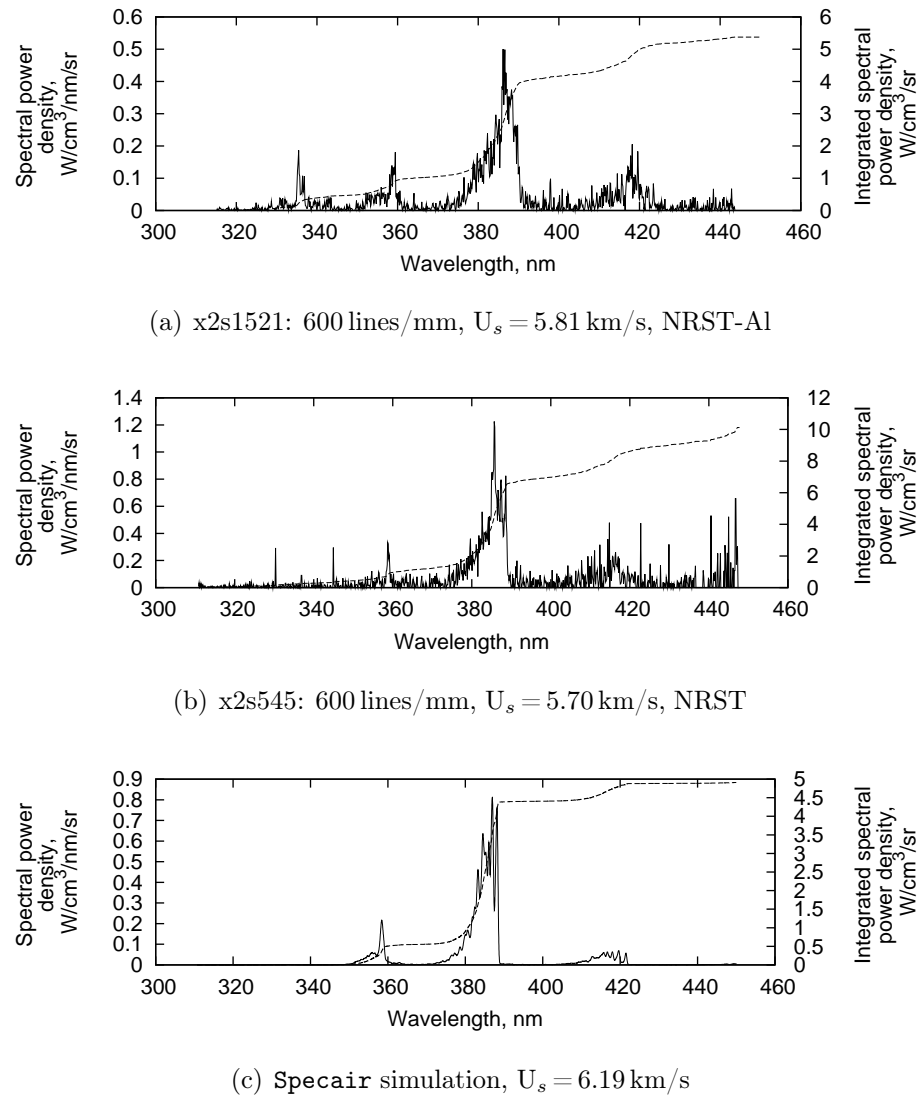


Figure 6.13 : A comparison of spectral power density and its cumulative integration for shots (a) x2s1521 and (b) x2s545 at the axial location of the peak shown in Figure 6.10. The data from shot x2s1521 was taken in the modified facility, while the x2s545 measurements were made in the older X2 facility. These data were taken by Brandis (2009a). A comparison with Specair is shown in (c). The freestream pressures for x2s1521 and x2s545 were 8 and 9 Pa respectively.

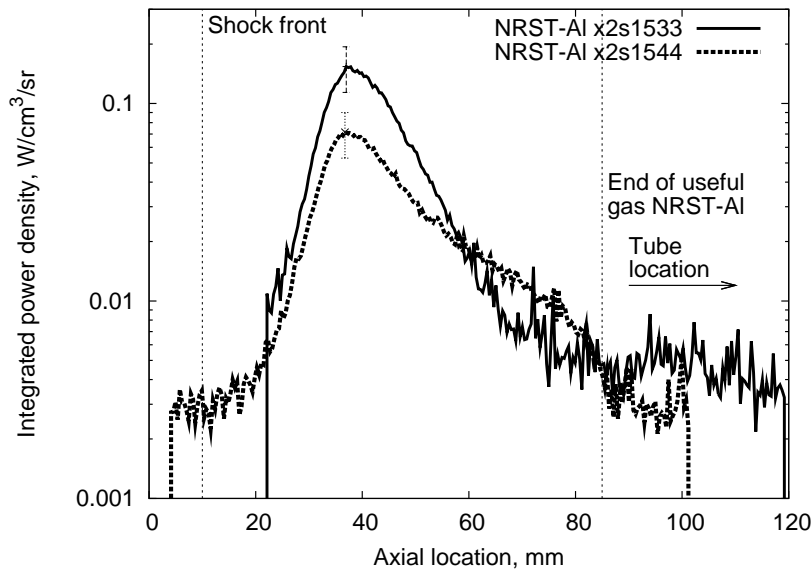


Figure 6.14 : An axial profile of the power density as the shock exited the shock tube at a freestream pressure of 4 Pa. The power densities are integrated over the wavelength range 310-450 nm. The data from shots x2s1533 and x2s1544 were taken in the modified facility.

than for the 13 and 8 Pa conditions. With such a small freestream pressure, the signal-to-noise ratio is somewhat poorer than for the other cases. Therefore, the condition was developed with a high shock speed in order to produce a stronger signal. The spectral results of x2s1533 were taken with a 150 lines/mm grating centred at 380 nm, while the data from x2s1544 used a 600 lines/mm grating. The power density was integrated over a wavelength range of 310-450 nm and a spatial width equivalent to the tunnel width. Although the front of the shock is not in the image in x2s1533, there is a very strong agreement in the rise time and peak nonequilibrium level between the two experiments. A slight difference is visible in the comparison of the decay rate behind the shock.

It can be seen in the image that there is a significant length of test gas available at this test condition, which was previously unobtainable in the nonreflected shock tube mode. The test time available in the modified facility for a simulated Titan atmosphere at 4 Pa freestream pressure was 118 mm. As for the previous conditions, this resulted in the limit of the useful axial power density data being a result of the presence of the shock tube exit in the image, rather than the end of the test time. The signal-to-noise ratio of the experimental results is also quite high for such a low pressure.

Unfortunately, no computational comparison is possible for the axial profile of power density. The collisional-radiative code **Mutation** was unable to resolve a solution for the 4 Pa freestream condition.

As for the results from the 13 and 8 Pa conditions, Figure 6.15 presents the spectral power density for the 600 lines/mm grating centred at 380 nm. This spectral power density is calculated at the axial location of the nonequilibrium peak value indicated in Figure 6.14, and the results are consistent with those presented in Figures 6.7, 6.3, and 6.11. These data were recorded during shot x2s1544, at a shock speed of 9.8 km/s. The locations of spectral bands for various species are labelled in this figure: CN(B-X); $N_2^+(B-X)$ and NH(A-X). The dominating species is the CN violet, across the three vibronic spectral bands ($\Delta v = -1, 0, +1$). There is also a considerable amount of NH present, producing a strong peak at approximately 335 nm.

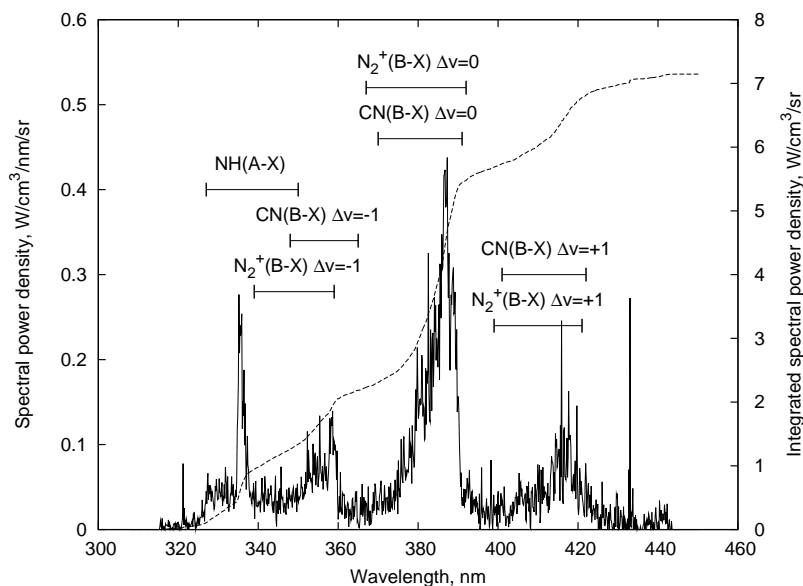


Figure 6.15 : NRST-Al spectral power density and its cumulative integration for shot x2s1544 at the axial location of the peak shown in Figure 6.14. Important species are indicated. The freestream pressure was 4 Pa and the 600 lines/mm grating was used.

Figure 6.16 presents three spectra typical of the 4 Pa condition at a shock speed of approximately 9.8 km/s, demonstrating the range of spectral resolution which was achieved in the experiments. As CN violet was found to be the primary radiating species present in the flow, the images focussed on the CN(B-X) $\Delta v = 0$ band.

As was previously mentioned, no experimental data exists for spectral investigations at freestream pressures of 4 Pa in other shock tube facilities. Therefore, in Figure 6.17, the experimental data from x2s1544 is compared to computational results from the code **Specair**.

Figure 6.17(b) plots the results of the **Specair** simulations for the 8 Pa condition at a shock speed of 6.19 km/s. The computational spectra included N_2 B-A (First Positive),

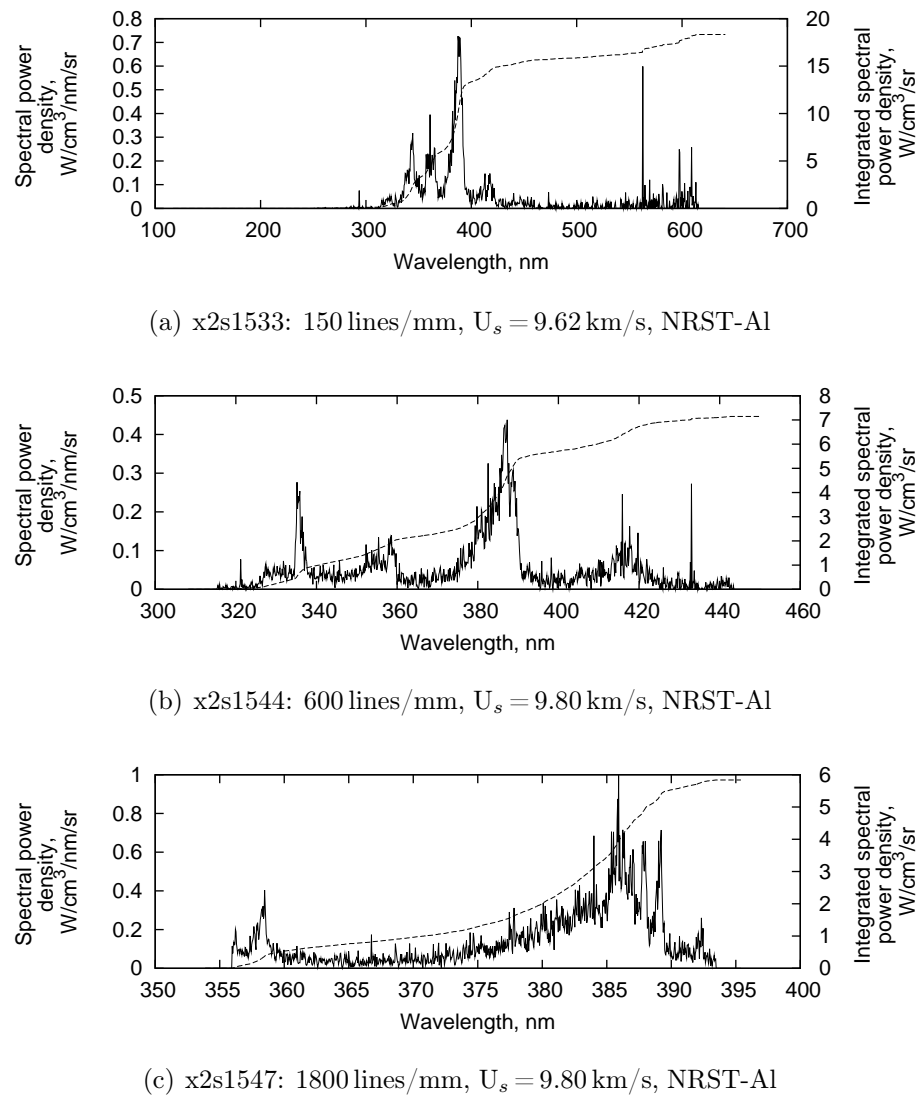
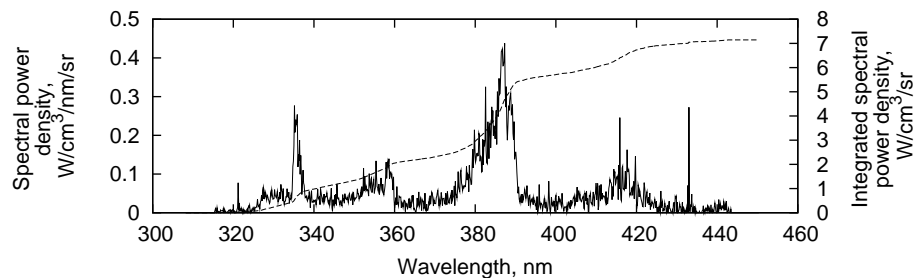


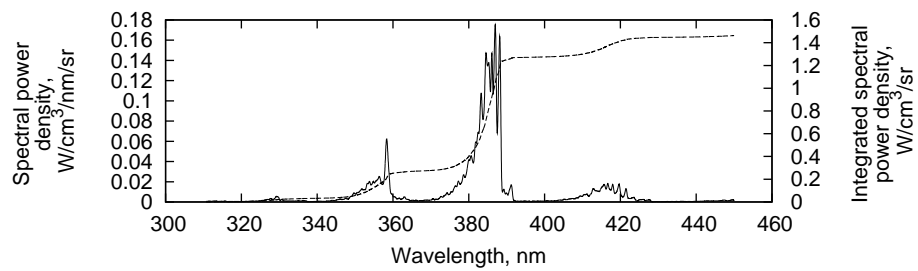
Figure 6.16 : NRST-Al spectral power density and its cumulative integration for shots x2s1533, x2s1544, and x2s1547 at the axial location of the peak shown in Figure 6.14. No measurements exist at a comparable condition in the older X2 facility. The freestream pressure was 4 Pa.

CN B-X (Violet), N₂ C-B (Second Positive), N₂⁺ B-X (First Negative), and NH (A-X) vibronic spectral bands over the wavelength range 310-450 nm. The atomic lines of N and C were also included. It can be seen that the results are approximately half the intensity of the experimental level.

Leaks in the dump tank and the limits of the vacuum system resulted in an estimated drop in methane concentration of 0.41 % from the nominal 2 %. This contamination of the test gas was the deciding factor in marking the lower limit of the NRST-Al facility at 4 Pa for a Titan simulated atmosphere. It does result in a fluctuation in the strengths of the CN(B-X) $\Delta v=0$ and NH(A-X) spectral bands, and must be taken into account when comparisons are made against the data.



(a) x2s1544: 600 lines/mm, $U_s = 9.80$ km/s, NRST-Al



(b) Specair simulation, $U_s = 9.04$ km/s

Figure 6.17 : A comparison of spectral power density and its cumulative integration for shots (a) x2s1544 at the axial location of the peak shown in Figure 6.14 and (b) Specair. The freestream pressure was 4 Pa.

6.4 A note on shot-to-shot consistency

In order for these experimental data to be useful as a benchmark for comparison, it is necessary to show that the NRST-Al facility produced reproducible and consistent results. In Figures 6.18, 6.19, and 6.20, the shot-to-shot variation of the spectral data is shown. The experimental data used are from the spectral measurements taken with

the 600 lines/mm grating, centred on a wavelength 380 nm. The power density at the nonequilibrium peak behind the shock is integrated over all wavelengths captured in the spectral data (approximately 310 to 450 nm) and plotted by shot number.

In Figure 6.18, the shot-to-shot variation is shown for the 13 Pa condition. The horizontal line represents the data captured by (Brandis 2009a) in the older NRST facility. This data shows good agreement with the NRST-Al data. Some further variation does occur for x2s1469 and x2s1470. This can be explained as an effect of the shock speed. For x2s1469 and x2s1494, the measured shock speed was lower than the average experimental value (5.84 and 6.17 km/s, respectively). In both cases, the measured peak power density integrated over the captured range (approximately 310 to 450 nm) was visibly lower than the value measured in faster shots. Shot x2s1470 had a significantly faster shock speed (6.87 km/s), resulting in a larger than expected peak integrated power density measurement. The most likely cause of the remaining shot-to-shot variation is the uncertainty in the final contamination of the test gas due to air leakage in the dump tank prior to the experiment.

In Figure 6.19, there is a clear difference between the measured peak values for the first four experiments and the last four experiments. The shock speeds for all experiments in both groups vary across a similar range, indicating that this change is not due to fluctuations in the shock speed. The same test gas source was used for all of these experiments, and no significant changes in experimental procedure occurred between shots x2s1517 and x2s1518. The most likely source of the discrepancy is an unmarked, increased leak of air into the facility. A comparison with shot x2s545, taken by Brandis (2009a) for a 9 Pa freestream condition, indicates that experimental data recorded for this condition after shot x2s1517 are the most reliable sources.

As for the 13 Pa condition, the shot-to-shot variation of the 4 Pa condition remains, for the most part, within the error bands estimated for the measured spectral data. This is shown in Figure 6.20.

6.5 Further discussion and summary of results

The primary aim of this thesis was to demonstrate that it is possible to produce calibrated measurements of radiative heat transfer in the nonequilibrium region of a shock wave at pressures lower than 13 Pa. This was to be achieved through:

1. the modification of the X2 facility to allow experimentation at low pressures in nonreflected shock tube mode;

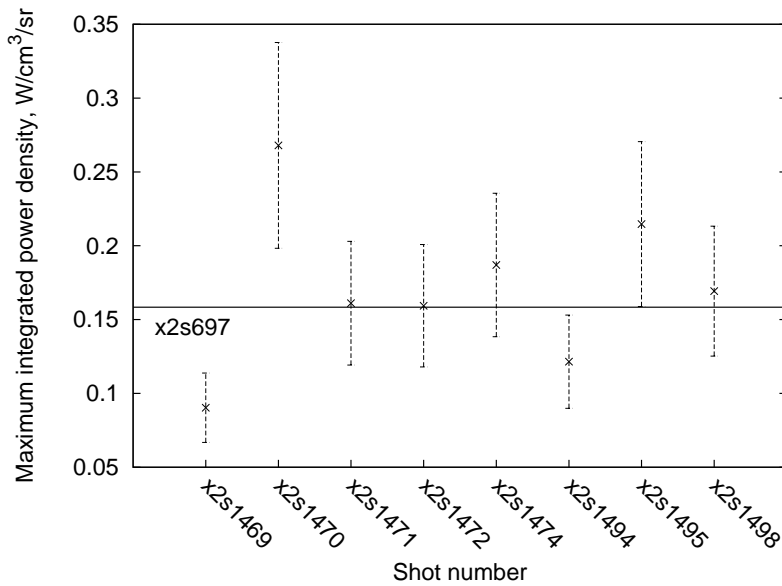


Figure 6.18 : Shot-to-shot variation of the integrated power density for the 13 Pa condition. This data was taken for experiments captured with the 600 lines/mm grating, centred on a wavelength 380 nm. Power density is integrated over the full range (approximately 310-450 nm) at the nonequilibrium peak. The horizontal line indicates the data at the nonequilibrium peak captured and integrated over the same wavelength range by Brandis (2009a).

2. the investigation and analysis of the flow conditions produced;
3. the performance of radiative heat transfer measurements at low pressures using emission spectroscopy;
4. the identification and minimisation of any contamination effects from the tube material, driver gas, and diaphragms and
5. the interpretation of the spectral data with reference to the latest radiation results.

The first two points were discussed in Chapter 5. In this chapter, spectral results at pressures as low as 4 Pa in a simulated Titan atmosphere were presented and comparisons of the spectral data made to both experimental work completed by Brandis (2009a) and computational simulations using the electronically specific collisional-radiative model **Mutation** (Brandis 2011) and **Specair**, achieving the goals of the project - in particular, point three.

For the 13 Pa conditions, there was very good agreement between the experimental results for the axial power density profile in the NRST-Al facility and the unmodified facility. The comparison of the nonequilibrium peak behind the shock front was also very

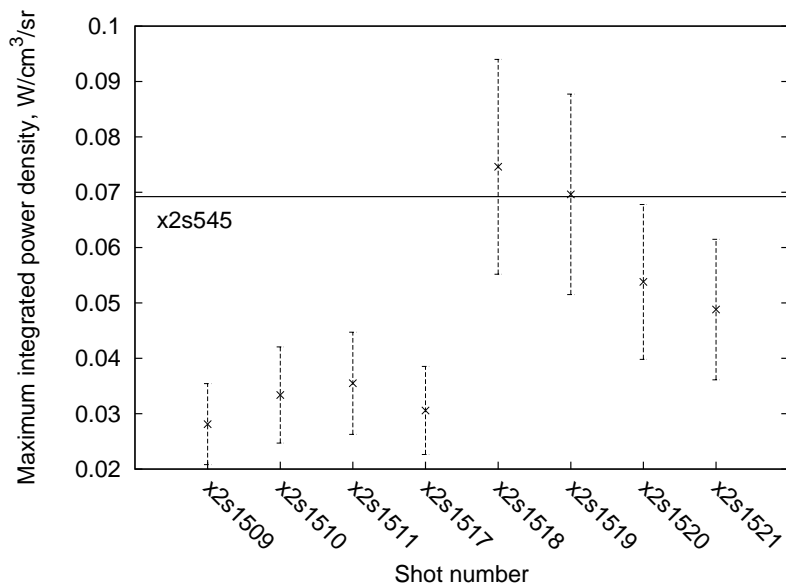


Figure 6.19 : Shot-to-shot variation of the integrated power density for the 8 Pa condition. This data was taken for experiments captured with the 600 lines/mm grating, centred on a wavelength 380 nm. Power density is integrated over the full range (approximately 310-450 nm) at the nonequilibrium peak. The horizontal line indicates the data at the nonequilibrium peak captured and integrated over the same wavelength range by Brandis (2009a). The data captured by Brandis was taken for a freestream pressure of 9 Pa.

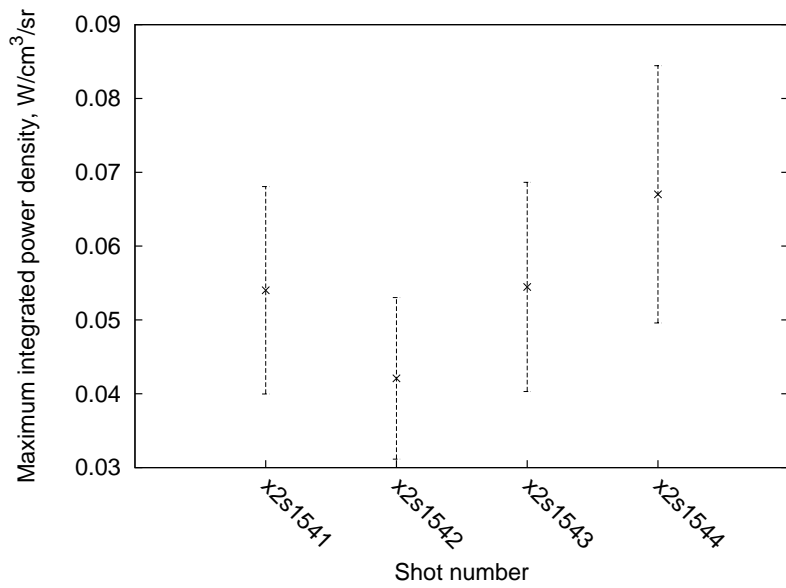


Figure 6.20 : Shot-to-shot variation of the integrated power density for the 4 Pa condition. This data was taken for experiments captured with the 600 lines/mm grating, centred on a wavelength 380 nm. Power density is integrated over the full range (approximately 310-450 nm) at the nonequilibrium peak.

consistent between the NRST-Al and **Mutation** results. However, there was a discrepancy in the comparison of the decay rate of the nonequilibrium peak with the computational model. As discussed in Chapter 2, this is possibly due to the electronically specific nature of the collisional-radiative model and might be improved upon by using a vibrationally specific modification such as used in the ViSpeN code (Brandis 2009a). The identification of this anomaly is an indication of the usefulness of a facility in which such measurements as these are possible.

For the 8 Pa conditions, the comparison of the axial profile of power density between facilities showed that the NRST-Al achieved very good agreement with the previous facility, despite the comparison being made with a 9 Pa condition due to the lack of experimental data at 8 Pa in the unmodified facility. Importantly, there was a significant difference between the experimental and **Mutation** calculations, both in the level of the nonequilibrium peak and in the decay rate.

No comparison of the axial profile of power density was possible for the 4 Pa condition between facilities or with computational results. In the case of the experimental data, this was to be expected, as the aim of these experiments was to extend the capture of experimental data beyond the capabilities of previous facilities. Reliable numerical simulations are not yet available for these flow conditions, however this experimental data provides a benchmark for the future validation of such simulations.

No noise removal was performed for these results, however, the observed signal-to-noise ratio improved markedly in the modified facility in comparison with previous experiments (Brandis 2009a). This is due to a combination of using improved optical components and the larger length of test gas in the transverse direction. Observation of the axial profile of the power density may also be used to indicate the arrival of the termination of the test gas. From the results presented, it can be seen that, as well as producing usable flow at lower pressure, a longer length of test gas was available in the NRST-Al facility at similar pressures.

Spectral power density plots at the nonequilibrium peak behind the shock indicated that the species present remained consistent for all three conditions (13, 8, and 4 Pa). The observable CN violet vibronic spectral bands ($\Delta v = -1, 0, +1$) proved to be the dominant radiator, as expected from previous experiments and calculations discussed in Chapter 1, although there was also a significant amount of NH present, producing a strong peak at approximately 335 nm.

The fourth aim of this thesis was to identify and minimise any contamination effects from the tube material, driver gas, and diaphragms. Investigation of the spectral results found that there were no peaks corresponding to aluminium, iron, or calcium associated

with the mylar visible above the level of the noise, indicating that the tube material and diaphragms had a negligible effect on the data recorded at the location of the nonequilibrium peak. In the plots of axial power density profiles, the test length available was found to be increased in the NRST-Al over the unmodified X2 facility. This resulted in negligible contamination effects from the presence of the driver gas for the results in the region of the nonequilibrium peak.

The spectral comparison between the experimental results in the modified facility and the older facility showed very good agreement, however there was an observable variation in the strengths of the CN(B-X) $\Delta v=0$ and NH(A-X) spectral bands. With such low test gas pressures, the most likely cause of this discrepancy was contamination of the test gas during the experimental setup. Unfortunately, while this effect was minimised as much as possible during experiments by flushing the test gas through the facility, minimising leaks, and ensuring the minimum delay possible between filling the test gas and conducting the experiment, attempting to conduct spectral investigations at such low test pressures meant that variations were unavoidable. A number of experiments were conducted with each grating at all test conditions in order to provide as much information as possible regarding this variation.

Further investigation into the shot-to-shot variation of the power density measurements were completed for the three conditions. It was found that there was good repeatability between shots, although variations in shock speed did result in significant deviations from the standard values. A selection of early experiments at the 8 Pa condition did demonstrate some deviation from the expected results, and the most likely cause of this discrepancy is a contamination of the test gas prior to the experiment. Indeed, small shot-to-shot variations of the shock speed and the amount of air leaking into the test section prior to the experiment are expected to be the cause of the remaining, smaller deviations in results. In general, the NRST-Al facility produced reasonably consistent results at each condition.

Computational comparisons of the spectral radiant power density were made using the Specair program. The computational spectra included N₂ B-A (First Positive), CN B-X (Violet), N₂ C-B (Second Positive), N₂⁺ B-X (First Negative), and NH (A-X) vibronic spectral bands over the wavelength range 310-450 nm. The atomic lines of N and C were also included. For the 13 and 8 Pa conditions, the computational spectra provided a very close agreement with the experimental data in terms of the absolute intensity. However, for the 4 Pa condition, the computational levels were approximately half the intensity of the experimental. Consistent differences also occurred in the estimation of the NH(A-X) and N₂⁺ (B-X) $\Delta v=+1$ vibronic spectral bands. This is most likely due to the CEA2 code calculating the equilibrium species concentrations, which have decayed from the

concentrations expected near the nonequilibrium peak where the experimental data is extracted.

Summary and Conclusions

In the Introduction, it was stated that the primary aim of this thesis was to demonstrate that it is possible to produce calibrated measurements of radiative heat transfer in the nonequilibrium region of a shock layer at pressures lower than 13 Pa. Specifically, this was to be achieved through:

- the modification of the X2 facility to allow experimentation at low pressures in nonreflected shock tube mode;
- the investigation and analysis of the flow conditions produced;
- the performance of radiative heat transfer measurements at low pressures using emission spectroscopy;
- the identification and minimisation of any contamination effects from the tube material, driver gas, and diaphragms and
- the interpretation of the spectral data with reference to the latest radiation models.

In Chapter 1, background information on hypersonic test facilities and a summary of experimental and computational investigations for simulated Titan atmospheres available in published literature were presented. In particular, this chapter sought to justify the interest in gathering radiative heat transfer data in a shock tunnel facility. A number of major points were highlighted by this review:

- There is a significant variation in the calculated values of radiation heat flux in Titan atmospheres between various computational methods, and the peak radiative

heating on the surface of an entry vehicle may even be significantly larger than the convective heating rate for some trajectory points. This highlights the need for experimental data measuring the radiative heating to provide reference points for the validation of the computational codes.

- Previous experimental data has been limited to pressures above 9 Pa, and it is necessary to extend the experimental capabilities to higher altitude conditions in order to provide validation data for computational modelling.
- At high altitudes, nonequilibrium effects are significant and must be considered in the computational modelling of the aerothermodynamics. With such strong influences from nonequilibrium processes, it is necessary to move into collisional-radiative modelling in order to accurately match the experimental radiation heat flux results.

Having identified the necessity of using collisional-radiative models to accurately model the radiative heat transfer in the low pressure, high speed entry flows of interest here, a further review of these collisional-radiative models was conducted in Chapter 2. These methods are quite computationally expensive, and the extension from electronically specific models to vibrationally specific models can add a significant computational effort. For simulated Titan atmospheres, a compromise involving the addition of specific vibrational energy levels to an electronically specific model (ViSpeN) was found to provide a significant improvement in the comparison of computational and experimental results. There is, however, still a clear need for additional spectral measurements to provide computational validation, especially in the VUV region ($\leq 200\text{nm}$). Further investigations of the rotational population distributions of the important molecular species present in the spectra are also warranted.

Chapters 3 and 4 outlined the experimental and computational investigations undertaken as part of this thesis. The test conditions, facility modifications necessary to reach the desired test conditions, and experimental diagnostics were detailed. A description was provided of the various computational codes used to provide a comparison with the experimental data and the computational domains involved in each calculation. A summary of the required modifications for successfully generating shock tube conditions at the desired low freestream pressures is as follows:

- The expansion tube facility was modified to run in nonreflected shock tube mode.
- The shock tube bore diameter was increased.
- A secondary driver section was added.

Finally, the results of the various experimental and computational experiments were presented in Chapters 5 and 6. These results included shock speed analyses, measurements of the available test gas, investigations into the flow quality in the modified facility, and the emission spectroscopy measurements.

The mean experimental shock speed for the 13, 8, and 4 Pa Titan condition was found to be 6.41, 6.19, and 9.04 km/s respectively. For the 13 and 8 Pa conditions, it was found that there was a negligible attenuation of the shock speed in the shock tube. The attenuation of the shock speed for the 4 Pa condition remained small, although not negligible. The effect of the step area change in the shock tube was investigated, due to the perturbations formed in the flow at this location. The perturbations were of two different characteristic types: the unsteady waves, which established the flow after diaphragm rupture, and a quasi-steady wave pattern which formed for a limited time in the expanding driver gas. Experimental indications were that the shock marched ahead of the disturbances, creating a core of uniform, high quality flow at the tube exit. Additionally, it was found that the shock exiting the aluminium tube remained planar near the centreline, where the spectral images were focussed. Coupled with the high speed video footage and EILMER3 simulations, this consistency in shock speed, the planar shock at the exit of the shock tube, and the negligible effects of the perturbations on the test gas flow indicated that the NRST-Al facility was capable of producing high quality test flow.

The Pitot pressure traces recorded in the modified facility provided information regarding the test time and core diameter of the usable test gas produced. However, as the response time of the Pitot pressure signals were of a similar order to the total available test time, it was difficult to use the pressure traces to provide an estimate of the available test gas. Therefore, numerical calculations with L1d3 and analytical results were used to provide additional information for comparison. For the three conditions simulating a Titan entry at 13, 8, and 4 Pa, the usable test gas length was found to be 173, 124, and 118 mm respectively, consistently larger than the area imaged by the spectrometer. The test gas was found to have a core diameter of 85 mm, 80 mm, and 50 mm for the 13, 8, and 4 Pa conditions respectively, just under half of the diameter of the shock tube. Static pressure tracs also indicated steady pressure levels during the test time.

Although it was not possible to test at freestream pressures as low as 1 Pa in a Titan mixture due to residual dump tank leakage and air contamination of the test gas, results were gathered for the NRST-Al facility in a 1 Pa air condition. Further work is required on this condition before it can be considered usable as there was no obvious indication of the arrival of the driver gas behind the test gas in the Pitot pressure traces.

Comparisons of the axial profile of radiant power density between the experimental results in the NRST-Al facility, the experimental data from the unmodified facility,

and with the computational results obtained with the electronically specific collisional-radiative model Mutation showed very good agreement for the 13 Pa condition. However, the Mutation calculations were unable to fully match the decay rate of the nonequilibrium peak behind the shock tube at all conditions. As discussed in Chapter 2, this is possibly due to the electronically specific nature of the collisional-radiative model, and could be improved upon by using a vibrationally specific modification such as used in the ViSpeN code (Brandis 2009a). The computational model was also unable to completely match the level of the nonequilibrium peak for the 8 Pa condition and could not generate a solution for the 4 Pa condition. The observed signal-to-noise ratio improved markedly in the modified facility in comparison with previous experiments due to a combination of using improved optical components and the larger length of test gas in the transverse direction.

Spectral power density plots at the nonequilibrium peak behind the shock indicated that the CN violet spectral bands ($\Delta v = -1, 0, +1$) were the dominant radiator. Investigation of the spectral results also found that there were no peaks corresponding to aluminium, iron, or mylar visible above the level of the noise, indicating that the tube material and diaphragms had a negligible effect on the data recorded at the location of the nonequilibrium peak. In the plots of axial power density profiles, the test length available was found to be increased in the NRST-Al over the unmodified X2 facility. This resulted in negligible contamination effects from the presence of the driver gas for the results in the region of the nonequilibrium peak.

The spectral comparison between the experimental results in the modified facility and the older facility showed very good agreement, however there was an observable variation in the strengths of the CN(B-X) $\Delta v = 0$ and NH(A-X) spectral bands. With such low test gas pressures, the most likely cause of this discrepancy was contamination of the test gas with air during the experimental setup. Unfortunately, while this effect was reduced as much as possible during experiments by flushing the test gas through the facility, minimising leaks, and ensuring the minimum delay possible between filling the test gas and conducting the experiment, attempting to conduct spectral investigations at such low test pressures meant that variations were unavoidable. A number of experiments were conducted with each grating at all test conditions in order to provide as much information as possible regarding this variation.

For the 13 and 8 Pa conditions, computational spectra produced with the **Specair** program provided a very close agreement with the experimental data in terms of the absolute intensity. However, for the 4 Pa condition, the computational levels were approximately half the intensity of the experimental. Consistent differences also occurred in the estimation of the NH(A-X) and N₂⁺ (B-X) $\Delta v = +1$ vibronic spectral bands. This is most likely

due to the CEA2 code (used to provide input to the **Specair** simulations) calculating the equilibrium species concentrations, which have decayed from the concentrations expected near the nonequilibrium peak where the experimental data is extracted.

Future Recommendations

A freestream pressure of 4 Pa was the lowest pressure condition measurable in the modified X2 facility. This was primarily due to leaks in the dump tank, the result of which was a minimum evacuation pressure of approximately 0.8 Pa and very fast air contamination of the test gas. As an initial step in the improvement of results in the X2 facility, it would be of great benefit to improve the accuracy of operational conditions by reducing leaks in the gas systems and to improve the quality of the vacuum achieved in the dump tank section.

The X3 facility at the University of Queensland, having a larger bore diameter than the X2 facility could be modified in a similar manner, potentially to a bore of as much as 500 mm. Depending on the vacuum achieved and the diameter of the tube, this would allow for an extension of the measurements presented in this thesis to much lower freestream pressure conditions and would provide a valuable extension of the low pressure conditions investigated in this work.

The extension of this work to include other simulated atmospheres, such as the gas giants, Venus, Mars, or an Earth entry would also be of great value in providing further benchmark data.

In the comparison of the nonequilibrium peak level of the power density between the experimental facilities and the Mutation simulations, there was an interesting trend. There was a good agreement for the 13 Pa conditions, but a large discrepancy for the 8 Pa condition comparison, and solution failed to resolve for the 4 Pa condition. The most likely explanation for this trend is that the low freestream pressure conditions require the extension of the collisional-radiative method to a rarefied flowfield solver. An adaptation of the collisional-radiative method to a rarefied flowfield solver would make an interesting future project.

As the spectral data presented in this work was collected and analysed, it was observed that the spectrograph and ICCD camera setup exhibited some unusual trends. One such example of this behaviour is the nonlinear relationship between the measured signal and the exposure time at the very small exposure times required for these experiments. Further investigation into these effects is necessary in order to fully account for this variation in response.

An interesting follow-on to this work is the proposal at NASA Ames to install a 24 inch diameter section on the EAST facility for radiation studies at even lower densities.

In summary, this thesis was successful in achieving its primary aim, acquiring emission spectroscopy data for three simulated Titan entry conditions at 13, 8, and 4 Pa freestream pressure and comparing these results to published experimental data and radiation models. With suitable calibration, absolute measurements of spectral radiances were obtained, indicating the value of the facility in providing high quality benchmark data for further understanding radiating flows.

References

- Adamovich, I., S. Macheret, J. William Rich, and C. Treanor (1998). Vibrational energy transfer rates using a forced harmonic oscillator model. *Journal of Thermophysics and Heat Transfer* 12(1), 57–65.
- Allen, C. (1962). *Astrophysical quantities*. Athlone Press.
- Anderson, J. D. (1989). *Hypersonic and High Temperature Gas Dynamics*. New York: McGraw-Hill. Reprinted by the American Institute of Aeronautics and Astronautics, Reston, VA, 2000.
- Arnold, J. and R. Nicholls (1972). A shock tube determination of the electronic transition moment of the CN red band system. *Journal of Quantitative Spectroscopy and Radiative Transfer* 12(10), 1435–1452.
- Bacri, J. and A. Gomes (1978). Influence of atom-atom collisions on thermal equilibrium in argon arc discharges at atmospheric pressure. *Journal of Physics D: Applied Physics* 11(16), 2185–2198.
- Bacri, J., M. Lagreca, and A. Medani (1982). Composition of a quasi-homogeneous stationary nitrogen plasma at atmospheric pressure. *Physica C* 113, 403.
- Bacri, J. and A. Medani (1982). Electron diatomic molecule weighted total cross section calculation: III. main inelastic processes for N₂ and N₂⁺. *Physica C* 112, 101–118.
- Bailey, R. W., J. L. Hall, and T. R. Spilker (2003). Titan aerocapture mission and space-craft design overview. In *39th AIAA/ASME/SAE/ASEE Joint Propulsion Conference and Exhibit*, Huntsville, Alabama. AIAA Paper 2003-4800.
- Baillion, M., J. Pallegoix, and J. Soler (1997). Huygens probe aerothermodynamics. In *32nd Thermophysics Conference*, Atlanta, GA. AIAA Paper 97-2476.

- Balakrishnan, A., C. Park, and M. Green (1986). Radiative viscous shock layer analysis of Fire, Apollo and PSET flight data. *Progress in Astronautics and Aeronautics* 103, 514–540.
- Bartlett, E., M. Abbott, W. Nicolet, and C. Moyer (1970). Improved heat-shield design procedures for manned entry systems, part 2: Application to Apollo. Technical Report Report 70-15, Aerotherm Corporation.
- Baulch, D., C. Cobos, R. Cox, C. Esser, P. Frank, T. Just, J. Kerr, M. Pilling, J. Troe, R. Walker, and J. Warnatz (1992). Evaluated kinetic data for combustion modelling. *Journal of Physical Chemistry Reference Data* 21(3), 411–429.
- Baulch, D., C. Cobos, R. Cox, P. Frank, G. Hayman, T. Just, J. Kerr, T. Murrels, M. Pilling, J. Troe, R. Walker, and J. Warnatz (1994). Evaluated kinetic data for combustion modelling, supplement I. *Journal of Physical Chemistry Reference Data* 26(6), 847–1033.
- Bauschlicher, C. and S. Langhoff (1988). Theoretical study of the dissociation energy and the red and violet band systems of CN. *Astrophysical Journal, Part 1* 332, 531–538.
- Bernstein, H. (1953). A double-diaphragm shock tube to produce transient high Mach number flows. *Journal of the Aeronautical Sciences* 20, 790.
- Bhatia, A. and S. Kastner (1995). The neutral oxygen spectrum 1: Collisionally excited level populations and line intensities under optically thin conditions. *The Astrophysical Journal. Supplement Series* 96, 325–341.
- Bose, D., E. McCorkle, D. Bogdanoff, and G. Allen (2009). Comparisons of air radiation model with shock tube measurements. In *47th AIAA Aerospace Sciences Meeting*, Orlando, Florida.
- Bose, D., M. J. Wright, and D. W. Bogdanoff (2005). Modeling and experimental validation of CN radiation behind a strong shock wave. In *43rd AIAA Aerospace Sciences Meeting and Exhibit*, Reno, Nevada. AIAA Paper 2005-0768.
- Bose, D., M. J. Wright, and D. W. Bogdanoff (2006). Modeling and experimental validation of CN radiation behind a strong shock wave. *Journal of Thermophysics and Heat Transfer* 20(2), 220–230.
- Boyd, I., K. Trumble, and M. Wright (2007). Nonequilibrium particle and continuum analyses of Stardust entry for near continuum conditions. In *39th AIAA Thermophysics Conference*, Miami, Florida. AIAA Paper 2007-4543.
- Boyd, I., J. Zhongy, D. Levin, and P. Jenniskens (2008). Flow and radiation analyses for Stardust entry at high altitude. In *46th AIAA Aerospace Sciences Meeting and*

- Exhibit*, Reno, Nevada.
- Brandis, A. (2009a). *Experimental study and modelling of non-equilibrium radiation during Titan and Martian entry*. Ph. D. thesis, School of Mechanical and Mining Engineering, The University of Queensland, Australia.
- Brandis, A. (2009b). Multi-quantum vibrational exchange simulation code. Personal communication.
- Brandis, A. (2011). Mutation simultation results. Personal communication.
- Bultel, A., B. Cheron, A. Bourdon, O. Motapon, and I. Schneider (2006). Collisional-radiative model in air for Earth re-entry problems. *Physics of Plasmas* 13, 043502–043502.
- Caillault, L., J. Andreasson, J. Risberg, and C. Laux (2006). Modeling the spectral radiation of a methane/nitrogen plasma - test case 4. In *2nd International Workshop on Radiation of High Temperature gases in Atmospheric Entry*.
- Caillault, L., L. Walpot, T. Magin, A. Bourdon, and C. Laux (2006). Radiative heating predictions for Huygens entry. *Journal of Geophysical Research* 111.
- Candler, G., D. Levin, R. Collins, P. Erdman, E. Zipf, and C. Howlett (1993). Theory of plume radiance from the Bow Shock Ultraviolet 2 Rocket Flight. *Journal of Thermophysics and Heat Transfer* 7(4), 709–716.
- Capitelli, M., G. Colonna, and I. Armenise (2002). State to state electron and vibrational kinetics in one dimensional nozzle and boundary layer flows. In D. F. et al. (Ed.), *Physico-chemical models for high enthalpy and plasma flows*. Von Karman Institute for Fluid Dynamics.
- Capitelli, M., G. Colonna, and F. Esposito (2004). On the coupling of vibrational relaxation with the dissociation-recombination kinetics: From dynamics to aerospace applications. *Journal of Physical Chemistry* 108, 8930–8934.
- Capitelli, M., C. Ferreira, B. Gordiets, and A. Osipov (2000). *Plasma kinetics in atmospheric gases*. Springer, New York.
- Capra, B. R. (2007). *Aerothermodynamic simulation of subscale models of the FIRE II and Titan Explorer vehicles in expansion tubes*. Ph. D. thesis, The University of Queensland, School of Engineering, St Lucia, Australia.
- Capra, B. R. and R. G. Morgan (2006). Radiative and total heat transfer measurements to a Titan Explorer model. In *14th AIAA/AHI Space Planes and Hypersonic Systems and Technologies Conference*, Canberra, Australia. AIAA Paper 2006-7934.

- Cauchon, D., C. McKee, and E. Cornette (1967). Spectral measurements of gas-cap radiation during project Fire flight experiments at reentry velocities near 11.4 km/s. Technical Report TM X-1389, NASA.
- Chauveau, S., J. Kelley, C. Laux, and C. Kruger (2003). Vibrationally specific modeling of nonequilibrium effects in air plasmas. In *41st Aerospace Sciences Meeting and Exhibit*, Reno, Nevada.
- Chauveau, S., C. Laux, J. Kelley, and C. Kruger (2002). Vibrationally specific collisional-radiative model for nonequilibrium air plasmas. In *33rd Plasmadynamics and Lasers Conference*, Maui, Hawaii.
- Cherniy, C. and S. Losev (1999). Development of thermal protection systems for interplanetary flight. Technical Report ISTC Report 036-96, Research Institute of Mechanics, Moscow.
- Curry, D. and E. Stephens (1970). Apollo ablator thermal performance at superorbital entry velocities. Technical Report TN D-5969, NASA.
- Davidson, D. and R. Hanson (1990). High temperature reaction rate coefficients derived from N-atom ARAS measurements and excimer photolysis of NO. *International Journal of Chemical Kinetics* 22, 843–861.
- Dean, A., D. Davidson, and R. Hanson (1991). A shock tube study of reactions of C atoms with H₂ and O₂ using excimer photolysis of C₃O₂ and C atom atomic resonance absorption spectroscopy. *Journal of Physical Chemistry* 95, 183–191.
- Dean, A. and R. Hanson (1992). CH and C-atom time histories in dilute hydrocarbon pyrolysis: Measurements and kinetic calculations. *International Journal of Chemical Kinetics* 24, 517–532.
- Dean, A., R. Hanson, and C. Bowman (1990). High temperature shock tube study of reactions of CH and C-atoms with N₂. In *23rd International Symposium on Combustion*, pp. 259–265.
- Dean, A., D. Kontinos, and M. Stackpoole (2008). Post-flight analysis of the Stardust sample return capsule Earth entry. In *46th Aerospace Sciences Meeting and Exhibit*, Reno, Nevada.
- Drawin, H. (1967). *Collision and transport cross sections*. Plasma Diagnostics. Euratom.
- Duff, R. E. (1959). Shock-tube performance at low initial pressure. *Physics of Fluids* 2(2), 207.
- Eichmann, T. (2009). SPEread code for extracting spectra into MATLAB. Personal communication.

- Erdman, P., E. Zipf, P. Espy, C. Howlett, D. Levin, and G. Candler (1993). In-situ measurements of UV and VUV radiation from a rocket plume and re-entry bow shock. *Journal of Thermophysics and Heat Transfer* 7(4), 704–708.
- Erdman, P., E. Zipf, P. Espy, C. Howlett, D. Levin, R. Collins, and G. Candler (1994). Measurements of ultraviolet radiation from a 5km/s bow shock. *Journal of Thermophysics and Heat Transfer* 8(3), 441–446.
- Erdman, P., E. Zipf, P. Espy, C. Howlett, D. Levin, R. Loda, and G. Candler (1993). Flight measurements of low velocity bow shock ultraviolet radiation. *Journal of Thermophysics and Heat Transfer* 7(1), 37–41.
- Esposito, F. and M. Capitelli (2005). QCT calculations for the process $N_2(v) + N \rightarrow N_2(v') + N$ in the whole vibrational range. *Chemical Physics Letters* 418(4-6), 581–585.
- Fertig, M., M. Winter, G. Herdrich, and H.-P. Roser (2008). Modelling of high speed earth entry. Technical Report IRS-08-P1, The European Space Agency.
- Fresnet, F., G. Baravian, L. Magne, S. Pasquier, C. Postel, V. Puech, and A. Rousseau (2002). Influence of water on NO removal by pulsed discharge in $N_2/H_2O/NO$ mixtures. *Plasma Sources Science Technology* 11, 153–160.
- Frost, R., P. Awakowicz, H. Summers, and N. Badnell (1998). Calculated cross sections and measured rate coefficients for electron-impact excitation of neutral and singly ionized nitrogen. *Journal of Applied Physics* 84(6), 2989–3003.
- Fujita, K. and T. Abe (1997). SPRADIAN, structured package for radiation analysis: Theory and application. Technical report, ISAS Report.
- Fujita, K. and T. Abe (2003). Development of a radiation analysis code for hypervelocity reentry applications. Technical report, The Institute of Space and Astronautical Science.
- Gessman, R., C. Laux, and C. Kruger (1997). Experimental study of kinetic mechanisms of recombining atmospheric pressure air plasmas. In *28th AIAA Plasmadynamics and Lasers Conference*, Atlanta, GA.
- Gökçen, T. (2004). Chemical kinetic model for simulations of atmospheric entry to Titan N_2-CH_4-Ar . In *AIAA Thermophysics Conference*, Portland, Oregon.
- Gomes, A. (1983). Criteria for partial LTE in an argon thermal discharge at atmospheric pressure; validity of the spectroscopically measured electronic temperature. *Journal of Physics D: Applied Physics* 16(3), 357–378.
- Gomes, A., A. Essoltani, and J. Bacri (1990). Collisional-radiative modelling of a non-equilibrium stationary oxygen plasma at atmospheric pressure, $3000 < j_e < 18000$.

- Journal of Quantitative Spectroscopy and Radiative Transfer* 43, 471–498.
- Gordillo-Vazquez, F. and J. Kunc (1995). Diagnostics of plasmas with substantial concentrations of atomic oxygen. *Physical Review E* 51(6), 6010–6015.
- Gordon, S. and B. McBride (1994). Computer program for calculation of complex chemical equilibrium compositions and applications: I. Analysis. Technical Report Reference Publication 1311, NASA.
- Grinstead, J., M. Wilder, J. Olejniczak, D. Bogdanoff, G. Allen, and K. Dang (2008). Shock heated air radiation measurements at lunar return conditions. In *46th AIAA Aerospace Sciences Meeting and Exhibit*, Reno, Nevada.
- Gryzinski, M. (1959). Classical theory of electronic and ionic inelastic collisions. *Physical Review* 115(2), 374–383.
- Guerra, V. and J. Loureiro (1997). Electron and heavy particle kinetics in a low-pressure nitrogen glow discharge. *Plasma Sources Science Technology* 6, 361–372.
- Hall, J., A. Eschenroeder, and P. Marrone (1962). Blunt-nose inviscid airflows with coupled nonequilibrium processes. *Journal of the Aerospace Sciences* 29(9), 1038–1051.
- Hamma, L. and H. Sacilotto (1992). Validation theorique du code NEQAIR dans le cadre du programme Huygens. Technical report, Aerospatiale.
- Henshall, B. (1956). The use of multiple diaphragms in shock tubes. Technical report, Aeronautical Research Council (18062).
- Hess, S. (2009). A low enthalpy test condition for the T4 shock tunnel. Diploma thesis, The University of Stuttgart.
- Hornung, H. (1988). 28th lanchester memorial lecture - experimental real-gas hyperonics. *Aeronautical Journal* 92(920), 379–389.
- Hornung, H. and J. Belanger (1990, June). Role and techniques of ground testing for simulation of flows up to orbital speed. In *16th AIAA Aerodynamic Ground Testing Conference*, Seattle, WA.
- Huber, K. and G. Herzberg (1979). *Molecular spectra and molecular structure, Vol IV, Constants of Diatomic Molecules*. Van Nostrand Reinhold.
- Jacobs, C. and R. Morgan (2009). Radiation measurements in rarefied titan atmospheres. In *47th AIAA Aerospace Sciences Meeting*, Orlando, FL.
- Jacobs, C., R. Morgan, T. Eichmann, and T. McIntyre (2011). Radiative heat transfer measurements in a nonreflected shock tube at low pressures. In *28th International Symposium on Shock Waves*, Manchester, UK.

- Jacobs, P., R. Gollan, A. Denman, B. O'Flaherty, D. Potter, P. Petrie-Repar, and I. Johnston (2010). Eilmer's theory book: Basic models for gas dynamics and thermochemistry. Technical Report 2010/09, Department of Mechanical Engineering, The University of Queensland.
- Jacobs, P. A. (1998a). MB_CNS: A computer program for the simulation of transient, compressible flows; 1998 update. Technical Report 7/98, Department of Mechanical Engineering, The University of Queensland.
- Jacobs, P. A. (1998b, November). Shock tube modelling with L1d. Technical Report 13/98, Department of Mechanical Engineering, The University of Queensland.
- Jacobs, P. A. (2011). A microcontroller-based delay generator for predicting shock arrival in the x2 expansion tube. Technical Report 2011/05, School of Mechanical Engineering, The University of Queensland.
- Jenniskens, P. (2008). Observations of the STARDUST sample return capsule entry with a slit-less Echelle Spectrograph. In *46th Aerospace Sciences Meeting and Exhibit*, Reno, Nevada.
- Jenniskens, P., D. Kontinos, D. Jordan, M. Wright, J. Olejniczak, G. Raiche, P. Wercincki, P. Desai, M. Taylro, H. Stenbaek-Nielsen, M. McHarg, S. Abe, T. Rairden, J. Albers, M. Winter, F. Harms, J. Wolf, D. ReVelle, P. Gural, R. Dantowitz, F. Rietmeijer, D. Hladiuk, and A. Hildebrand (2006). Preparing for the meteoric return of Stardust. In *Dust in Planetary Systems*, Kaua'i, Hawai'i.
- Johnston, C. (2006). *Nonequilibrium shock-layer radiative heating for Earth and Titan entry*. Ph. D. thesis, Virginia Polytechnic Institute and State University.
- Johnston, C., B. Hollis, and K. Sutton (2006). Radiative heating methodology for the Huygens probe. In *9th AIAA/ASME Joint Thermophysics and Heat Transfer Conference*, San Francisco, California.
- Johnston, C., B. Hollis, and K. Sutton (2008a). Non-Boltzmann modeling for air shock-layer radiation at lunar-return conditions. *Journal of Spacecraft and Rockets* 45(5), 879–890.
- Johnston, C., B. Hollis, and K. Sutton (2008b). Nonequilibrium stagnation-line radiative heating for Fire II. *Journal of Spacecraft and Rockets* 45(6), 1185–1195.
- Johnston, C., B. Hollis, and K. Sutton (2008c). Spectrum modeling for air shock-layer radiation at lunar-return conditions. *Journal of Spacecraft and Rockets* 45(5), 865–878.
- Knowles, P., H. Werner, J. Hay, and D. Cartwright (1988). The $a^2\pi-x^2\epsilon^+$ red and $b^2\epsilon^+-x^2\epsilon^+$ violet systems of the CN radical: Accurate multireference configuration

- interaction calculations of the radiative transition probabilities. *Journal of Chemical Physics* 89(12), 7334–7343.
- Koreeda, J., Y. Ohama, and H. Honma (1998). Imaging spectroscopy of the nonequilibrium shock front radiation in air. *Shock Waves* 8(2), 71–78.
- Kosarev, I., P. Sagulenko, V. Khorunzhenko, M. Nudnova, M. Lino da Silva, and A. Chikhaoui. Experimental investigation of radiating flux behind strong shock waves in CH₄:N₂ mixtures. In *4th International Workshop on Radiation of High Temperature Gases in Atmospheric Entry*, Lausanne, Switzerland.
- Kossyi, I., A. Kostinsky, and V. Silakov (1992). Kinetic scheme of the non-equilibrium discharge in nitrogen-oxygen mixtures. *Plasma Sources Science Technology* 1, 207.
- Kruse, T. and P. Roth (1997). Kinetics of C₂ reactions during high-temperature pyrolysis of acetylene. *Journal of Physical Chemistry* 101, 2138–2146.
- Kunc, J. and W. Soon (1989). Collisional-radiative nonequilibrium in partially ionized atomic nitrogen. *Physical Review A* 40(10), 5822–5843.
- Laub, B. (2003). Thermal protection concepts and issues for aerocapture at Titan. In *39th AIAA/ASME/SAE/ASEE Joint Propulsion Conference and Exhibit*, Huntsville, Alabama. AIAA Paper 2003-4954.
- Laux, C. (1993). *Optical diagnostics and radiative emission of air plasmas*. Ph. D. thesis, Stanford University.
- Laux, C. (2002). Radiation and nonequilibrium collisional-radiative models. In *von Karman Institute Lecture Series*, Physico-Chemical Modeling of High Enthalpy and Plasma Flows.
- Laux, C. (2006). Analysis of the 2004 EAST shock tube data. Technical report, Summer Sabbatical, NASA Ames Research Centre.
- Laux, C., R. Gessman, C. Kruger, F. Roux, F. Michaud, and S. Davis (2001). Rotational temperature measurements in air and Nitrogen plasmas using the first negative system of N₂⁺. *Journal of Quantitative Spectroscopy and Radiative Transfer* 68, 473–482.
- Lebreton, J.-P., O. Witasse, C. Sollazzo, T. Blancquaert, P. Couzin, A.-M. Schipper, J. Jones, D. Matson, L. Gurvits, D. Atkinson, B. Kazeminejad, and M. Pérez-Ayúcar (2005). An overview of the descent and landing of the Huygens probe on Titan. *Nature* 438, 758–764.
- Lee, E., C. Park, and K. Chang (2007). Shock-tube determination of CN reformation rate and a CO-N₂ mixture. *Journal of Thermophysics and Heat Transfer* 21(1), 50–56.

- Levin, D., M. Braunstein, G. Candler, R. Collins, and G. Smith (1994). Examination of theory for Bow Shock Ultraviolet Rocket Experiments - II. *Journal of Thermophysics and Heat Transfer* 8(3), 453–459.
- Levin, D., G. Candler, R. Collins, P. Erdman, E. Zipf, P. Espy, and C. Howlett (1993). Comparison of theory with experiment for the Bow Shock Ultraviolet Rocket Experiment. *Journal of Thermophysics and Heat Transfer* 7(1), 30–36.
- Levin, D., G. Candler, R. Collins, P. Erdman, E. Zipf, and C. Howlett (1994). Examination of theory for Bow Shock Ultraviolet Rocket Experiments - I. *Journal of Thermophysics and Heat Transfer* 8(3), 447–452.
- Lorentz, R., O. Witasse, J.-P. Lebreton, T. Blancquaert, I. de Pater, F. Mazoue, H. Roe, M. Lemmon, B. Burratti, S. Holmes, and K. Noll (2006). Huygens entry emission observation campaign, results and lessons learned. *Journal of Geophysical Research* 111.
- Lotz, W. (1968). Electron-impact ionization cross sections and ionization rate coefficients for atoms and ions from hydrogen to calcium. *Zeitschrift fur Physik* 216(3), 241–247.
- Macheret, S. and I. Adamovich (2000). Semiclassical modeling of state-specific dissociation rates in diatomic gases. *Journal of Chemical Physics* 113(17), 7351–7361.
- Magin, T., L. Caillault, A. Bourdon, and C. Laux (2006). Nonequilibrium radiation modelling for Huygens entry. *Journal of Geophysical Research* 111.
- Matsuda, A., K. Fujita, S. Sato, and T. Abe (2002). Experimental study of nonequilibrium phenomena behind strong shock waves generated in super-orbital reentry flight. In *8th AIAA/ASME Joint Thermophysics and Heat Transfer Conference*, St Louis, Missouri. AIAA Paper 2002-3101.
- Matsuda, A., K. Fujita, S. Sato, and T. Abe (2004). Nonequilibrium phenomena behind strong shock waves generated in superorbital reentry flight. *Journal of Thermophysics and Heat Transfer* 18(3), 342–348.
- Matsuda, A., K. Fujita, S. Sato, and T. Abe (2005). Absorption spectroscopy for temperature measurement behind a shock wave at super-orbital velocity. *Journal of Thermophysics and Heat Transfer* 19(3), 294–299.
- Mazoué, F., J. Graciano, L. Tournebize, and L. Marraffa (2005). Updated analysis of the radiative heat flux during the entry of the Huygens probe in the Titan atmosphere. In *5th European Symposium on aerothermodynamics for Space Vehicles*, Cologne, Germany.

- Mazoué, F. and L. Marraffa (2005a). Flow-field/radiation coupling analysis for Huygens probe entry into Titan atmosphere. In *38th AIAA Thermophysics Conference*, Toronto, Ontario.
- Mazoué, F. and L. Marraffa (2005b). Rebuilding flowfield and radiation testcase for Titan atmosphere. In *International Workshop on Radiation of High Temperature Gases in Atmospheric Entry II*, Porquerolles, France.
- McBride, B. and S. Gordon (1996). Computer program for calculation of complex chemical equilibrium compositions and applications: II. Users manual and program description. Technical Report Reference Publication 1311, NASA.
- McGilvray, M., R. Morgan, D. Potter, D. Buttsworth, and T. McIntyre (2010). Shock tube measurements in the X2 facility of radiation from CEV re-entry conditions: Final report. Technical report, NASA Report EG-CAP-10-65.
- Mee, D. (1993). Uncertainty analysis of conditions in the test section of the T4 shock tunnel. Technical report, Department of Mechanical Engineering, The University of Queensland.
- Mirels, H. (1963). Test time in low-pressure shock tubes. *Physics of Fluids* 6(9), 1201–1214.
- Morgan, R., T. McIntyre, D. Buttsworth, P. Jacobs, D. Potter, A. Brandis, R. Gollan, C. Jacobs, B. Capra, M. McGilvray, and T. Eichmann (2008a). Shock and expansion tube facilities for the study of radiating flows. Technical Report Annexe 1 of contract report AMOD-ECP-TN-011 (Aerothermo-Chemistry Models for Re-Entry Applications), European Space Agency.
- Morgan, R., T. McIntyre, P. Jacobs, M. McGilvray, D. van Diem, P. Gnoffo, M. Pulsonnetti, and M. Wright (2006). Radiation measurements in non reflected shock tunnels. In *25th AIAA Aerodynamic Measurement Technology and Ground Testing Conference*. AIAA Paper 2006-2958.
- Morgan, R. G. (2001). *Handbook of Shock Waves*, Volume 1, Chapter 4.3: Free Piston Driven Expansion Tubes, pp. 603–622. Academic Press, San Diego.
- Morgan, R. G., T. J. McIntyre, D. R. Buttsworth, P. A. Jacobs, D. F. Potter, A. M. Brandis, R. J. Gollan, C. M. Jacobs, B. R. Capra, M. McGilvray, and T. Eichmann (2008b). Impulse facilities for the simulation of hypersonic radiating flows. In *38th Fluid Dynamics Conference and Exhibit*, Seattle, Washington.
- Morioka, T., N. Sakurai, K. Maeno, and H. Honma (2000). Observation of nonequilibrium radiation behind strong shock waves in low-density air. *Journal of Visualization* 3(1), 51–61.

- National Institute of Standards and Technology (2003). NIST chemical kinetics database (standard reference database 17, version 7.0).
- Nelson, H., C. Park, and E. Whiting (1991). Titan atmospheric composition by hypervelocity shock-layer analysis. *Journal of Thermophysics and Heat Transfer* 5(2), 157–165.
- Neumann, R. (1989). *Hypersonics Volume 1: Defining the Hypersonic Environment*, Chapter Defining the Aerothermodynamic Methodology. Birkhauser Boston. Eds. J.J Bertin and R. Glowinski and J. Periaux.
- of Physics, M. I. and Technology (2009a). Results of the experiments for N₂, N₂:O₂ mixtures. Technical Report Contract Report 2, European Space Agency. Validation of Aerothermochemistry Models for Re-entry Applications.
- of Physics, M. I. and Technology (2009b). Results of the experiments for N₂, N₂:O₂ mixtures. Technical Report Contract Report 3, European Space Agency. Validation of Aerothermochemistry Models for Re-entry Applications.
- Olejniczak, J., D. Prabhu, D. Bose, and M. Wright (2004). Aeroheating analysis for the afterbody of a Titan probe. In *42nd Aerospace Sciences Meeting and Exhibit*, Reno, NV. AIAA Paper 2004-0486.
- Olejniczak, J., M. Wright, D. Prabhu, N. Takashima, B. Hollis, E. V. Zoby, and K. Sutton (2003). An analysis of the radiative heating environment for aerocapture at Titan. In *39th AIAA/ASME/SAE/ASEE Joint Propulsion Conference and Exhibit*, Huntsville, Alabama. AIAA Paper 2003-4953.
- Panesi, M. (2006). *Physical models for nonequilibrium plasma flow simulations at high speed re-entry conditions*. Ph. D. thesis, Universita degli Studi di Pisa and the von Karman Institute for Fluid Dynamics.
- Panesi, M., T. Magin, A. Bourdon, A. Bultel, and O. Chazot (2007). Simulation of nonequilibrium reentry air plasmas by means of a collisional-radiative model. In *38th AIAA Plasmadynamics and Lasers Conference*, Miami, Florida.
- Panesi, M., T. Magin, A. Bourdon, A. Bultel, and O. Chazot (2008). Analysis of the FIRE II flight experiment by means of a collisional radiative model. In *46th AIAA Aerospace Sciences Meeting and Exhibit*, Reno, Nevada.
- Park, C. (1985). Nonequilibrium air radiation (NEQAIR) program: User's manual. Technical Report TM86707, NASA Technical Memorandum.
- Park, C. (1988). Assessment of a two-temperature model for dissociating and weakly ionizing nitrogen. *Journal of Thermophysics and Heat Transfer* 2(1), 8–16.
- Park, C. (1990). *Nonequilibrium hypersonic aerothermodynamics*. John Wiley & Sons.

- Park, C. (2004). Stagnation point radiation for Apollo 4. *Journal of Thermophysics and Heat Transfer* 18(3), 1603–1609.
- Park, C. (2008a, January). Rate parameters for electronic excitation of diatomic molecules: 1. electron-impact processes. In *46th AIAA Aerospace Sciences Meeting and Exhibit*, Reno, NV. AIAA 2008-1206.
- Park, C. (2008b, January). Rate parameters for electronic excitation of diatomic molecules: 2. heavy particle-impact processes. In *46th AIAA Aerospace Sciences Meeting and Exhibit*, Reno, NV. AIAA 2008-1446.
- Park, C. (2008c, January). Rate parameters for electronic excitation of diatomic molecules: 3. cn radiation behind a shock wave. In *46th AIAA Aerospace Sciences Meeting and Exhibit*, Reno, NV. AIAA 2008-1276.
- Park, C., J. Howe, R. Jaffe, and G. Candler (1994). Review of chemical-kinetic problems of future NASA missions, II: Mars entries. *Journal of Thermophysics and Heat Transfer* 8(1), 9–23.
- Park, C., R. Jaffe, and H. Patridge (2001). Chemical-kinetics parameters for hyperbolic Earth entry. *Journal of Thermophysics and Heat Transfer* 15(1), 76–90.
- Pierrot, L. (1999). Chemical kinetics and vibrationally-specific collisional-radiative models for nonequilibrium Nitrogen plasmas. Technical report, ESA Postdoctoral Fellowship.
- Pierrot, L., C. Laux, and C. Kruger (1998, June 15-18). Vibrationally-specific collisional-radiative model for nonequilibrium Nitrogen plasmas. In *29th Plasmadynamics and Lasers Conference*, Alberquerque, NM.
- Pierrot, L., L. Yu, R. Gessman, C. Laux, and C. Kruger (1999). Collisional-radiative modeling of nonequilibrium effects in Nitrogen plasmas. In *30th Plasmadynamics and Lasers Conference*, Norfolk, VA.
- Pintassilgo, C., G. Cernogore, and J. Loureiro (2001). Spectroscopy study and modeling of an afterglow created by a low-pressure pulsed discharge in N₂-CH₄. *Plasma Sources Science Technology* 10, 147–161.
- Playez, M. (2006). *Titan Atmosphere Plasma Characterization using Spectroscopic Measurement Techniques*. Ph. D. thesis, Ecole Centrale Paris.
- Potter, D., R. Gollan, T. Eichmann, T. McIntyre, R. Morgan, and P. Jacobs (2008, January). Simulation of CO₂-N₂ expansion tunnel flows for the study of radiating shock layer. In *46th AIAA Aerospace Sciences Meeting*, Reno, Nevada.
- Ramjaun, D., M. Dumitrescu, and R. Brun (1999). Kinetics of free radicals behind strong shock waves. *Journal of Thermophysics and Heat Transfer* 13(2), 219–225.

- Ried, R., W. Rochelle, and J. Milhoan (1972). Radiative heating to the Apollo Command Module: engineering predictions and flight measurement. Technical Report NASA-TM-X-58091, NASA.
- Rond, C. and P. Boubert (2009). Chemical kinetic and radiative simulations for Titan atmospheric entry. *Journal of Thermophysics and Heat Transfer* 23(1), 72–82.
- Rond, C., P. Boubert, J.-M. Felio, and A. Chikhaoui (2007). Radiation measurements in a shock tube for Titan mixtures. *Journal of Thermophysics and Heat Transfer* 21(3), 638–646.
- Roose, T. R., R. Hanson, and C. Kruger (1978). Decomposition of NO in the presence of NH₃. In *11th International Symposium on Shock Tubes and Waves*, pp. 245–253.
- Roshko, A. (1960). On flow duration in low-pressure shock tubes. *Physics of Fluids* 3(6), 835.
- Sarrette, J., A. Gomès, J. Bacri, C. Laux, and C. Kruger (1995a). Collisional-radiative modeling of quasi-thermal air plasmas with electronic temperatures between 2000 and 13,000 K: I. *Journal of Quantitative Spectroscopy and Radiative Transfer* 53, 125–141.
- Sarrette, J., A. Gomès, J. Bacri, C. Laux, and C. Kruger (1995b). Collisional-radiative modeling of quasi-thermal air plasmas with electronic temperatures between 2,000 and 13,000 K: II. *Journal of Quantitative Spectroscopy and Radiative Transfer* 53, 143–152.
- Schwartz, R., K. Slawsky, and Z. Herzfeld (1952). Calculation of vibrational relaxation times in gases. *Journal of Chemical Physics* 20(10), 1591–1598.
- Scott, M. (2006). *Development and Modelling of Expansion Tubes*. Ph. D. thesis, Division of Mechanical Engineering, School of Engineering, The University of Queensland.
- Sharma, S. and W. Gillespie (1991). Nonequilibrium and equilibrium shock front radiation measurement. *Journal of Thermophysics and Heat Transfer* 5(3), 257–265.
- Smith, A., T. Gogel, P. Vandevelde, and L. Marraffa (1996). Plasma radiation database PARADE final report. Technical report, ESTEC Contract 11148/94/NL/FG.
- Sommer, T., T. Kruse, and P. Roth (1997). Perturbation study on the reaction of C₂ with N₂ in high-temperature C60/Ar + N₂ mixtures. *Journal of Physical Chemistry* 101, 3720–3725.
- Soon, W. and J. Kunc (1990). Thermal nonequilibrium in partially ionized atomic oxygen. *Physical Review A* 41(2), 825–843.

- Stackpoole, M., S. Sepka, I. Cozumuta, and D. Kontinos (2008). Post-flight evaluation of Stardust sample return capsule forebody heatshield material. In *46th AIAA Aerospace Sciences Meeting and Exhibit*, Reno, Nevada.
- Stalker, R. (1989). Hypervelocity aerothermodynamics with chemical nonequilibrium. *Annual Review of Fluid Mechanics* 21, 37–60.
- Stalker, R. and D. Plumb (1968). Diaphragm-type shock tube for high shock speeds. *Nature* 218, 789–790.
- Sutton, K. (1984). Air radiation revisited. In *19th AIAA Thermophysics Conference*, Snowmass, Colorado. AIAA Paper 1984-1733.
- Takashima, N., B. R. Hollis, V. E. Zoby, K. Sutton, J. Olejniczak, M. J. Wright, and D. Prabhu (2003). Preliminary aerothermodynamics of Titan aerocapture aeroshell. In *39th AIAA/ASME/SAE/ASEE Joint Propulsion Conference and Exhibit*, Huntsville, Alabama. AIAA Paper 2003-4952.
- Teulet, P., J. Sarrette, and A. Gomès (1999). Calculation of electron impact inelastic cross sections and rate coefficients for diatomic molecules. *Journal of Quantitative Spectroscopy and Radiative Transfer* 1, 549–569.
- Teulet, P., J. Sarrette, and A. Gomès (2001). Collisional-radiative modelling of one- and two-temperature air and air-sodium plasmas at atmospheric pressure with temperatures of 2000–12000 K. *Journal of Quantitative Spectroscopy and Radiative Transfer* 70(2001), 159–187.
- Trumble, K., I. Cozmuta, S. Sepka, and P. Jenniskens (2008). Post-flight aerothermal analysis of the Stardust sample return capsule. In *46th Aerospace Sciences Meeting and Exhibit*, Reno, Nevada.
- Tsang, W. (1992). Chemical kinetic data base for propellant combustion II: Reactions involving CN, NCO and HNCO. *Journal of Physical Chemistry Reference Data* 21(4), 753–791.
- Tsang, W. and J. Herron (1991). Chemical kinetic data base for propellant combustion I: Reactions involving NO, NO₂, HNO, HNO₂, HCN and N₂O. *Journal of Physical Chemistry Reference Data* 20(4), 609–663.
- van Regemorter, H. (1962). Rate of collisional excitation in stellar atmospheres. *Astrophysical Journal* 136, 906–915.
- Walpot, L., L. Caillault, R. Molina, C. Laux, and T. Blancquaert (2006). Convective and radiative heat flux prediction of Huygens entry on Titan. *Journal of Thermophysics and Heat Transfer* 20(4), 663–671.

- Wang, Y. and C. Mak (1995). Transferable tight-bonding potential for hydrocarbons. *Chemical Physics Letters* 235, 37–46.
- Way, D. W., R. W. Powell, K. T. Edquist, J. P. Masciarelli, and B. R. Starr (2003). Aerocapture simulation and performance for the Titan Explorer mission. In *39th AIAA/ASME/SAE/ASEE Joint Propulsion Conference and Exhibit*, Huntsville, Alabama. AIAA Paper 2003-4951.
- Whiting, E., C. Park, Y. Liu, J. Arnold, and J. Paterson (1996). NEQAIR96, nonequilibrium and equilibrium radiative transport and spectra program: User's manual. Technical report, NASA. Reference Publication 1389.
- Winter, M. and G. Herdrich (2008). Heat shield temperatures and plasma radiation obtained from spectroscopic observation of the STARDUST re-entry in the near UV. In *46th AIAA Aerospace Sciences Meeting and Exhibit*, Reno, Nevada.
- Winter, M. and C. Laux (2008). N2-CH4 and air and ablation products flows: Status, facilities, instrumentation, test plan. Technical report, European Space Agency. AMOD-ECP-TN-011.
- Witasse, O., J. Lebreton, M. Bird, R. Dutta-Roy, W. Folkner, R. Preston, S. Asmar, L. Gurvits, S. Pogrebenko, I. Avruch, R. Campbell, H. Bignall, M. Garrett, H. van Langevelde, S. Parsley, C. Reynolds, A. Szomoru, J. Reynolds, C. Phillips, R. Sault, A. Tzioumis, F. Ghigo, G. Langston, W. Brisken, J. Romney, A. Mujunen, J. Ritakari, S. Tingay, R. Dodson, C. van't Klooster, T. Blancquaert, A. Coustenis, E. Gendron, B. Sicardy, M. Hirtzig, D. Luz, A. Negrao, T. Kostiuk, T. Livengood, M. Hartung, I. de Pater, M. Adamkovics, R. Lorenz, H. Roe, E. Schaller, M. Brown, A. Bouchez, C. Trujillo, B. Buratti, L. Caillault, T. Magin, A. Bourdon, and C. Laux (2006). Overview of the coordinated ground-based observations of Titan during the Huygens mission. *Journal of Geophysical Research - Planets* 111(E7).
- Wooldridge, S., R. Hanson, and C. Bowman (1996). A shock tube study of reactions of CN with HCN, OH and H₂ using CN and OH laser absorption. *International Journal of Chemical Kinetics* 28, 245–258.
- Wright, M., J. Olejniczak, L. Walpot, E. Raynaud, T. Magin, L. Caillault, and B. Hollis (2006). A code calibration study for Huygens entry aeroheating. In *44th AIAA Aerospace Sciences Meeting and Exhibit*, Reno, Nevada.
- Wright, M. J., D. Bose, and J. Olejniczak (2004). The impact of flowfield-radiation coupling on aeroheating for Titan aerocapture. In *42nd Aerospace Sciences Meeting and Exhibit*, Reno, Nevada. AIAA Paper 2004-0484.
- Yelle, R., D. Strobel, E. Lellouch, and D. Gautier (1997). Engineering models for Titan's atmosphere: Huygens science, payload and mission. Technical report, European

- Space Agency. ESA-SP-1177.
- Zalogin, G., P. Kozlov, L. Kuznetsova, S. Losev, V. Makarov, Y. Romanenko, and S. Surzhikov (2001). Radiation excited by shock waves in a $CO_2 - N_2 - Ar$ mixture: experiment and theory. *Technical Physics* 71(6), 10–16.
- Zatsarinny, O. and S. Tayal (2003). Electron collisional excitation rates for O I using the b-spline r-matrix approach. *The Astrophysical Journal. Supplement Series* 148, 575–582.

APPENDIX A

Spectrometry Notes

A.1 Alignment procedure

Initially, a laser diode is placed in an alignment tool attached to the end of the tube such that it is located on the centreline of the flow and in the centre of the region of interest, see Figures A.2 and A.3. Two aluminium mirrors affixed to the optical table, on which the spectrometer rests, are used as a combined beam rotator and periscope to turn the image of the horizontal flow so that it falls onto the vertical spectrometer entrance slit. During alignment, two irises are used to ensure that the laser diode beam is aligned normal to and centred on the face of the spectrometer entrance slit.

With the laser diode and extra irises removed from the system, the alignment tool is moved such that the slats, evenly spaced 10 mm apart, are located at the start of the desired capture area as shown in Figure A.3 and a fluorescent light source is placed behind the slats. An $f=100\text{ mm}$ UV fused silica spherical mirror and a straightening mirror are placed such that the light is focussed on the spectrometer slit, and an iris of aperture 15 mm diameter was placed before the lens to reduce unwanted light entering the spectrometer and to limit the solid angle (as shown in Figure 3.8). The spectrometer was placed such that the edges of the slat images on the ICCD were as close to a step change as possible - to within 2 pixels for these experiments.

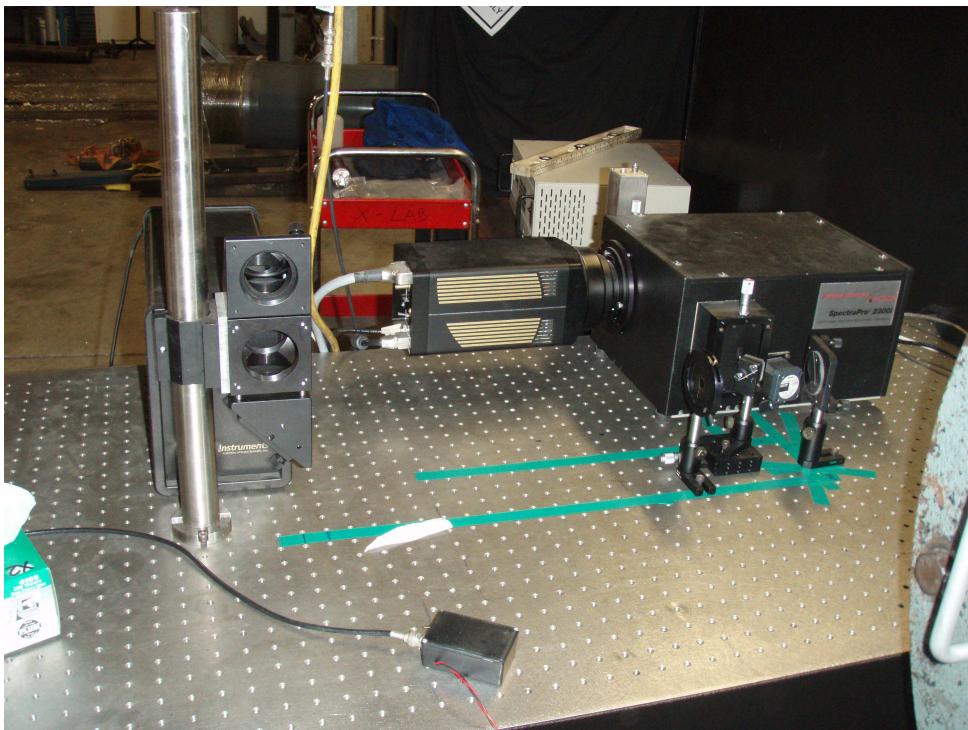


Figure A.1 : *Photograph of the final optical layout used in the nonreflected shock tube experiments.*

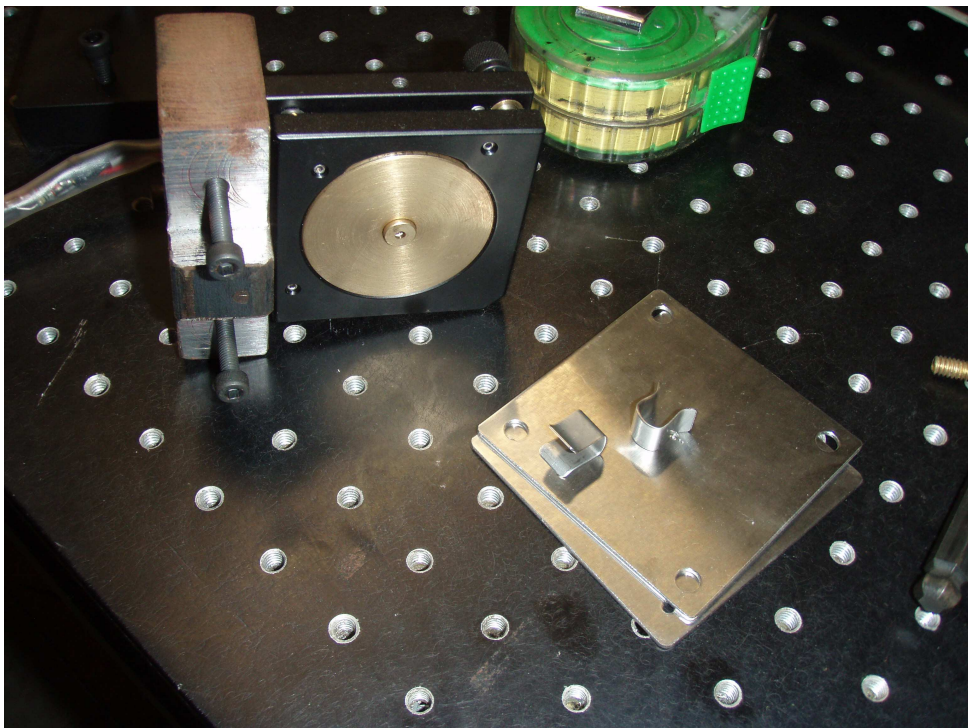


Figure A.2 : *Photograph of the alignment tool used for locating the laser diode on the centreline of the tube.*

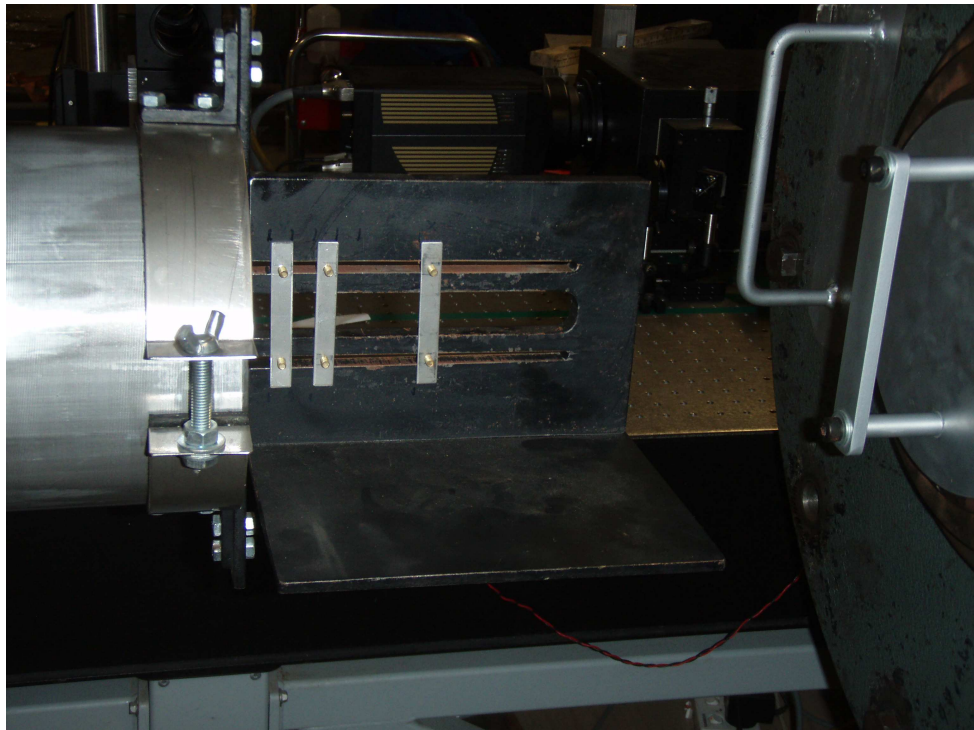


Figure A.3 : *Photograph of the alignment tool set up with the slats.*

The spectrometer is used to ensure that the optical equipment is aligned correctly and to measure the magnification observed in the image. Spectral images show the breaks in the light where the slats are located, allowing the measurement of the number of pixels per millimeter on the vertical axis of the image as shown in Figure A.4.

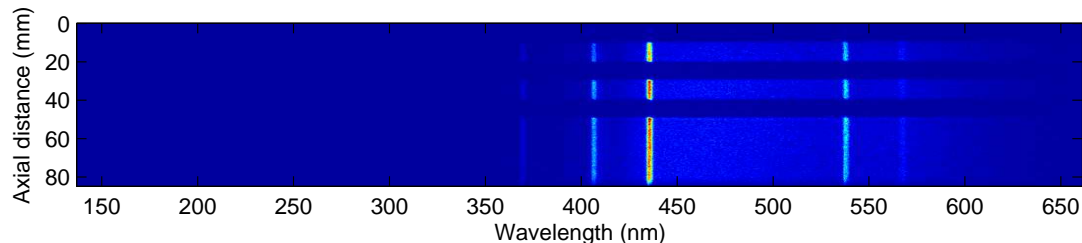


Figure A.4 : *Spectral image of the alignment tool taken with a fluorescent light. The vertical axis is the horizontal distance along the centreline of the flow in 256 pixels. This image is used to determine the number of pixels per millimeter.*

A.2 Non-linear response of the spectrometer

It was observed in measurements taken in collaboration with Troy Eichmann that the PI-MAX camera used for the experiments had a non-linear response to variations in exposure time (see Figure A.5). This deviation from the expected linear response was significant

for the range of exposure times used in this thesis and was included in the calibration of the spectral data. The value used in the calibrations is given in Table A.1 for a gain of 240 on the ICCD.

Exposure time	Scaling factor from 10 μs
100 ns	66.02
200 ns	39.84
500 ns	18.20
1 μs	9.55

Table A.1 : *Measured scaling factor for converting the 10 μs calibration exposures to the experimental exposure time.*

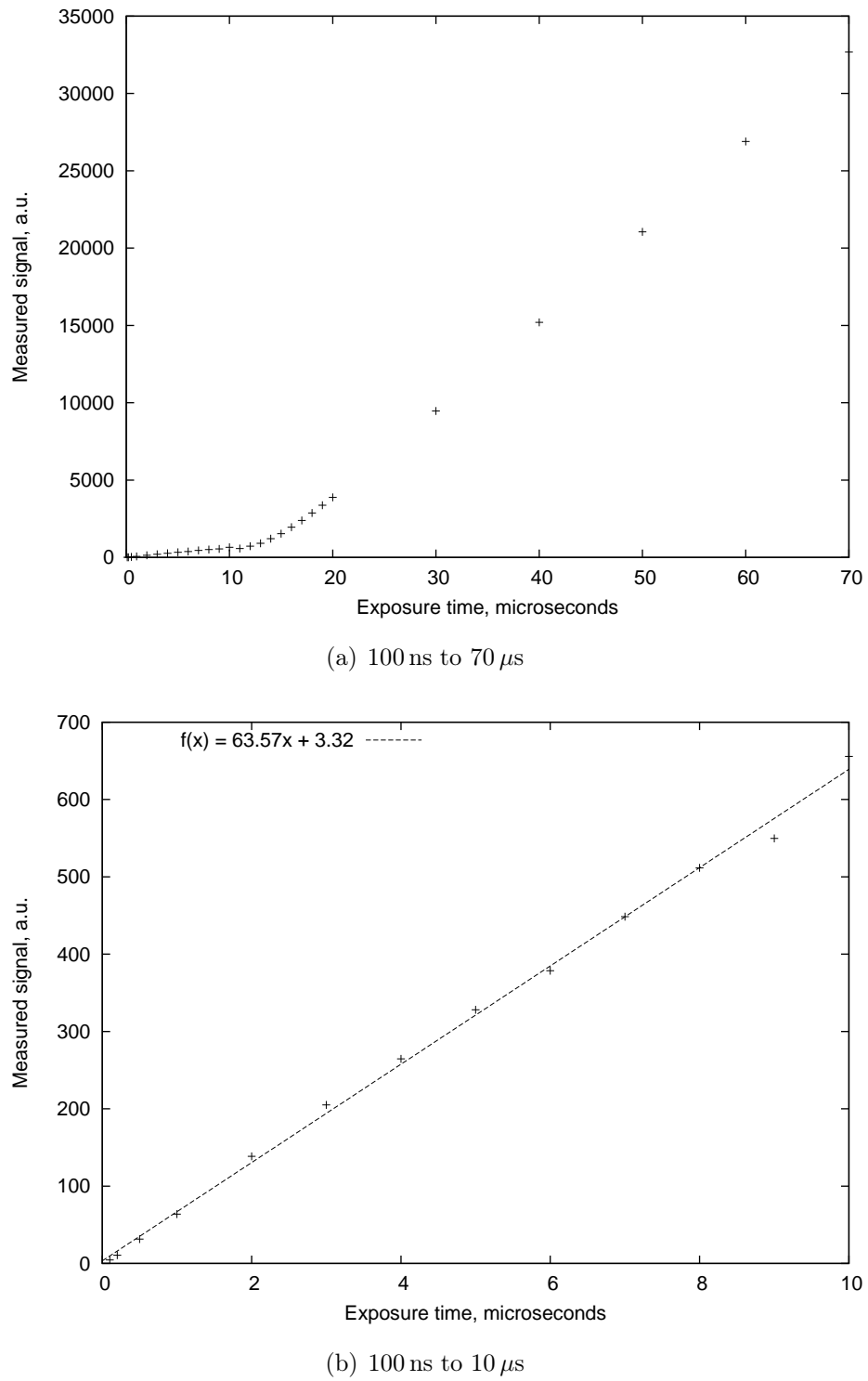


Figure A.5 : Variation of camera response with exposure time.

APPENDIX B

Uncertainty Analysis

All the experimental measurements undertaken in the shock tube experiments have an associated level of uncertainty, which is detailed here. These experimental measurements are broken into the flow condition measurements (shock speed, pressure, ...) and the spectral measurements.

B.1 Flow condition

Over the course of the experimental campaigns conducted in this work, the following measurements were made:

- the static pressure in the secondary driver tube;
- the static pressure in the shock tube and
- the pitot pressure at the exit of the shock tube.

B.1.1 Shock speed uncertainty

The shock speed in the facility at each location was calculated using the time of flight between each static pressure transducer in the relevant section and their separation distance. Static pressure transducers were flush-mounted to the walls of the tube and used

Table B.1 : *The percentage uncertainty in the measurement of the location of the shock arrival.*

Transducer	Distance (mm)	Uncertainty (%)
st1 to st2	233.0	2.15
st2 to st3	231.0	2.16
st3 to at1	910.0	0.55
at1 to at2	250.0	2.00
at2 to at3	250.0	2.00
al1 to al2	1000.0	0.50
al2 to al3	1000.0	0.50
al3 to al4	1000.0	0.50
al4 to al5	500.0	1.00

to indicate the time at which the shock passed that point in the facility. The accuracy of the shock speed therefore depends upon the accuracy of the measurement of both the shock arrival time and the distance travelled by the shock between measurements.

Inaccuracies in the measurement of the shock arrival time were a function of the sampling rate of the data acquisition system. The NI acquisition system was set to a sampling rate of 2.5 MHz for all experimental work in this report. This sampling rate results in pressure data being recorded every $0.4\ \mu\text{s}$. Due to electrical noise, vibration, and the response time of the PCB transducers themselves, the accuracy of the time of shock arrival is estimated as being $1.2\ \mu\text{s}$.

For a shock speed of 10 km/s, the time between samples corresponds to a distance of 4 mm. The location of each static pressure transducer was measured to an accuracy of approximately 1 mm. The combination of these two uncertainties results in the location of the shock at each measurement being accurate to 5 mm.

The final estimated uncertainty in the calculation of the shock speed is given by the sum of the square of the relative errors in the time and distance measurements (Mee 1993). That is,

$$X_u = \sqrt{X_{time}^2 + X_{location}^2} \quad (\text{B.1})$$

This uncertainty ranges in value from 0.5 to 3.1 % down the length of the facility.

B.1.2 Pressure measurements

The accuracy of the measurement of all fill pressures depends on the accuracy of the gauge used to measure the pressure and the leakage of air into the tubes during filling.

For the compression tube and secondary driver gases, the fill pressure is measured with a Varian gauge. The accuracy of the gauges is assumed to be $\pm 5\%$ when any drift in the gauge is removed by taking a zero reading.

The leak rate in the secondary driver tube was measured at approximately 90 Pa/hour. During an experiment, the helium in the secondary driver is left for less than 10 minutes, corresponding to a maximum leak of 15 Pa. The experimental conditions required a minimum fill pressure of 10 kPa, making the maximum uncertainty in the pressure due to this leak 0.15%.

For the compression tube, the leak rate measured was approximately 50 Pa/hour. This lead to a maximum leak of 17 Pa due to the 20 minute delay between filling the compression tube and firing the shot. As the fill pressure for all experiments was 30 kPa, the uncertainty in the fill pressure measurement in the compression tube was 0.06%.

Therefore, for both the compression tube and secondary driver fill pressures, the uncertainty is dominated by the effect of the gauge accuracy rather than the leak rate, and was assumed to be $\pm 5\%$.

For the test gas, a Barocell gauge (full scale measurement of 1 torr) was used to measure the fill pressure. The accuracy of this gauge is assumed to be $\pm 2\%$. The leak rate of the shock tube and dump tank sections combined was measured at 3.08 Pa/minute.

Prior to the experiments, the shock tube and dump tank were evacuated to a maximum value of 0.1 Pa. The sections were then flushed twice with the Titan atmospheric gas mixture to a value of 8 Pa. Following this, the test gas was added approximately 20 seconds prior to the completion of the experiment. This resulted in a reduction of the methane concentration in the Titan test mixture of 0.15% for the 13 Pa condition, 0.23% for the 8 Pa condition, and 0.41% for the 4 Pa condition.

The static and Pitot pressure measurements are taken using PCB piezoelectric transducers. For these transducers, uncertainties in the calibration and the mounting result affect the value of the pressure measured. Estimates of these uncertainties are $\pm 2\%$ and $\pm 4\%$ respectively, leading to an overall accuracy of $\pm 4.5\%$.

B.2 Spectral measurements

The uncertainty of the spectral measurements is dependent on the accuracy of the signal magnitude calibration, the wavelength dimension calibration, and the axial dimension calibration. In calculating the accuracy of the signal magnitude calibration, there are contributions from the calibration image, experimental image, and the optical component losses.

This section is adapted and expanded from the uncertainty analysis provided by McGilvray et al. (2010).

B.2.1 Signal magnitude uncertainty

B.2.1.1 Contributions of the calibration image

The calibration source used for all calibration images was an Optronics Laboratories OL-200M tungsten-halogen spectral lamp. This lamp has a quoted uncertainty of <1% in the measurement of the emitted spectral radiance 500 mm from the centreline of the lamp. The accuracy of the measured distance between lamp and spectrometer slit is ± 2.5 mm and the spectral irradiance varies by $\frac{500^2}{d^2}$, where d is the distance in mm from lamp centre to slit. This distance cannot be measured more accurately, as the effective size of the radiating element is 25×4.5 mm cylinder, enclosed in a vacuum glass casing of ≈ 20 mm diameter. Therefore, the overall accuracy of the spectral irradiance emitted from the calibration lamp is 2.25% (using the root mean square approach).

The signal measured on the ICCD is recorded in the units of ‘counts’, and there is an inherent uncertainty of $\pm(\text{counts})^{0.5}$ in each pixel’s measurement prior to the removal of the thermal noise. The thermal noise (background) also has an uncertainty of ± 3 counts for a 95% confidence level measured over 10 frames and averaged across the entire ICCD.

The light that reaches the ICCD plane also has an uncertainty associated with it, due to imperfections in the optics and grating. By taking an average over 10 frames and 245 axial pixels (24500 data points averaged to give a single calibration count at each wavelength), the level of uncertainty is reduced proportional to the number of frames, which is needed in the UV where the number of counts is low. This value is currently assumed to be of the same order as the background noise.

Taking an average level of counts across calibration of 40 counts, the calibration image has an combined average uncertainty level of $\pm 20\%$.

The properties of the calibration lamp are such that it produces a stronger signal at the larger wavelengths in the calibration range. Therefore, at larger wavelengths and lower resolution gratings, the uncertainty due to the calibration will be less than the average due to the increased signal strength.

B.2.1.2 Contributions of the optical components

As the calibration procedure does not take into account optical losses due to individual components in the imaging system, these losses must be quantified and included in the

final calculation. The calibration of the raw shot data includes the inverse of product of the transmission efficiencies of all the external optical components (optical losses). As there are five of these (1 planar window, 3 planar mirrors, 1 focussing mirror), the uncertainties of each individual measurement contributes to the overall uncertainty of the system. Each transmission is measured from the relative magnitudes of signals with and without the specific item being tested, so errors in absolute measurement of radiance are decoupled from the resultant uncertainty. Uncertainty remains due to the non repeatability of lamp output ($\sim < 1\%$) and errors in the ICCD when repeatably re-recording an invariant input. The latter error is reduced by multiple recordings and averaging.

On this basis, the uncertainty in each individual measurement is calculated to be $< 5\%$. When coupled together in series, this results in an overall uncertainty of 13.5% due to the external optical components in the system.

The magnification is measured optically as the ratio of the distance from the focussing mirror to the slit (100 mm) and the distance from the centreline of the facility to the focussing mirror (1578 mm), with an uncertainty of ± 5 mm in each measurement. This gives an overall uncertainty of $\pm 5\%$ in the calculation of the magnification.

The solid angle is calculated from the geometrically measured iris radius (15 mm) and distance from the iris to the tube centreline (1458 mm), which have an uncertainty of ± 0.2 mm and ± 5 mm respectively. This leads to an overall uncertainty of 1.6% in the calculated solid angle.

B.2.1.3 Contributions of the experimental image

Unlike the calibration image, the shot image cannot take advantage of averaging over a large number of pixels. Pixels that receive higher levels of radiation will have a higher signal to noise ratio. Overall, the associated uncertainty has been estimated to be ± 20 counts at each axial position/wavelength pixel. For spectra which have low signal counts (high resolution spectra, low spectral peaks), this level is extremely high. For an average level of 200 counts across the whole spectra tested (low resolution), the average uncertainty is $\pm 10\%$.

B.2.1.4 Summary

The overall signal magnitude ($\text{W}/(\text{m}^2 \cdot \text{nm} \cdot \text{sr})$) of each ICCD pixel is a combination of the above effects. If one assumes that all sources of uncertainty are equally probable and that there are no coupling effects between these sources, then the average overall uncertainty in the signal magnitude is $\pm 26\%$.

B.2.2 Wavelength dimension uncertainty

All three installed gratings in the UV spectrometer system were used in these experiments, and a calibration of the spectrometer wavelength was conducted each time the grating was modified. A mercury lamp with strong, recognisable peaks was used to provide this calibration. The WinSpec program driving the spectrometer uses a second order polynomial to fit the wavelength scale to these peaks. Therefore, the wavelength accuracy is estimated to be $\pm 1\text{ nm}$ as the curve fitting process does allow for a slight shift in wavelength location.

B.2.3 Axial dimension uncertainty

The calculation of the uncertainty in the calibration of axial dimension of the ICCD array is dependent on four issues. These are;

- The smearing of the signal due to the shock motion during the exposure time.
- The location of the end of the image frame with respect to the end of the shock tube.
- The relative distance between different portions of the image.
- The light is radiating in all directions, and a pixel can collect radiation for a region of gas within a range of axial locations.

B.2.3.1 Contribution of exposure time

The nominal exposure time of the experimental images was 100 ns. During this time, the shock propagated (on average) 0.6 mm for the 13 and 8 Pa conditions and 0.9 mm for the 4 Pa condition. The axial dimension of the ICCD array contains 256 pixels which capture light from the 5.7 mm long entrance slit. As the magnification of the optical system was 0.063, each pixel of the ICCD axial dimension represented 0.35 mm of axial flow. This means that the data gathered by each pixel contains data averaged against distance relative to the shock over as much as 1 mm.

It is, however, possible to digitally correct for this effect when comparing numerical predictions of radiation models with the experimental data. This effect is the dominant error term when defining the location of any pixel and other uncertainties in axial location should be interpreted in the context of this rather large displacement. Due to the large and non-linear gradients in the radiation near the shock, the effects of this smearing are

more significant there, and have less effect further back from the shock where equilibrium conditions are approached. The high peaks of spectral lines are likely to be truncated to some extent due to this smearing.

B.2.3.2 Location of shock tube

Knowledge of the location of the edge of the image in relation to the shock tube exit at the moment of exposure is also necessary as it is also possible to digitally correct for this in numerical predictions. This relative location is fixed for all experimental results gathered in a single campaign (all results presented in this work come from a single campaign). This location is not the same during the experimental exposure as it is before an experiment, as the shock tube (and everything upstream) recoils a distance of approximately 20 mm during a shot. The location of the tube exit before a shot can be found by using a dummy alignment exposure, where it can be clearly seen as a shadow on the image. It is then possible to discover the location of the tube during an experiment by adjusting for the expected recoil. In practice, however, the end of the tube can also be seen on the experimental image as a sharp drop in signal over a distance of approximately 3 mm.

B.2.3.3 Contribution of relative distances

The relative distances between the various parts of the image are defined by the optical magnification of the system and the number of pixels used to capture the image. This can be defined to an accuracy of ± 0.5 mm, and over the full screen represents a minor but quantifiable error. The axial distance is calibrated by imaging an illuminated scale grid of known dimensions on the tube centreline. This creates an image containing a sequence of bright and dark patches with known geometrical separations.

As the distance at the centreline of the tube can be measured to within ± 0.5 mm for a length of 50 mm (half of the captured length at the centreline of the facility), this gives an uncertainty of $\pm 1\%$. This corresponds to a length of 143 pixels (0.35 mm of flow imaged per pixel) with an accuracy of ± 3 pixels due to the smearing at either edge (uncertainty of $\pm 2\%$).

Therefore, the overall uncertainty of this contribution is (from the sum of the squares method) $\pm 2.2\%$.

B.2.3.4 Contribution of off-axis light

The light from certain parts of the image is traversing the test section at angles of up to 0.034 radians to the flow. In doing so, it collects radiation from a region of gas spanning as much as 2.7 mm in the axial direction.

APPENDIX C

Simulation Scripts

C.1 L1d3 simulations

C.1.1 Full facility simulation

This python code provides the input required to simulate the full modified facility using L1d3.

```
1 # cond_13Pa.py
2 # A python program to define the conditions in X2
3 # Rarefied Titan condition with piston dynamics
4 # Carolyn Jacobs
5
6 # Non-reacting
7 # Viscous
8 # Titan gas, 98% N2 / 2% CH4
9 # 13 Pa condition
10 # 2 June 2009
11
12 # Geometry altered to that of the new aluminium section in more detail
13 # and includes a second helium driver
14
15 # Geometry details
16 loc_res = -3.890 # Location of left end of reservoir
17 loc_pis = 0.000 # Location of piston launch
18 loc_pis2 = 4.394 # Location of piston at diaphragm rupture
19 loc_pd = 4.810 # Location of primary diaphragm
20 loc_sd = 8.234 # Location of secondary diaphragm
21 loc_td = 9.515 # Location of tertiary diaphragm
22
23 length_a = 0.250 # See diagram p86 of expl workbook for definition
24 length_b = 4.731 # Length of new rarefied tube
25 loc_end = loc_td + length_a + length_b
```

```

26 # Radius details for whole tube
27 rad_a = 0.3160 # Reservoir
28 rad_b = 0.2568 # Driver tube
29 rad_c = 0.0850 # Shock tube
30 rad_d = 0.1556 # New rarefied tube
31
32 # Set the number of cells in each region
33 ncells_res = 300
34 ncells_driver = 300
35 ncells_shock = 300
36 ncells_accel = 300
37
38 # Set the test gas pressure
39 p_test = 13.0
40
41 # Set viscosity
42 vis = 1
43
44 # Set the driver details
45 n_frac_ar = 0.15 # Mole fraction of Ar in primary driver
46 p_res = 1.0e6 # Reservoir gauge pressure
47 p_res_act = p_res + 1.0e5 # Reservoir actual pressure
48 p_driver = 3.0e4 # Primary driver pressure
49 p_sec_driver = 30.0e3 # Secondary driver pressure
50 p_sec_burst = 75.0e3 # Mylar secondary diaphragm
51
52 # Calculate the mass fraction of the driver from the mole fraction
53 n_frac_he = 1.0 - n_frac_ar
54 mmass_ar = 39.95
55 mmass_he = 4.003
56 mf_ar = n_frac_ar * mmass_ar / ((n_frac_ar * mmass_ar) + (n_frac_he * mmass_he))
57 mf_he = n_frac_he * mmass_he / ((n_frac_ar * mmass_ar) + (n_frac_he * mmass_he))
58
59 # Set the title information
60 gdata.title = 'X2 NRST: L1d3 LUT_MIX for 13 Pa test gas with Al tube and piston'
61
62 # Select the equilibrium Titan model
63 select_gas_model(fname='LUT-plus-Ar-He-air.lua')
64 gdata.reacting_flag = 0
65
66 # Species order: LUT Ar He Air
67 titan_gas = [ 1.0, 0.0, 0.0, 0.0 ]
68 primary_driver = [ 0.0, 0.15, 0.85, 0.0 ]
69 secondary_driver = [ 0.0, 0.0, 1.0, 0.0 ]
70 reservoir = [ 0.0, 0.0, 0.0, 1.0 ]
71
72 # Define the tube walls
73 add_break_point(loc_res, rad_a, 0)
74 add_break_point(loc_pis-0.110, rad_a, 0)
75 add_break_point(loc_pis-0.010, rad_b, 0)
76 add_break_point(loc_pis, rad_b, 0) # Piston launch station
77 add_break_point(loc_pis2, rad_b, 0) # Location of stationary piston at burst
78 add_break_point(loc_pd-0.210, rad_b, 0)
79 add_break_point(loc_pd-0.110, rad_c, 0)
80 add_break_point(loc_pd-0.010, rad_c, 0)
81 add_break_point(loc_pd, rad_c, 0) # Primary diaphragm station
82 add_break_point(loc_td, rad_c, 0) # Tertiary diaphragm station
83 add_break_point(loc_td+length_a-0.200, rad_c, 0)
84 add_break_point(loc_td+length_a, rad_d, 0)
85 add_break_point(loc_end, rad_d, 0)
86
87 left_wall = VelocityEnd(x0=loc_res, v=0.0)
88 res_gas = GasSlug(p=p_res_act, u=0.0, T=296.0, nn=ncells_res, to_end_L=0,
89                 to_end_R=1, cluster_strength=0.0, hcells=1,
90                 viscous_effects=vis, adiabatic_flag=0,
91                 massf=reservoir,
92                 label='compressed air to push the piston')
93 piston = Piston(m=35.0, d=rad_b, xL0=0.0, xR0=0.341, v0=0.0,
94                 front_seal_f=0.4, front_seal_area=0.020*0.2568*math.pi,
95                 is_restrain=0, with_brakes=0,
96                 x_buffer=4.4795, hit_buffer=0,
97                 label='single stage x2 piston')
98 driver_gas = GasSlug(p=p_driver, u=0.0, T=296.0, nn=ncells_driver, to_end_L=1,
99                 to_end_R=1, cluster_strength=1.05, hcells=1,
100                viscous_effects=vis, adiabatic_flag=0,
101                massf=primary_driver,
102                label='compressed argon/helium driver gas')
103 diaphragm = GasInterface(x0=loc_pd)

```

```

104 shock_gas = GasSlug(p=p_sec_driver, u=0.0, T=296.0, nn=ncells_shock,
105     to_end_L=1, to_end_R=1, cluster_strength=1.02, hcells=1,
106     viscous_effects=vis, adiabatic_flag=0,
107     massf=secondary_driver,
108     label='secondary helium driver in the shock tube')
109 secondary_diaphragm = Diaphragm(x0=loc_td, p_burst=p_sec_burst, is_burst=0,
110     dt_hold=5.0e-6, dt_blend=0.0, dx_blend=0.0)
111 accelerated_gas = GasSlug(p=p_test, u=0.0, T=296.0, nn=ncells_accel,
112     to_end_L=1, to_end_R=0, cluster_strength=1.02,
113     hcells=1, viscous_effects=vis, adiabatic_flag=0,
114     massf=titan_gas,
115     label='LUT test gas in the acceleration tube')
116 right_free = FreeEnd(x0=loc_end)
117 assemble_gas_path(left_wall, res_gas, piston, driver_gas, diaphragm, shock_gas,
118     secondary_diaphragm, accelerated_gas, right_free)
119
120 # Add some global data
121 gdata.n = 1000
122
123 # Add a loss region
124 add_loss_region(4.6, 4.8, 0.35) # Change of Diameter at primary
125 add_loss_region(-0.05, 0.0, 0.35) # COD at piston launch
126 add_loss_region(loc_pd, loc_pd+0.010, 0.35) # Losses at the secondary
127 add_loss_region(loc_td, loc_td+0.010, 0.35) # Losses at the tertiary
128 add_loss_region(loc_td+length_a, loc_td+length_a+0.010, 0.35)
129 # COD inside new connection
130
131 # Set some time-stepping parameters
132 gdata.dt_init = 1.0e-9
133 gdata.max_time = 1.0e-2
134 gdata.max_step = 25000000
135 gdata.cfl = 0.25
136 gdata.t_order = 2
137 gdata.x_order = 2
138
139 # Determine the extraction of data information
140 add_dt_plot(0.0, 1.0e-6, 1.0e-6)
141 add_history_loc(-1.500)
142 add_history_loc(3.500)
143 add_history_loc(4.510)
144 add_history_loc(4.520)
145 add_history_loc(4.530)
146 add_history_loc(4.720)
147 add_history_loc(7.381) # st1
148 add_history_loc(7.614) # st2
149 add_history_loc(7.845) # st3
150 add_history_loc(8.755) # at1
151 add_history_loc(9.005) # at2
152 add_history_loc(9.255) # at3
153 add_history_loc(loc_td-0.020) # MBCNS starting point
154 add_history_loc(loc_td+length_a+0.781) # a11
155 add_history_loc(loc_td+length_a+1.781) # a12
156 add_history_loc(loc_td+length_a+2.781) # a13
157 add_history_loc(loc_td+length_a+3.781) # a14
158 add_history_loc(loc_td+length_a+4.281) # a15/6
159 add_history_loc(loc_end)

```

C.1.2 Simulation without piston dynamics

This python code provides the input required to simulate the modified facility using L1d3 from the rupture of the primary diaphragm (ie. without any piston dynamics).

```

1 # cond_13Pa_nopiston.py
2 # A python program to define the conditions in X2
3 # Rarefied Titan condition without piston dynamics
4 # Carolyn Jacobs
5
6 # Non-reacting
7 # Viscous
8 # Titan gas, 98% N2 / 2% CH4
9 # 13 Pa condition
10 # 2 June 2009

```

```

11 # Geometry altered to that of the new aluminium section in more detail
12 # and includes a second helium driver
13
14 # Geometry details
15 loc_res = -3.890 # Location of left end of reservoir
16 loc_pis = 0.000 # Location of piston launch
17 loc_pis2 = 4.394 # Location of piston at diaphragm rupture
18 loc_pd = 4.810 # Location of primary diaphragm
19 loc_sd = 8.234 # Location of secondary diaphragm
20 loc_td = 9.515 # Location of tertiary diaphragm
21
22 length_a = 0.250 # See diagram p86 of expl workbook for definition
23 length_b = 4.731 # Length of new rarefied tube
24 loc_end = loc_td + length_a + length_b
25
26 # Radius details for whole tube
27 rad_a = 0.3160 # Reservoir
28 rad_b = 0.2568 # Driver tube
29 rad_c = 0.0850 # Shock tube
30 rad_d = 0.1556 # New rarefied tube
31
32 # Set the number of cells in each region
33 ncells_res = 40
34 ncells_driver = 300
35 ncells_shock = 300
36 ncells_accel = 300
37
38 # Set the test gas pressure
39 p_test = 13.0
40
41 # Set viscosity
42 vis = 1
43
44 # Set the driver details
45 n_frac_ar = 0.15 # Mole fraction of Ar in primary driver
46 p_res = 1.0e6 # Reservoir gauge pressure
47 p_res_act = p_res + 1.0e5 # Reservoir actual pressure
48 p_driver = 3.0e4 # Primary driver pressure
49 p_sec_driver = 30.0e3 # Secondary driver pressure
50 p_sec_burst = 75.0e3 # Mylar secondary diaphragm
51
52 # Calculate the mass fraction of the driver from the mole fraction
53 n_frac_he = 1.0 - n_frac_ar
54 mmass_ar = 39.95
55 mmass_he = 4.003
56 mf_ar = n_frac_ar * mmass_ar / ((n_frac_ar * mmass_ar) + (n_frac_he * mmass_he))
57 mf_he = n_frac_he * mmass_he / ((n_frac_ar * mmass_ar) + (n_frac_he * mmass_he))
58
59 # Set the title information
60 gdata.title = 'X2 NRST: L1d3 LUT_MIX for 13 Pa test gas with Al tube and no piston'
61
62 # Select the equilibrium Titan model
63 select_gas_model(fname='LUT-plus-Ar-He.lua')
64 gdata.reacting_flag = 0
65
66 # Species order: LUT Ar He
67 titan_gas = [ 1.0, 0.0, 0.0 ]
68 primary_driver = [ 0.0, 0.15, 0.85 ]
69 secondary_driver = [ 0.0, 0.0, 1.0 ]
70
71 # Define the tube walls
72 add_break_point(loc_pis2, rad_b, 0) # Location of stationary piston at burst
73 add_break_point(loc_pd-0.210, rad_b, 0)
74 add_break_point(loc_pd-0.110, rad_c, 0)
75 add_break_point(loc_pd, rad_c, 0) # Primary diaphragm station
76 add_break_point(loc_td, rad_c, 0) # Tertiary diaphragm station
77 add_break_point(loc_td+length_a-0.200, rad_c, 0)
78 add_break_point(loc_td+length_a, rad_d, 0)
79 add_break_point(loc_end, rad_d, 0)
80
81 left_wall = VelocityEnd(x0=loc_pis2+0.1705, v=0.0)
82 driver_gas = GasSlug(p=15.5e6, u=0.0, T=3500.0, nn=ncells_driver, to_end_L=1,
83                         to_end_R=1, cluster_strength=1.05, hcells=1,
84                         viscous_effects=vis, adiabatic_flag=0,
85                         massf=primary_driver,
86                         label='compressed argon/helium driver gas')
87 diaphragm = GasInterface(x0=loc_pd)
88

```

```

89 shock_gas = GasSlug(p=p_sec_driver, u=0.0, T=296.0, nn=ncells_shock,
90                      to_end_L=1, to_end_R=1, cluster_strength=1.02, hcells=1,
91                      viscous_effects=vis, adiabatic_flag=0,
92                      massf=secondary_driver,
93                      label='secondary helium driver in the shock tube')
94 secondary_diaphragm = Diaphragm(x0=loc_td, p_burst=p_sec_burst, is_burst=0,
95                                   dt_hold=5.0e-6, dt_blend=0.0, dx_blend=0.0)
96 accelerated_gas = GasSlug(p=p_test, u=0.0, T=296.0, nn=ncells_accel,
97                           to_end_L=1, to_end_R=0, cluster_strength=1.02,
98                           hcells=1, viscous_effects=vis, adiabatic_flag=0,
99                           massf=titan_gas,
100                          label='LUT test gas in the acceleration tube')
101 right_free = FreeEnd(x0=loc_end)
102 assemble_gas_path(left_wall, driver_gas, diaphragm, shock_gas,
103                     secondary_diaphragm, accelerated_gas, right_free)
104
105 # Add some global data
106 gdata.n = 1000
107
108 # Add a loss region
109 add_loss_region(4.6, 4.8, 0.35)           # Change of Diameter at primary
110 add_loss_region(-0.05, 0.0, 0.35)         # COD at piston launch
111 add_loss_region(loc_pd, loc_pd+0.010, 0.35) # Losses at the secondary
112 add_loss_region(loc_td, loc_td+0.010, 0.35) # Losses at the tertiary
113 add_loss_region(loc_td+length_a, loc_td+length_a+0.010, 0.35)
114 # COD inside new connection
115
116 # Set some time-stepping parameters
117 gdata.dt_init = 1.0e-9
118 gdata.max_time = 1.0e-2
119 gdata.max_step = 25000000
120 gdata.cfl = 0.25
121 gdata.t_order = 2
122 gdata.x_order = 2
123
124 # Determine the extraction of data information
125 add_dt_plot(0.0, 1.0e-6, 1.0e-6)
126 add_history_loc(4.720)
127 add_history_loc(7.381)                   # st1
128 add_history_loc(7.614)                   # st2
129 add_history_loc(7.845)                   # st3
130 add_history_loc(8.755)                   # at1
131 add_history_loc(9.005)                   # at2
132 add_history_loc(9.255)                   # at3
133 add_history_loc(loc_td-0.020)           # MBCNS starting point
134 add_history_loc(loc_td+length_a+0.781)  # a11
135 add_history_loc(loc_td+length_a+1.781)  # a12
136 add_history_loc(loc_td+length_a+2.781)  # a13
137 add_history_loc(loc_td+length_a+3.781)  # a14
138 add_history_loc(loc_td+length_a+4.281)  # a15/6
139 add_history_loc(loc_end)

```

C.2 Eilmer3 simulations

This python code provides the input required to simulate the modified facility using EILMER3 from the rupture of the primary diaphragm (ie. without any piston dynamics).

```

1 #####
2 ## 13Pa_grid1.py
3 ## X2 in nonreflected shock mode with aluminium shock tube
4 ##
5 ## Developed from x2_nrst.py prepared by Rowan Gollan
6 ## 28-Sep-2006
7 ##
8 ## Modified to aluminium tube and eilmer3 by Carolyn Jacobs
9 ## 03-Jun-2009
10 ## Further modifications July 2011
11 ##
12 #####
13
14 # ----- preamble -----
15

```

```

16 import os
17 import sys
18 from math import pi, sin
19
20 # ----- definitions -----
21
22 sin45 = sin(pi/4.0)
23
24 # ----- set global data -----
25
26 gdata.title = "13Pa X2 NRST-Al, Titan mix (98% N2 - 2% CH4)"
27
28 # Set equilibrium or finite-rate option
29 chemistry = 0           # 0 = equilibrium, 1 = finite-rate
30
31 # Two-dimensional axisymmetric simulation
32 gdata.dimensions = 2
33 gdata.axisymmetric_flag = 1
34
35 # Select the equilibrium Titan model
36 select_gas_model(fname='LUT-plus-Ar-He.lua')
37 gdata.reacting_flag = 0
38
39 # Parameters for job control
40 gdata.flux_calc = ADAPTIVE
41 gdata.viscous_flag = 1
42 gdata.max_time = 5.0e-3
43 gdata.max_step = 1000000
44 gdata.dt = 1.0e-8
45 gdata.dt_plot = 5.0e-5
46 gdata.dt_history = 5.0e-7
47 gdata.x_order = 2
48 gdata.t_order = 2          # Perhaps need 2=Predictor-Corrector instead??
49 gdata.cfl = 0.25          # Perhaps need 0.25 instead??
50 gdata.stringnt_cfl = 1    # Uses different cell widths in different index
51 gdata.shear_tolerance = 0.05 # Try and solve the recirculation negative T probs
52
53 # ----- gas mixture definitions -----
54 # Secondary driver initial conditions
55 p10 = 30000.0            # Pa
56 T10 = 296.0               # K
57 u10 = 0.0
58
59 # Shock tube initial conditions
60 p20 = 13.0                # Pa
61 T20 = 296.0                # K
62 u20 = 0.0
63
64 Twall = T10
65
66 # Grid resolution
67 res_factor = 1
68
69 # Species order:      LUT   Ar     He
70 titan_gas      = [ 1.0, 0.0, 0.0 ]
71 primary_driver = [ 0.0, 0.15, 0.85 ]
72 secondary_driver = [ 0.0, 0.0, 1.0 ]
73
74 test_gas = FlowCondition(p=p20, u=u20, v=0.0, T=T20, massf=titan_gas)
75 driver_gas = FlowCondition(p=p10, u=u10, v=0.0, T=T10, massf=secondary_driver)
76 driver_start = FlowCondition(15.5e6, u=0.0, v=0.0, T=2200.0, massf=primary_driver)
77
78 # ----- geometry dimensions -----
79
80 L_tube = 4.731            # m, total length of tube
81
82 # Get the piston location at diaphragm rupture from the L1d2.event file
83 piston = 4.433+0.341/2.0  # m (centre + 1/2width to get piston face)
84
85 # Define cross-section of shock tube in the (x,y)-plane.
86 # Dimensions are in metres.
87 loc_pd = 4.810             # m, primary diaphragm
88 loc_st = piston             # m, start of tube
89 loc_sd = 9.515              # m, secondary diaphragm
90 loc_ac2 = loc_sd + 0.250    # m, area change in shock tube
91 loc_et = loc_ac2 + L_tube  # m, end of tube
92 loc_dt = loc_et - 0.250    # m, start of dump tank
93 loc_es = loc_et + 1.000    # m, end of simulation

```

```

94
95 tube_thickness = 10.0e-3 # m, thickness of shock tube wall
96 dump_tank_radius = 0.100 # m, distance from outer al surface to inner dt surface
97
98 rad_pd = 0.2568/2.0 # m, radius of the primary driver tube
99 rad_dr = 0.085/2.0 # m, radius of the secondary driver tube
100 rad_al = 0.1556/2.0 # m, radius of the aluminium shock tube
101 rad_tt = rad_al + tube_thickness # m, radius of Al tube including thickness
102 rad_dt = rad_tt + dump_tank_radius # m, radius of dump tank simulation area
103
104 transition_radius = 25.0e-3
105 end_driver = 4.675
106 end_transition = 4.7
107
108 # Transducer locations
109 a11 = loc_sd + 0.250 + 0.781
110 a12 = a11 + 1.000
111 a13 = a12 + 1.000
112 a14 = a13 + 1.000
113 a15 = a14 + 0.500
114
115 transducer_locations = {
116     'st1' : 7.381, # m
117     'st2' : 7.614, # m
118     'st3' : 7.845, # m
119     'at1' : 8.755, # m
120     'at2' : 9.005, # m
121     'at3' : 9.255, # m
122     'a11' : a11, # m
123     'a12' : a12, # m
124     'a13' : a13, # m
125     'a14' : a14, # m
126     'a15' : a15 # m
127 }
128
129 # Number of blocks in each tube
130 N1 = 5 # blocks in secondary driver tube
131 N2 = 5 # blocks in shock tube
132 NDX = 1 # blocks in x-dir of dump tank
133 NDY = 2 # blocks in y-dir of dump tank
134 NA = 1 # blocks in adapter/recess blocks
135
136 # Overall discretisation
137 beta = 1.05
138 nnx = 5000*res_factor # number of cells along the shock tube
139 nny = 50*res_factor
140 nny0 = int((rad_pd - rad_dr)/rad_dr*nny)
141 nny6 = int((rad_al - rad_dr)/rad_dr*nny)
142 nny9 = int(tube_thickness/rad_dr*nny)
143 nny10 = int((rad_dt - rad_tt)/rad_al * nny)
144 nnx0 = int((end_transition - loc_st)/L_tube*nnx)
145 nnx2 = int((loc_pd - end_transition)/L_tube*nnx)
146 nnx3 = int((loc_sd - loc_pd)/L_tube*nnx)
147 nnx4 = int((loc_ac2 - loc_sd)/L_tube*nnx)
148 nnx7 = int((loc_es - loc_et)/L_tube*nnx)
149 nnx11 = int((loc_et - loc_dt)/L_tube*nnx)
150
151 a = Node(loc_st, 0.0)
152 b = Node(loc_st, rad_dr+transition_radius*(1.0-sin45))
153 c = Node(loc_st, rad_pd)
154 d = Node(end_driver, rad_pd)
155 e = Node(end_driver, rad_dr+transition_radius)
156 f = Node(end_driver+transition_radius*(1.0-sin45), rad_dr+transition_radius*(1.0-sin45))
157 g = Node(end_transition, rad_dr)
158 h = Node(end_transition, rad_dr+transition_radius)
159 i = Node(loc_pd, rad_dr)
160 j = Node(loc_pd, 0.0)
161 k = Node(end_driver+transition_radius*(1.0-sin45), 0.0)
162 l = Node(loc_sd, rad_dr)
163 m = Node(loc_ac2, rad_al)
164 n = Node(loc_ac2, rad_dr)
165 o = Node(loc_ac2, 0.0)
166 p = Node(loc_sd, 0.0)
167 q = Node(loc_et, rad_al)
168 r = Node(loc_et, rad_tt)
169 s = Node(loc_dt, rad_tt)
170 t = Node(loc_dt, rad_dt)
171 u = Node(loc_et, rad_dt)

```

```

172 v = Node(loc_es, rad_dt)
173 w = Node(loc_es, rad_tt)
174 x = Node(loc_es, rad_al)
175 y = Node(loc_es, 0.0)
176 z = Node(loc_et, 0.0)
177 aa = Node(loc_et, rad_dr)
178 ab = Node(loc_es, rad_dr)
179
180 n0 = Line(c, d)
181 e0 = Polyline([Arc(f, e, h), Line(e, d)])
182 w0 = Line(b, c)
183 s0n1 = Line(b, f)
184
185 e1w2 = Line(k, f)
186 s1 = Line(a, k)
187 w1 = Line(a, b)
188
189 n2 = Polyline([Arc(f, g, h), Line(g, i)])
190 e2w3 = Line(j, i)
191 s2 = Line(k, j)
192
193 n3 = Line(i, l)
194 e3w4 = Line(p, l)
195 s3 = Line(j, p)
196
197 n4 = Line(l, n)
198 e4w5 = Line(o, n)
199 s4 = Line(p, o)
200
201 n5s6 = Line(n, aa)
202 e5w7 = Line(z, aa)
203 s5 = Line(o, z)
204
205 n6 = Line(m, q)
206 e6w8 = Line(aa, q)
207 w6 = Line(n, m)
208
209 n7s8 = Line(aa, ab)
210 e7 = Line(y, ab)
211 s7 = Line(z, y)
212
213 n8s9 = Line(q, x)
214 e8 = Line(ab, x)
215
216 n9s10 = Line(r, w)
217 e9 = Line(x, w)
218 w9 = Line(q, r)
219
220 n10 = Line(u, v)
221 e10 = Line(w, v)
222 w10e11 = Line(r, u)
223
224 n11 = Line(t, u)
225 s11 = Line(s, r)
226 w11 = Line(s, t)
227
228 # Clustering
229 left_stretch = RobertsClusterFunction(0, 1, beta)
230 right_stretch = RobertsClusterFunction(1, 0, beta)
231 both_stretch = RobertsClusterFunction(1, 1, beta)
232
233 blk_0 = Block2D(make_patch(n0, e0, s0n1, w0),
234     nni=nnx0, nnj=nny0,
235     bc_list=[FixedTBC(Twall), FixedTBC(Twall), AdjacentBC(), FixedTBC(Twall)],
236     cf_list=[None, None, None, None],
237     fill_condition=driver_start, label="blk_0")
238
239 blk_1 = Block2D(make_patch(s0n1, e1w2, s1, w1),
240     nni=nnx0, nnj=nny,
241     bc_list=[AdjacentBC(), AdjacentBC(), SlipWallBC(), FixedTBC(Twall)],
242     cf_list=[None, None, None, None],
243     fill_condition=driver_start, label="blk_1")
244
245 blk_2 = Block2D(make_patch(n2, e2w3, s2, e1w2),
246     nni=nnx2, nnj=nny,
247     bc_list=[FixedTBC(Twall), AdjacentBC(), SlipWallBC(), AdjacentBC()],
248     cf_list=[None, left_stretch, None, None],
249     fill_condition=driver_start, label="blk_2")

```

```

250
251 blk_3 = SuperBlock2D(make_patch(n3, e3w4, s3, e2w3),
252                         nni=nnx3, nnj=nny,
253                         nbi=N1, nbj=1,
254                         bc_list=[FixedTBC(Twall), AdjacentPlusUDFBC("diaphragm.lua"), SlipWallBC(),
255                                     AdjacentBC()],
256                         cf_list=[None, left_stretch, None, left_stretch],
257                         fill_condition=driver_gas, label="blk_3")
258
259 B3 = Block.blockList[-1]
260
261 blk_4 = SuperBlock2D(make_patch(n4, e4w5, s4, e3w4),
262                         nni=nnx4, nnj=nny,
263                         nbi=1, nbj=1,
264                         bc_list=[FixedTBC(Twall), AdjacentBC(), SlipWallBC(), AdjacentPlusUDFBC("diaphragm",
265                                     .lua)],
266                         cf_list=[None, left_stretch, None, left_stretch],
267                         fill_condition=test_gas, label="blk_4")
268
269 B4 = Block.blockList[-1]
270
271 blk_5 = SuperBlock2D(make_patch(n5s6, e5w7, s5, e4w5),
272                         nni=nnx, nnj=nny,
273                         nbi=N2, nbj=1,
274                         bc_list=[AdjacentBC(), AdjacentBC(), SlipWallBC(), AdjacentBC()],
275                         cf_list=[right_stretch, left_stretch, right_stretch, left_stretch],
276                         fill_condition=test_gas, label="blk_5")
277
278 blk_6 = SuperBlock2D(make_patch(n6, e6w8, n5s6, w6),
279                         nni=nnx, nnj=nny6,
280                         nbi=N2, nbj=1,
281                         bc_list=[FixedTBC(Twall), AdjacentBC(), AdjacentBC(), FixedTBC(Twall)],
282                         cf_list=[right_stretch, left_stretch, right_stretch, left_stretch],
283                         fill_condition=test_gas, label="blk_6")
284
285 blk_7 = SuperBlock2D(make_patch(n7s8, e7, s7, e5w7),
286                         nni=nnx7, nnj=nny,
287                         nbi=NDX, nbj=1,
288                         bc_list=[AdjacentBC(), ExtrapolateOutBC(), SlipWallBC(), AdjacentBC()],
289                         cf_list=[None, left_stretch, None, left_stretch],
290                         fill_condition=test_gas, label="blk_7")
291
292 blk_8 = SuperBlock2D(make_patch(n8s9, e8, n7s8, e6w8),
293                         nni=nnx7, nnj=nny6,
294                         nbi=NDX, nbj=1,
295                         bc_list=[AdjacentBC(), ExtrapolateOutBC(), AdjacentBC(), AdjacentBC()],
296                         cf_list=[None, None, None, None],
297                         fill_condition=test_gas, label="blk_8")
298
299 blk_9 = SuperBlock2D(make_patch(n9s10, e9, n8s9, w9),
300                         nni=nnx7, nnj=nny9,
301                         nbi=NDX, nbj=1,
302                         bc_list=[AdjacentBC(), ExtrapolateOutBC(), AdjacentBC(), FixedTBC(Twall)],
303                         cf_list=[None, None, None, None],
304                         fill_condition=test_gas, label="blk_9")
305
306 blk_10 = SuperBlock2D(make_patch(n10, e10, n9s10, w10e11),
307                         nni=nnx7, nnj=nny10,
308                         nbi=NDX, nbj=NDY,
309                         bc_list=[FixedTBC(Twall), ExtrapolateOutBC(), AdjacentBC(), AdjacentBC()],
310                         cf_list=[None, None, None, None],
311                         fill_condition=test_gas, label="blk_10")
312
313 blk_11 = SuperBlock2D(make_patch(n11, w10e11, s11, w11),
314                         nni=nnx11, nnj=nny10,
315                         nbi=NA, nbj=NDY,
316                         bc_list=[FixedTBC(Twall), AdjacentBC(), FixedTBC(Twall), FixedTBC(Twall)],
317                         cf_list=[None, None, None, None],
318                         fill_condition=test_gas, label="blk_11")
319
320 ##### Workaround for the AdjacentPlusUDFBC() for SuperBlock2D
321 # Workaround for the AdjacentPlusUDFBC() for SuperBlock2D
322 diaphragm_us = B3
323 diaphragm_ds = B4
324 connect_blocks_2D(diaphragm_us, EAST, diaphragm_ds, WEST, with_udf=1, filename="diaphragm.lua", is_wall
=0, use_udf_flux=0)

```

```

325 #####
326 # ----- result extraction -----
327 sketch.scales(0.04, 1.0)
328 sketch.origin(0.05,0.05)
329 sketch.xaxis(0.0, 25.0, 5.0, -0.01)
330 sketch.yaxis(0.0, 0.1, 0.05, -0.10)
331
332 # Set the history cell locations
333 radial_locations = [0.0, 0.05*rad_al, 0.5*rad_al, rad_al]
334 transducer_keys = ['st1', 'st2', 'st3', 'at1', 'at2', 'at3', 'all', 'al2', 'al3', 'al4', 'al5']
335
336 for key in transducer_keys:
337     for iy, y in enumerate(radial_locations):
338         HistoryLocation(transducer_locations[key], y, label="%s-%d" % (key, iy))
339
340 HistoryLocation(loc_et+1.0e-2, rad_al/3.0, label="Pitot")
341
342

```

A script describing the secondary diaphragm was adapted from the work of Hess (2009).

```

1 --- diaphragm.lua
2 --- Lua script for the user-defined functions
3 --- called by the AdjacentPlusUDFBC.
4 ---
5 --- Adapted from udf-slip-wall.lua
6 --- Stefan Hess, 01-Jun-2009
7
8
9 --- User defined variables
10 -----
11 p_burst=75.0e3
12 is_burst=false
13 -----
14
15 function reflect_normal_velocity(ux, vy, cosX, cosY)
16     -- Copied from cns_bc.h.
17     un = ux * cosX + vy * cosY;      -- Normal velocity
18     vt = -ux * cosY + vy * cosX;    -- Tangential velocity
19     un = -un;                      -- Reflect normal component
20     ux = un * cosX - vt * cosY;    -- Back to Cartesian coords
21     vy = un * cosY + vt * cosX;
22     return ux, vy
23 end
24
25 function ghost_cell(args)
26     -- Function that returns the flow state for a ghost cell
27     -- for use in the inviscid flux calculations.
28     --
29     -- args contains t, x, y, z, csX, csY, csZ, i, j, k, which_boundary
30     i = args.i; j = args.j; k = args.k
31     cell1 = sample_flow(block_id, i, j, k)
32     if args.which_boundary == NORTH then
33         cell0 = sample_flow(block_id, i, j+1, k)
34         cell2 = sample_flow(block_id, i, j-1, k)
35     elseif args.which_boundary == EAST then
36         cell0 = sample_flow(block_id, i-1, j, k)
37         cell2 = sample_flow(block_id, i-1, j, k)
38     elseif args.which_boundary == SOUTH then
39         cell0 = sample_flow(block_id, i, j-1, k)
40         cell2 = sample_flow(block_id, i, j+1, k)
41     elseif args.which_boundary == WEST then
42         cell0 = sample_flow(block_id, i-1, j, k)
43         cell2 = sample_flow(block_id, i+1, j, k)
44     end
45
46     if is_burst==false then
47         if math.abs(cell0.p-cell1.p)>=p_burst then
48             is_burst=true
49             print("Diaphragm burst at t=",args.t,", in block,i,j = ",block_id,i,j)
50             return nil, nil
51         end
52         cell1.u, cell1.v =
53             reflect_normal_velocity(cell1.u, cell1.v, args.csX, args.csY)

```

```
54     cell2.u, cell2.v =
55         reflect_normal_velocity(cell1.u, cell1.v, args.csX, args.csY)
56     return cell1, cell2
57   else
58     return nil, nil
59   end
60 end
61
62 function zero_normal_velocity(ux, vy, cosX, cosY)
63   -- Just the interesting bits from reflect_normal_velocity().
64   vt = -ux * cosY + vy * cosX;      -- Tangential velocity
65   ux = -vt * cosY;                  -- Back to Cartesian coords
66   vy =  vt * cosX;                 -- just tangential component
67   return ux, vy
68 end
69
70 function interface(args)
71   -- Function that returns the conditions at the boundary
72   -- when viscous terms are active.
73   --
74   -- args contains t, x, y, z, csX, csY, csZ, i, j, k, which_boundary
75   if is_burst==false then
76     cell = sample_flow(block_id, args.i, args.j, args.k)
77     cell.u, cell.v = zero_normal_velocity(cell.u, cell.v, args.csX, args.csY)
78     return cell
79   else
80     return nil
81   end
82 end
```


APPENDIX D

Calibration Code for Emission Spectroscopy

D.1 Main code

All of the final codes were written in MATLAB. An example of the code used to process the experimental data is given here.

```
1 %%%%%%
2 %
3 % Control script to run the calibration code %
4 %
5 % Written by Carolyn Jacobs %
6 % 18-Nov-2010 %
7 %
8 %%%%%%
9 %
10 %%%%%%
11 % SETUP DETAILS %
12 %%%%%%
13 %
14 clear all
15 close all
16 clc
17 %
18 % Spectrometer setup details
19 specSetup.message = 'Spectrometer settings are as per C. Jacobs (Aug 2010)';
20 specSetup.irisRad = 15.0e-3 / 2.0;      % Radius of iris , m
21 specSetup.m1Dist = 576.0e-3;           % Distance from centreline to first mirror , m
22 specSetup.mirrorDist = 240.0e-3;        % Distance between mirrors , m
23 specSetup.irisDist = 642.0e-3;          % Distance from second mirror to iris , m
24 specSetup.lensDist = 120.0e-3;          % Distance from iris to curved mirror , m
25 specSetup.specDist = 100.0e-3;          % Distance from curved mirror to slit , m
26 specSetup.tubeDiameter = 155.0e-3;       % Width of tube exit , m
27 %
28 % Calibration lamp file
29 lampFile = 'S-1197N0.std';
30 %
```

```

31 %%%%%%%%%%%%%%%%%%%%%%%%%%%%%%%%%%%%%%
32 % 13 Pa
33 %%%%%%%%%%%%%%%%%%%%%%%%%%%%%%%%%%%%%%
34
35 % Parameters needed for the calculation of the Gouillard number
36 density = 1.4671e-4; % kg/m^3
37 velocity = 6410.0; % m/s
38 test_length = 0.173; % m
39
40 shotName = 'x2s1470';
41 dataDirectory = fullfile('..', 'experimental', shotName);
42 calibFile = 'calibration_600BLZ_100micronslit_10usexposure_2frames_100accumulations_240gain.SPE';
43 calibType = 'multiframe-acc100';
44 specSetup.apertureRad = 100.0e-6; % Spectrometer slit width, m
45 expScaling = 66.02; % calibExp / imageExp scaling factor
46 lossMethod = 'fromMeasurement';
47 specDir = '../spectroscopic/Carolyn-component-calib/';
48 specFile = '600 grating -380nm-exp50us-2frames-100acc-10um.SPE';
49 calibration(dataDirectory, calibFile, calibType, lampFile, shotName, specSetup, density, velocity, test_length,
   expScaling, lossMethod, specDir, specFile);
50
51 close all;

```

D.2 Main function

```

1 function [] = calibration(dataDirectory, calibFile, calibType, lampFile, shotName, specSetup, density, velocity
   , test_length, expScaling, lossMethod, specDir, specFile);
2
3 %%%%%%%%%%%%%%%%%%%%%%%%%%%%%%%%%%%%%%
4 %
5 % Calibration code for spectroscopic data
6 %
7 % Version 8
8 % Written by Carolyn Jacobs
9 % 28-April-2011
10 %
11 % Based on the calibration codes previously written by Troy Eichmann,
12 % Aaron Brandis, and older versions of this same code
13 %
14 %%%%%%%%%%%%%%%%%%%%%%%%%%%%%%%%%%%%%%
15
16 % SETUP DETAILS
17 %%%%%%%%%%%%%%%%%%%%%%%%%%%%%%%%%%%%%%
18
19 fprintf(1,'-----\n');
20 fprintf(1,'File: calibration.m\n\n');
21 fprintf(1,'Emission spectroscopy calibration procedure\n\n');
22 fprintf(1,'Carolyn Jacobs\n');
23 fprintf(1,'Centre for Hypersonics\n');
24 fprintf(1,'The University of Queensland, Australia\n');
25 fprintf(1,'-----\n');
26 fprintf(1,'Initial setup\n');
27
28 clipThreshold = 400; % Threshold for hot pixel clipping
29 figureCount = 0; % Start a counter for the figures
30 plotCalib = 1; % Switch for plotting calibration images
31 plotFigures = 1; % Switch for plotting other images
32
33 % Data directory
34 fprintf(1,'Data files sourced from the directory:\n\t %s\n', dataDirectory);
35
36 % Settings for the calibration files
37 calibFileNoOptics = fullfile(dataDirectory, calibFile);
38 fprintf(1,'Calibration file:\n\t %s\n', calibFileNoOptics);
39
40 % Settings for the shot file
41 shotFile = fullfile(dataDirectory, [shotName, 'UV.SPE']);
42 backgroundFile = fullfile(dataDirectory, [shotName, 'UV_background.SPE']);
43 fprintf(1,'Data file being calibrated:\n\t %s\n', shotFile);
44
45 % Spectrometer setup details
46 fprintf(1,'%\n', specSetup.message)
47 apertureRad = specSetup.apertureRad; % Spectrometer slit width, m

```

```

49 irisRad = specSetup.irisRad; % Radius of iris , m
50 m1Dist = specSetup.m1Dist; % Dist from CL to 1st mirror , m
51 mirrorDist = specSetup.mirrorDist; % Dist between mirrors , m
52 irisDist = specSetup.irisDist; % Dist from 2nd mirror to iris , m
53 lensDist = specSetup.lensDist; % Dist from iris to curved mirror , m
54 specDist = specSetup.specDist; % Dist from curved mirror to slit , m
55 tubeDiameter = specSetup.tubeDiameter;% Width of tube exit , m
56
57 % Calculate the magnification of the system
58 preIris = m1Dist + mirrorDist + irisDist; % Total dist between iris and CL
59 magnification = specDist / (preIris + lensDist);
60 fprintf(1,'nMagnification of image: %f\n',magnification);
61
62 % Define the dimensions of the test flow
63 slitHeight = 6.7 * 1.0e-3; % Height of slit capture , m
64 testLength = slitHeight / magnification; % Length of image captured , m
65 fieldWidth = tubeDiameter; % ASSUME: 100% FOCUS + NO EXPANSION
66
67 % Calculate focal length and f-number of the system
68 focalLength = 1.0 / ((1.0 / (preIris + lensDist)) + (1.0 / specDist));
69 fNo = focalLength / (irisRad * 2.0);
70
71 % Calculate solid angle
72 solidAngle = pi * (irisRad^2) / (preIris^2);
73 fprintf(1,'nSolid angle: %f e-6 sr\n',solidAngle*1e6);
74
75 % Create the mask for the ICCD array
76 width = 1024;
77 height = 256;
78 maskWidth = 50;
79 mask = [ zeros(10,width); zeros(height-20,maskWidth) ...
80 ones(height-20,width-(2*maskWidth)) zeros(height-20,maskWidth); ...
81 zeros(10,width) ];
82 maskStrip = [ zeros(1,maskWidth) ones(1,width-(2*maskWidth)) ...
83 zeros(1,maskWidth) ];
84
85 % Calculate the axial distance array , mm
86 axialDist = zeros(1,height);
87 for axialCount = 1:height
88 axialDist(axialCount) = (axialCount - 1) * slitHeight * 1.0e3 / ...
89 (magnification * height);
90 end
91
92 %%%%%%%%
93 % LOAD SHOT AND BACKGROUND DATA
94 %%%%%%%%
95
96 % Import data files
97 try
98 [shotData,shotWavelength,shotDescription] = SPEread(shotFile);
99 catch exception
100 % Did the read fail because the file could not be found?
101 if ~exist(shotFile, 'file')
102 fprintf(1,'nERROR: Loading shot data failed. Filename does not exist.');
103 % Try modifying the filename extension.
104 altShotFile = strrep(shotFile, '.SPE', '.spe');
105 fprintf(1,'nNew data file being calibrated:\n\t%s\n', altShotFile);
106 [shotData,shotWavelength,shotDescription] = SPEread(altShotFile);
107 end
108 end
109 shotDescription
110
111 % Define the exposure time of the data image (s)
112 imageExp = shotDescription.exposure_us * 1.0e-6;
113 fprintf(1,'nExposure time for data images: %e seconds\n',imageExp);
114
115 % Mask the wavelength and the shot data
116 % shotWavelengthMask = shotWavelength(maskWidth:width-maskWidth);
117 % shotImage = shotData.*mask;
118 shotImage = shotData;
119
120 % Plotting images for the calibration description
121 if plotCalib == 1
122 % Plot the original data in colour
123 figureCount = figureCount + 1;
124 figure(figureCount);
125 imagesc(shotWavelength, axialDist, shotImage);
126 % title(['Original shot data for ' shotName]);

```

```

127 xlabel('Wavelength (nm)');
128 ylabel('Axial distance (mm)');
129 axis image;
130 figureName = fullfile(dataDirectory, [shotName, '_original']);
131 print('-depsc', figureName);
132
133 % Comment out - Linux version of Matlab doesn't handle the surface plots
134 % well...
135 % figureCount = figureCount + 1;
136 % figure(figureCount);
137 % surf(shotWavelength, axialDist, shotImage);
138 % shading interp;
139 % % title(['Original shot data for ' shotName]);
140 % xlabel('Wavelength (nm)');
141 % ylabel('Axial distance (mm)');
142 % zlabel('Intensity (counts)');
143 % axis image;
144 % figureName = fullfile(dataDirectory, [shotName, '_original_surf']);
145 % print('-depsc', figureName);
146
147 % Save the data for the unprocessed shot
148 unprocessedShotFile = fullfile(dataDirectory, [shotName, '_unprocessedshot.dat']);
149 s1 = fopen(unprocessedShotFile, 'w');
150 fprintf(s1, '# Unprocessed data for shot %s \n', shotName);
151 fprintf(s1, '# Units are counts \n');
152 fprintf(s1, '# Columns are wavelength, axialDist, shotImage \n');
153 for axialCount = 1:length(shotWavelength)
154     for axialCount2 = 1:length(axialDist)
155         fprintf(s1, '%f \t %f \t %f \n', shotWavelength(axialCount), axialDist(axialCount2),
156                 shotImage(axialCount2, axialCount));
157     end
158 end
159 fclose(s1);
160
161 % Subtract out the background
162 % Use the first 20 pixel horizontal strip
163 disp('Using a corner strip to generate background level.');
164 shotBackground = shotData(:, 2:21);
165 meanShotBackground = mean(mean(shotBackground));
166 shotImageBG = (shotImage - meanShotBackground);
167
168 % Fix up any values that go negative
169 shotImageBG(shotImageBG <= 0.0) = [1.0e-9];
170
171 % Plotting images for the calibration description
172 if plotCalib == 1
173     % Plot the subtracted background data in colour
174     figureCount = figureCount + 1;
175     figure(figureCount);
176     imagesc(shotWavelength, axialDist, shotImageBG);
177     % title(['Shot data with background noise subtracted for ' shotName]);
178     xlabel('Wavelength (nm)');
179     ylabel('Axial distance (mm)');
180     axis image;
181     figureName = fullfile(dataDirectory, [shotName, '_background']);
182     print('-depsc', figureName);
183
184 % Comment out - Linux version of Matlab doesn't handle the surface plots
185 % well...
186 % figureCount = figureCount + 1;
187 % figure(figureCount);
188 % surf(shotWavelength, axialDist, shotImageBG);
189 % shading interp;
190 % % title(['Shot data with background noise subtracted for ' shotName]);
191 % xlabel('Wavelength (nm)');
192 % ylabel('Axial distance (mm)');
193 % zlabel('Intensity (counts)');
194 % axis image;
195 % figureName = fullfile(dataDirectory, [shotName, '_background_surf']);
196 % print('-depsc', figureName);
197
198 % Save the data for the background subtracted shot
199 backgroundShotFile = fullfile(dataDirectory, [shotName, '_backgroundsubtractedshot.dat']);
200 s2 = fopen(backgroundShotFile, 'w');
201 fprintf(s2, '# Background subtracted data for shot %s \n', shotName);
202 fprintf(s2, '# Units are counts \n');
203 fprintf(s2, '# Columns are wavelength, axialDist, shotImageBG \n');

```

```

204     for axialCount = 1:length(shotWavelength)
205         for axialCount2 = 1:length(axialDist)
206             fprintf(s2, '%f \t %f \t %f \n', shotWavelength(axialCount), axialDist(axialCount2),
207                     shotImageBG(axialCount2, axialCount));
208         end
209     fclose(s2);
210 end
211
212 % Remove hot pixels from the data
213 shotImageFilter = cosmic_filter(shotImageBG, clipThreshold);
214
215 % Plotting images for the calibration description
216 if plotCalib == 1
217     % Plot the hot pixel removed data in colour
218     figureCount = figureCount + 1;
219     figure(figureCount);
220     imagesc(shotWavelength, axialDist, shotImageFilter);
221     % title(['Shot data with hot pixel noise subtracted for ' shotName]);
222     xlabel('Wavelength (nm)');
223     ylabel('Axial distance (mm)');
224     axis image;
225     figureName = fullfile(dataDirectory, [shotName, '_cosmic']);
226     print('-depsc', figureName);
227
228 % Save the data for the background subtracted shot
229 filteredShotFile = fullfile(dataDirectory, [shotName, '_cosmicfiltershot.dat']);
230 s3 = fopen(filteredShotFile, 'w');
231 fprintf(s3, '# Background subtracted data for shot %s \n', shotName);
232 fprintf(s3, '# Units are counts \n');
233 fprintf(s3, '# Columns are wavelength, axialDist, shotImageFilter \n');
234 for axialCount = 1:length(shotWavelength)
235     for axialCount2 = 1:length(axialDist)
236         fprintf(s3, '%f \t %f \t %f \n', shotWavelength(axialCount), axialDist(axialCount2),
237                 shotImageFilter(axialCount2, axialCount));
238     end
239 end
240 fclose(s3);
241
242 % Final shot image after processing is complete
243 shotImageFinal = shotImageFilter;
244
245 % LOAD CALIBRATION DATA
246 % Load the calibration file for no optics
247 [calibImage, calibWavelength, calibDescription] = SPEread(calibFileNoOptics);
248 calibDescription
249
250 % Define the exposure time of the data image(s)
251 calibExp = calibDescription.exposure_us * 1.0e-6;
252 fprintf(1, '\nExposure time for calibration images: %e seconds\n', calibExp);
253
254 switch calibType
255     case {'multiframe'}
256         % Ignoring the first frame, take an average of the other 9 images
257         calibImage = calibImage(:, :, 2:size(calibImage, 3));
258         calibImage = mean(calibImage, 3);
259     case {'multiframe-acc100'}
260         % Remove the first frame and divide second by number of accumulations
261         calibImage = calibImage(:, :, 2) ./ 100;
262     case {'accumulation'}
263         % Divide through by the number of accumulations
264         calibImage = calibImage / 100;
265     otherwise
266         disp('Calibration image does not fit standard types.')
267 end
268
269 % Mask the wavelength
270 % calibWavelengthMask = calibWavelength(maskWidth:width-maskWidth);
271 % calibImage = calibImage.*mask;
272
273 % Plotting images for the calibration description
274 if plotCalib == 1
275     % Plot the original data in colour
276     figureCount = figureCount + 1;

```

```

280 figure.figureCount;
281 imagesc(calibWavelength, axialDist, calibImage);
282 % title(['Original calibration data for ' shotName]);
283 xlabel('Wavelength (nm)');
284 ylabel('Axial distance (mm)');
285 axis image;
286 figureName = fullfile(dataDirectory, [shotName, '_calib_original']);
287 print('-depsc', figureName);
288
289 % Save the data for the unprocessed calibration
290 unprocessedCalibFile = fullfile(dataDirectory, [shotName, '_unprocessedcalib.dat']);
291 s4 = fopen(unprocessedCalibFile, 'w');
292 fprintf(s4, '# Unprocessed calibration for shot %s \n', shotName);
293 fprintf(s4, '# Units are counts \n');
294 fprintf(s4, '# Columns are wavelength, axialDist, calibImage \n');
295 for axialCount = 1:length(shotWavelength)
296     for axialCount2 = 1:length(axialDist)
297         fprintf(s4, '%f \t %f \t %f \n', shotWavelength(axialCount), axialDist(axialCount2),
298                 calibImage(axialCount2, axialCount));
299     end
300 end
301 fclose(s4);
302
303 % Subtract out the background using the shot background file (should be
304 % about the same)
305 % Use the first 20 pixel horizontal strip
306 disp('Using corner strip to generate background level')
307 calibBackground = calibImage(:, 2:21);
308 meanCalibBackground = mean(mean(calibBackground));
309 calibImageBG = (calibImage - meanCalibBackground);
310
311 figureCount = figureCount + 1;
312 figure(figureCount);
313 plot(shotWavelength, calibImage(20,:))
314
315 % Fix up any values that go negative
316 calibImageBG(calibImageBG <= 0.0) = [1.0e-9];
317
318 % Plotting images for the calibration description
319 if plotCalib == 1
320     % Plot the original data in colour
321     figureCount = figureCount + 1;
322     figure(figureCount);
323     imagesc(calibWavelength, axialDist, calibImage);
324     % title(['Calibration data with background noise subtracted for ' shotName]);
325     xlabel('Wavelength (nm)');
326     ylabel('Axial distance (mm)');
327     axis image;
328     figureName = fullfile(dataDirectory, [shotName, '_calib_background']);
329     print('-depsc', figureName);
330
331     % Save the data for the background subtracted calibration
332     backgroundCalibFile = fullfile(dataDirectory, [shotName, '_backgroundsubtractedcalib.dat']);
333     s5 = fopen(backgroundCalibFile, 'w');
334     fprintf(s5, '# Background subtracted calibration for shot %s \n', shotName);
335     fprintf(s5, '# Units are counts \n');
336     fprintf(s5, '# Columns are wavelength, axialDist, calibImageBG \n');
337     for axialCount = 1:length(shotWavelength)
338         for axialCount2 = 1:length(axialDist)
339             fprintf(s5, '%f \t %f \t %f \n', shotWavelength(axialCount), axialDist(axialCount2),
340                     calibImageBG(axialCount2, axialCount));
341     end
342 end
343 fclose(s5);
344
345 % Remove hot pixels from the data
346 calibImageFilter = cosmic_filter(calibImageBG, clipThreshold);
347
348 % Plotting images for the calibration description
349 if plotCalib == 1
350     % Plot the hot pixel removed data in colour
351     figureCount = figureCount + 1;
352     figure(figureCount);
353     imagesc(shotWavelength, axialDist, calibImageFilter);
354     % title(['Shot data with hot pixel noise subtracted for ' shotName]);
355     xlabel('Wavelength (nm)');

```

```

356 ylabel('Axial distance (mm)');
357 axis image;
358 figureName = fullfile(dataDirectory, [shotName, '_calib_cosmic']);
359 print('-depsc', figureName);
360
361 % Save the data for the background subtracted shot
362 filteredCalibFile = fullfile(dataDirectory, [shotName, '_cosmicfiltercalib.dat']);
363 s6 = fopen(filteredCalibFile, 'w');
364 fprintf(s6, '# Hot pixel subtracted calibration for shot %s \n', shotName);
365 fprintf(s6, '# Units are counts \n');
366 fprintf(s6, '# Columns are wavelength, axialDist, calibImageFilter \n');
367 for axialCount = 1:length(shotWavelength)
368     for axialCount2 = 1:length(axialDist)
369         fprintf(s6, '%f \t %f \t %f \n', shotWavelength(axialCount), axialDist(axialCount2),
370                 calibImageFilter(axialCount2, axialCount));
371     end
372 end
373 fclose(s6);
374
375 % Final calibration image after processing is complete
376 calibImageFinal = calibImageFilter;
377
378 %%%%%%%%%%%%%%%%%%%%%%%%%%%%%%%%%%%%%%
379 % CALCULATE CALIBRATION CURVE WITHOUT OPTICS
380 %%%%%%%%%%%%%%%%%%%%%%%%%%%%%%%%%%%%%%
381
382 % Import calibration curve data
383 calibStandard = load(lampFile);
384
385 % Add an extra data point to zero things below 250nm
386 calibStandard = [ 200, 0 ; calibStandard ];
387
388 % Spline fit the region of interest in the calibration data
389 calFit = spline(calibStandard (:,1),calibStandard (:,2),shotWavelength);
390
391 if min(shotWavelength) < 250.0
392     % Find all wavelengths greater than (or equal to) 250nm
393     zeroWavelength = shotWavelength >= 250.0;
394
395     % For all data points below a wavelength of 250nm, zero the calFit matrix
396     calFit = calFit .* zeroWavelength;
397 end
398
399 % Spread the calFit over all axial positions
400 calFit = ones(256,1) * calFit;
401
402 % Plotting images for the calibration description
403 if plotCalib == 1
404     % Plot the curve fit for the values from the standard
405     figureCount = figureCount + 1;
406     figure(figureCount);
407     plot(shotWavelength, calFit(1,:), '-.', ...
408          calibStandard (:,1), calibStandard (:,2), 'g+');
409     legend('Spline fit', 'Calibration data');
410     % title('Calibration curve data with spline fit ');
411     xlabel('Wavelength (nm)');
412     ylabel('Spectral Irradiance (W/(cm^2 nm))');
413     figureName = fullfile(dataDirectory, [shotName, '_calibcurve']);
414     print('-depsc', figureName);
415 end
416
417 %%%%%%%%%%%%%%%%%%%%%%%%%%%%%%%%%%%%%%
418 % CALCULATE THE LOSSES INCURRED IN THE OPTICAL SYSTEM
419 %%%%%%%%%%%%%%%%%%%%%%%%%%%%%%%%%%%%%%
420
421 switch lossMethod
422 case {'fromFile'}
423     % Load the mirror data
424     mirrorReflectivity = load('f01-mirrors.dat');
425     windowTransmissivity = 0.90;
426     curvedReflectivity = load('g01-mirrors.dat');
427
428     % Spline fit the region of interest in the reflectivity data
429     Ref1Fit = spline(mirrorReflectivity (:,1),mirrorReflectivity (:,2)/100,shotWavelength);
430     Ref2Fit = spline(curvedReflectivity (:,1),curvedReflectivity (:,2)/100,shotWavelength);
431
432     % Spread the calFit over all axial positions

```

```

433 Ref1Fit = ones(256,1) * Ref1Fit;
434 Ref2Fit = ones(256,1) * Ref2Fit;
435
436 % Calculate the optical efficiency
437 opticalEfficiency = windowTransmissivity .* Ref1Fit .* Ref1Fit .* ...
438 .* Ref2Fit;
439
440 case {'fromMeasurement'}
441 % Create the strings describing the files needed
442 squareFile = strcat(specDir,'square-',specFile);
443 roundFile = strcat(specDir,'round-',specFile);
444 curvedFile = strcat(specDir,'spherical-',specFile);
445 windowFile = strcat(specDir,'window-',specFile);
446 specFile = strcat(specDir,specFile);
447
448 % Load the experimental data
449 [specBase, specWavelength, specDesc] = SPEread(specFile);
450 [squareData, squareWavelength, squareDesc] = SPEread(squareFile);
451 [roundData, roundWavelength, roundDesc] = SPEread(roundFile);
452 [curvedData, curvedWavelength, curvedDesc] = SPEread(curvedFile);
453 [windowData, windowWavelength, windowDesc] = SPEread(windowFile);
454
455 % Extract the rows of interest and average
456 % NB. use second frame only
457 ROI = fix(height/2.0); % Choose to look at the centre of the images
458 squareReflectivity = mean(squareData(ROI-2:ROI+2,:,:2),1) ./ mean(specBase(ROI-2:ROI+2,:,:2),1);
459 roundReflectivity = mean(roundData(ROI-2:ROI+2,:,:2),1) ./ mean(specBase(ROI-2:ROI+2,:,:2),1);
460 curvedReflectivity = mean(curvedData(ROI-2:ROI+2,:,:2),1) ./ mean(specBase(ROI-2:ROI+2,:,:2),1);
461 windowTransmissivity = mean(windowData(ROI-2:ROI+2,:,:2),1) ./ mean(specBase(ROI-2:ROI+2,:,:2),1)
462 ;
463
464 % Spread the averaged result over all axial positions
465 squareReflectivity = ones(256,1) * squareReflectivity;
466 roundReflectivity = ones(256,1) * roundReflectivity;
467 curvedReflectivity = ones(256,1) * curvedReflectivity;
468 windowTransmissivity = ones(256,1) * windowTransmissivity;
469
470 % Calculate the optical efficiency
471 opticalEfficiency = windowTransmissivity .* squareReflectivity ...
472 .* roundReflectivity .* roundReflectivity ...
473 .* curvedReflectivity;
474
475 otherwise
476 disp('ERROR: Incorrect calculation of optical losses');
477 end
478
479 % Plot the optical efficiency data in colour
480 if plotFigures == 1
481 figureCount = figureCount + 1;
482 figure(figureCount);
483 plot(shotWavelength, opticalEfficiency(1,:));
484 colormap(hot);
485 title(['Efficiency for ' shotName]);
486 xlabel('Wavelength (nm)');
487 ylabel('Axial distance (mm)');
488 axis image;
489 figureName = fullfile(dataDirectory, [shotName, '_efficiency']);
490 print('-depsc', figureName);
491 end
492 %%%%%%%%%%%%%%%%%%%%%%%%%%%%%%%%%%%%%%
493 % CALIBRATE AND CLEAN UP THE CALIBRATED IMAGE
494 %%%%%%%%%%%%%%%%%%%%%%%%%%%%%%%%%%%%%%
495
496 % Adjustment factor for the optics
497 calibAdjust = (magnification)^2.0 ./ opticalEfficiency;
498
499 % Get a final calibration image with units
500 % [ W / cm^2 nm count] by dividing the raw calibration shot by calibExpand
501 finalCalibration = calibAdjust.*calibFit./calibImageFinal;
502
503 % Calculate the calibrated spectral radiance from the shot
504 % W/(cm^2 nm sr)
505 % - Scale the exposure time based on the linearity curve
506 % (expScaling = calibExp / imageExp)
507 radianceFactor = expScaling / solidAngle;
508 spectralRadiance = shotImageFinal.*radianceFactor.*finalCalibration;
509

```

```

510 % Mask the edges of the ICCD array
511 spectralRadiance = spectralRadiance.*mask;
512
513 % Fix up any values that go negative
514 spectralRadiance(spectralRadiance<=0.0) = [1.0e-9];
515
516 % % Clip any values that are divided by close to 0 by calibImageFinal
517 % spectralRadiance(spectralRadiance>clipThreshold) = [clipThreshold];
518
519 % Save a copy of the unfiltered radiance image
520 unfilteredSpectralRadiance = spectralRadiance;
521
522 % Plot the radiance data in colour
523 if plotFigures == 1
524     figureCount = figureCount + 1;
525     figure(figureCount);
526     imagesc(shotWavelength, axialDist, unfilteredSpectralRadiance);
527     colormap(hot);
528     title(['Calibrated spectral radiance data for ' shotName]);
529     xlabel('Wavelength (nm)');
530     ylabel('Axial distance (mm)');
531     axis image;
532     figureName = fullfile(dataDirectory, [shotName, '_plotradiance']);
533     print('-depsc', figureName);
534 end
535
536 %%%%%%
537 % CALCULATE SPECTRAL PROPERTIES
538 %%%%%%
539
540 % Calculate the calibrated spectral power density from the shot
541 % W/(cm^3 nm sr)
542 spectralPowerDensity = spectralRadiance ./ (100.0 * fieldWidth);
543 % The factor of 100 comes from the fact that the testLength is in m
544 % and the spectral radiance and spectral power density units are cm
545
546 % Calculate the calibrated radiance from the shot
547 % W/(cm^2 sr)
548 radiance = sum(spectralRadiance, 2) * (shotWavelength(2) - shotWavelength(1));
549
550 if plotFigures == 1
551     % Plot the summed spectral radiance curve
552     figureCount = figureCount + 1;
553     figure(figureCount);
554     plot(axialDist, radiance');
555     title('Spectral radiance (sum)');
556     xlabel('Axial distance, mm');
557     ylabel('Radiance (summed), W/(cm^2 sr)');
558     figureName = fullfile(dataDirectory, [shotName, '_rad']);
559     print('-depsc', figureName);
560 end
561
562 % Calculate the calibrated power density from the shot
563 % W/(cm^3 sr)
564 powerDensity = radiance ./ (100.0 * fieldWidth);
565
566 % Plot the power density curve
567 if plotFigures == 1
568     figureCount = figureCount + 1;
569     figure(figureCount);
570     plot(axialDist, powerDensity);
571     title('Power density (sum)');
572     xlabel('Axial distance, mm');
573     ylabel('Power density, W/(cm^3 sr)');
574     figureName = fullfile(dataDirectory, [shotName, '_powerdensity']);
575     print('-depsc', figureName);
576 end
577
578 try
579     % Calculate the calibrated radiance and power density from the shot from 310nm to 450nm
580     % W/(cm^2 sr)
581     band1=find(shotWavelength>310&shotWavelength<450);
582     minBand1 = band1(1);
583     maxBand1 = band1(end);
584     radBand1 = sum(spectralRadiance(:,minBand1:maxBand1),2) * ...
585         (shotWavelength(2) - shotWavelength(1));
586     PDBand1 = radBand1 ./ (100.0 * fieldWidth);
587

```

```

588 % Plot the summed spectral radiance curve from 310nm to 450nm
589 figureCount = figureCount + 1;
590 figure(figureCount);
591 plot(axialDist, radBand1');
592 title('Radiance (summed 310-450nm)');
593 xlabel('Axial distance, mm');
594 ylabel('Radiance, W/(cm^2 sr)');
595 figureName = fullfile(dataDirectory, [shotName, '_rad_310_450']);
596 print('-depsc', figureName);
597
598 % Plot the power density curve from 310nm to 450nm
599 figureCount = figureCount + 1;
600 figure(figureCount);
601 plot(axialDist, PDBand1);
602 title('Power density (summed 310-450nm)');
603 xlabel('Axial distance, mm');
604 ylabel('Power density, W/(cm^3 sr)');
605 figureName = fullfile(dataDirectory, [shotName, '_powerdensity_310_450']);
606 print('-depsc', figureName);
607
608 % Calculate the Goulard number from 310-450nm
609 q_rad = max(radBand1); % W/cm^2/sr
610 goulard = 1.0e4 * q_rad * test_length / (2.0 * density * (velocity^3));
611 fprintf(1, '\nGoulard number: %f\n', goulard);
612
613 catch
614 disp('ERROR: Range 310-450nm out of bounds');
615 end
616
617 try
618 % Calculate the calibrated radiance and power density from the shot from 400nm to 430nm
619 % W/(cm^2 sr)
620 band2=find(shotWavelength>400&shotWavelength<430);
621 minBand2 = band2(1);
622 maxBand2 = band2(end);
623 radBand2 = sum(spectralRadiance(:,minBand2:maxBand2),2) * ...
624 (shotWavelength(2) - shotWavelength(1));
625 PDBand2 = radBand2 ./ (100.0 * fieldWidth);
626
627 if plotFigures == 1
628 % Plot the summed spectral radiance curve from 400nm to 430nm
629 figureCount = figureCount + 1;
630 figure(figureCount);
631 plot(axialDist, radBand2');
632 title('Radiance (summed 400-430nm)');
633 xlabel('Axial distance, mm');
634 ylabel('Radiance, W/(cm^2 sr)');
635 figureName = fullfile(dataDirectory, [shotName, '_rad_400_430']);
636 print('-depsc', figureName);
637
638 % Plot the power density curve from 400nm to 430nm
639 figureCount = figureCount + 1;
640 figure(figureCount);
641 plot(axialDist, PDBand2);
642 title('Power density (summed 400-430nm)');
643 xlabel('Axial distance, mm');
644 ylabel('Power density, W/(cm^3 sr)');
645 figureName = fullfile(dataDirectory, [shotName, '_powerdensity_400_430']);
646 print('-depsc', figureName);
647 end
648
649 catch
650 disp('ERROR: Range 400-430nm out of bounds');
651 end
652
653 try
654 % Calculate the calibrated radiance and power density from the shot from 310nm to 470nm
655 % W/(cm^2 sr)
656 band3=find(shotWavelength>310&shotWavelength<470);
657 minBand3 = band3(1);
658 maxBand3 = band3(end);
659 radBand3 = sum(spectralRadiance(:,minBand3:maxBand3),2) * ...
660 (shotWavelength(2) - shotWavelength(1));
661 PDBand3 = radBand3 ./ (100.0 * fieldWidth);
662
663 if plotFigures == 1
664 % Plot the summed spectral radiance curve from 400nm to 430nm
665 figureCount = figureCount + 1;

```

```

666 figure.figureCount;
667 plot(axialDist, radBand3);
668 title('Radiance (summed 310-470nm)');
669 xlabel('Axial distance, mm');
670 ylabel('Radiance, W/(cm^2 sr)');
671 figureName = fullfile(dataDirectory, [shotName, '_rad_310_470']);
672 print('-depsc', figureName);
673
674 % Plot the power density curve from 400nm to 430nm
675 figureCount = figureCount + 1;
676 figure.figureCount;
677 plot(axialDist, PDBand3);
678 title('Power density (summed 310-470nm)');
679 xlabel('Axial distance, mm');
680 ylabel('Power density, W/(cm^3 sr)');
681 figureName = fullfile(dataDirectory, [shotName, '_powerdensity_310_470']);
682 print('-depsc', figureName);
683 end
684
685 catch
686 disp('ERROR: Range 310-470nm out of bounds');
687 end
688
689 % Calculate the maximum spectral radiance from the shot
690 maxRow=find(radiance==max(radiance(:)));
691 maxSpectralRadiance = spectralRadiance(maxRow,:);
692
693 % Calculate the cumulative sum of the maximum spectral radiance
694 maxSpectralRadianceSUM = cumsum(maxSpectralRadiance) * (shotWavelength(2) - shotWavelength(1));
695
696 if plotFigures == 1
697 % Plot the maximum spectral radiance curve
698 figureCount = figureCount + 1;
699 figure.figureCount;
700 [AX,H1,H2]=plotyy(shotWavelength, maxSpectralRadiance, ...
701 shotWavelength, maxSpectralRadianceSUM);
702 title('Maximum Spectral Radiance');
703 xlabel('Wavelength, nm');
704 set(get(AX(1),'Ylabel'),'String','Maximum Spectral Radiance, W/(cm^2 nm sr)');
705 set(get(AX(2),'Ylabel'),'String','Integrated Spectral Radiance, W/(cm^2 sr)');
706 figureName = fullfile(dataDirectory, [shotName, '_maxspectralrad']);
707 print('-depsc', figureName);
708 end
709
710 % Calculate the maximum power density from the shot
711 maxSpectralPowerDensity = maxSpectralRadiance / fieldWidth;
712
713 % Calculate the cumulative sum of the maximum spectral power density
714 maxSpectralPowerDensitySUM = cumsum(maxSpectralPowerDensity) * (shotWavelength(2) - shotWavelength(1));
715
716 % Plot the maximum spectral power density curve
717 figureCount = figureCount + 1;
718 figure.figureCount;
719 [ax,h1,h2]=plotyy(shotWavelength, maxSpectralPowerDensity, ...
720 shotWavelength, maxSpectralRadianceSUM);
721 title('Maximum spectral power density');
722 xlabel('Wavelength, nm');
723 set(get(ax(1),'Ylabel'),'String','Maximum spectral power density, W/(cm^3 nm sr)');
724 set(get(ax(2),'Ylabel'),'String','Integrated Spectral Power Density, W/(cm^3 sr)');
725 figureName = fullfile(dataDirectory, [shotName, '_maxspectralPD']);
726 print('-depsc', figureName);
727
728 % Calculate the spectral radiance from the shot 25mm from the maximum
729 downRow=maxRow+60;
730 downSpectralRadiance = spectralRadiance(downRow,:);
731
732 % Calculate the cumulative sum of the spectral radiance 25mm from peak
733 downSpectralRadianceSUM = cumsum(downSpectralRadiance) * (shotWavelength(2) - shotWavelength(1));
734
735 if plotFigures == 1
736 % Plot the spectral radiance curve 25mm from peak
737 figureCount = figureCount + 1;
738 figure.figureCount;
739 [AX,H1,H2]=plotyy(shotWavelength, downSpectralRadiance, ...
740 shotWavelength, downSpectralRadianceSUM);
741 title('Spectral radiance 25mm downstream of peak');
742 xlabel('Wavelength, nm');
743 set(get(AX(1),'Ylabel'),'String','Spectral Radiance, W/(cm^2 nm sr)');

```

```

744 set(get(AX(2), 'Ylabel'), 'String', 'Integrated Spectral Radiance, W/(cm^2 sr)');
745 figureName = fullfile(dataDirectory, [shotName, '_down25mm_spectralrad']);
746 print('-depsc', figureName);
747 end
748
749 % Calculate the power density from the shot 25mm from peak
750 downSpectralPowerDensity = downSpectralRadiance / fieldWidth;
751
752 % Calculate the cumulative sum of the spectral power density 25mm from peak
753 downSpectralPowerDensitySUM = cumsum(downSpectralPowerDensity) * (shotWavelength(2) - shotWavelength(1));
754
755 % Plot the maximum spectral power density curve 25mm from peak
756 figureCount = figureCount + 1;
757 figure(figureCount);
758 [ax,h1,h2]=plotyy(shotWavelength, downSpectralPowerDensity, ...
759 shotWavelength, downSpectralRadianceSUM);
760 title('Spectral power density 25mm downstream of peak');
761 xlabel('Wavelength, nm');
762 set(get(ax(1), 'Ylabel'), 'String', 'Spectral power density, W/(cm^3 nm sr)');
763 set(get(ax(2), 'Ylabel'), 'String', 'Integrated Spectral Power Density, W/(cm^3 sr)');
764 figureName = fullfile(dataDirectory, [shotName, '_down25mm_spectralPD']);
765 print('-depsc', figureName);
766
767 % SAVE RESULTS
768
769 % Save everything in Matlab format as a backup
770 saveFile = fullfile(dataDirectory, [shotName '_data.mat']);
771 save(saveFile, 'shotWavelength', 'maxSpectralPowerDensity', ...
772 'maxSpectralRadiance', 'axialDist', 'radiance', 'powerDensity', ...
773 'maxSpectralPowerDensitySUM', 'maxSpectralRadianceSUM', ...
774 'spectralRadiance', 'spectralPowerDensity', ...
775 'calibImageFinal', 'shotImageFinal', 'radBand1', 'PDBand1');
776
777
778 % Axial sum of radiance
779 radianceFile = fullfile(dataDirectory, [shotName, '_radiance.dat']);
780 f1 = fopen(radianceFile, 'w');
781 fprintf(f1, '# Experimental data taken from the modified X2 NRST-Al facility \n');
782 fprintf(f1, '# Source: C. Jacobs (2011). Radiation in low density hypervelocity flows. Cotutelle PhD Thesis at The University of Queensland, Australia and Ecole Centrale Paris, France. \n\n');
783 fprintf(f1, '# Axial sum of radiance data for shot number %s \n', shotName);
784 fprintf(f1, '# Units are W / (cm^2 sr) \n');
785 fprintf(f1, '# Columns are axialDist, radiance \n');
786 for axialCount = 1:length(axialDist)
787     fprintf(f1, '%f \t %f \n', axialDist(axialCount), radiance(axialCount));
788 end
789 fclose(f1);
790
791 % Axial sum of power density
792 PDFfile = fullfile(dataDirectory, [shotName, '_PD.dat']);
793 f2 = fopen(PDFfile, 'w');
794 fprintf(f2, '# Experimental data taken from the modified X2 NRST-Al facility \n');
795 fprintf(f2, '# Source: C. Jacobs (2011). Radiation in low density hypervelocity flows. Cotutelle PhD Thesis at The University of Queensland, Australia and Ecole Centrale Paris, France. \n\n');
796 fprintf(f2, '# Axial sum of power density data for shot number %s \n', shotName);
797 fprintf(f2, '# Units are W / (cm^3 sr) \n');
798 fprintf(f2, '# Columns are axialDist, powerDensity \n');
799 for axialCount = 1:length(axialDist)
800     fprintf(f2, '%f \t %f \n', axialDist(axialCount), powerDensity(axialCount));
801 end
802 fclose(f2);
803
804 % Maximum spectral radiance
805 maxSpectralRadianceFile = fullfile(dataDirectory, [shotName, '_maxspectralradiance.dat']);
806 f3 = fopen(maxSpectralRadianceFile, 'w');
807 fprintf(f3, '# Experimental data taken from the modified X2 NRST-Al facility \n');
808 fprintf(f3, '# Source: C. Jacobs (2011). Radiation in low density hypervelocity flows. Cotutelle PhD Thesis at The University of Queensland, Australia and Ecole Centrale Paris, France. \n\n');
809 fprintf(f3, '# Maximum spectral radiance data for shot number %s \n', shotName);
810 fprintf(f3, '# This data taken at axial pixel location %f \n', maxRow);
811 fprintf(f3, '# Units are W / (cm^2 nm sr) \n');
812 fprintf(f3, '# Columns are shotWavelength, maxSpectralRadiance \n');
813 for axialCount = 1:length(shotWavelength)
814     fprintf(f3, '%f \t %f \n', shotWavelength(axialCount), maxSpectralRadiance(axialCount));
815 end
816 fclose(f3);

```

```

818 % Maximum spectral power density
819 maxSpectralPDFFile = fullfile(dataDirectory, [shotName, '_maxspectralPD.dat']);
820 f4 = fopen(maxSpectralPDFFile, 'w');
821 fprintf(f4, '# Experimental data taken from the modified X2 NRST-Al facility \n');
822 fprintf(f4, '# Source: C. Jacobs (2011). Radiation in low density hypervelocity flows. Cotutelle PhD
823 Thesis at The University of Queensland, Australia and Ecole Centrale Paris, France. \n\n');
824 fprintf(f4, '# Maximum spectral power density data for shot number %s , shotName);
825 fprintf(f4, '# This data taken at axial pixel location %f \n', maxRow);
826 fprintf(f4, '# Units are W / (cm3 nm sr) \n');
827 fprintf(f4, '# Columns are shotWavelength , maxSpectralPowerDensity \n');
828 for axialCount = 1:length(shotWavelength)
829     fprintf(f4, '%f \t %f \n', shotWavelength(axialCount), maxSpectralPowerDensity(axialCount));
830 end
831 fclose(f4);

832 % Integrated maximum spectral radiance
833 maxSpectralRadianceFileSUM = fullfile(dataDirectory, [shotName, '_maxspectralradianceSUM.dat']);
834 f5 = fopen(maxSpectralRadianceFileSUM, 'w');
835 fprintf(f5, '# Experimental data taken from the modified X2 NRST-Al facility \n');
836 fprintf(f5, '# Source: C. Jacobs (2011). Radiation in low density hypervelocity flows. Cotutelle PhD
837 Thesis at The University of Queensland, Australia and Ecole Centrale Paris, France. \n\n');
838 fprintf(f5, '# Integrated maximum spectral radiance data for shot number %s , shotName);
839 fprintf(f5, '# Units are W / (cm2 sr) \n');
840 fprintf(f5, '# Columns are shotWavelength , cumulative maxSpectralRadiance \n');
841 for axialCount = 1:length(shotWavelength)
842     fprintf(f5, '%f \t %f \n', shotWavelength(axialCount), maxSpectralRadianceSUM(axialCount));
843 end
844 fclose(f5);

845 % Integrated maximum spectral power density
846 maxSpectralPDFFileSUM = fullfile(dataDirectory, [shotName, '_maxspectralPDSUM.dat']);
847 f6 = fopen(maxSpectralPDFFileSUM, 'w');
848 fprintf(f6, '# Experimental data taken from the modified X2 NRST-Al facility \n');
849 fprintf(f6, '# Source: C. Jacobs (2011). Radiation in low density hypervelocity flows. Cotutelle PhD
850 Thesis at The University of Queensland, Australia and Ecole Centrale Paris, France. \n\n');
851 fprintf(f6, '# Integrated maximum spectral power density data for shot number %s , shotName);
852 fprintf(f6, '# Units are W / (cm3 sr) \n');
853 fprintf(f6, '# Columns are shotWavelength , cumulative maxSpectralPowerDensity \n');
854 for axialCount = 1:length(shotWavelength)
855     fprintf(f6, '%f \t %f \n', shotWavelength(axialCount), maxSpectralPowerDensitySUM(axialCount));
856 end
857 fclose(f6);

858 % Final calibrated radiance image
859 radianceImageFile = fullfile(dataDirectory, [shotName, '_radianceImage.dat']);
860 f7 = fopen(radianceImageFile, 'w');
861 fprintf(f7, '# Experimental data taken from the modified X2 NRST-Al facility \n');
862 fprintf(f7, '# Source: C. Jacobs (2011). Radiation in low density hypervelocity flows. Cotutelle PhD
863 Thesis at The University of Queensland, Australia and Ecole Centrale Paris, France. \n\n');
864 fprintf(f7, '# Radiance data for entire camera image %s , shotName);
865 fprintf(f7, '# Units are W / (cm2 sr) \n');
866 fprintf(f7, '# Columns are shotWavelength , axialDist , spectralRadiance \n');
867 for axialCount = 1:length(shotWavelength)
868     for axialCount2 = 1:length(axialDist)
869         fprintf(f7, '%f \t %f \t %f \n', shotWavelength(axialCount), axialDist(axialCount2),
870                 spectralRadiance(axialCount2, axialCount));
871     end
872 end
873 fclose(f7);

874 % Final calibrated power density image
875 powerDensityImageFile = fullfile(dataDirectory, [shotName, '_powerDensityImage.dat']);
876 f8 = fopen(powerDensityImageFile, 'w');
877 fprintf(f8, '# Experimental data taken from the modified X2 NRST-Al facility \n');
878 fprintf(f8, '# Source: C. Jacobs (2011). Radiation in low density hypervelocity flows. Cotutelle PhD
879 Thesis at The University of Queensland, Australia and Ecole Centrale Paris, France. \n\n');
880 fprintf(f8, '# Power density data for entire camera image %s , shotName);
881 fprintf(f8, '# Units are W / (cm2 sr) \n');
882 fprintf(f8, '# Columns are shotWavelength , axialDist , spectralPowerDensity \n');
883 for axialCount = 1:length(shotWavelength)
884     for axialCount2 = 1:length(axialDist)
885         fprintf(f8, '%f \t %f \t %f \n', shotWavelength(axialCount), axialDist(axialCount2),
886                 spectralPowerDensity(axialCount2, axialCount));
887     end
888 end
889 fclose(f8);

```

```

889 % Uncalibrated shot image
890 rawImageFile = fullfile(dataDirectory, [shotName, '_rawImage.dat']);
891 f9 = fopen(rawImageFile, 'w');
892 fprintf(f9, '# Experimental data taken from the modified X2 NRST-Al facility \n');
893 fprintf(f9, '# Source: C. Jacobs (2011). Radiation in low density hypervelocity flows. Cotutelle PhD
894 Thesis at The University of Queensland, Australia and Ecole Centrale Paris, France. \n\n');
895 fprintf(f9, '# Uncalibrated data image %s \n', shotName);
896 fprintf(f9, '# Units are counts \n');
897 fprintf(f9, '# Columns are shotWavelength, axialDist, rawImage \n');
898 for axialCount = 1:length(shotWavelength)
899     for axialCount2 = 1:length(axialDist)
900         fprintf(f9, '%f \t %f \t %f \n', shotWavelength(axialCount), axialDist(axialCount2),
901             shotImageFinal(axialCount2, axialCount));
902     end
903 end
904 fclose(f9);

905 if exist('radBand1')
906     % Axial sum of radiance from 310 to 450 nm
907     radianceFile2 = fullfile(dataDirectory, [shotName, '_radiance_310-450.dat']);
908     f10 = fopen(radianceFile2, 'w');
909     fprintf(f10, '# Experimental data taken from the modified X2 NRST-Al facility \n');
910     fprintf(f10, '# Source: C. Jacobs (2011). Radiation in low density hypervelocity flows. Cotutelle
911     PhD Thesis at The University of Queensland, Australia and Ecole Centrale Paris, France. \n\n');
912     fprintf(f10, '# Axial sum of radiance data for shot number %s from 310 to 450 nm\n', shotName);
913     fprintf(f10, '# Units are W / (cm2 sr) \n');
914     fprintf(f10, '# Columns are axialDist, radiance \n');
915     fprintf(f10, '# Min wavelength %f : Max wavelength %f\n', minBand1, maxBand1);
916     for axialCount = 1:length(axialDist)
917         fprintf(f10, '%f \t %f \n', axialDist(axialCount), radBand1(axialCount));
918     end
919     fclose(f10);

920     % Axial sum of power density from 310 to 450 nm
921     PDFFile2 = fullfile(dataDirectory, [shotName, '_PD_310-450.dat']);
922     f11 = fopen(PDFFile2, 'w');
923     fprintf(f11, '# Experimental data taken from the modified X2 NRST-Al facility \n');
924     fprintf(f11, '# Source: C. Jacobs (2011). Radiation in low density hypervelocity flows. Cotutelle
925     PhD Thesis at The University of Queensland, Australia and Ecole Centrale Paris, France. \n\n');
926     fprintf(f11, '# Axial sum of power density data for shot number %s from 310 to 450 nm\n', shotName);
927     fprintf(f11, '# Units are W / (cm3 sr) \n');
928     fprintf(f11, '# Columns are axialDist, powerDensity \n');
929     fprintf(f11, '# Min wavelength %f : Max wavelength %f\n', minBand1, maxBand1);
930     for axialCount = 1:length(axialDist)
931         fprintf(f11, '%f \t %f \n', axialDist(axialCount), PDBand1(axialCount));
932     end
933     fclose(f11);
934 end

935 if exist('radBand2')
936     % Axial sum of radiance from 400 to 430 nm
937     radianceFile3 = fullfile(dataDirectory, [shotName, '_radiance_400-430.dat']);
938     f12 = fopen(radianceFile3, 'w');
939     fprintf(f12, '# Experimental data taken from the modified X2 NRST-Al facility \n');
940     fprintf(f12, '# Source: C. Jacobs (2011). Radiation in low density hypervelocity flows. Cotutelle
941     PhD Thesis at The University of Queensland, Australia and Ecole Centrale Paris, France. \n\n');
942     fprintf(f12, '# Axial sum of radiance data for shot number %s from 400 to 430 nm\n', shotName);
943     fprintf(f12, '# Units are W / (cm2 sr) \n');
944     fprintf(f12, '# Columns are axialDist, radiance \n');
945     fprintf(f12, '# Min wavelength %f : Max wavelength %f\n', minBand2, maxBand2);
946     for axialCount = 1:length(axialDist)
947         fprintf(f12, '%f \t %f \n', axialDist(axialCount), radBand2(axialCount));
948     end
949     fclose(f12);

950     % Axial sum of power density from 400 to 430 nm
951     PDFFile3 = fullfile(dataDirectory, [shotName, '_PD_400-430.dat']);
952     f13 = fopen(PDFFile3, 'w');
953     fprintf(f13, '# Experimental data taken from the modified X2 NRST-Al facility \n');
954     fprintf(f13, '# Source: C. Jacobs (2011). Radiation in low density hypervelocity flows. Cotutelle
955     PhD Thesis at The University of Queensland, Australia and Ecole Centrale Paris, France. \n\n');
956     fprintf(f13, '# Axial sum of power density data for shot number %s from 400 to 430 nm\n', shotName);

```

```

955 fprintf(f13, '# Units are W / (cm3 sr) \n');
956 fprintf(f13, '# Columns are axialDist, powerDensity \n');
957 fprintf(f13, '# Min wavelength %f : Max wavelength %f\n', minBand2, maxBand2);
958 for axialCount = 1:length(axialDist)
959     fprintf(f13, '%f \t %f \n', axialDist(axialCount), PDBand2(axialCount));
960 end
961 fclose(f13);
962
963 if exist('radBand3')
964 % Axial sum of radiance from 310 to 470 nm
965 radianceFile4 = fullfile(dataDirectory, [shotName, '_radiance_310-470.dat']);
966 f14 = fopen(radianceFile4, 'w');
967 fprintf(f14, '# Experimental data taken from the modified X2 NRST-Al facility \n');
968 fprintf(f14, '# Source: C. Jacobs (2011). Radiation in low density hypervelocity flows. Cotutelle
969 PhD Thesis at The University of Queensland, Australia and Ecole Centrale Paris, France. \n\n');
970 fprintf(f14, '# Axial sum of radiance data for shot number %s from 310 to 470 nm\n', shotName);
971 fprintf(f14, '# Units are W / (cm2 sr) \n');
972 fprintf(f14, '# Columns are axialDist, radiance \n');
973 fprintf(f14, '# Min wavelength %f : Max wavelength %f\n', minBand3, maxBand3);
974 for axialCount = 1:length(axialDist)
975     fprintf(f14, '%f \t %f \n', axialDist(axialCount), radBand3(axialCount));
976 end
977 fclose(f14);
978
979 % Axial sum of power density from 310 to 470 nm
980 PDFfile4 = fullfile(dataDirectory, [shotName, '_PD_310-470.dat']);
981 f15 = fopen(PDFfile4, 'w');
982 fprintf(f15, '# Experimental data taken from the modified X2 NRST-Al facility \n');
983 fprintf(f15, '# Source: C. Jacobs (2011). Radiation in low density hypervelocity flows. Cotutelle
984 PhD Thesis at The University of Queensland, Australia and Ecole Centrale Paris, France. \n\n');
985 fprintf(f15, '# Axial sum of power density data for shot number %s from 310 to 470 nm\n', shotName);
986 fprintf(f15, '# Units are W / (cm3 sr) \n');
987 fprintf(f15, '# Columns are axialDist, powerDensity \n');
988 fprintf(f15, '# Min wavelength %f : Max wavelength %f\n', minBand3, maxBand3);
989 for axialCount = 1:length(axialDist)
990     fprintf(f15, '%f \t %f \n', axialDist(axialCount), PDBand3(axialCount));
991 end
992 fclose(f15);
993
994 % Down 25mm spectral radiance
995 downSpectralRadianceFile = fullfile(dataDirectory, [shotName, '_down25mm_spectralradiance.dat']);
996 f16 = fopen(downSpectralRadianceFile, 'w');
997 fprintf(f16, '# Experimental data taken from the modified X2 NRST-Al facility \n');
998 fprintf(f16, '# Source: C. Jacobs (2011). Radiation in low density hypervelocity flows. Cotutelle PhD
999 Thesis at The University of Queensland, Australia and Ecole Centrale Paris, France. \n\n');
1000 fprintf(f16, '# Spectral radiance data 25mm from peak for shot number %s \n', shotName);
1001 fprintf(f16, '# This data taken at axial pixel location %f \n', downRow);
1002 fprintf(f16, '# Units are W / (cm2 nm sr) \n');
1003 fprintf(f16, '# Columns are shotWavelength, downSpectralRadiance \n');
1004 for axialCount = 1:length(shotWavelength)
1005     fprintf(f16, '%f \t %f \n', shotWavelength(axialCount), downSpectralRadiance(axialCount));
1006 end
1007 fclose(f16);
1008
1009 % Down 25mm spectral power density
1010 downSpectralPDFile = fullfile(dataDirectory, [shotName, '_down25mm_spectralPD.dat']);
1011 f17 = fopen(downSpectralPDFile, 'w');
1012 fprintf(f17, '# Experimental data taken from the modified X2 NRST-Al facility \n');
1013 fprintf(f17, '# Source: C. Jacobs (2011). Radiation in low density hypervelocity flows. Cotutelle PhD
1014 Thesis at The University of Queensland, Australia and Ecole Centrale Paris, France. \n\n');
1015 fprintf(f17, '# Spectral power density data 25mm from peak for shot number %s \n', shotName);
1016 fprintf(f17, '# This data taken at axial pixel location %f \n', downRow);
1017 fprintf(f17, '# Units are W / (cm3 nm sr) \n');
1018 fprintf(f17, '# Columns are shotWavelength, downSpectralPowerDensity \n');
1019 for axialCount = 1:length(shotWavelength)
1020     fprintf(f17, '%f \t %f \n', shotWavelength(axialCount), downSpectralPowerDensity(axialCount));
1021 end
1022 fclose(f17);
1023
1024 % Integrated maximum spectral radiance
1025 downSpectralRadianceFileSUM = fullfile(dataDirectory, [shotName, '_down25mm_spectralradianceSUM.dat']);
1026 f18 = fopen(downSpectralRadianceFileSUM, 'w');
1027 fprintf(f18, '# Experimental data taken from the modified X2 NRST-Al facility \n');

```

```

1026 fprintf(f18, '# Source: C. Jacobs (2011). Radiation in low density hypervelocity flows. Cotutelle PhD
1027 Thesis at The University of Queensland, Australia and Ecole Centrale Paris, France. \n\n');
1028 fprintf(f18, '# Integrated spectral radiance data 25mm from peak for shot number %s \n', shotName);
1029 fprintf(f18, '# Units are W / (cm2 sr) \n');
1030 fprintf(f18, '# Columns are shotWavelength, cumulative downSpectralRadiance \n');
1031 for axialCount = 1:length(shotWavelength)
1032     fprintf(f18, '%f \t %f \n', shotWavelength(axialCount), downSpectralRadianceSUM(axialCount));
1033 end
1034 fclose(f18);

1035 % Integrated maximum spectral power density
1036 downSpectralPDFFileSUM = fullfile(dataDirectory, [shotName, '_down25mm_spectralPDSUM.dat']);
1037 f19= fopen(downSpectralPDFFileSUM, 'w');
1038 fprintf(f19, '# Experimental data taken from the modified X2 NRST-Al facility \n');
1039 fprintf(f19, '# Source: C. Jacobs (2011). Radiation in low density hypervelocity flows. Cotutelle PhD
1040 Thesis at The University of Queensland, Australia and Ecole Centrale Paris, France. \n\n');
1041 fprintf(f19, '# Integrated spectral power density data 25mm from peak for shot number %s \n', shotName);
1042 ;
1043 fprintf(f19, '# Units are W / (cm3 sr) \n');
1044 fprintf(f19, '# Columns are shotWavelength, cumulative down SpectralPowerDensity \n');
1045 for axialCount = 1:length(shotWavelength)
1046     fprintf(f19, '%f \t %f \n', shotWavelength(axialCount), downSpectralPowerDensitySUM(axialCount));
1047 end
1048 fclose(f19);

```

D.3 Other functions

The function written to read the .SPE file created by the spectrometer was written by Eichmann (2009) and called `SPEread.m`.

```

1 function [spectra, wavelength, varargout] = SPEread(filename)
2 % SPEread Reads a Princeton Instruments Winspec SPE file into Matlab
3 % Troy Eichmann
4 % 22-July-2009
5 % Version 1.4
6 %
7 % [spectra, wavelength] = SPEread(filename)
8 % spectra is an array of size (x, y, frames)
9 % wavelength is a vector of size (x)
10 %
11 % [spectra, wavelength, FileInfo] = SPEread(filename)
12 % spectra is an array of size (x, y, frames)
13 % wavelength is a vector of size (x)
14 % FileInfo is a structure containing information specified in the header
15 % .Version          SPE header version
16 % .Date            DD/MM/YY
17 % .Grating          grating lines/mm
18 % .CenterWavelength_nm grating position center wavelength in nm
19 % .Gain             camera gain (0-255)
20 % .BracketPulsing   bracket pulsing (On/Off)
21 % .Mode              trigger mode (Shutter/Gate)
22 % .exposure_ms      exposure time in ms (Shutter mode)
23 % .exposure_us      exposure time in us (Gate mode)
24 % .delay_us         trigger delay in us (Gate mode)
25 %
26 % Ref:
27 % Appendix C
28 % WinSpec Spectroscopic Software Manual Version 2.51
29 % October 17, 2006
30 %
31 %
32 fid = fopen(filename, 'r');
33 %
34 %-----
35 % Read 4100 byte header
36 %-----
37 %
38 header = fread(fid, 4100, 'uint8');
39 %
40 % The X dimension of the stored data is in "xdim"
41 % (Offset 42)
42 status = fseek(fid, 42, 'bof');

```

```

43 xdim = fread(fid, 1, 'uint16');
44 % The Y dimension of the stored data is in "ydim"
45 % (Offset 656)
46 status = fseek(fid, 656, 'bof');
47 ydim = fread(fid, 1, 'uint16');
48
49 % The number of frames of data stored is in "NumFrames"
50 % (Offset 1446)
51 status = fseek(fid, 1446, 'bof');
52 NumFrames = fread(fid, 1, 'uint32');
53
54 % The type of data stored in a frame is in "datatype"
55 % (Offset 108)
56 status = fseek(fid, 108, 'bof');
57 datatype = fread(fid, 1, 'uint16');
58 % NOTE: This code only tested with unsigned short datatype
59 switch datatype
60 case 0 %float (4 bytes)
61     datatype='float';
62 case 1 %long (4 bytes)
63     datatype='long';
64 case 2 %short (2 bytes)
65     datatype='int16';
66 case 3 %unsigned short (2 bytes)
67     datatype='uint16';
68 end
69
70 % The order of the calibration polynomial is in "polynom_order"
71 % type char (Offset 3101)
72 status = fseek(fid, 3101, 'bof');
73 polynom_order = fread(fid, 1, 'char');
74
75 % The coefficients of the polynomial (0 to 5) are in "polynom_coeff[6]"
76 % type double (Offset 3263)
77 status = fseek(fid, 3263, 'bof');
78 for i=1:6
79     polynom_coeff(i) = fread(fid, 1, 'double');
80 end
81
82 % Build wavelength scale from calibration polynomial
83 % NOTE: This scale is only as good as the calibration stored in the
84 % SPE file and may contain considerable error.
85 wavelength=zeros(1,xdim);
86 for i = 0 : polynom_order
87     wavelength = wavelength + polynom_coeff(i + 1) * [1:xdim] .^ i;
88 end
89
90 % Software version number is in "SW_version"
91 % type char[16] (Offset 688)
92 status = fseek(fid, 688, 'bof');
93 SW_version = char(fread(fid, 16, 'char'))';
94 FileInfo.Version = SW_version;
95
96 % Date is in "date" as MM/DD/YY
97 % type char[10] (Offset 20)
98 status = fseek(fid, 20, 'bof');
99 date = char(fread(fid, 10, 'char'))';
100 FileInfo.Date = date;
101
102 % Grating blaze is in "SpecGrooves"
103 % type float (Offset 650)
104 status = fseek(fid, 650, 'bof');
105 SpecGrooves = fread(fid, 1, 'float');
106 FileInfo.Grating = SpecGrooves;
107
108 % The center wavelength in nm is in "SpecCenterWlNm"
109 % type float (Offset 72)
110 status = fseek(fid, 72, 'bof');
111 SpecCenterWlNm = fread(fid, 1, 'float');
112 FileInfo.CenterWavelength_nm = SpecCenterWlNm;
113
114 % The gain (0-255) is in "PImaxGain"
115 % short (Offset 148)
116 status = fseek(fid, 148, 'bof');
117 PImaxGain = fread(fid, 1, 'uint16');
118 FileInfo.Gain = PImaxGain;
119
120

```

```

121 % alternative exposure time in seconds in Shutter mode is in "exp_sec"
122 % type float (Offset 10)
123 status = fseek(fid, 10, 'bof');
124 exp_sec = fread(fid, 1, 'float');

125 % The Pulser mode is in "PulserMode" Repetitive/Sequential
126 % type short (Offset 110)
127 status = fseek(fid, 110, 'bof');
128 PulserMode = fread(fid, 1, 'uint16');

129 % The exposure time is in "PulseRepWidth" (usec)
130 % type float (Offset 118)
131 status = fseek(fid, 118, 'bof');
132 PulseRepWidth = fread(fid, 1, 'float');

133 % The trigger delay is in "PulseRepDelay" (usec)
134 % type float (Offset 122)
135 status = fseek(fid, 122, 'bof');
136 PulseRepDelay = fread(fid, 1, 'float');

137 % The bracket pulsing mode is in "PulseBracketUsed" (On/Off)
138 % type int (Offset 4058)
139 status = fseek(fid, 4058, 'bof');
140 PulseBracketUsed = fread(fid, 1, 'int8');
141 if PulseBracketUsed == 0
142     FileInfo.BracketPulsing='Off';
143 else
144     FileInfo.BracketPulsing='On';
145 end

146 % timing mode is in "mode"
147 % type int (Offset 8)
148 status = fseek(fid, 8, 'bof');
149 mode = fread(fid, 1, 'int8');

150 % NOTE: This code only tested by trial and error with test cases
151 % since no guide is given to what 'mode' represents
152 switch mode
153 case 1 % Shutter mode
154     FileInfo.Mode = 'Shutter';
155     FileInfo.exposure_ms = exp_sec*1e3;
156 case 26 % Gate mode
157     FileInfo.Mode = 'Gate';
158     FileInfo.exposure_us = PulseRepWidth;
159     FileInfo.delay_us = PulseRepDelay;
160 otherwise % Include all available data
161     FileInfo.Mode = 'Unknown';
162     if exp_sec > 0; FileInfo.exposure_ms = exp_sec*1e3; end
163     FileInfo.exposure_us = PulseRepWidth;
164     FileInfo.delay_us = PulseRepDelay;
165 end

166 %-----
167 % The data follows the header beginning at offset 4100.
168 % Data is stored as sequential points.
169 %-----

170 status = fseek(fid, 4100, 'bog');

171 % Initialize array

172 spectra = zeros(ydim, xdim, NumFrames);

173 for i = 1:NumFrames
174     imagedata = fread(fid, xdim * ydim, datatype);
175     spectra(:, :, i) = double(reshape(imagedata, xdim, ydim));
176 end

177 fclose(fid);

178 % return header data if requested
179 if nargout > 2; varargout(1) = {FileInfo}; end

```

D.4 Calibration lamp data file

The data for the calibration lamp S-1197N0.std is given below.

```
1 250,2.13338E-08
2 260,3.691254E-08
3 270,6.045517E-08
4 280,7.78034E-08
5 290,1.425364E-07
6 300,2.084281E-07
7 310,2.950972E-07
8 320,4.019911E-07
9 330,5.378375E-07
10 340,7.033271E-07
11 350,9.025547E-07
12 360,1.134121E-06
13 370,1.401278E-06
14 380,1.706379E-06
15 390,2.059393E-06
16 400,2.442309E-06
17 450,4.921275E-06
18 500,8.155352E-06
19 555,1.210649E-05
20 600,1.525083E-05
21 654.6,1.874438E-05
22 700,2.114541E-05
23 800,2.453637E-05
24 900,2.563871E-05
25 1050,2.433556E-05
26 1100,2.344202E-05
```


APPENDIX E

Experimental Summary

This Appendix contains a tabulated summary of the experimental conditions, including fill pressures and shock speeds at each transducer location.

Number	Reservoir	Fill pressure (Pa)		Driver	Secondary driver	Shock tube	Driver mixture		Shock speed in driver tube (m/s)		Shock speed in shock tube (m/s)	
		% He	% Ar				st1-st2	st2-st3	st3-st1	at1-at2	at2-at3	al1-al2
x2s1460	1.15e6	3.0e4	3.0e4	13.0	85/15	4314.81	4215.33	4246.32	3906.25	6925.21	6775.07	6925.21
x2s1463	1.15e6	3.0e4	3.0e4	13.0	85/15	4283.09	4246.32	4246.32	6666.67	6443.30	6613.76	6578.95
x2s1465	1.15e6	3.0e4	3.0e4	13.0	85/15	4251.82	4246.32	4251.82	6925.21	6084.97	6053.28	6720.43
x2s1468	1.15e6	3.0e4	3.0e4	13.0	85/15	4251.82	4184.78	4184.78	6830.60	6631.30	6811.99	6648.94
x2s1469	1.15e6	3.0e4	3.0e4	13.0	85/15	4073.43	3902.03	3902.03	5980.86	5952.38	6053.27	5841.12
x2s1470	1.15e6	3.0e4	3.0e4	13.0	85/15	4314.81	4277.78	4277.78	4139.07	7002.80	6811.99	6963.79
x2s1471	1.15e6	3.0e4	3.0e4	13.0	85/15	4314.81	4277.78	4277.78	4006.41	6702.41	6493.51	6684.49
x2s1472	1.15e6	3.0e4	3.0e4	13.0	85/15	4251.82	4184.78	4184.78	4084.97	6925.21	6702.41	6906.08
x2s1473	1.15e6	3.0e4	3.0e4	13.0	85/15	4251.82	4154.68	4154.68	6250.00	6142.51	6250.00	6281.41
x2s1474	1.15e6	3.0e4	3.0e4	13.0	85/15	4314.81	4277.78	4277.78	4194.63	6983.24	6830.60	6830.60
x2s1475	1.15e6	3.0e4	3.0e4	13.0	85/15	4251.82	4154.68	4154.68	6203.47	3453.04	6097.56	6127.45
x2s1476	1.15e6	3.0e4	3.0e4	13.0	85/15	4283.09	4246.32	4246.32	4006.41	6811.99	6631.30	6648.94
x2s1477	1.15e6	3.0e4	3.0e4	13.0	85/15	4221.01	4184.78	4184.78	4111.84	6925.21	6811.99	6887.05
x2s1493	1.15e6	3.0e4	3.0e4	13.0	85/15	4236.36	4277.78	4277.78	4268.87	4166.67	4098.36	6849.32
x2s1494	1.15e6	3.0e4	3.0e4	13.0	85/15	4134.81	4200.00	4058.30	3731.34	6233.19	6211.18	6250.00
x2s1495	1.15e6	3.0e4	3.0e4	13.0	85/15	4314.81	4277.78	4277.78	4029.30	4166.67	6393.01	6890.55
x2s1498	1.15e6	3.0e4	3.0e4	13.0	85/15	4314.81	4125.00	4189.81	4166.67	4023.26	6849.32	6756.76
x2s1499	1.15e6	3.0e4	3.0e4	13.0	85/15	4236.36	4277.78	4151.38	3906.25	3787.88	6535.95	6451.61
x2s1500	1.15e6	3.0e4	3.0e4	13.0	85/15	4314.81	4277.78	4289.10	4098.36	4032.26	6849.32	6711.41
x2s1501	1.15e6	3.0e4	3.0e4	13.0	85/15	4160.71	3982.76	3709.02	3478.38	3333.33	6097.56	6060.61
x2s1503	1.15e6	3.0e4	3.0e4	13.0	85/15	4236.36	4052.63	3770.83	3472.22	3378.38	6172.84	6024.10
x2s1504	1.15e6	3.0e4	3.0e4	8.0	80/20	3949.15	3982.76	3973.80	3906.25	3906.25	7042.25	6849.32
x2s1505	1.15e6	3.0e4	3.0e4	8.0	80/20	4017.24	3915.25	3991.23	3906.25	3846.15	6756.76	6711.41
x2s1509	1.15e6	3.0e4	3.0e4	8.0	80/20	4017.24	3982.76	3956.52	3676.47	3571.43	6451.61	6289.31
x2s1510	1.15e6	3.0e4	3.0e4	8.0	80/20	4017.24	3982.76	3982.76	3424.66	3623.19	6250.00	6250.00
x2s1511	1.15e6	3.0e4	3.0e4	8.0	80/20	4087.72	4053.63	3888.89	3623.19	3521.13	6451.61	6289.31
x2s1513	1.15e6	3.0e4	3.0e4	8.0	80/20	4017.24	3982.76	3699.19	3378.38	3246.75	6060.61	5952.38
x2s1517	1.15e6	3.0e4	3.0e4	8.0	80/20	3949.15	3786.89	3554.69	3246.75	3125.00	5988.02	5917.16
x2s1518	1.15e6	3.0e4	3.0e4	8.0	80/20	4017.24	3982.76	3823.53	3521.13	3378.38	6250.00	6172.84
x2s1519	1.15e6	3.0e4	3.0e4	8.0	80/20	4087.72	3982.76	3888.89	3571.43	3378.38	6329.11	6134.97
x2s1520	1.15e6	3.0e4	3.0e4	8.0	80/20	3949.15	3850.00	3625.50	3324.66	3323.33	6329.11	6097.56
x2s1521	1.15e6	3.0e4	3.0e4	8.0	80/20	3584.62	3447.76	3447.76	3226.95	3246.75	6060.61	5847.95
x2s1522	1.15e6	3.0e4	3.0e4	8.0	80/20	3819.67	3666.67	3500.00	3205.13	3125.00	6060.61	6024.10
x2s1523	1.15e6	3.0e4	3.0e4	8.0	80/20	3949.15	3850.00	3850.00	3791.67	3521.13	3472.22	6289.31
x2s1524	1.15e6	3.0e4	3.0e4	8.0	80/20	3949.15	3850.00	3654.62	3333.33	3289.47	6097.56	6024.10
x2s1527	1.15e6	3.0e4	3.0e4	8.0	80/20	3819.67	3792.76	3792.76	3500.58	3164.56	6024.10	5952.38
x2s1528	1.15e6	3.0e4	3.0e4	8.0	80/20	4017.24	3982.76	3982.76	3731.34	3623.19	6410.20	6289.31
x2s1529	1.15e6	3.0e4	3.0e4	8.0	80/20	3883.33	3725.81	3527.13	3205.13	3125.00	5988.02	5917.16
x2s1530	1.15e6	3.0e4	3.0e4	8.0	80/20	4017.24	3982.76	3922.41	3676.47	3521.13	6329.11	6289.31
x2s1531	1.15e6	3.0e4	1.0e4	4.0	100/0	6131.58	6078.95	6066.67	5923.08	5813.95	5555.56	9615.38
x2s1532	1.15e6	3.0e4	1.0e4	4.0	100/0	6131.58	5923.08	5923.08	5606.67	5606.67	5613.95	9803.92
x2s1533	1.15e6	3.0e4	1.0e4	4.0	100/0	6297.30	6243.24	6066.67	5607.56	5813.95	6000.00	9615.38
x2s1534	1.15e6	3.0e4	1.0e4	4.0	100/0	6131.58	6078.95	5986.84	5681.82	5681.82	5681.82	9803.92
x2s1535	1.15e6	3.0e4	1.0e4	4.0	100/0	6131.58	6243.24	6148.65	6097.56	5952.38	10416.67	9900.99
x2s1536	1.15e6	3.0e4	1.0e4	4.0	100/0	6131.58	6078.95	5833.33	5852.38	5434.78	9708.74	9523.81
x2s1538	1.15e6	3.0e4	1.0e4	4.0	100/0	6297.30	6078.95	5917.71	5813.95	5681.82	9803.92	9433.96
x2s1539	1.15e6	3.0e4	1.0e4	4.0	100/0	5974.36	5775.00	5112.36	4464.29	4237.56	7812.50	7812.50
x2s1540	1.15e6	3.0e4	1.0e4	4.0	100/0	6297.30	6078.95	5321.64	4464.29	4310.34	8403.36	7936.51
x2s1541	1.15e6	3.0e4	1.0e4	4.0	100/0	6131.58	6078.95	5796.18	5555.56	5434.78	9174.31	9090.91
x2s1542	1.15e6	3.0e4	1.0e4	4.0	100/0	5825.00	5634.15	5170.45	4464.29	4310.34	7812.50	7874.02
x2s1543	1.15e6	3.0e4	1.0e4	4.0	100/0	6131.58	5923.08	5870.97	5813.95	5681.82	9803.92	9615.38
x2s1544	1.15e6	3.0e4	1.0e4	4.0	100/0	6131.58	6078.95	5909.09	5813.95	5682.38	10204.08	9708.74
x2s1545	1.15e6	3.0e4	1.0e4	4.0	100/0	5974.36	5775.00	5617.28	5208.33	5000.00	8695.65	8771.93
x2s1546	1.15e6	3.0e4	1.0e4	4.0	100/0	5065.22	4914.89	4460.78	4032.26	3906.25	7751.94	7692.31
x2s1547	1.15e6	3.0e4	1.0e4	4.0	100/0	6297.30	6078.95	6066.67	5952.38	10309.28	10000.00	9803.92

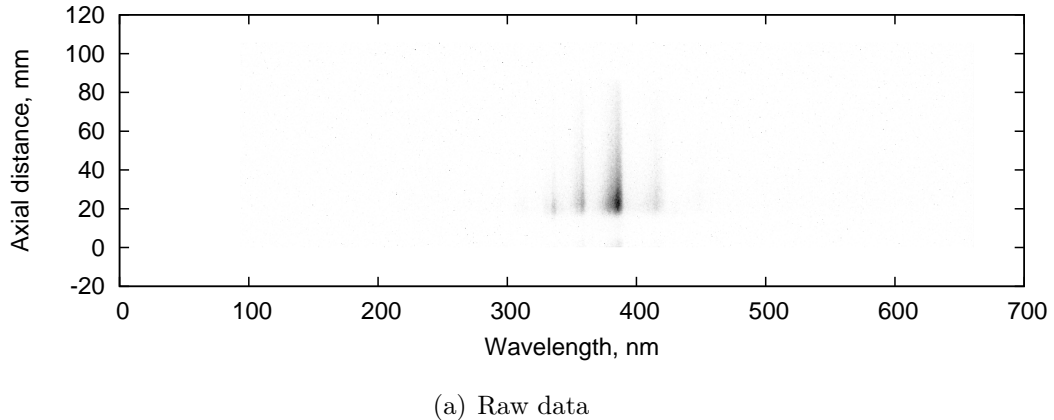
Table E.1 : Summary of the full pressures and shock speeds calculated at all transducer locations down the tube for all experiments.

APPENDIX F

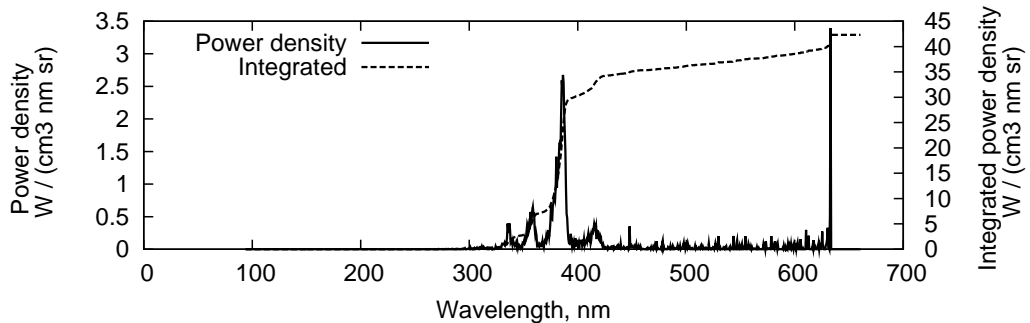
Calibrated Spectral Data

In this appendix, raw and calibrated emission spectroscopy data are presented for all experimental shots. In these images, the spectral power density is extracted for the axial location corresponding to the peak nonequilibrium region. The summed power density is calculated over the whole wavelength range of the image.

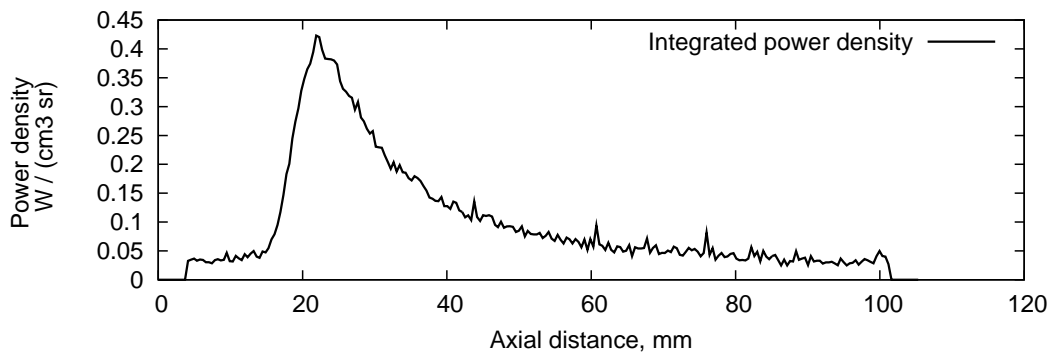
x2s1475			
Test gas pressure	13 Pa	Test gas mixture	98% N ₂ , 2% CH ₄
Shock speed	6.13 km/s	Grating	150 lines/mm
Exposure time	100 ns	Slit width	50 μ m



(a) Raw data



(b) Spectral power density



(c) Power density summed over entire wavelength range

Figure F.1 : Raw and calibrated data for x2s1475.

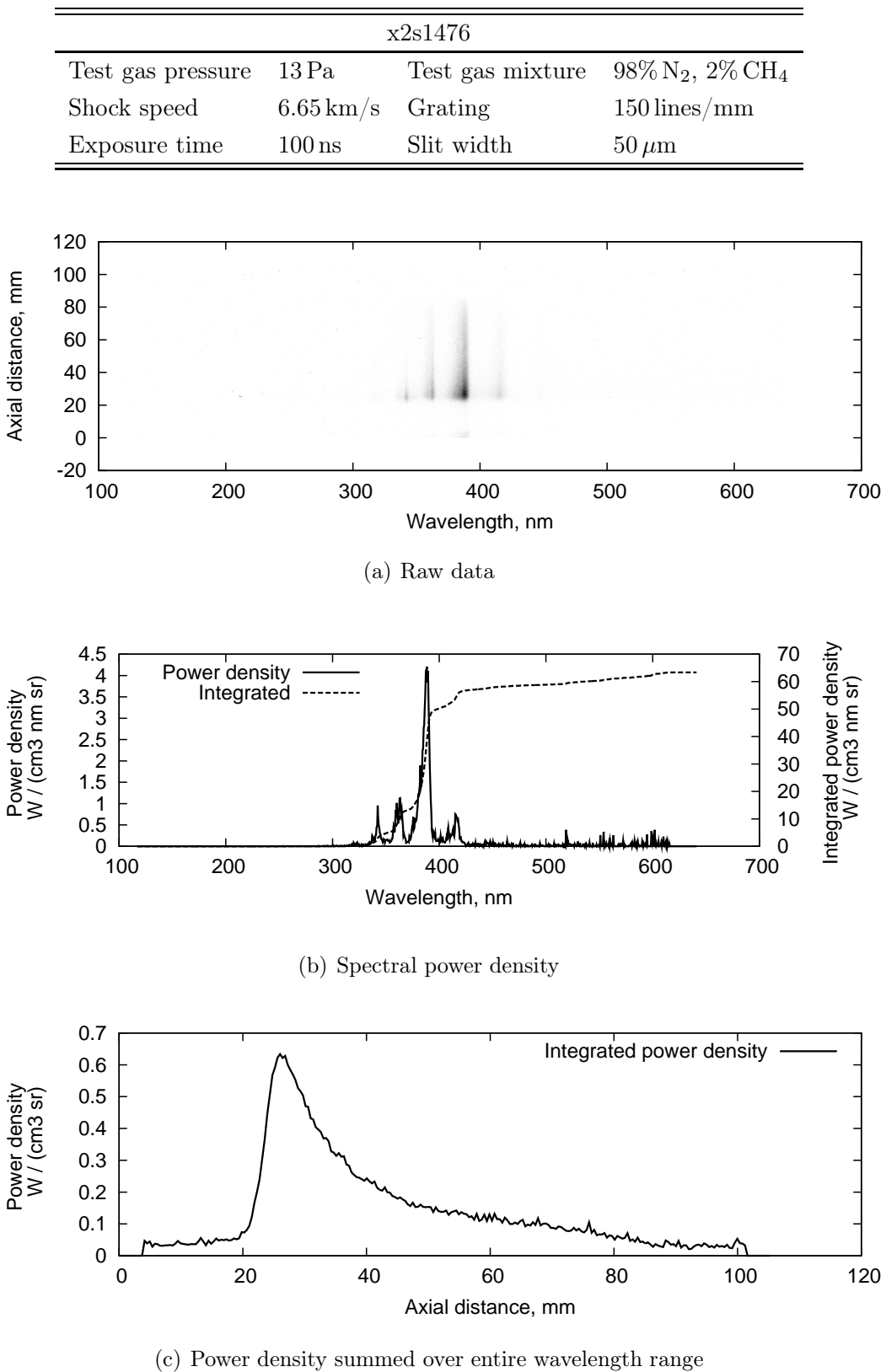


Figure F.2 : *Raw and calibrated data for x2s1476.*

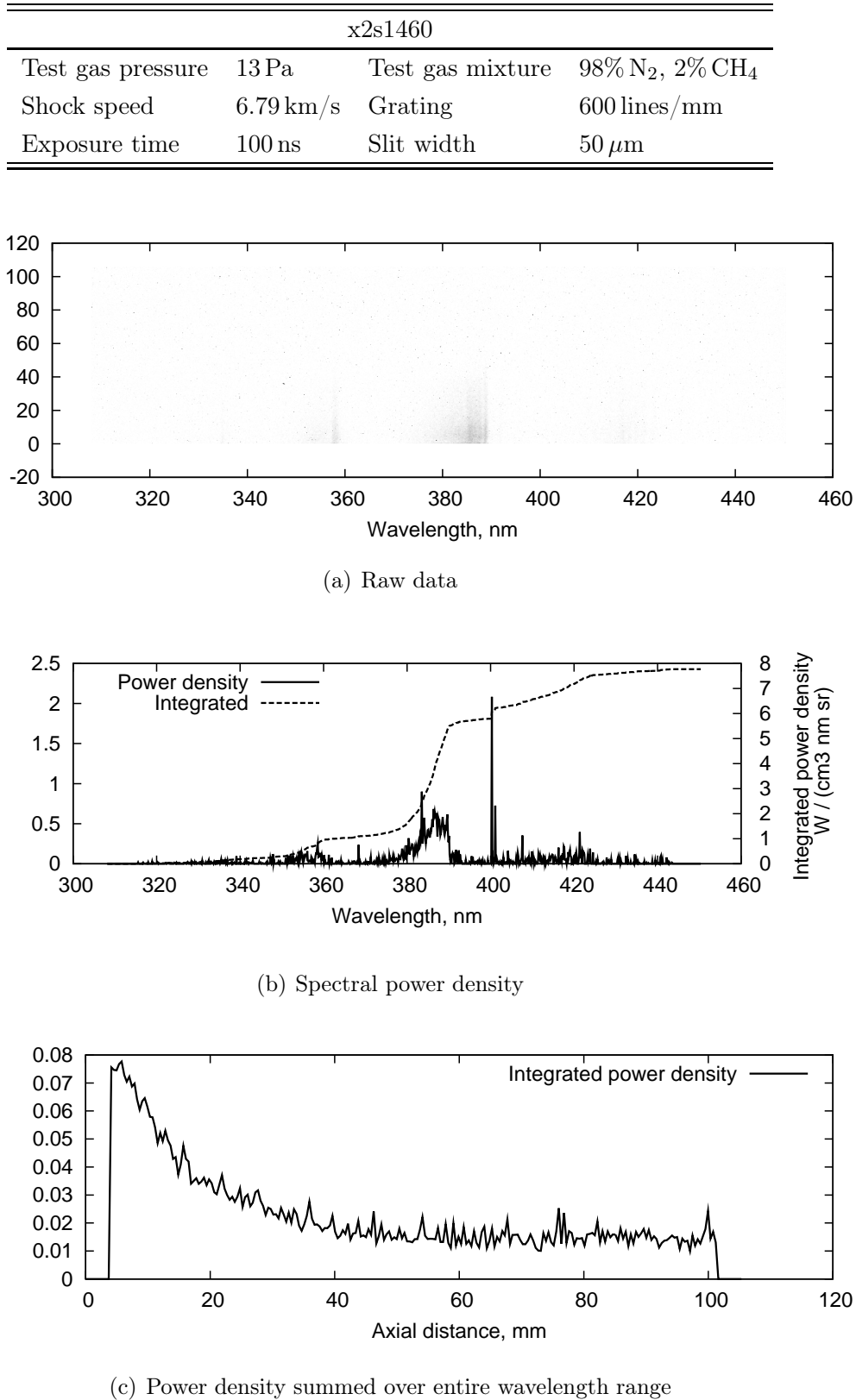


Figure F.3 : *Raw and calibrated data for x2s1460.*

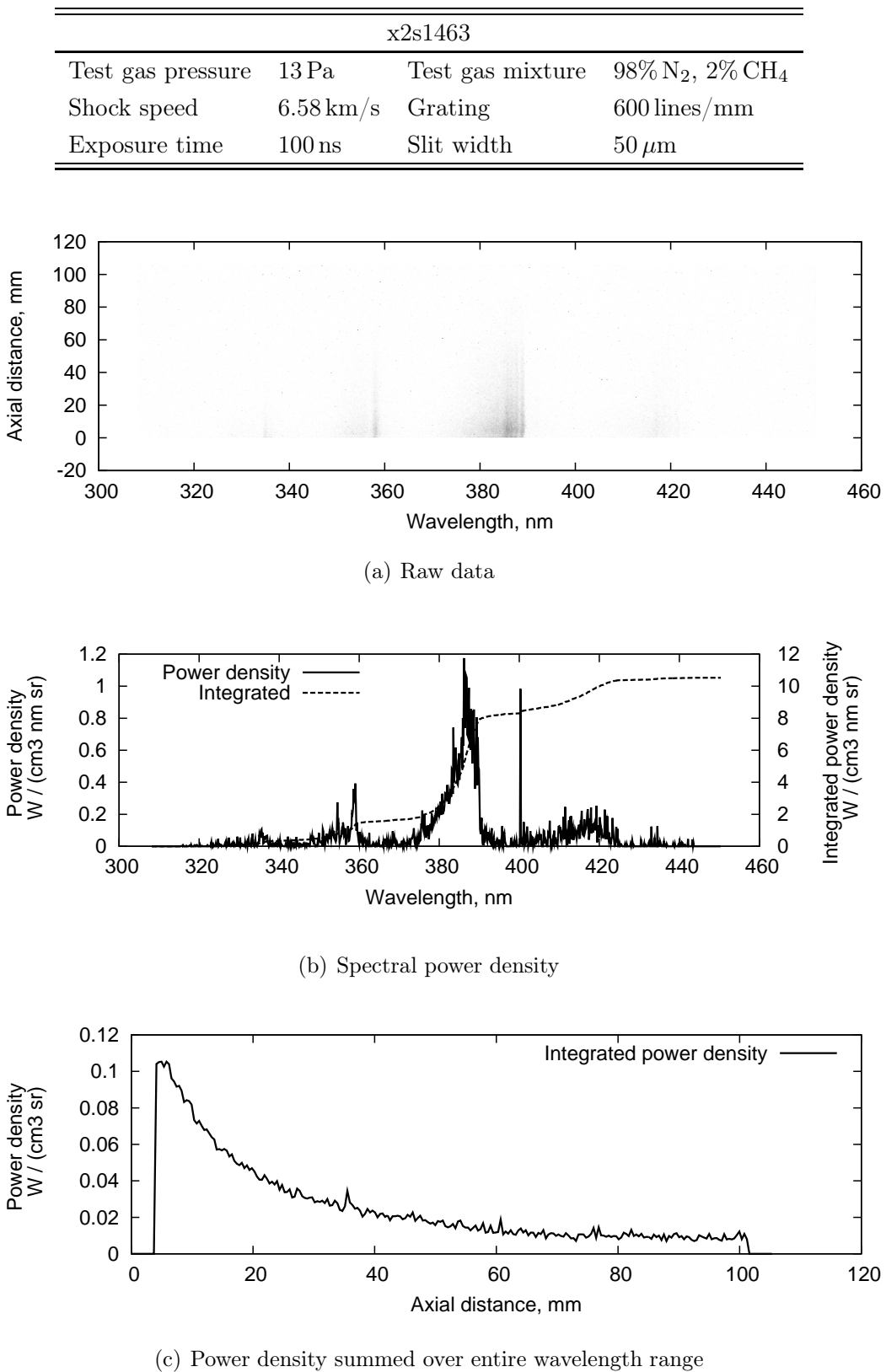


Figure F.4 : *Raw and calibrated data for x2s1463.*

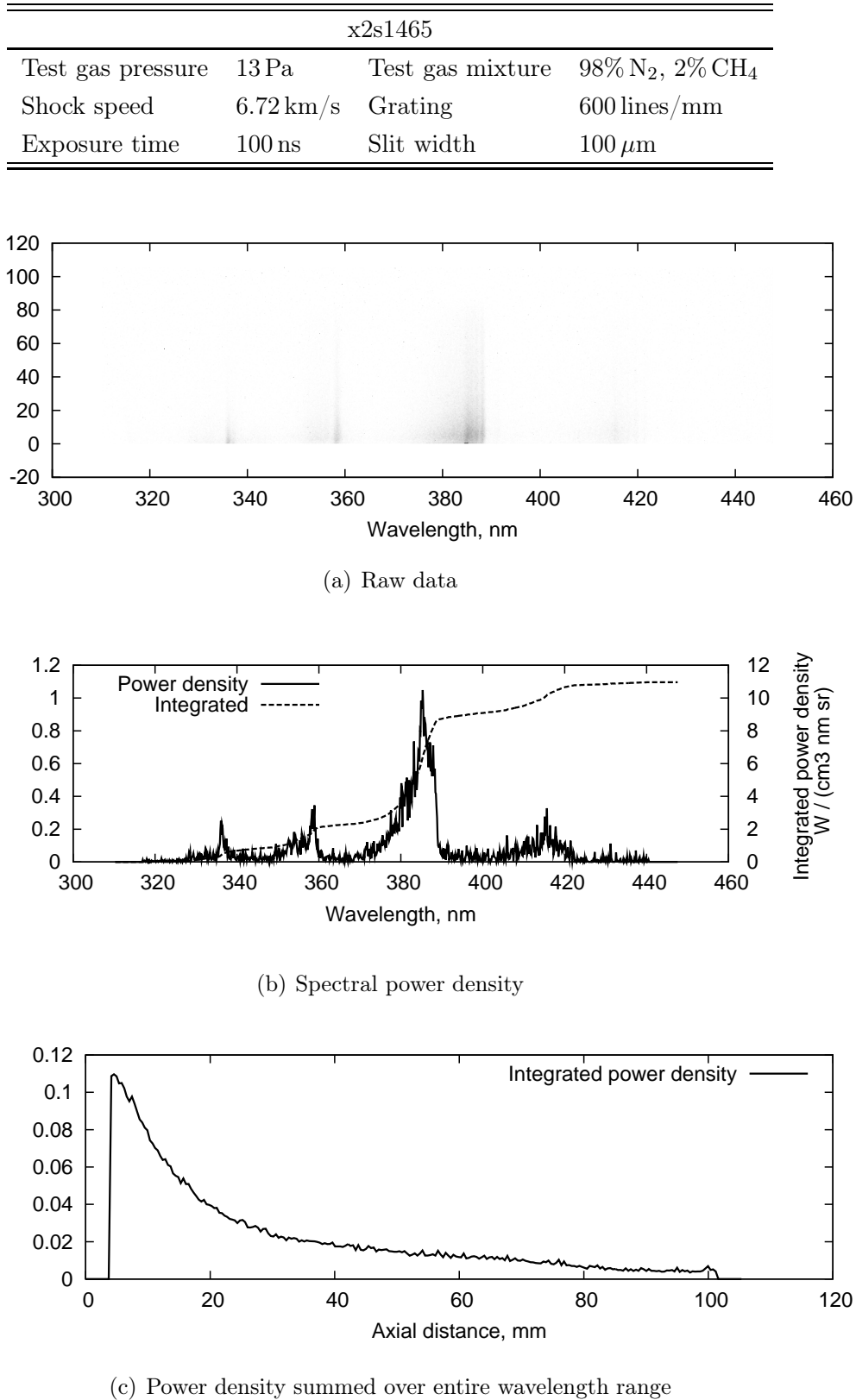
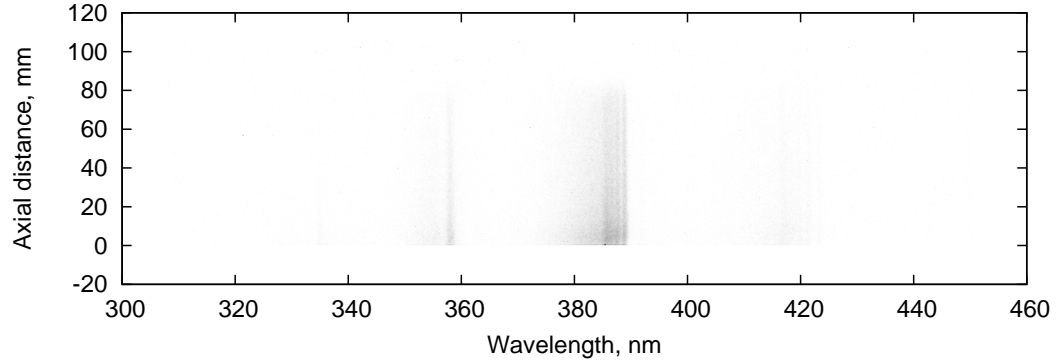
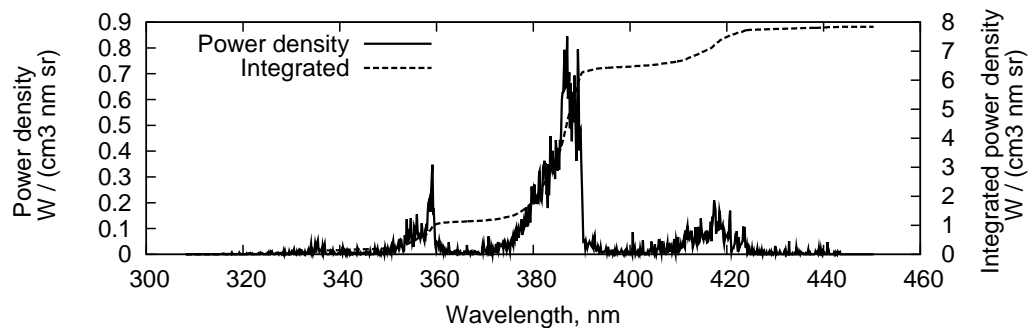


Figure F.5 : *Raw and calibrated data for x2s1465.*

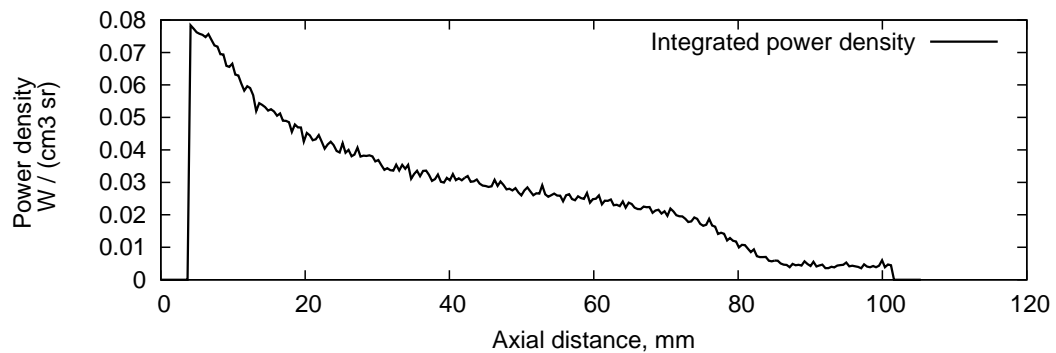
x2s1468			
Test gas pressure	13 Pa	Test gas mixture	98% N ₂ , 2% CH ₄
Shock speed	6.65 km/s	Grating	600 lines/mm
Exposure time	100 ns	Slit width	100 μ m



(a) Raw data



(b) Spectral power density



(c) Power density summed over entire wavelength range

Figure F.6 : *Raw and calibrated data for x2s1468.*

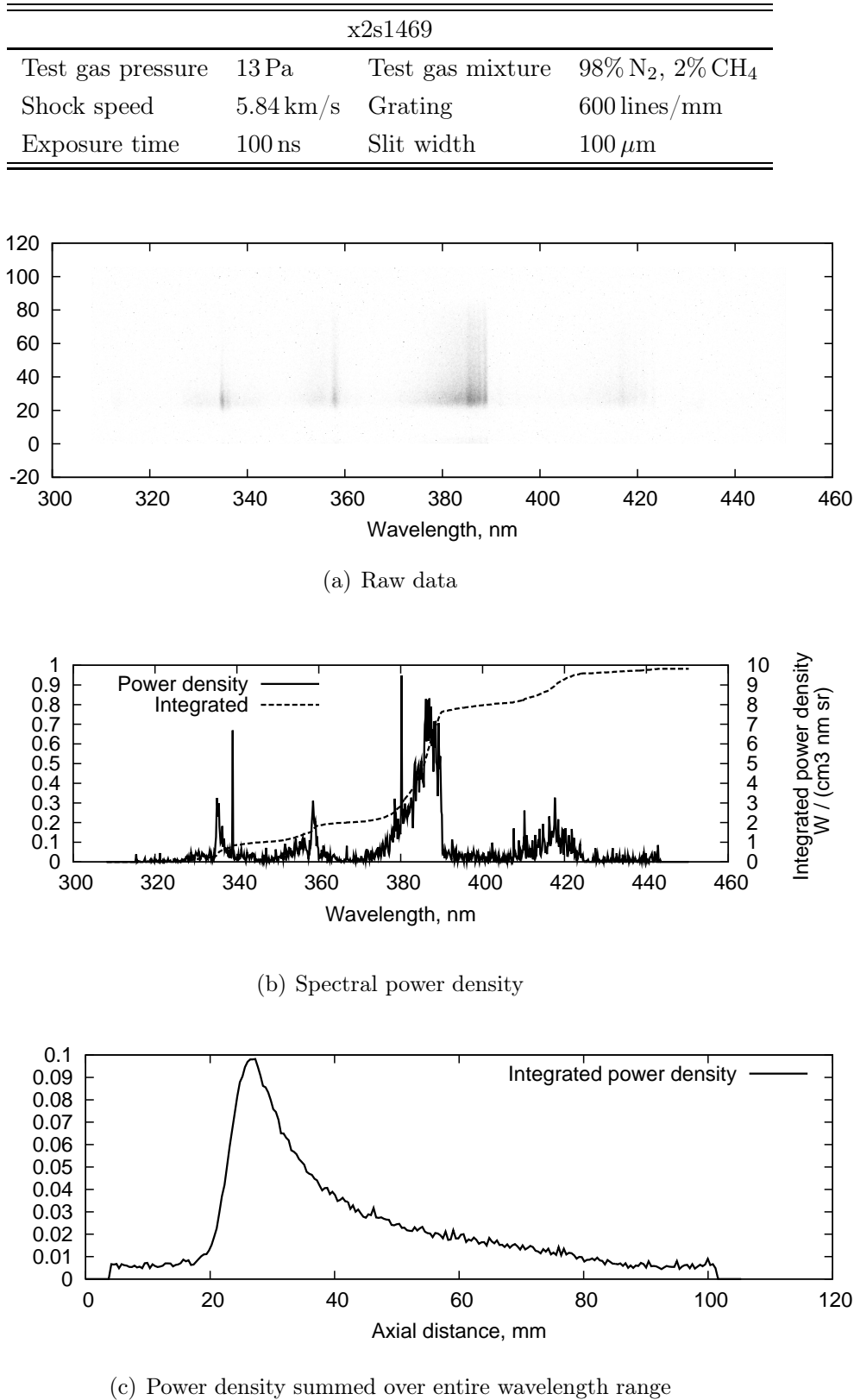


Figure F.7 : *Raw and calibrated data for x2s1469.*

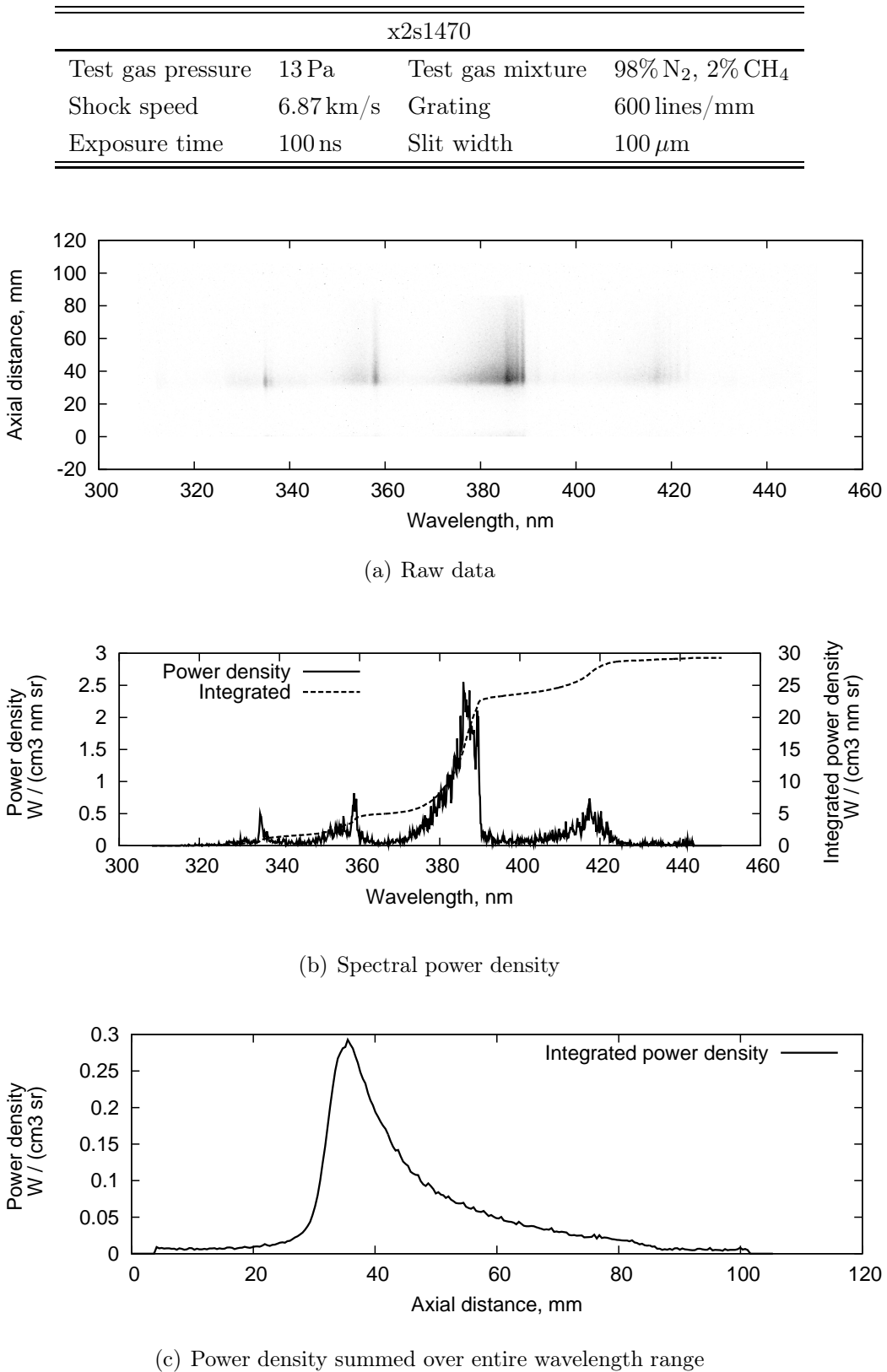


Figure F.8 : *Raw and calibrated data for x2s1470.*

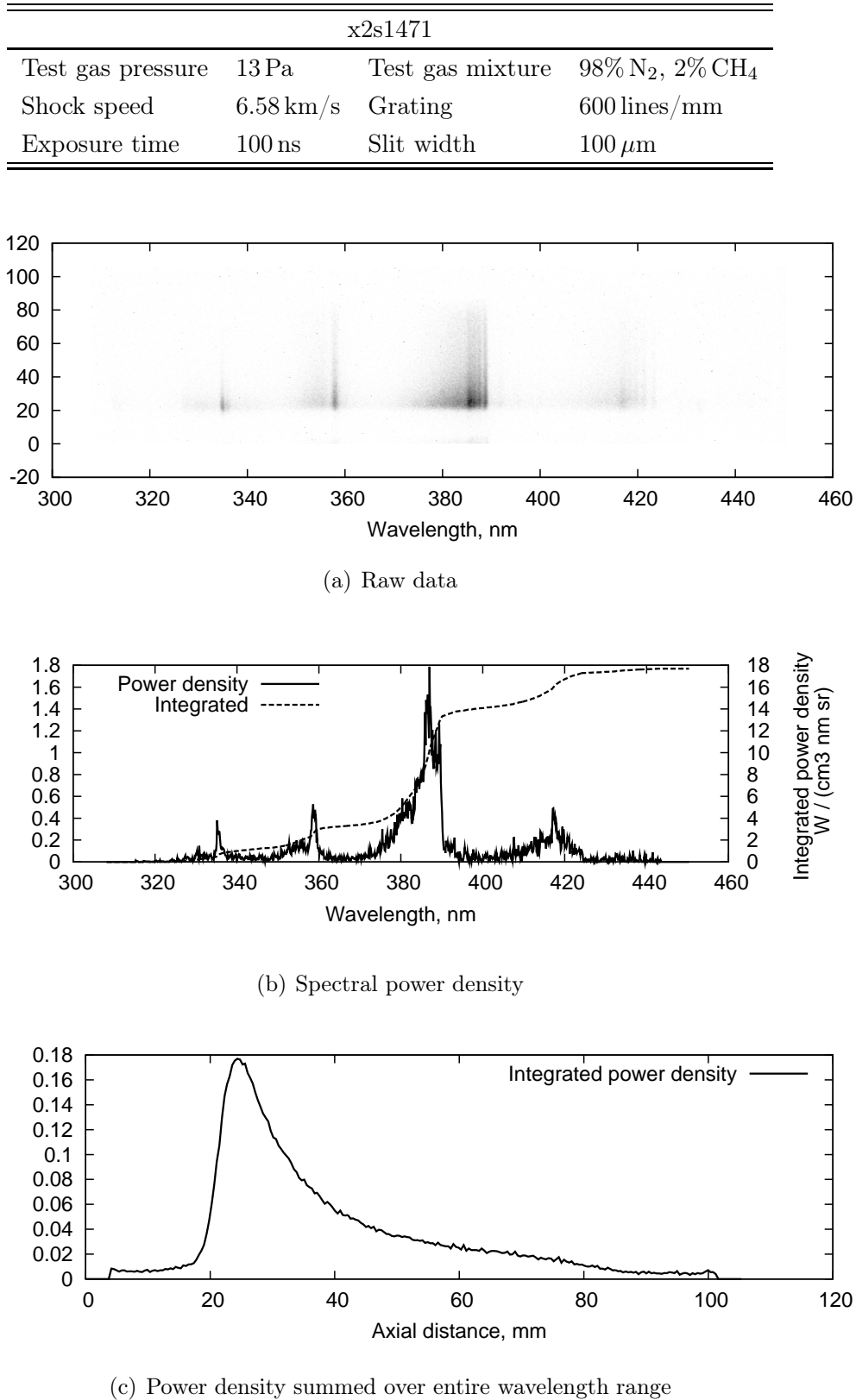
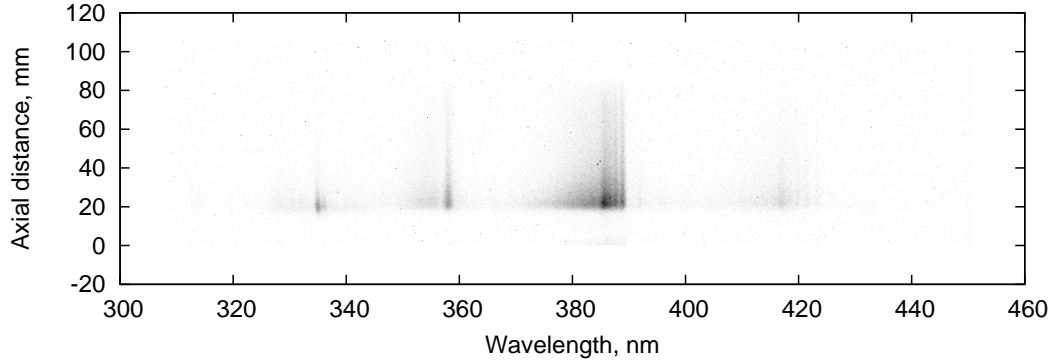
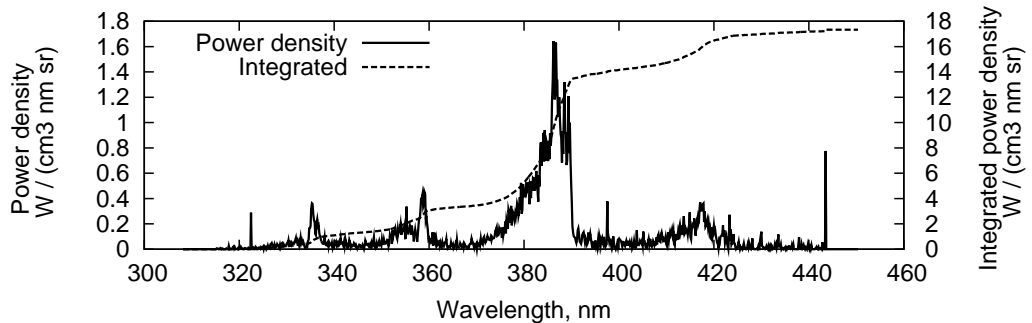


Figure F.9 : *Raw and calibrated data for x2s1471.*

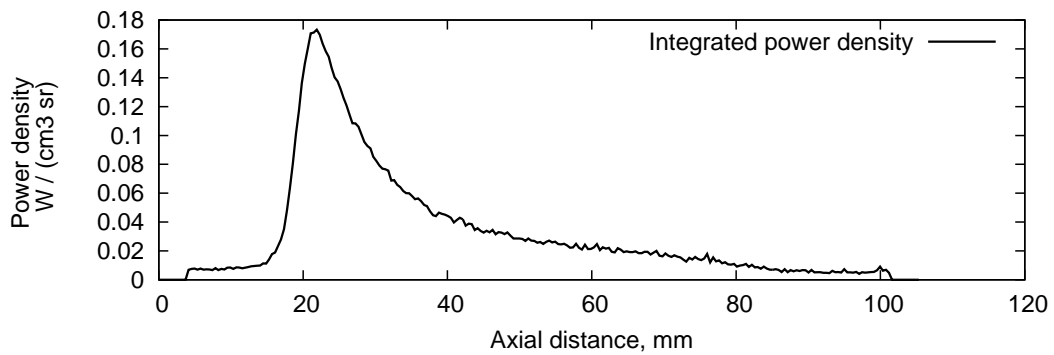
x2s1472			
Test gas pressure	13 Pa	Test gas mixture	98% N ₂ , 2% CH ₄
Shock speed	6.79 km/s	Grating	600 lines/mm
Exposure time	100 ns	Slit width	100 μ m



(a) Raw data



(b) Spectral power density



(c) Power density summed over entire wavelength range

Figure F.10 : *Raw and calibrated data for x2s1472.*

APPENDIX F

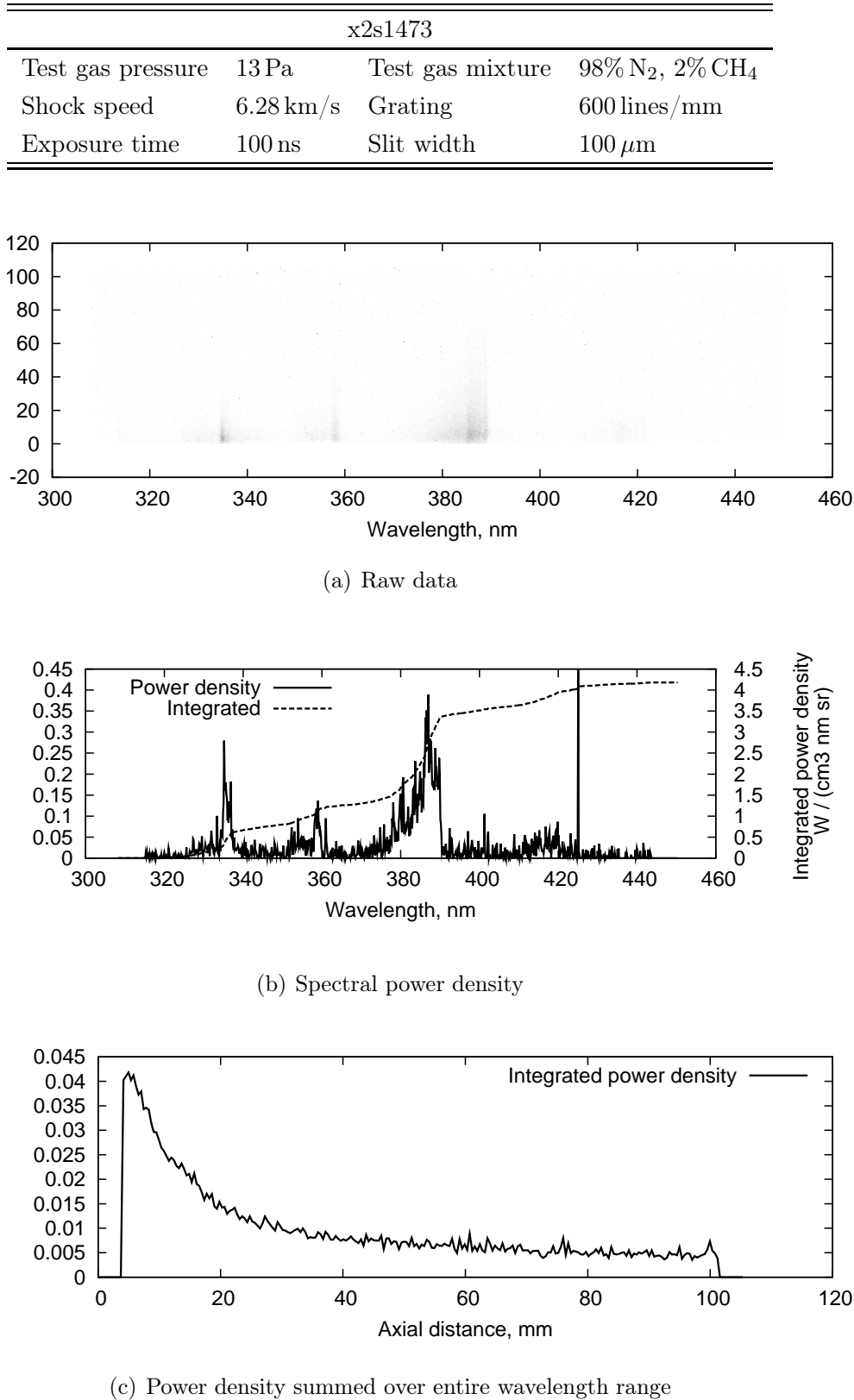


Figure F.11 : *Raw and calibrated data for x2s1473.*

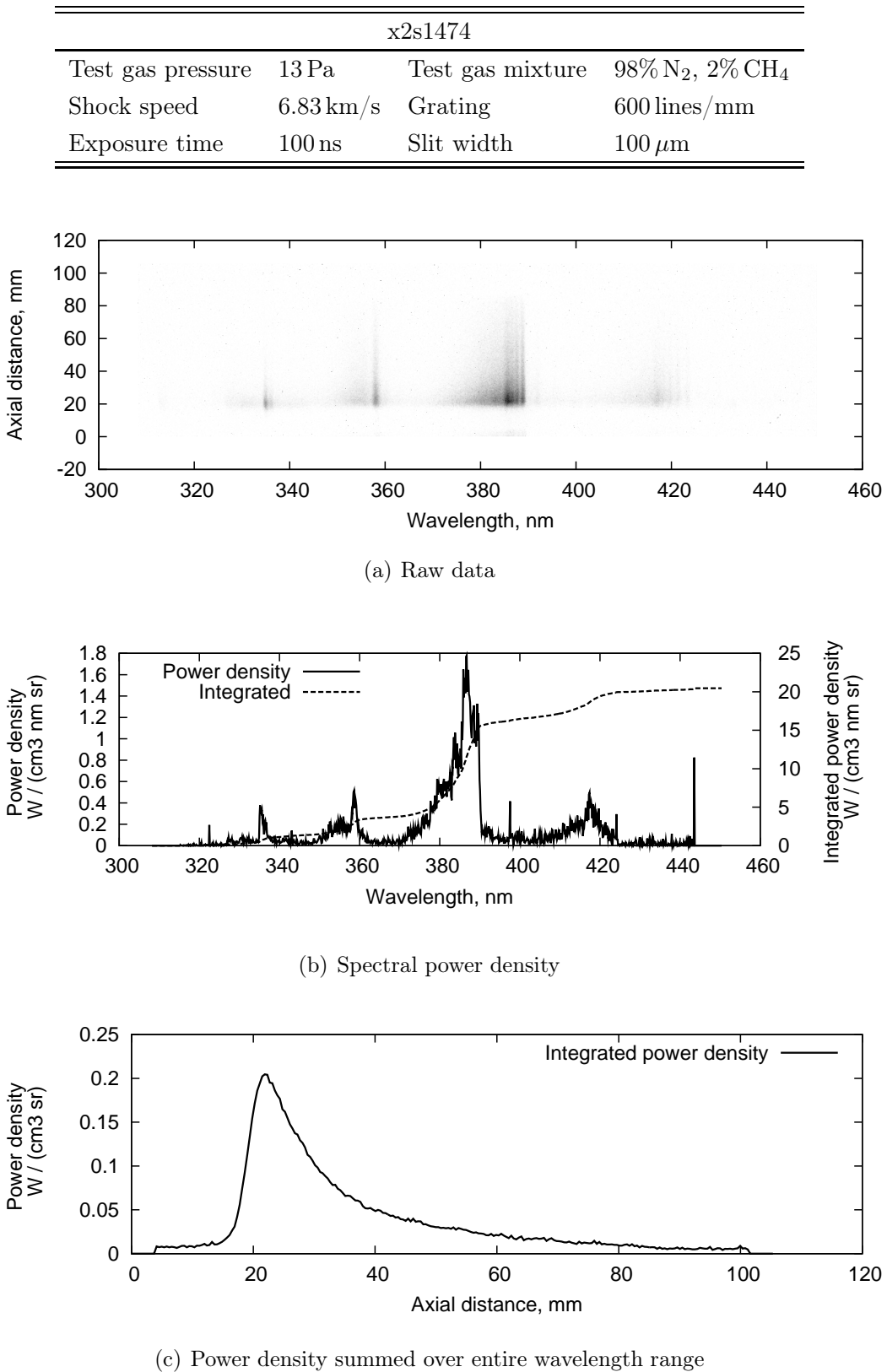


Figure F.12 : *Raw and calibrated data for x2s1474.*

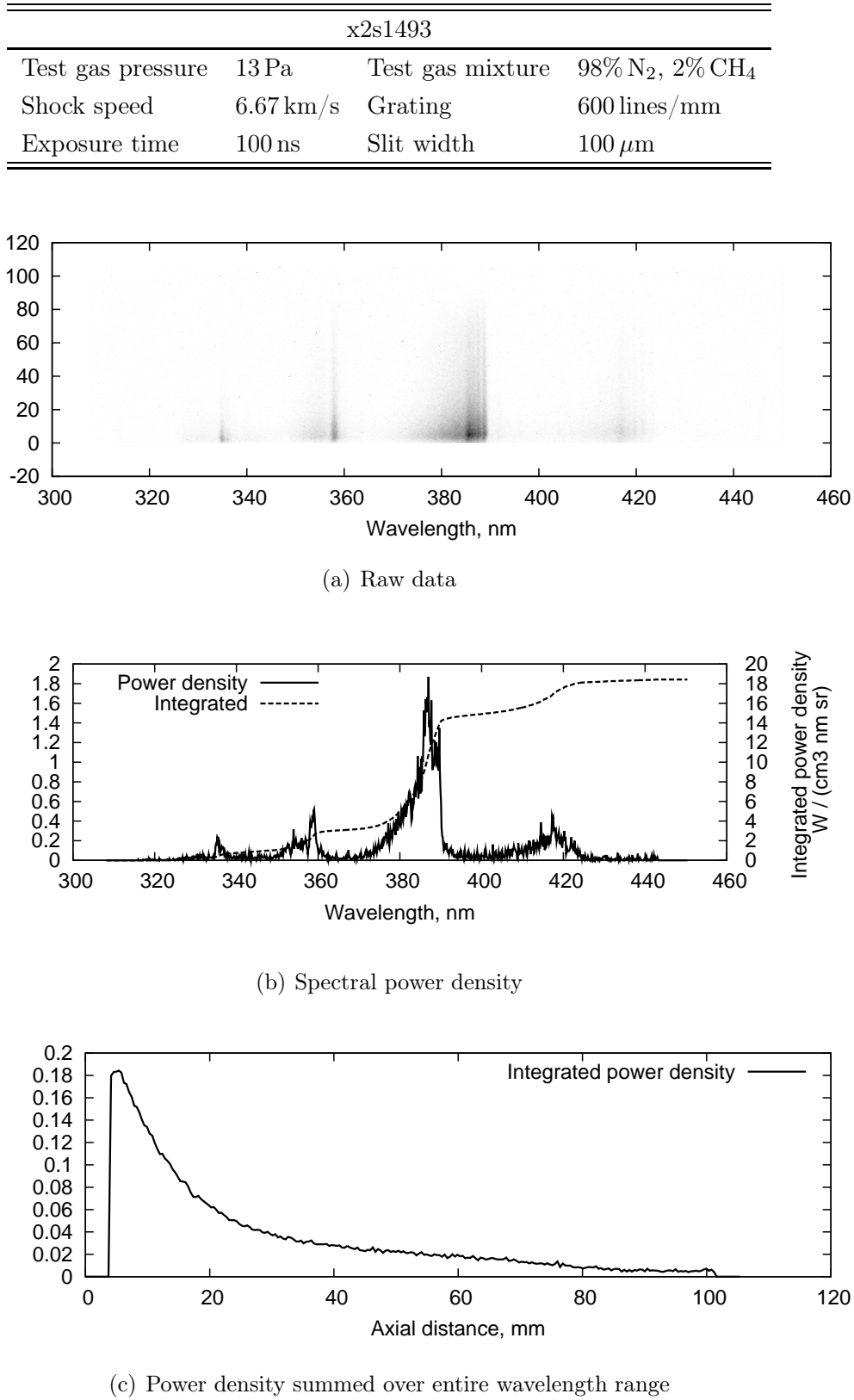
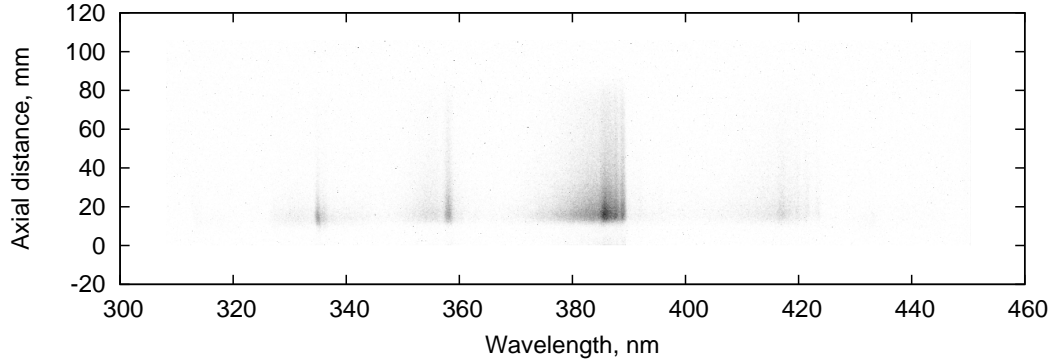
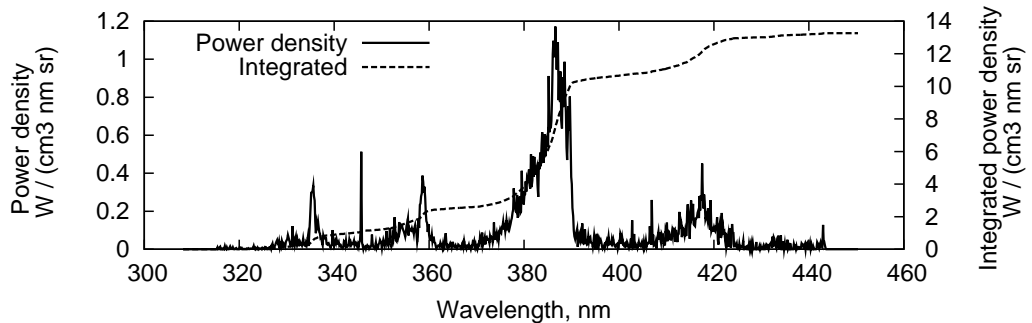


Figure F.13 : *Raw and calibrated data for x2s1493.*

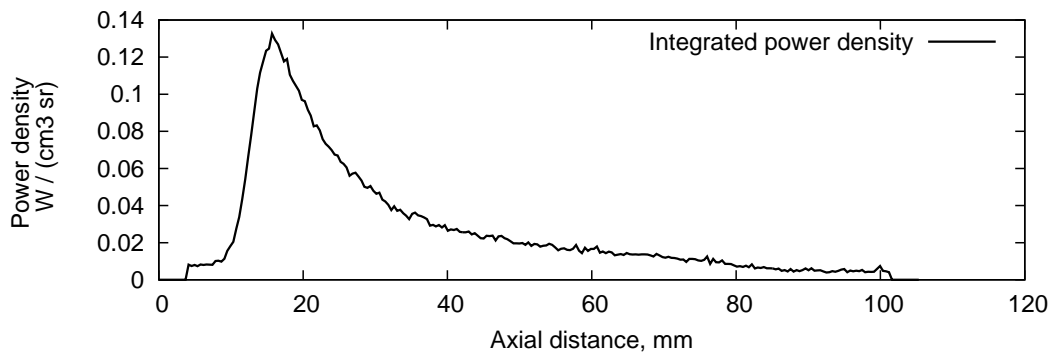
x2s1494			
Test gas pressure	13 Pa	Test gas mixture	98% N ₂ , 2% CH ₄
Shock speed	6.17 km/s	Grating	600 lines/mm
Exposure time	100 ns	Slit width	100 μ m



(a) Raw data



(b) Spectral power density



(c) Power density summed over entire wavelength range

Figure F.14 : Raw and calibrated data for x2s1494.

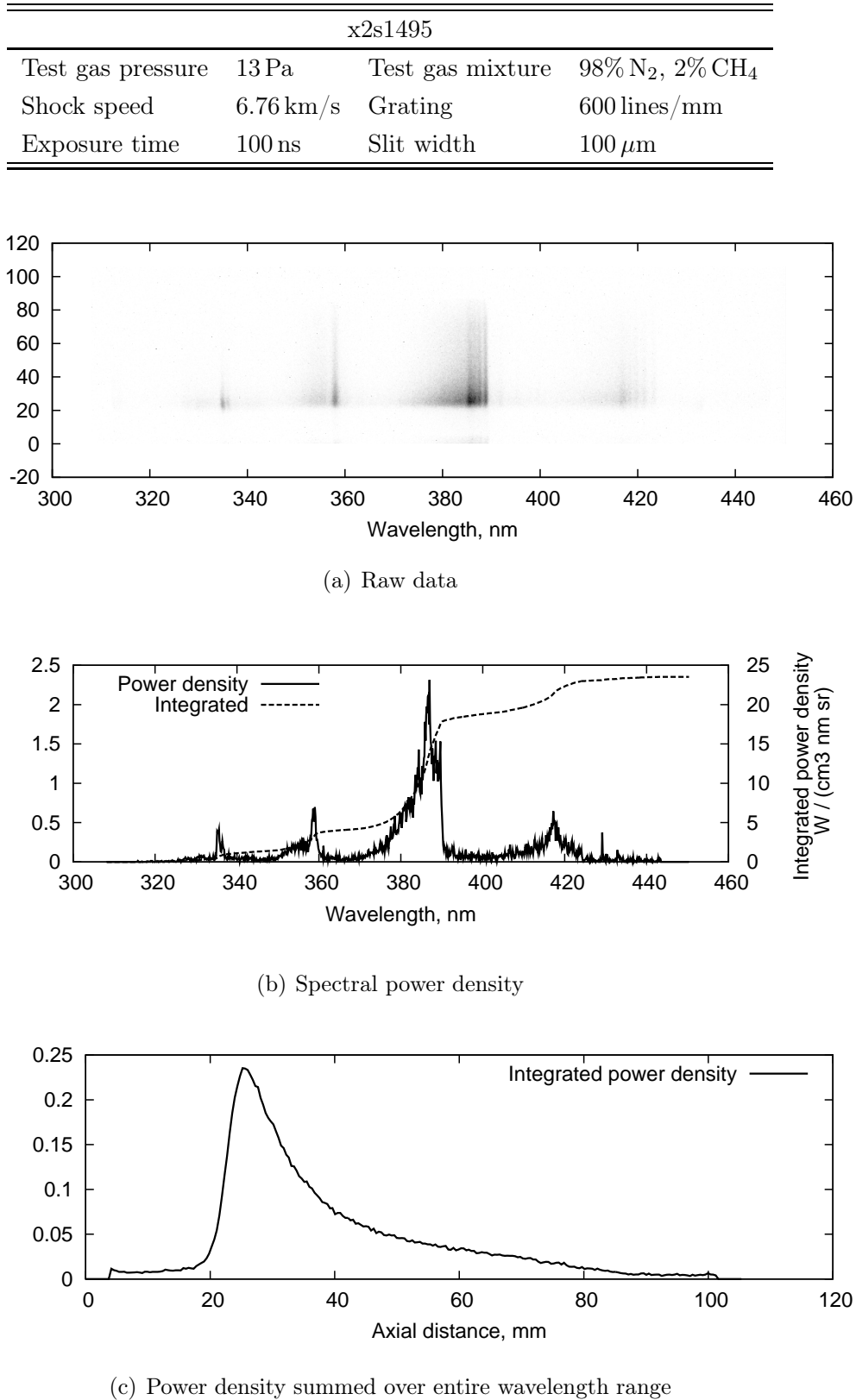


Figure F.15 : *Raw and calibrated data for x2s1495.*

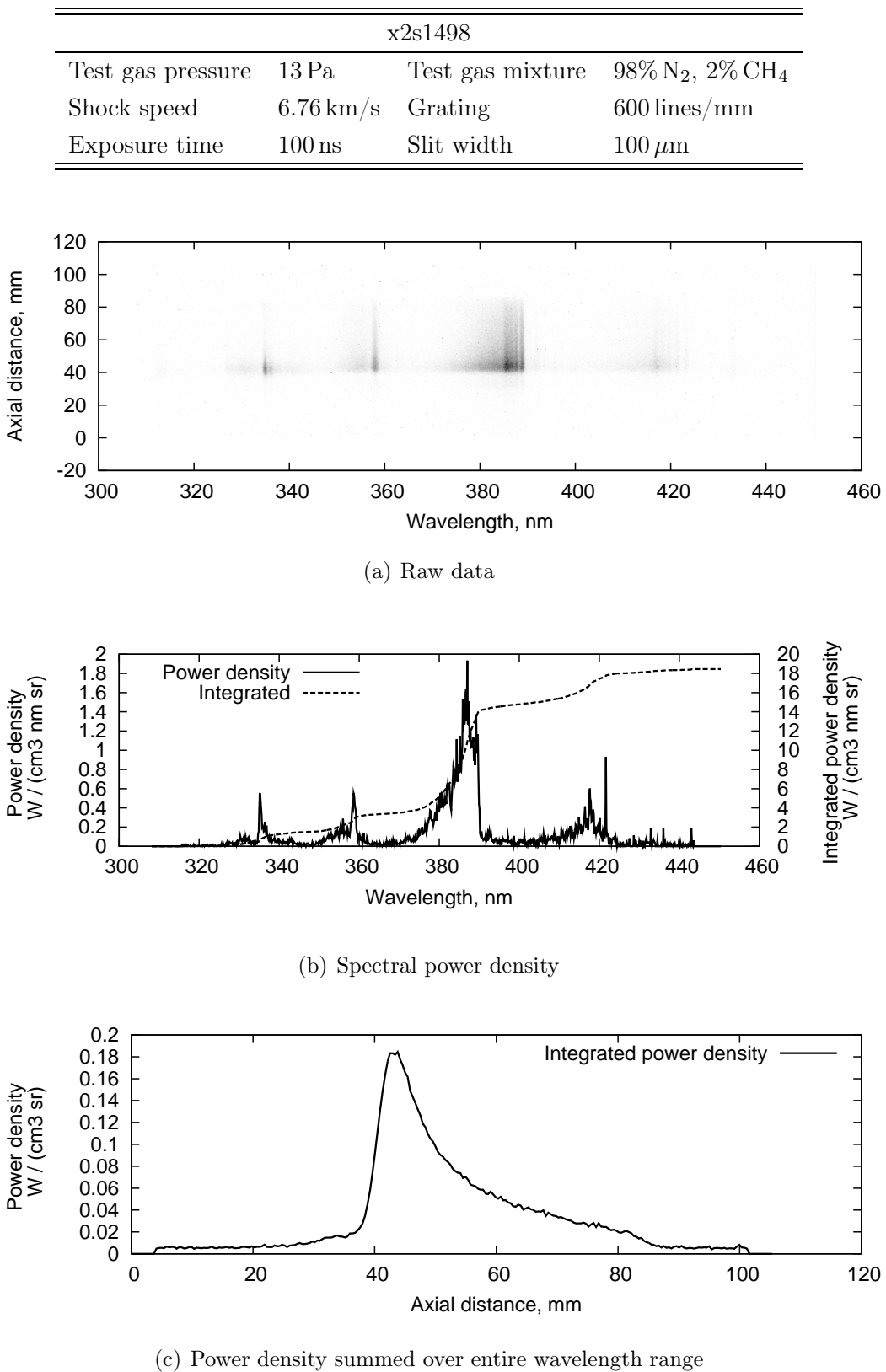


Figure F.16 : *Raw and calibrated data for x2s1498.*

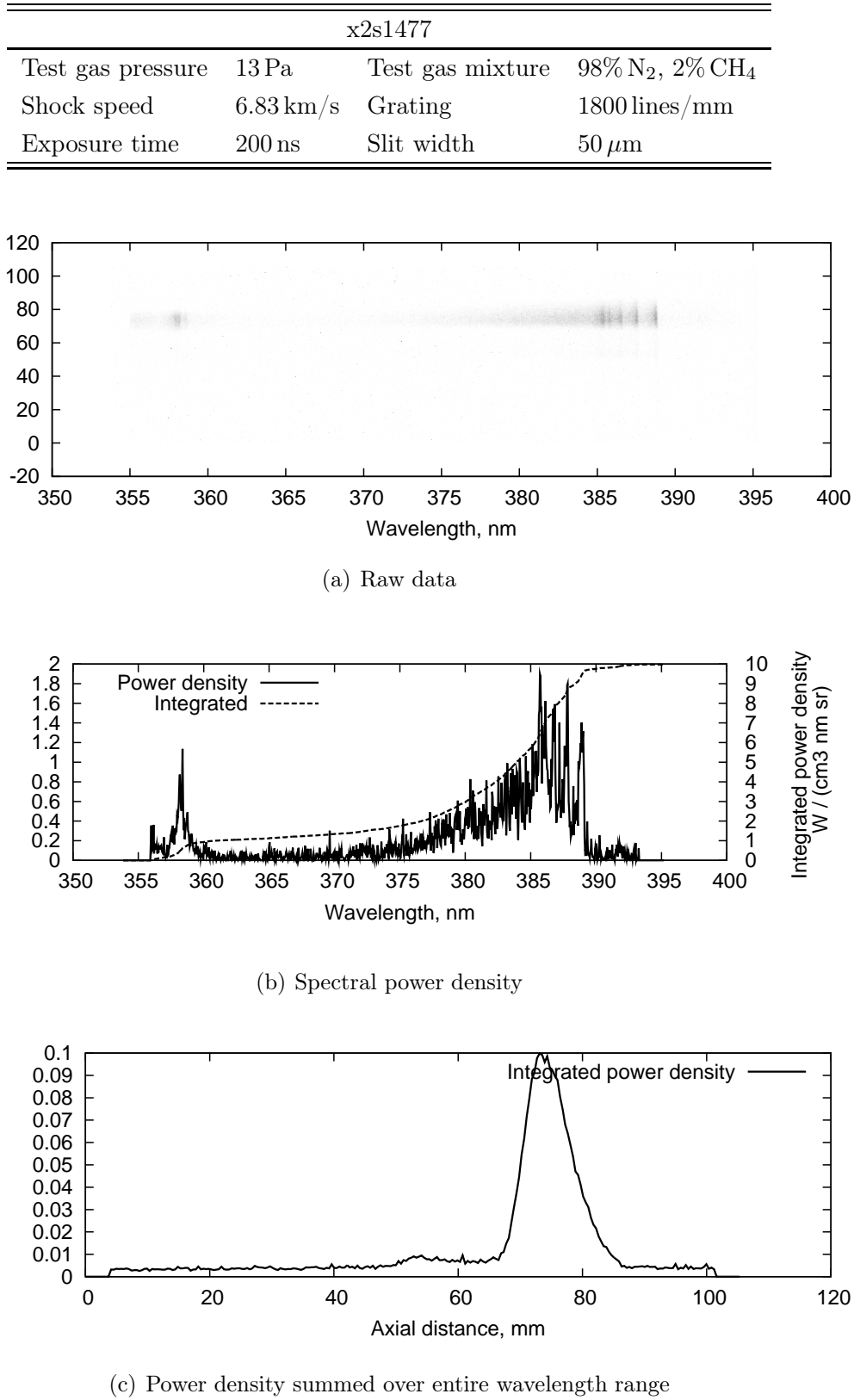
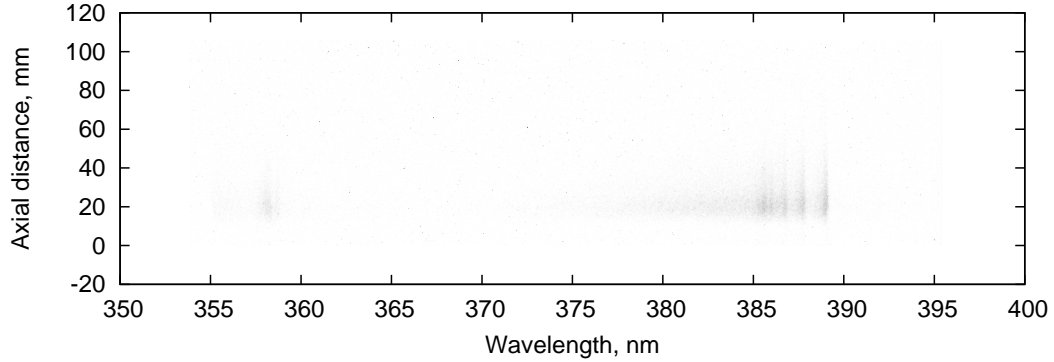
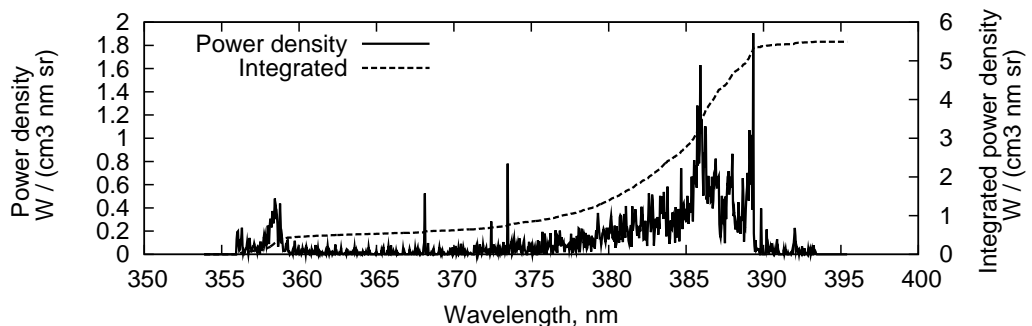


Figure F.17 : *Raw and calibrated data for x2s1477.*

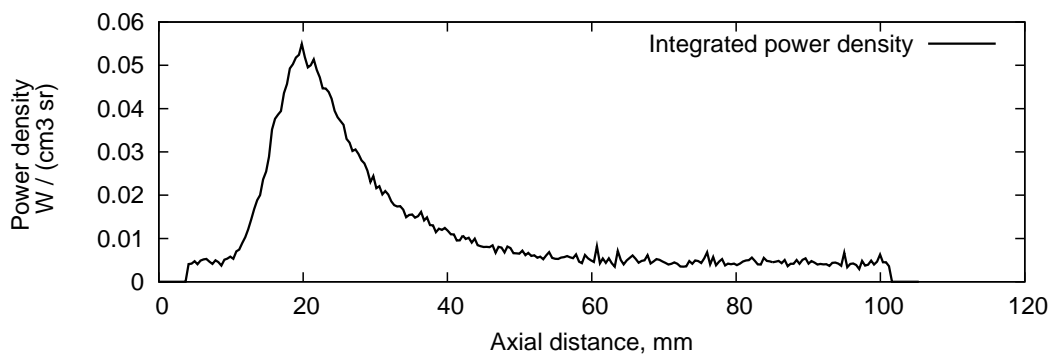
x2s1499			
Test gas pressure	13 Pa	Test gas mixture	98% N ₂ , 2% CH ₄
Shock speed	6.49 km/s	Grating	1800 lines/mm
Exposure time	200 ns	Slit width	50 μ m



(a) Raw data



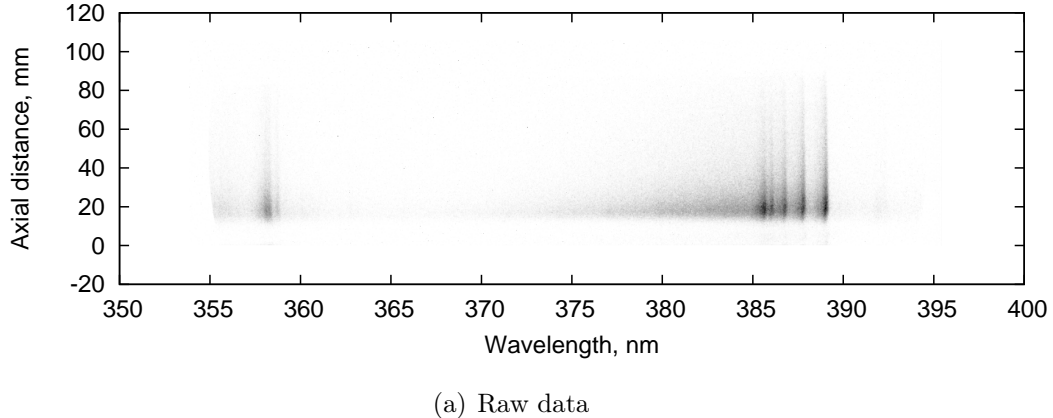
(b) Spectral power density



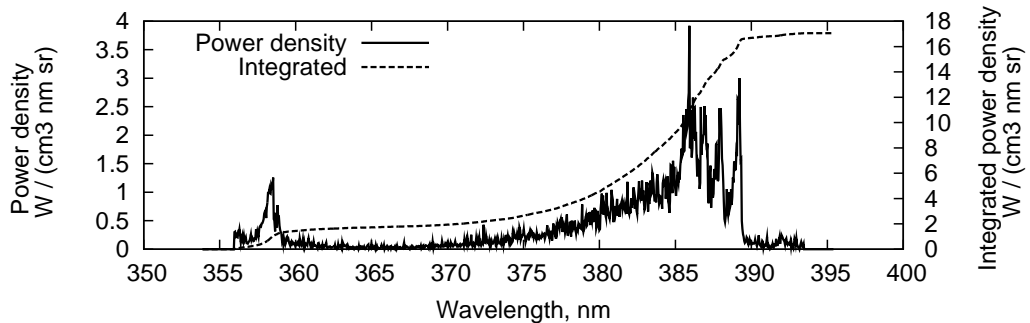
(c) Power density summed over entire wavelength range

Figure F.18 : Raw and calibrated data for x2s1499.

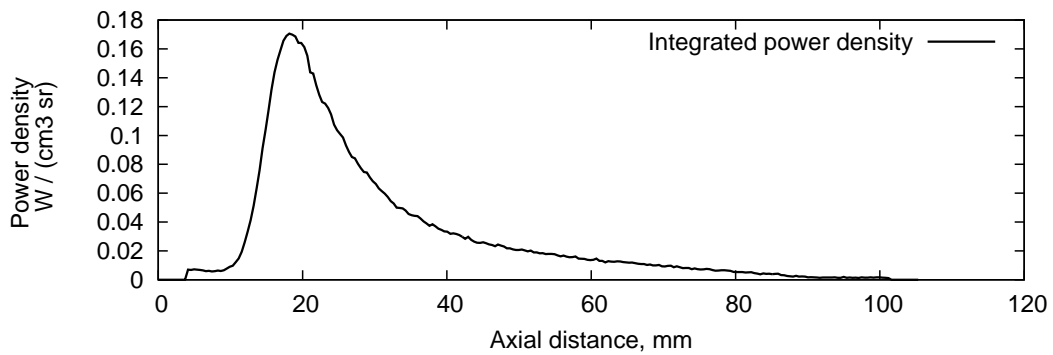
x2s1500			
Test gas pressure	13 Pa	Test gas mixture	98% N ₂ , 2% CH ₄
Shock speed	6.76 km/s	Grating	1800 lines/mm
Exposure time	500 ns	Slit width	50 μ m



(a) Raw data



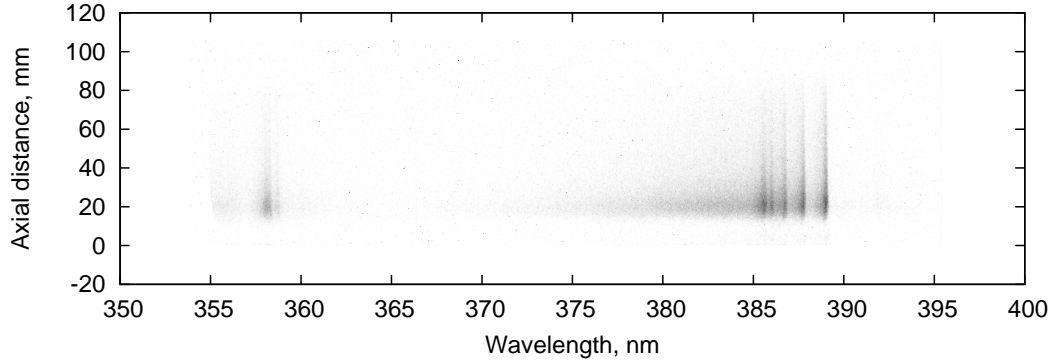
(b) Spectral power density



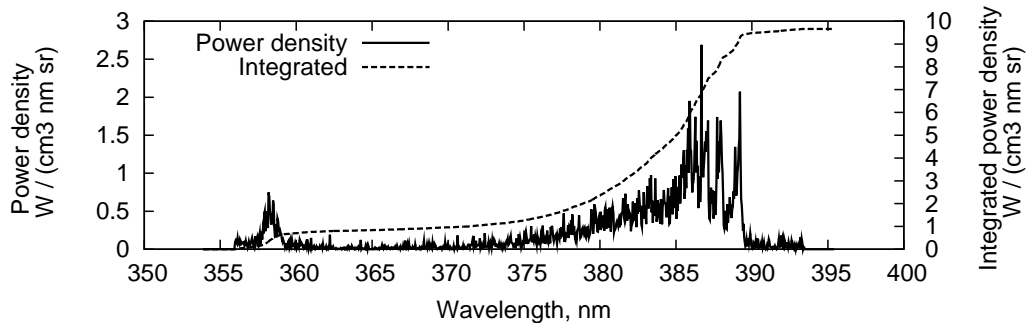
(c) Power density summed over entire wavelength range

Figure F.19 : *Raw and calibrated data for x2s1500.*

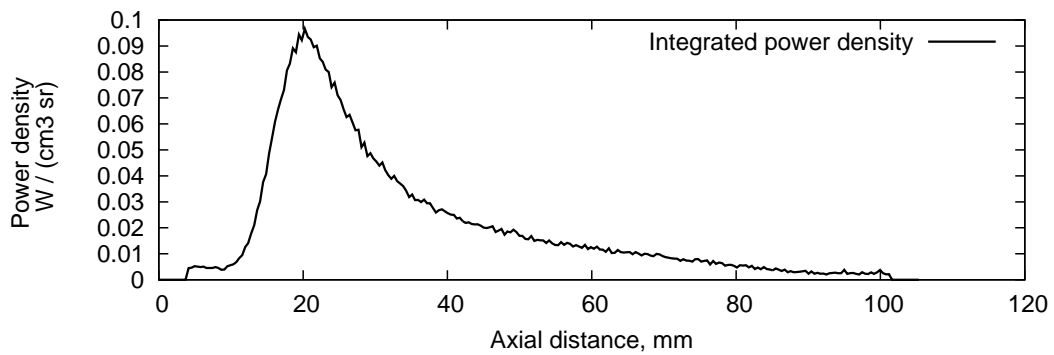
x2s1501			
Test gas pressure	13 Pa	Test gas mixture	98% N ₂ , 2% CH ₄
Shock speed	6.10 km/s	Grating	1800 lines/mm
Exposure time	1000 ns	Slit width	20 μ m



(a) Raw data



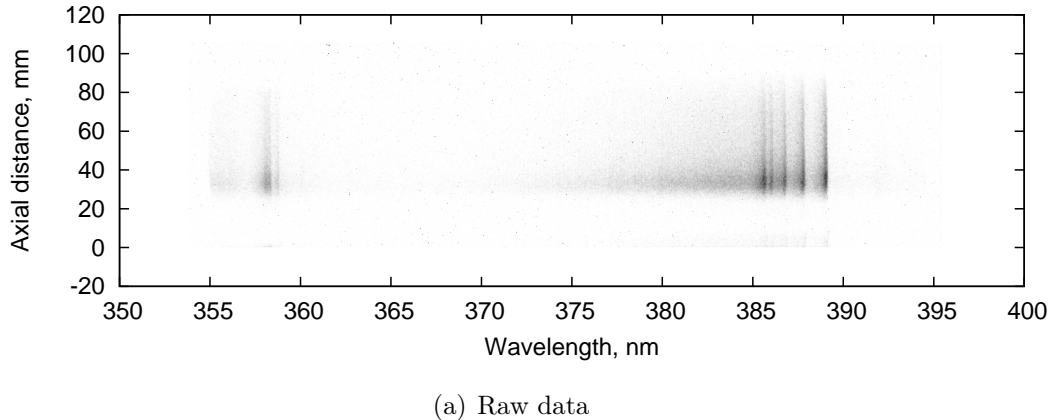
(b) Spectral power density



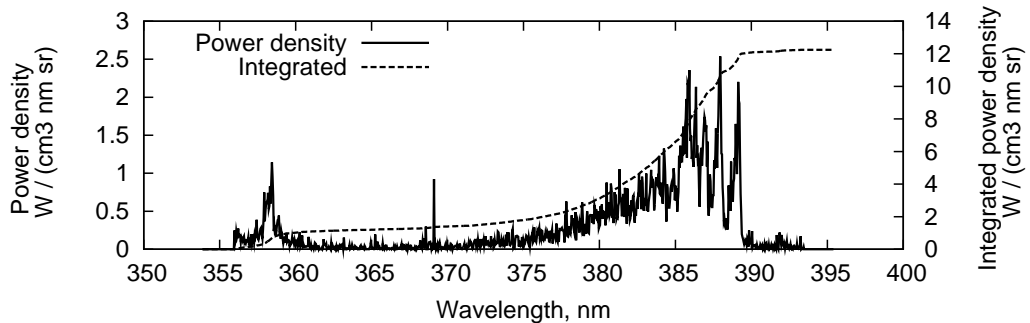
(c) Power density summed over entire wavelength range

Figure F.20 : *Raw and calibrated data for x2s1501.*

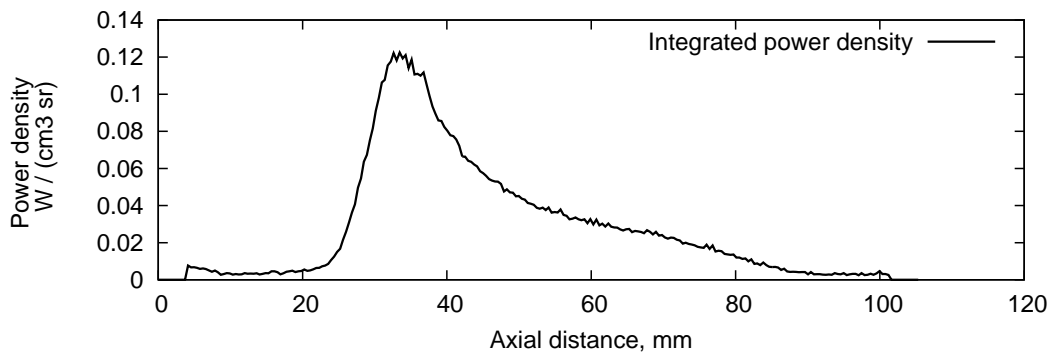
x2s1503			
Test gas pressure	13 Pa	Test gas mixture	98% N ₂ , 2% CH ₄
Shock speed	6.02 km/s	Grating	1800 lines/mm
Exposure time	1000 ns	Slit width	20 μ m



(a) Raw data



(b) Spectral power density



(c) Power density summed over entire wavelength range

Figure F.21 : *Raw and calibrated data for x2s1503.*

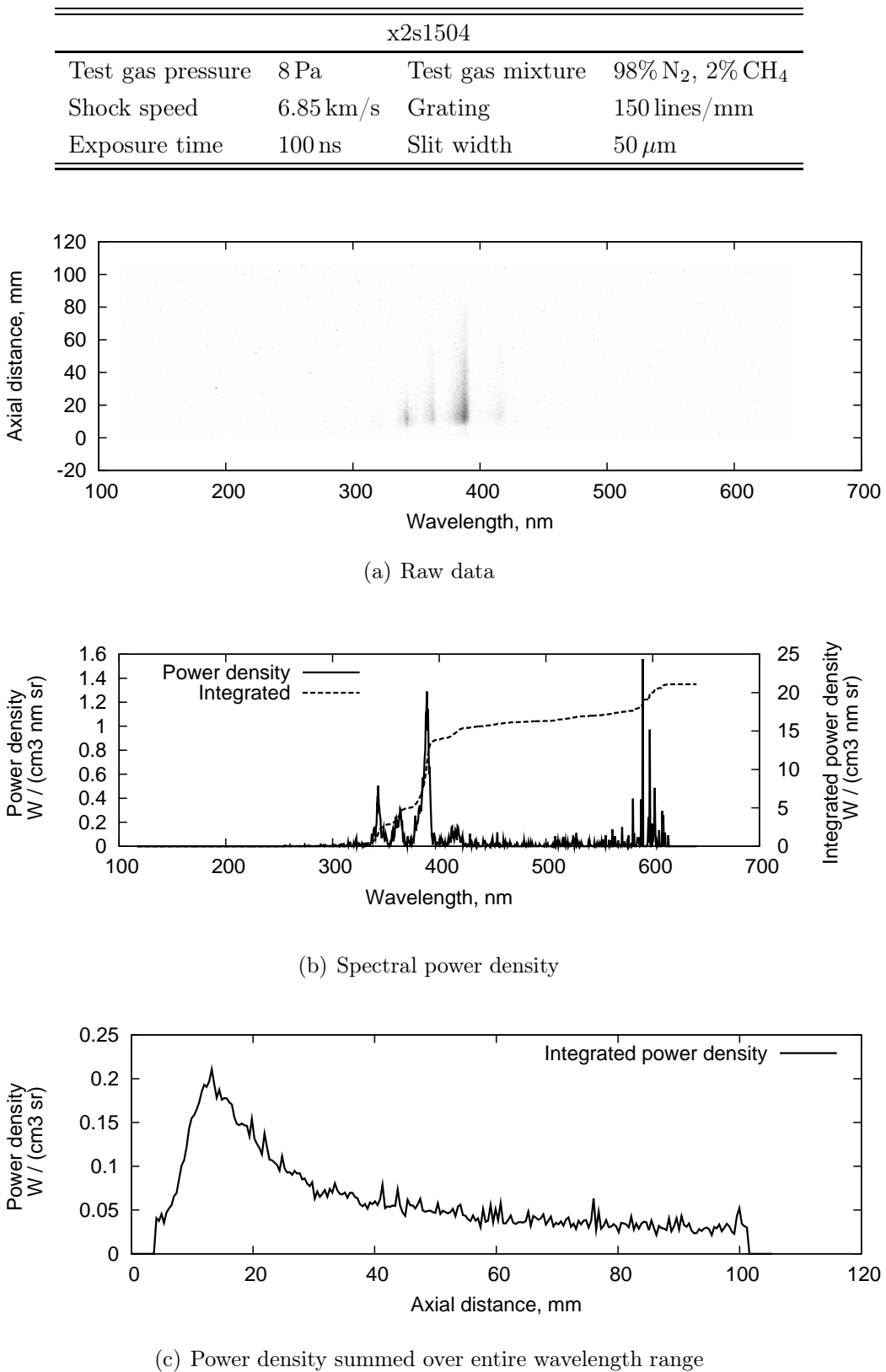


Figure F.22 : *Raw and calibrated data for x2s1504.*

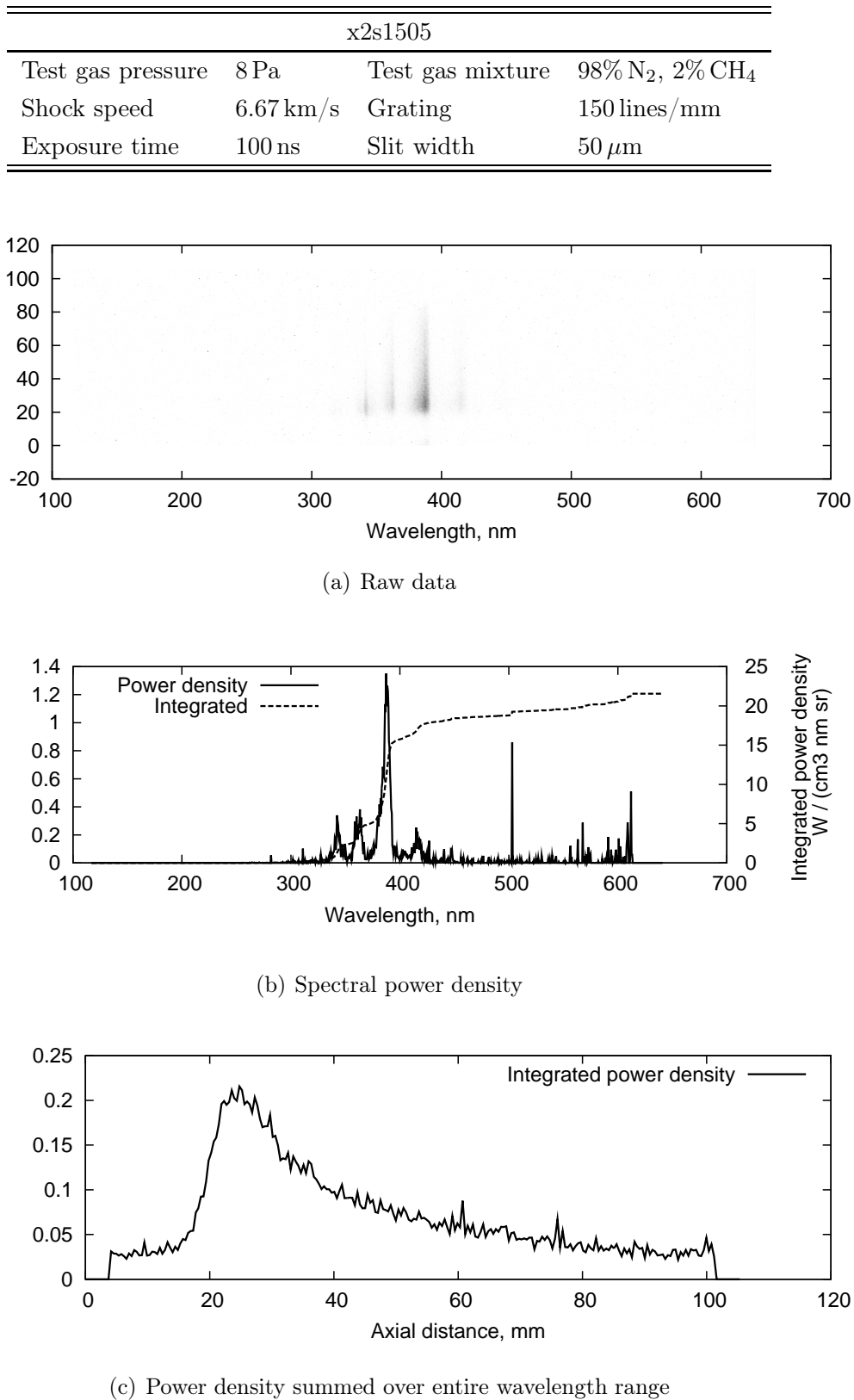


Figure F.23 : *Raw and calibrated data for x2s1505.*

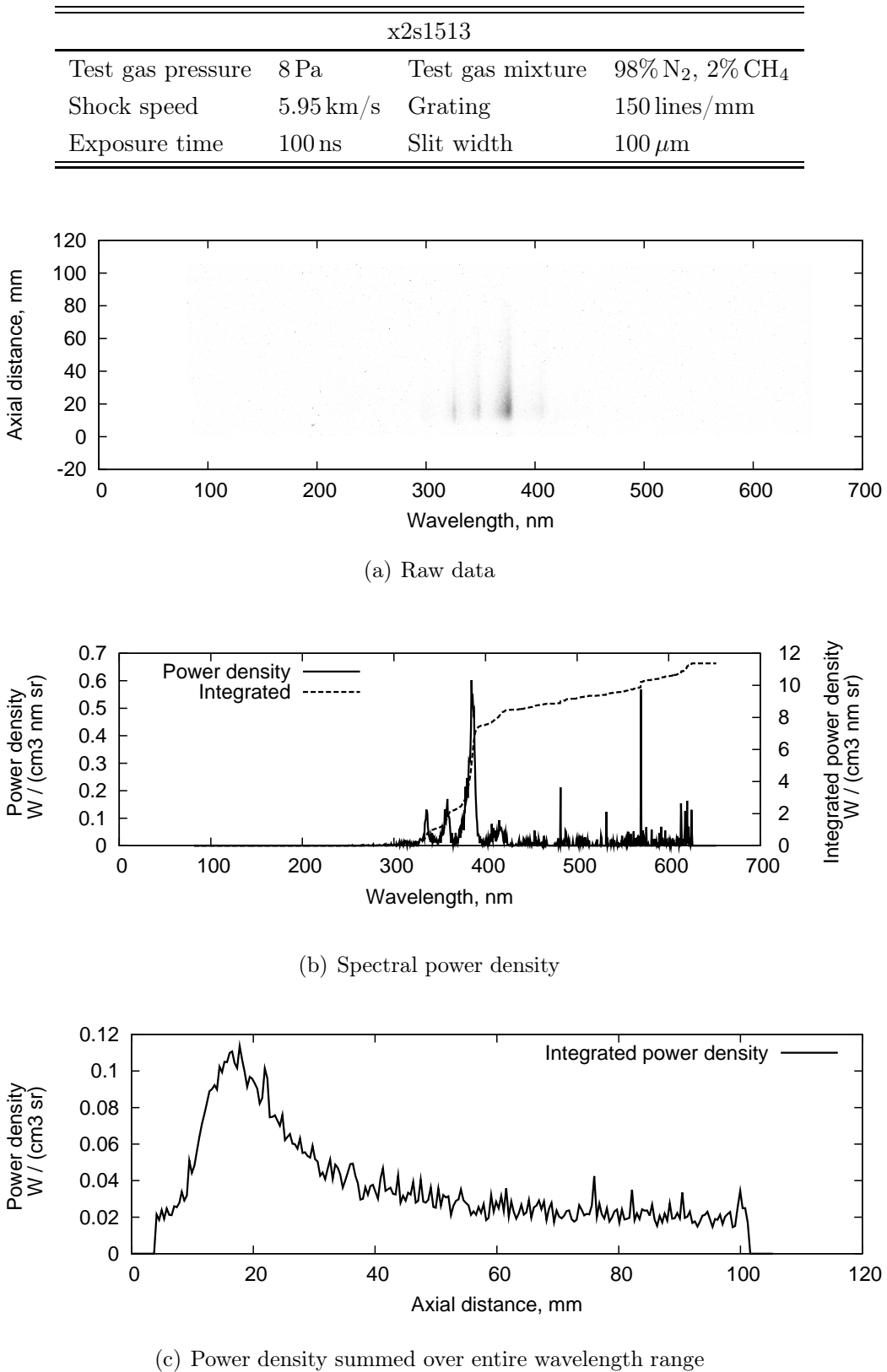


Figure F.24 : *Raw and calibrated data for x2s1513.*

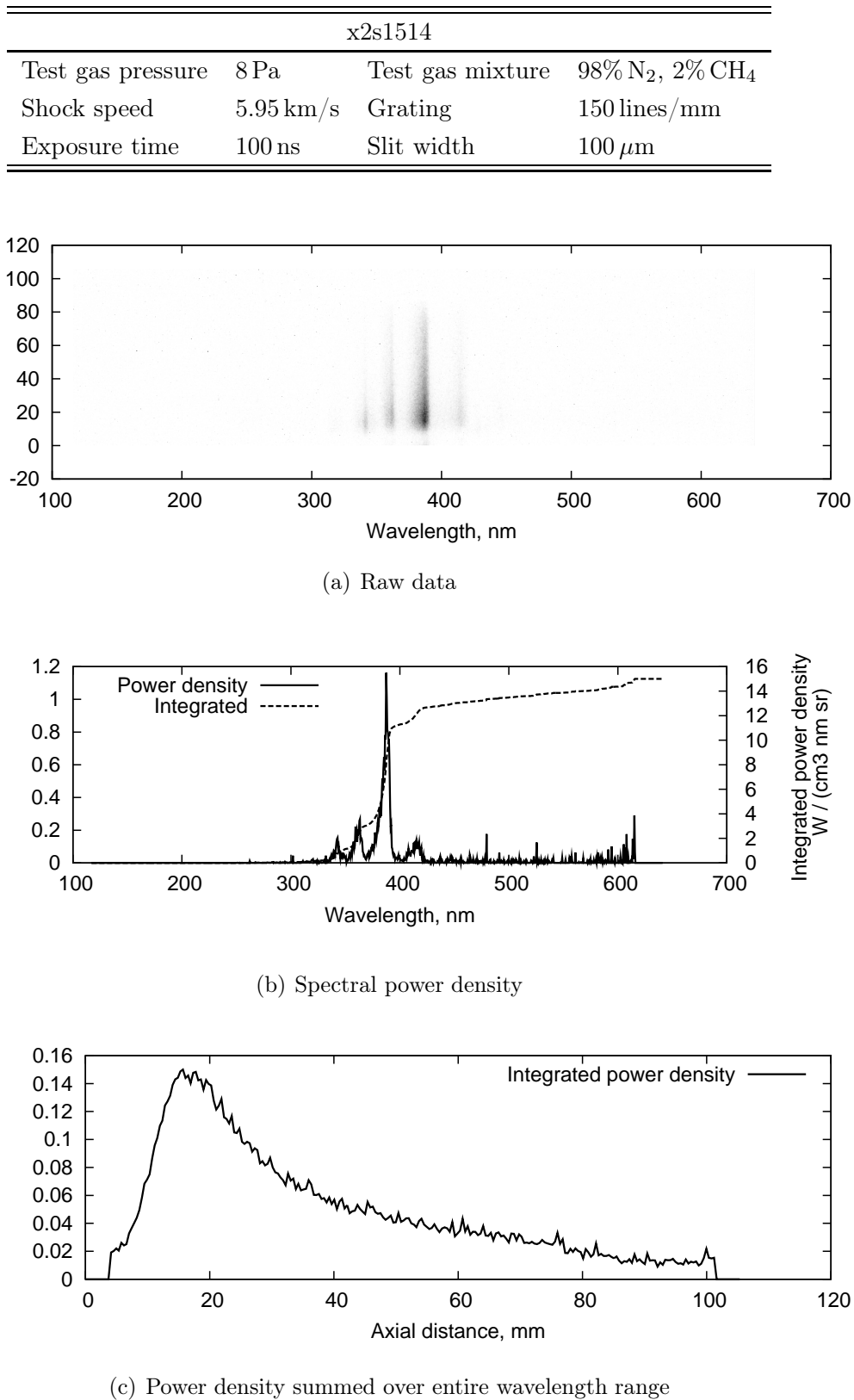


Figure F.25 : *Raw and calibrated data for x2s1514.*

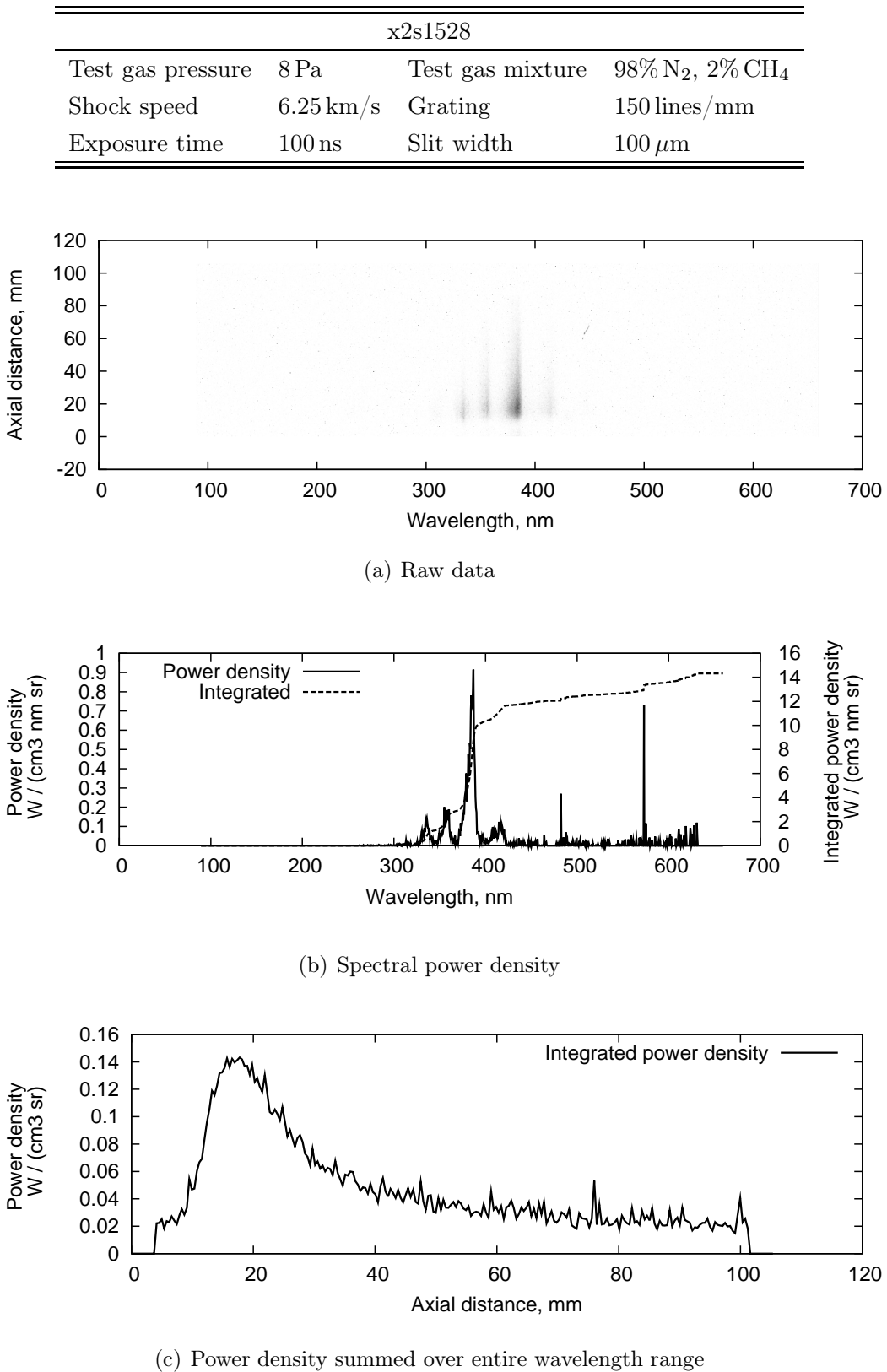


Figure F.26 : *Raw and calibrated data for x2s1528.*

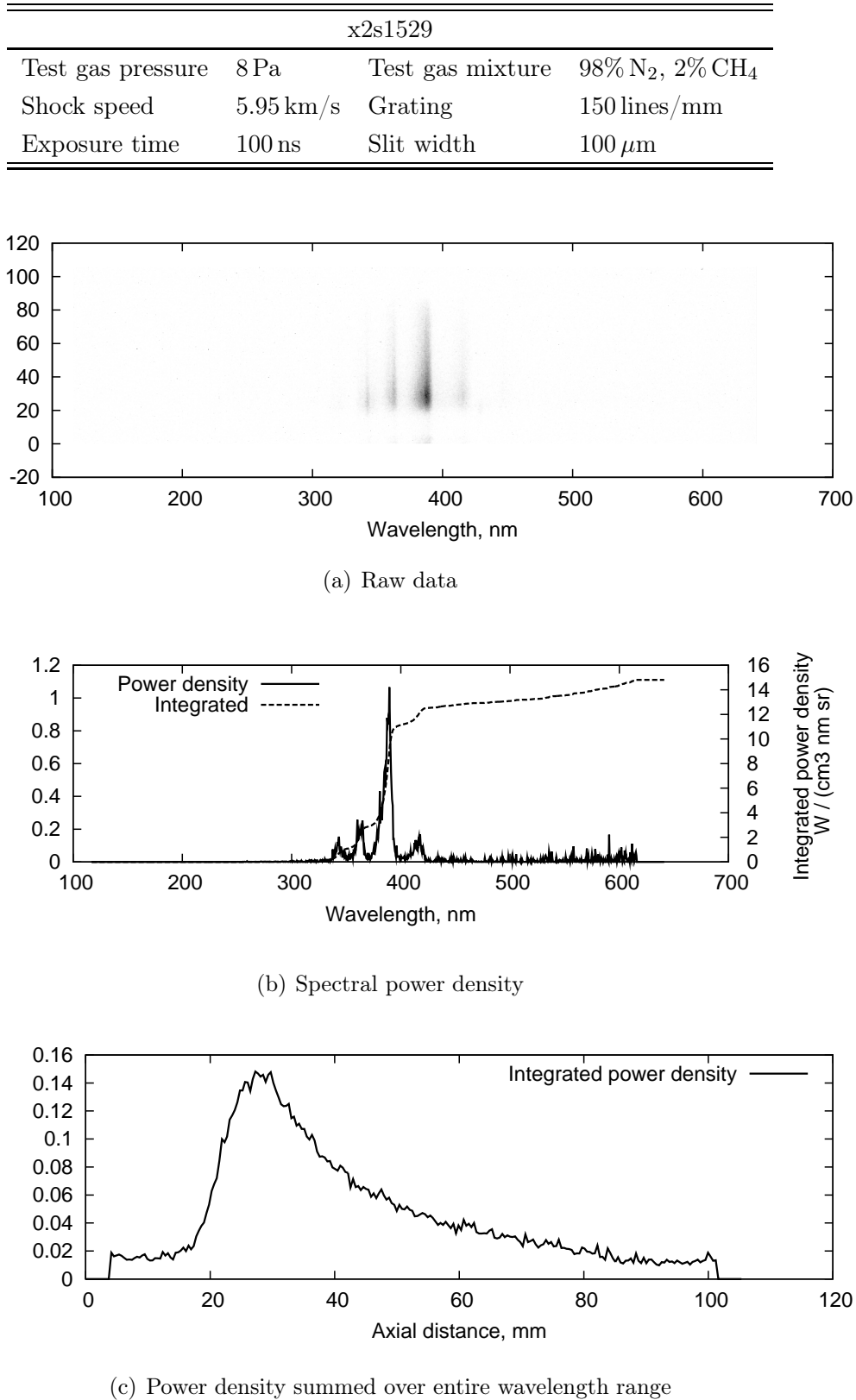
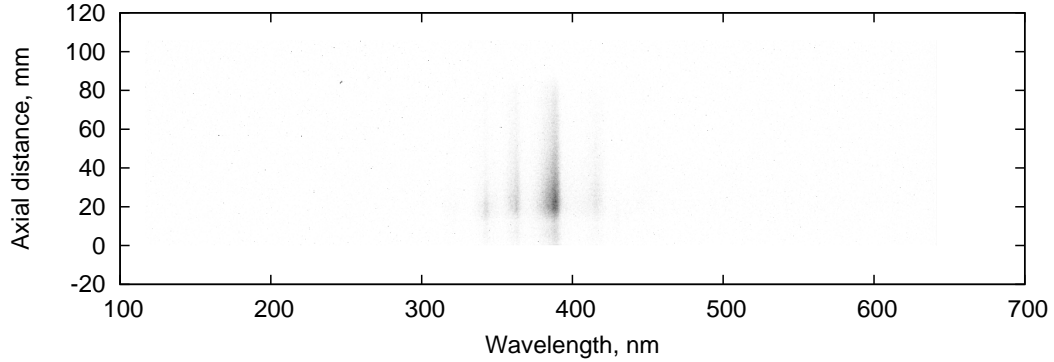
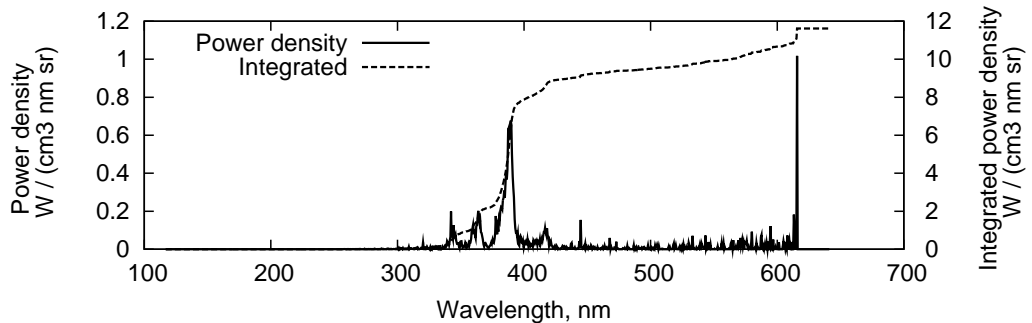


Figure F.27 : *Raw and calibrated data for x2s1529.*

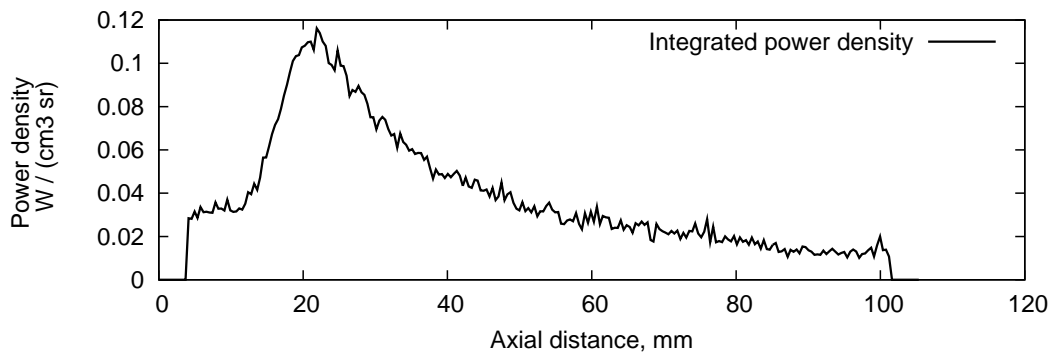
x2s1530			
Test gas pressure	8 Pa	Test gas mixture	98% N ₂ , 2% CH ₄
Shock speed	6.25 km/s	Grating	150 lines/mm
Exposure time	100 ns	Slit width	100 μ m



(a) Raw data



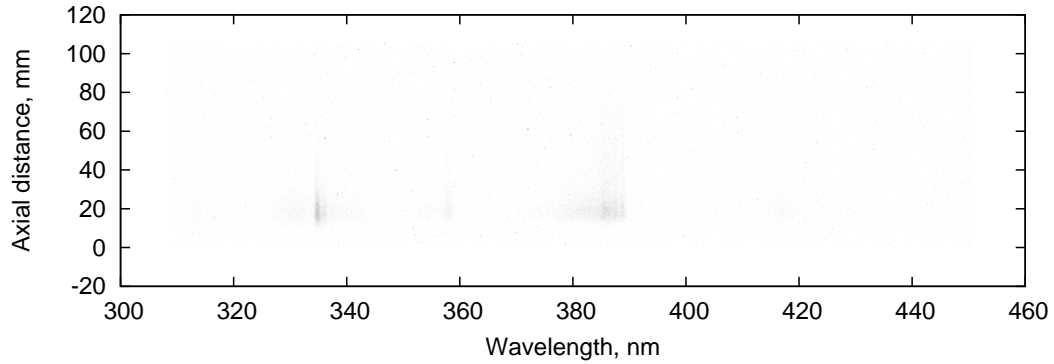
(b) Spectral power density



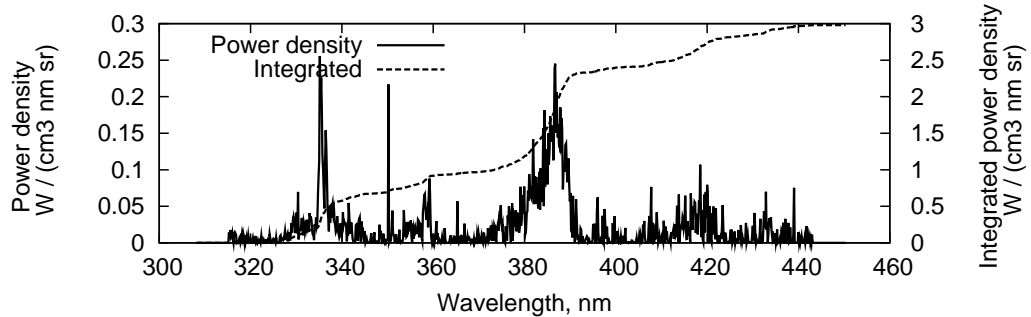
(c) Power density summed over entire wavelength range

Figure F.28 : Raw and calibrated data for x2s1530.

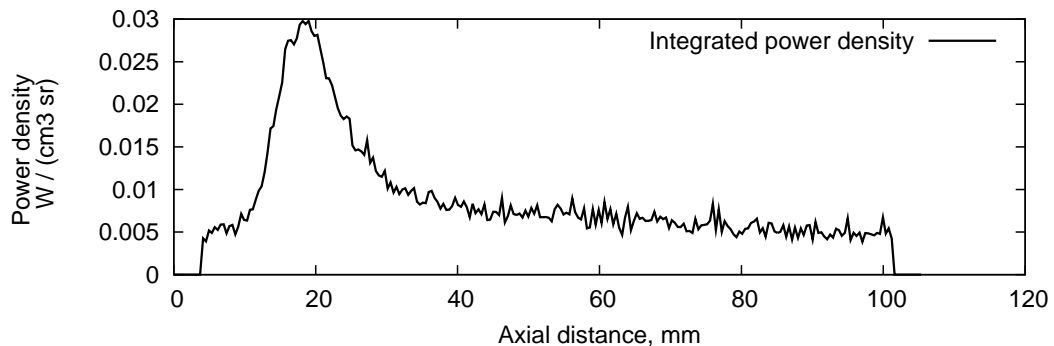
x2s1509			
Test gas pressure	8 Pa	Test gas mixture	98% N ₂ , 2% CH ₄
Shock speed	6.33 km/s	Grating	600 lines/mm
Exposure time	100 ns	Slit width	100 μ m



(a) Raw data



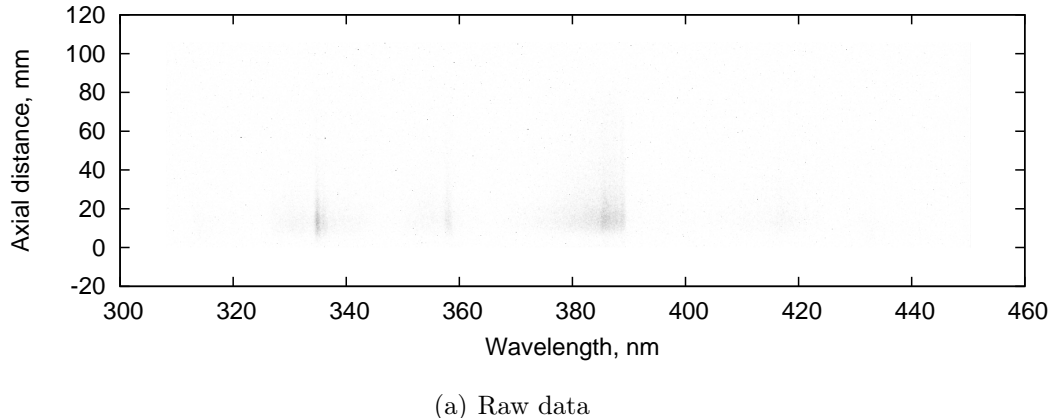
(b) Spectral power density



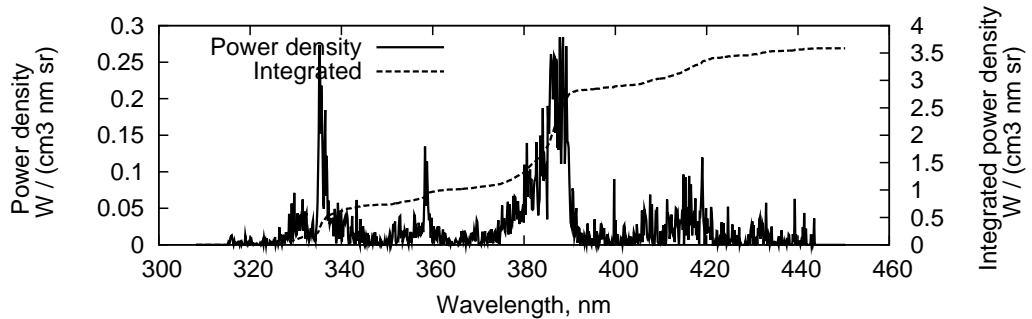
(c) Power density summed over entire wavelength range

Figure F.29 : *Raw and calibrated data for x2s1509.*

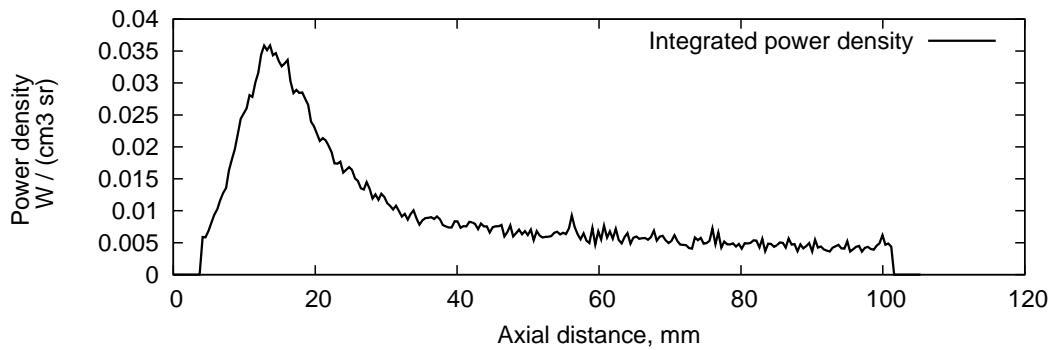
x2s1510			
Test gas pressure	8 Pa	Test gas mixture	98% N ₂ , 2% CH ₄
Shock speed	6.10 km/s	Grating	600 lines/mm
Exposure time	100 ns	Slit width	100 μ m



(a) Raw data



(b) Spectral power density



(c) Power density summed over entire wavelength range

Figure F.30 : *Raw and calibrated data for x2s1510.*

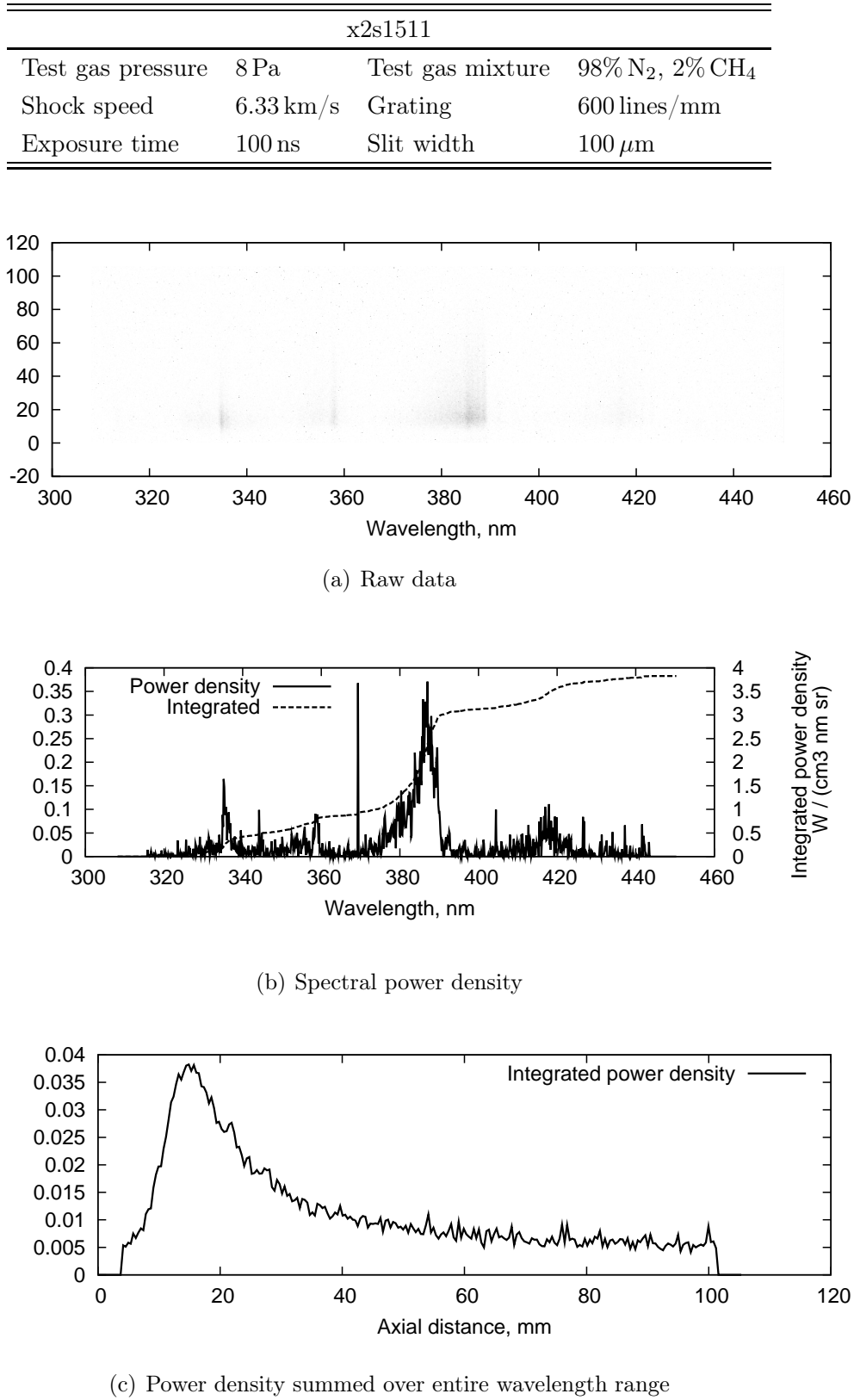
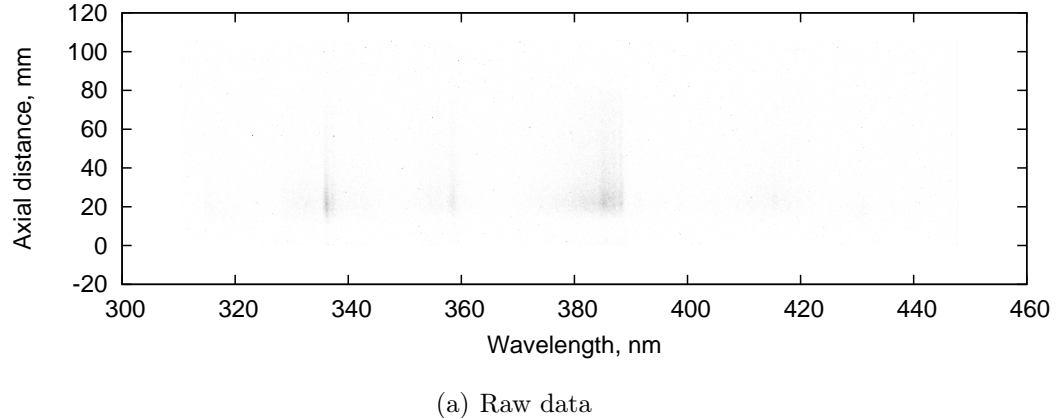
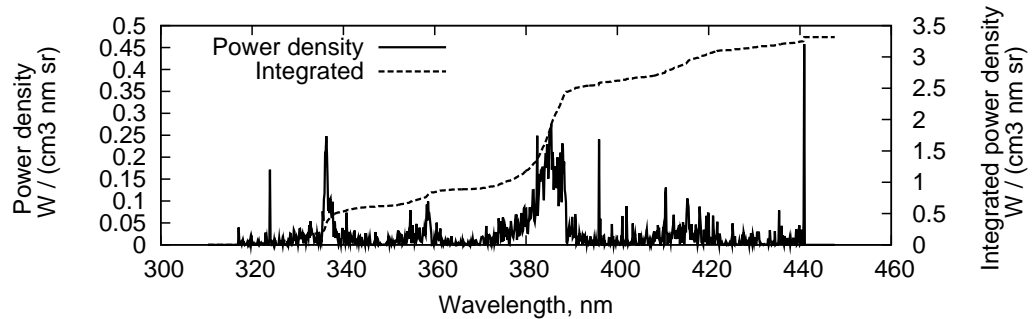


Figure F.31 : *Raw and calibrated data for x2s1511.*

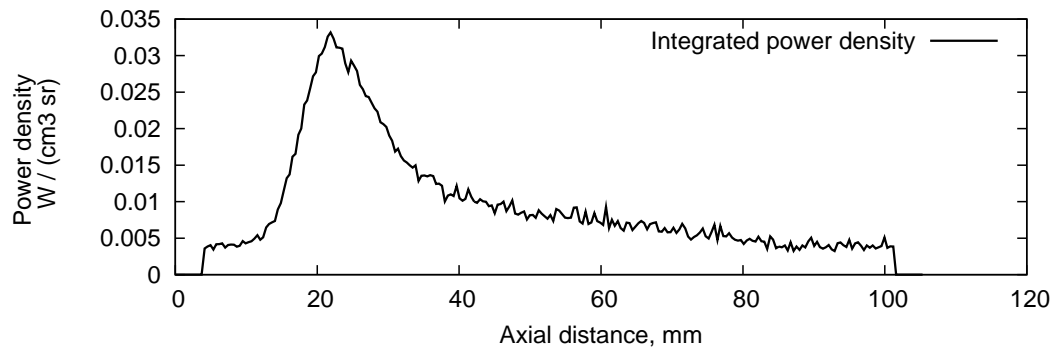
x2s1517			
Test gas pressure	8 Pa	Test gas mixture	98% N ₂ , 2% CH ₄
Shock speed	5.88 km/s	Grating	600 lines/mm
Exposure time	100 ns	Slit width	100 μ m



(a) Raw data



(b) Spectral power density



(c) Power density summed over entire wavelength range

Figure F.32 : *Raw and calibrated data for x2s1517.*

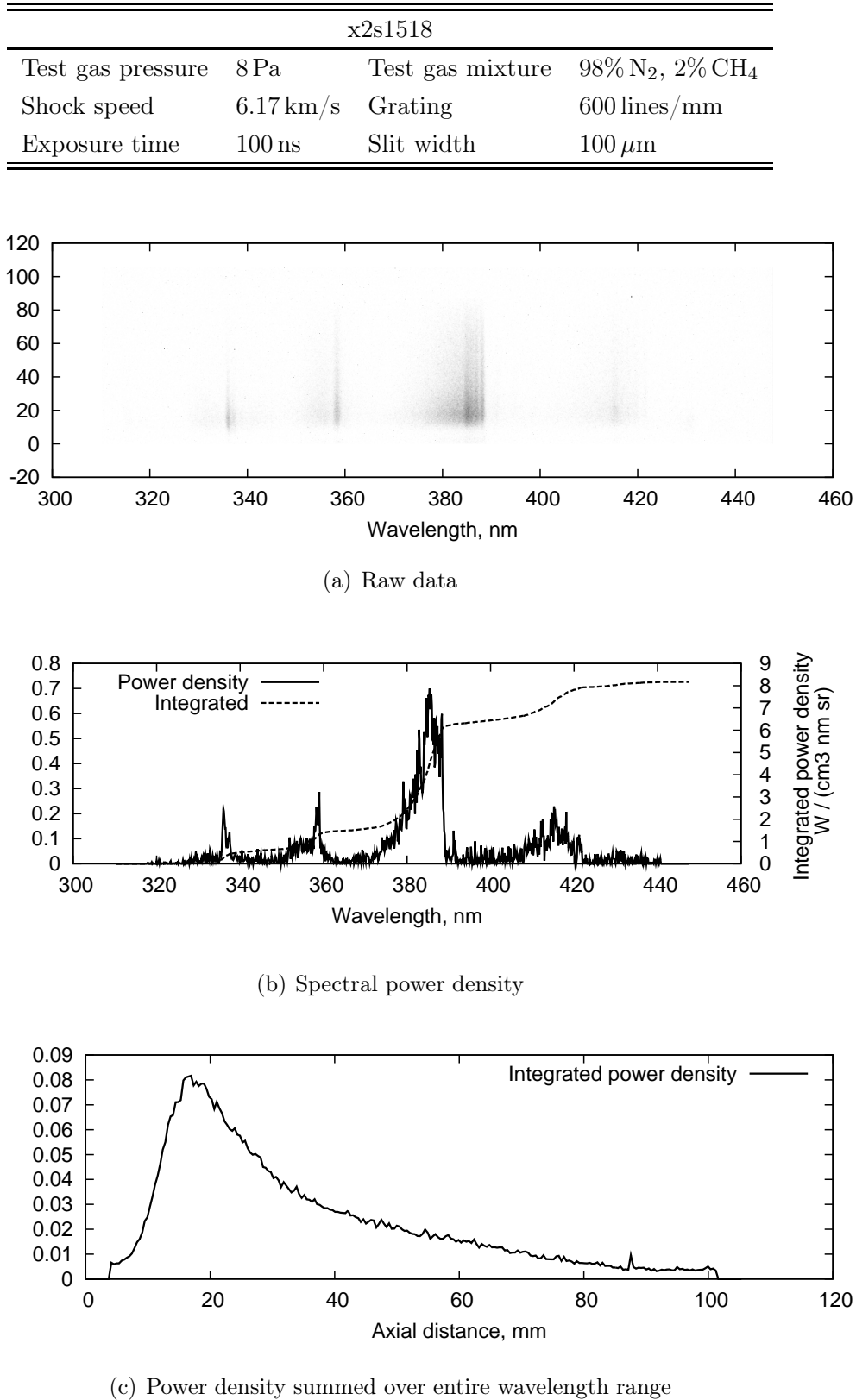


Figure F.33 : *Raw and calibrated data for x2s1518.*

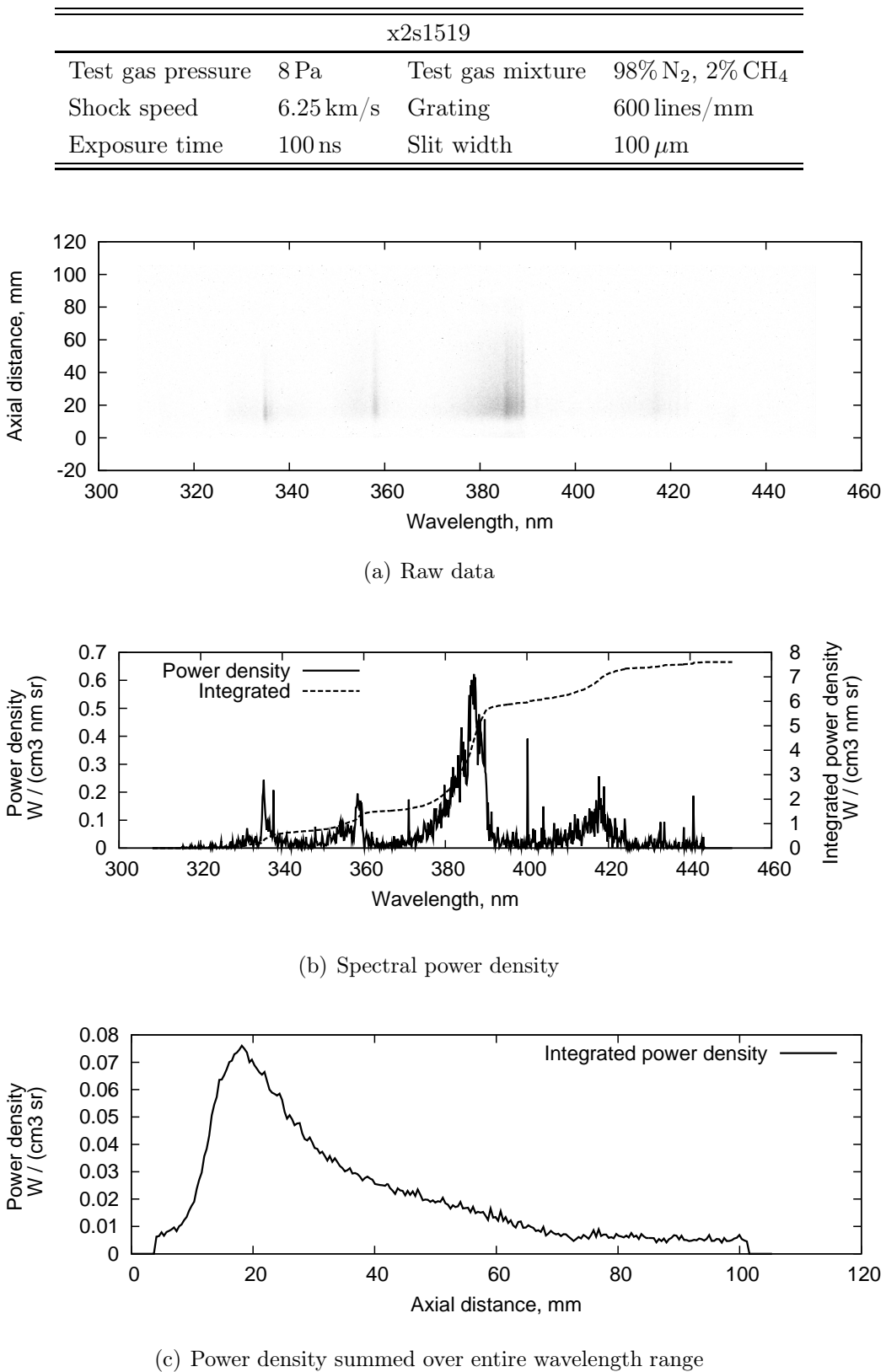


Figure F.34 : *Raw and calibrated data for x2s1519.*

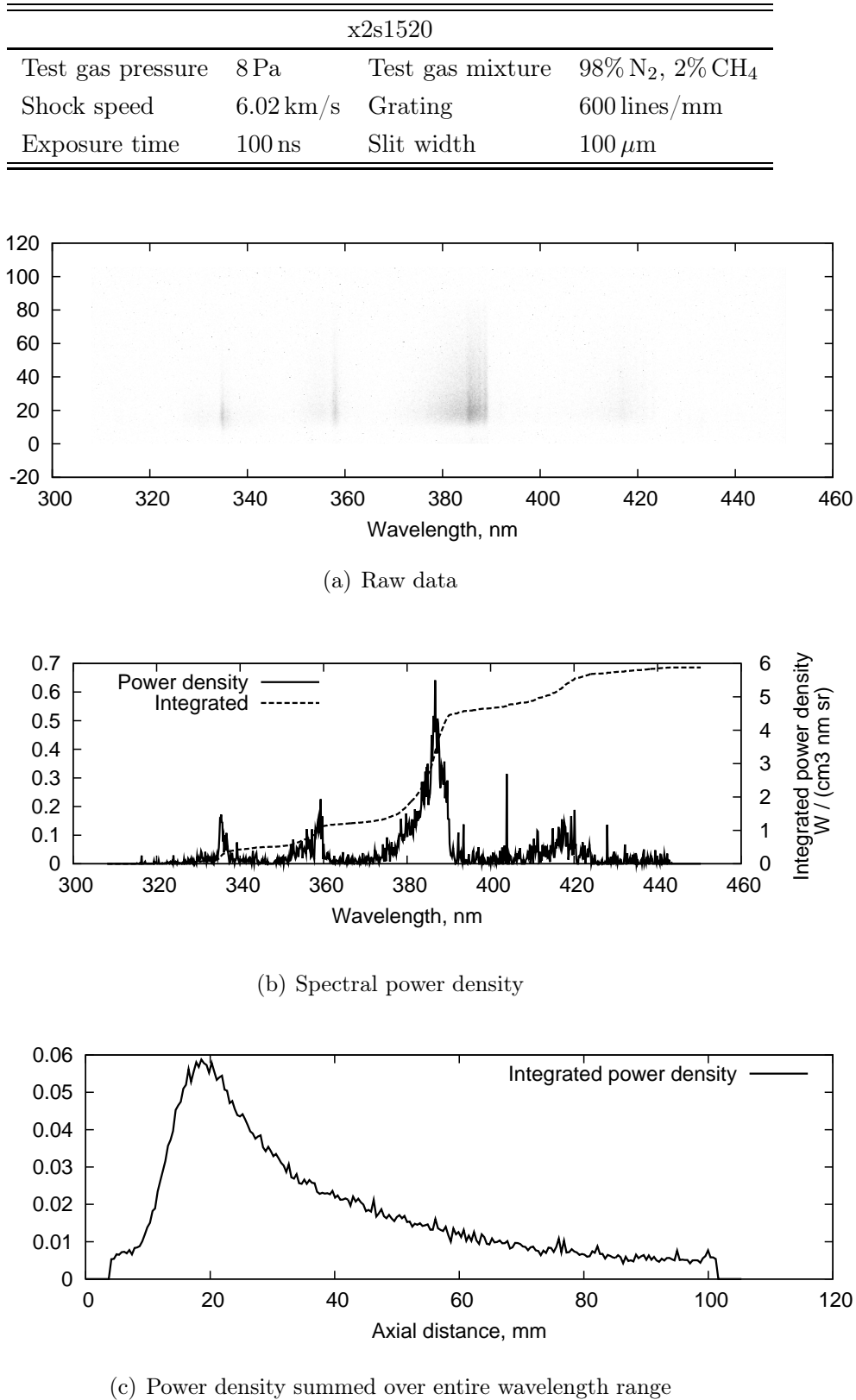
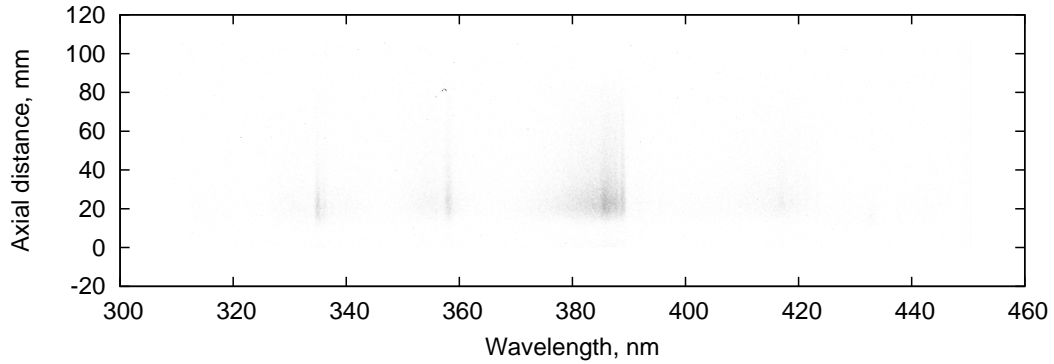
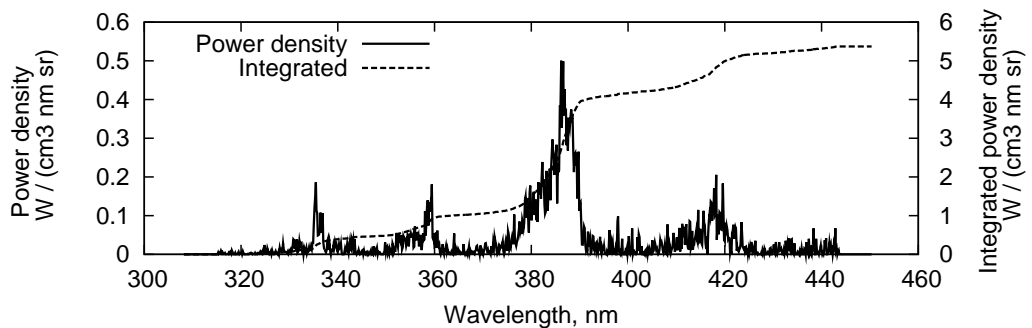


Figure F.35 : *Raw and calibrated data for x2s1520.*

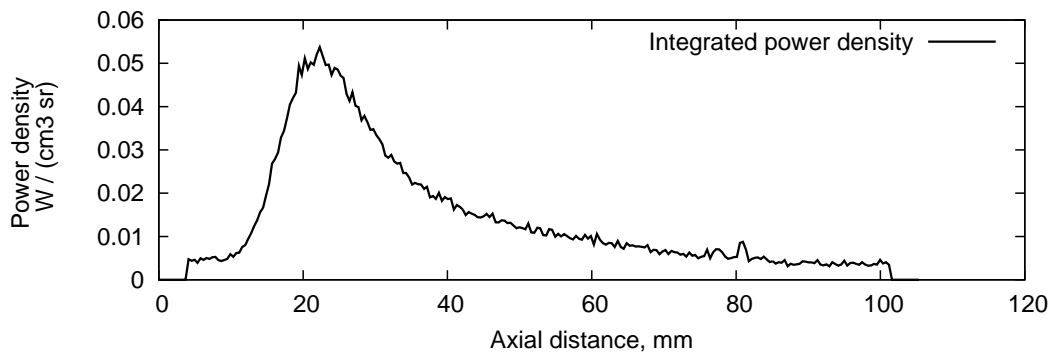
x2s1521			
Test gas pressure	8 Pa	Test gas mixture	98% N ₂ , 2% CH ₄
Shock speed	5.81 km/s	Grating	600 lines/mm
Exposure time	100 ns	Slit width	100 μ m



(a) Raw data



(b) Spectral power density



(c) Power density summed over entire wavelength range

Figure F.36 : Raw and calibrated data for x2s1521.

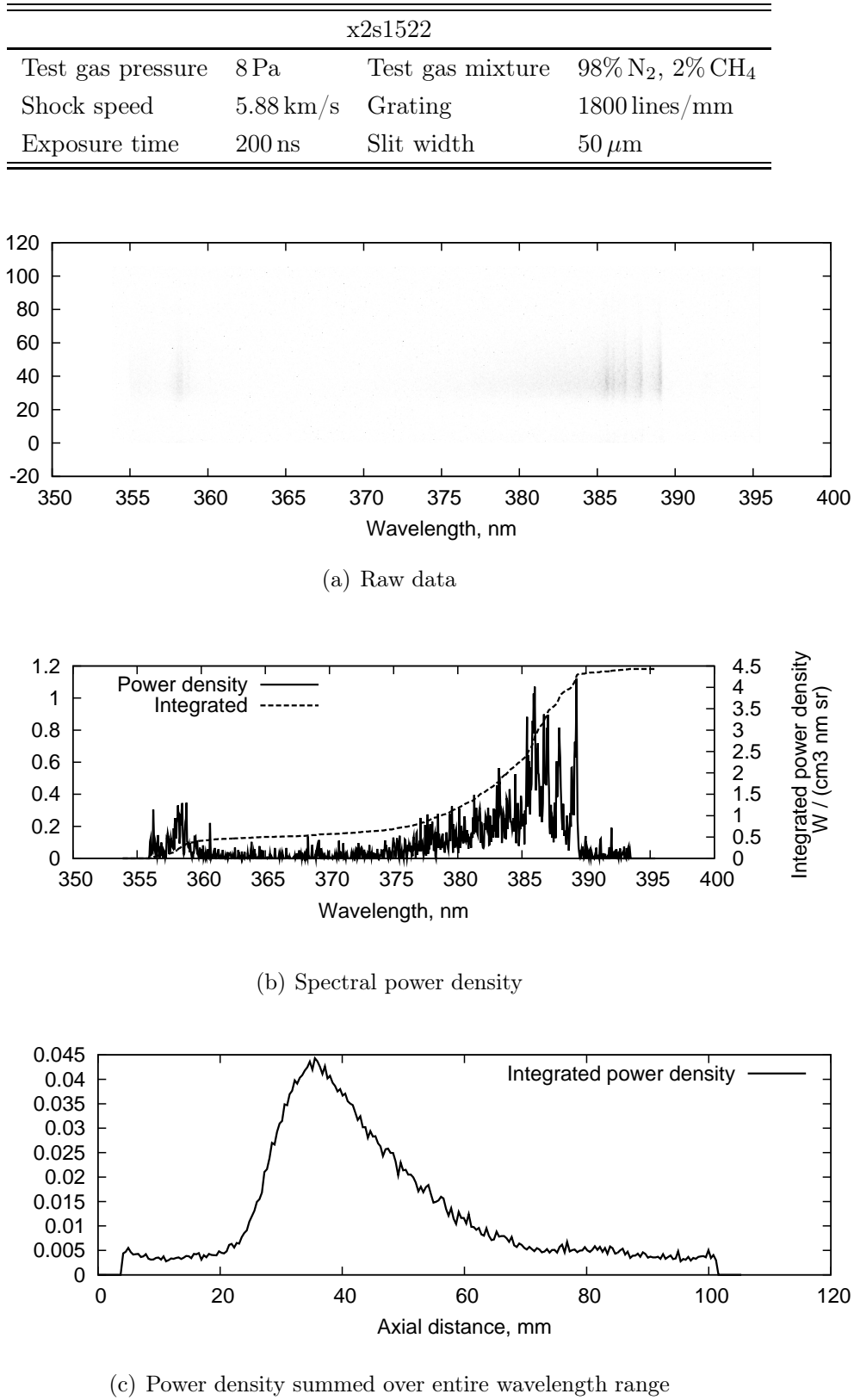


Figure F.37 : *Raw and calibrated data for x2s1522.*

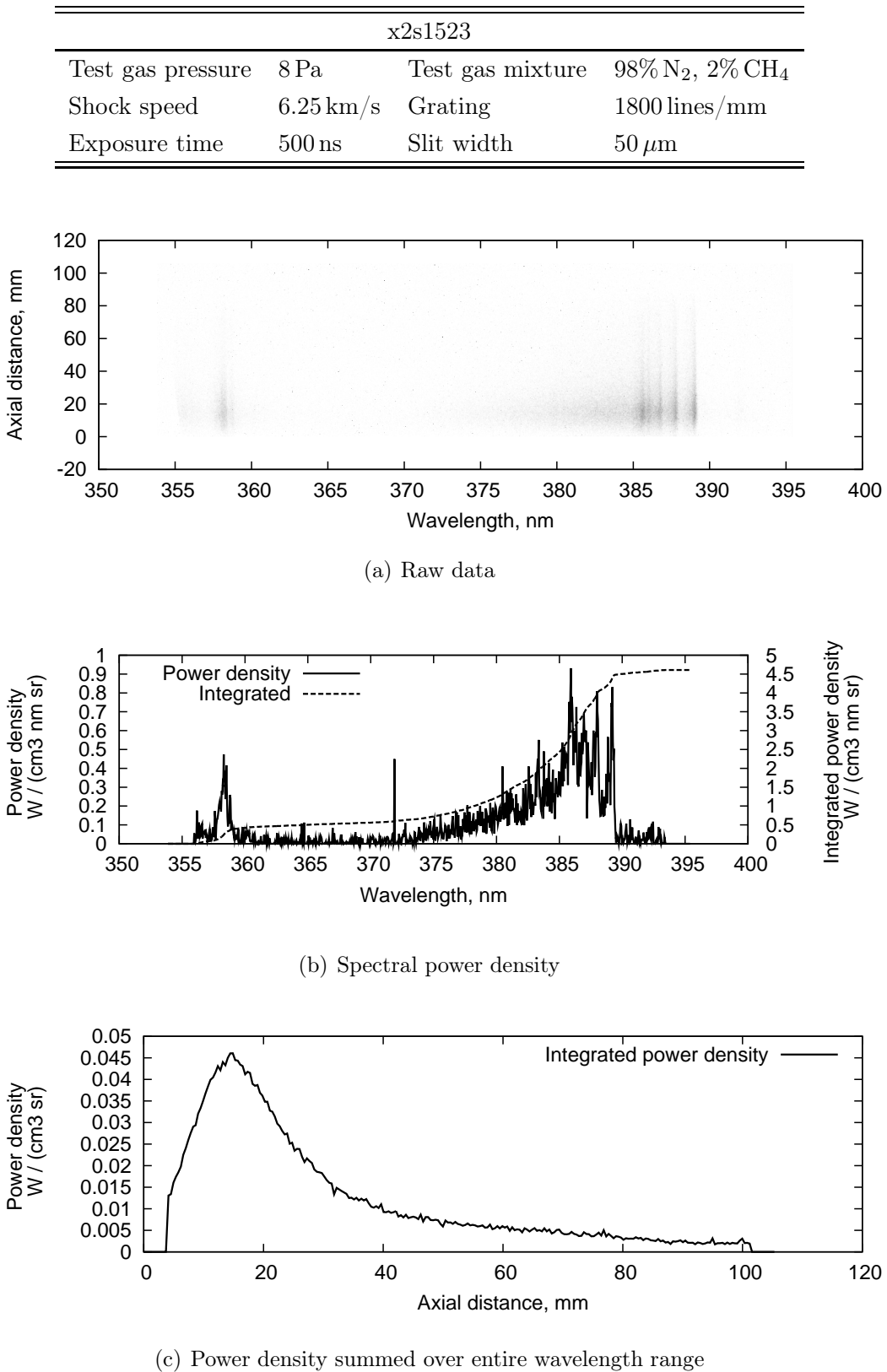
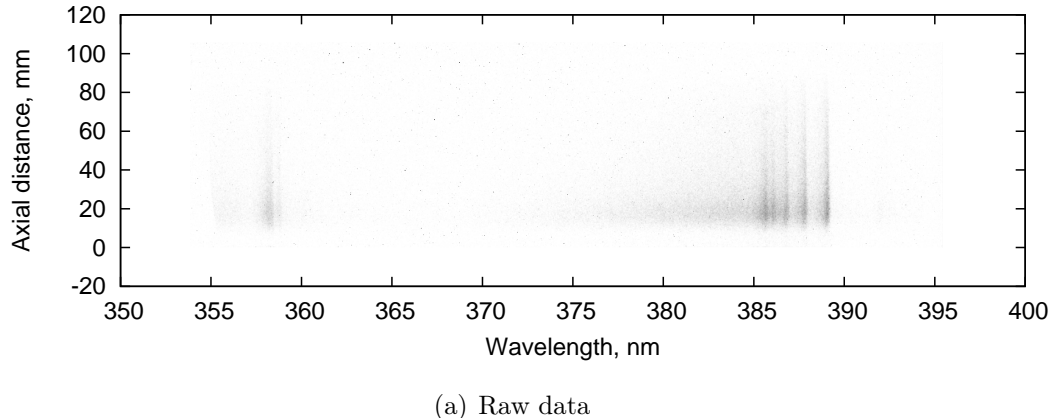
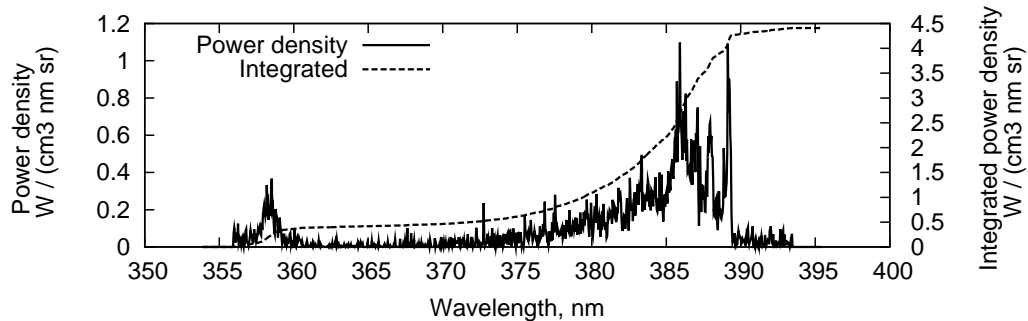


Figure F.38 : *Raw and calibrated data for x2s1523.*

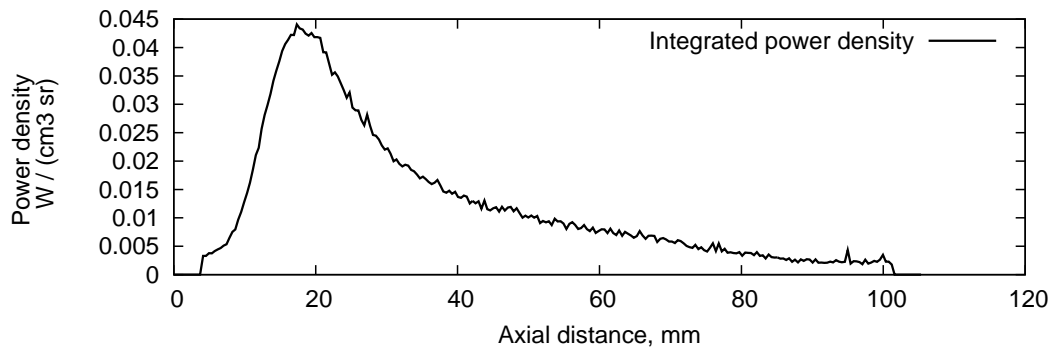
x2s1524			
Test gas pressure	8 Pa	Test gas mixture	98% N ₂ , 2% CH ₄
Shock speed	6.02 km/s	Grating	1800 lines/mm
Exposure time	500 ns	Slit width	50 μ m



(a) Raw data



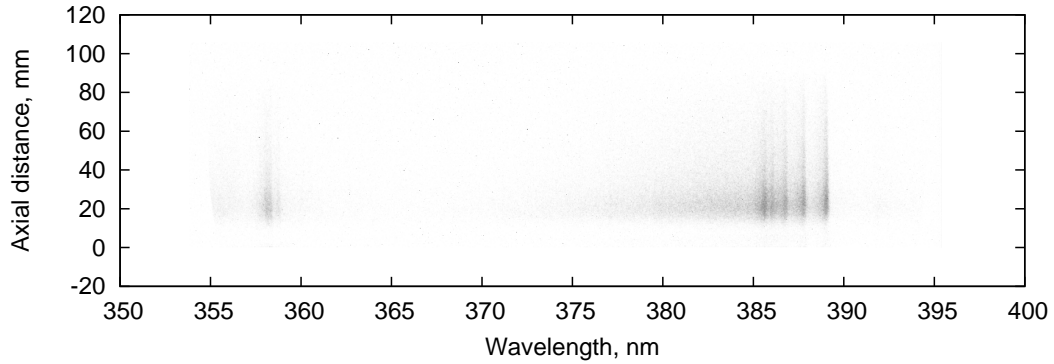
(b) Spectral power density



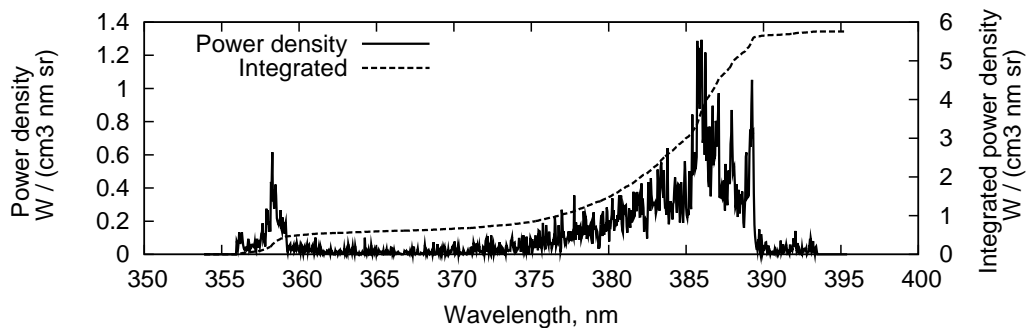
(c) Power density summed over entire wavelength range

Figure F.39 : *Raw and calibrated data for x2s1524.*

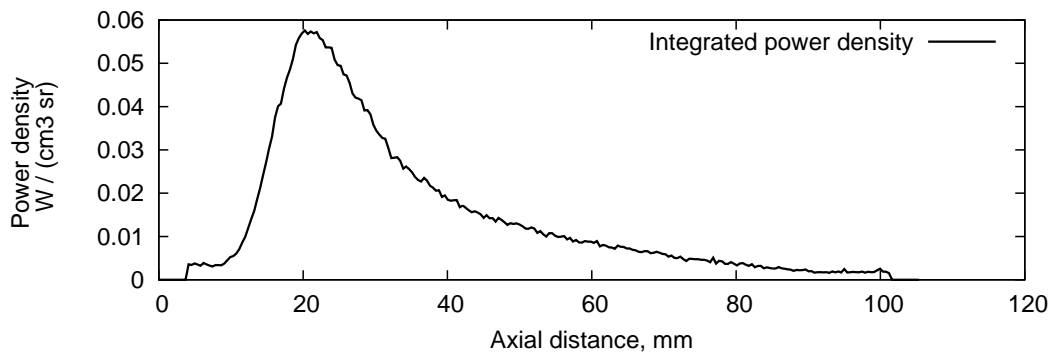
x2s1527			
Test gas pressure	8 Pa	Test gas mixture	98% N ₂ , 2% CH ₄
Shock speed	5.95 km/s	Grating	1800 lines/mm
Exposure time	500 ns	Slit width	50 μ m



(a) Raw data



(b) Spectral power density



(c) Power density summed over entire wavelength range

Figure F.40 : *Raw and calibrated data for x2s1527.*

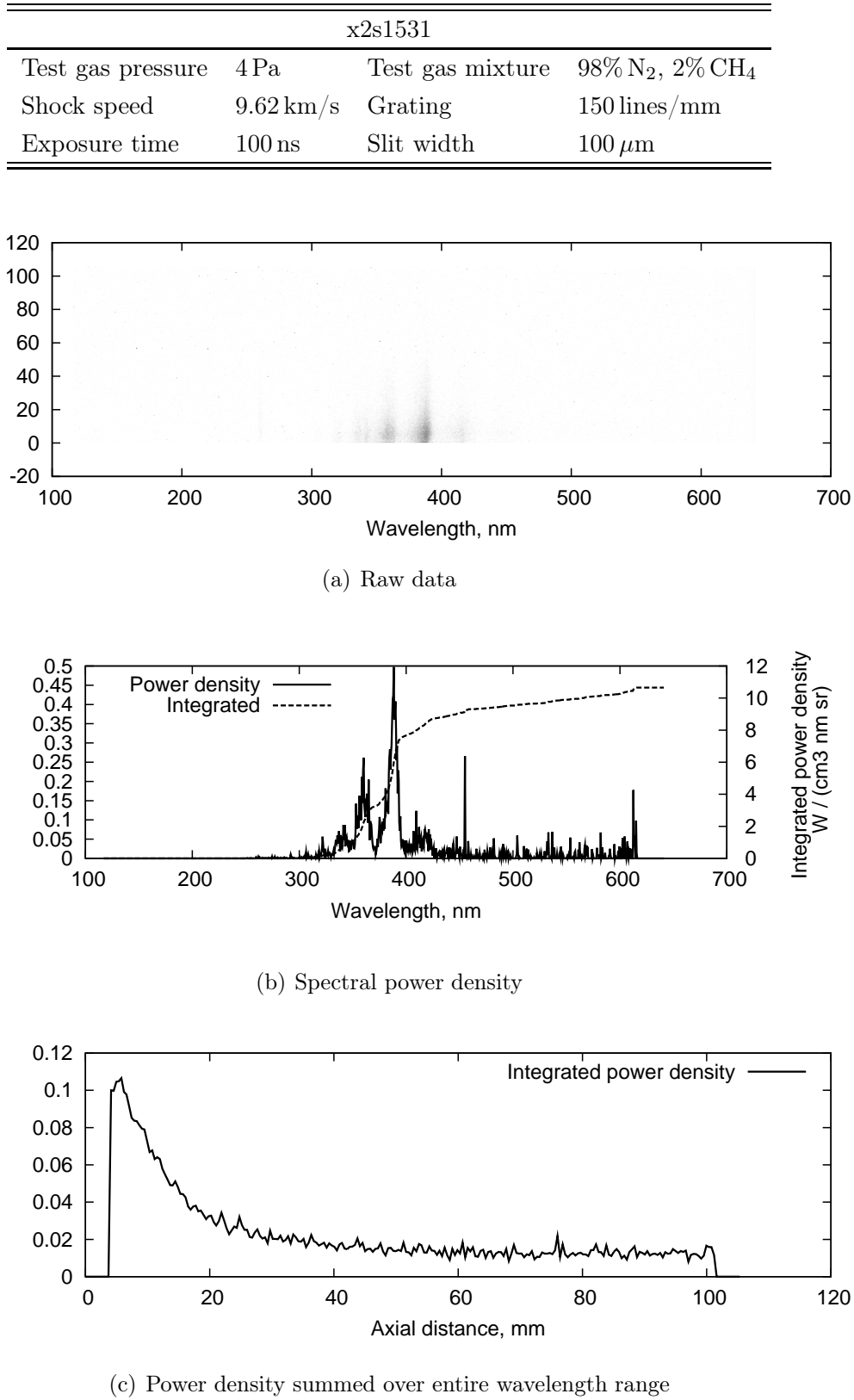


Figure F.41 : *Raw and calibrated data for x2s1531.*

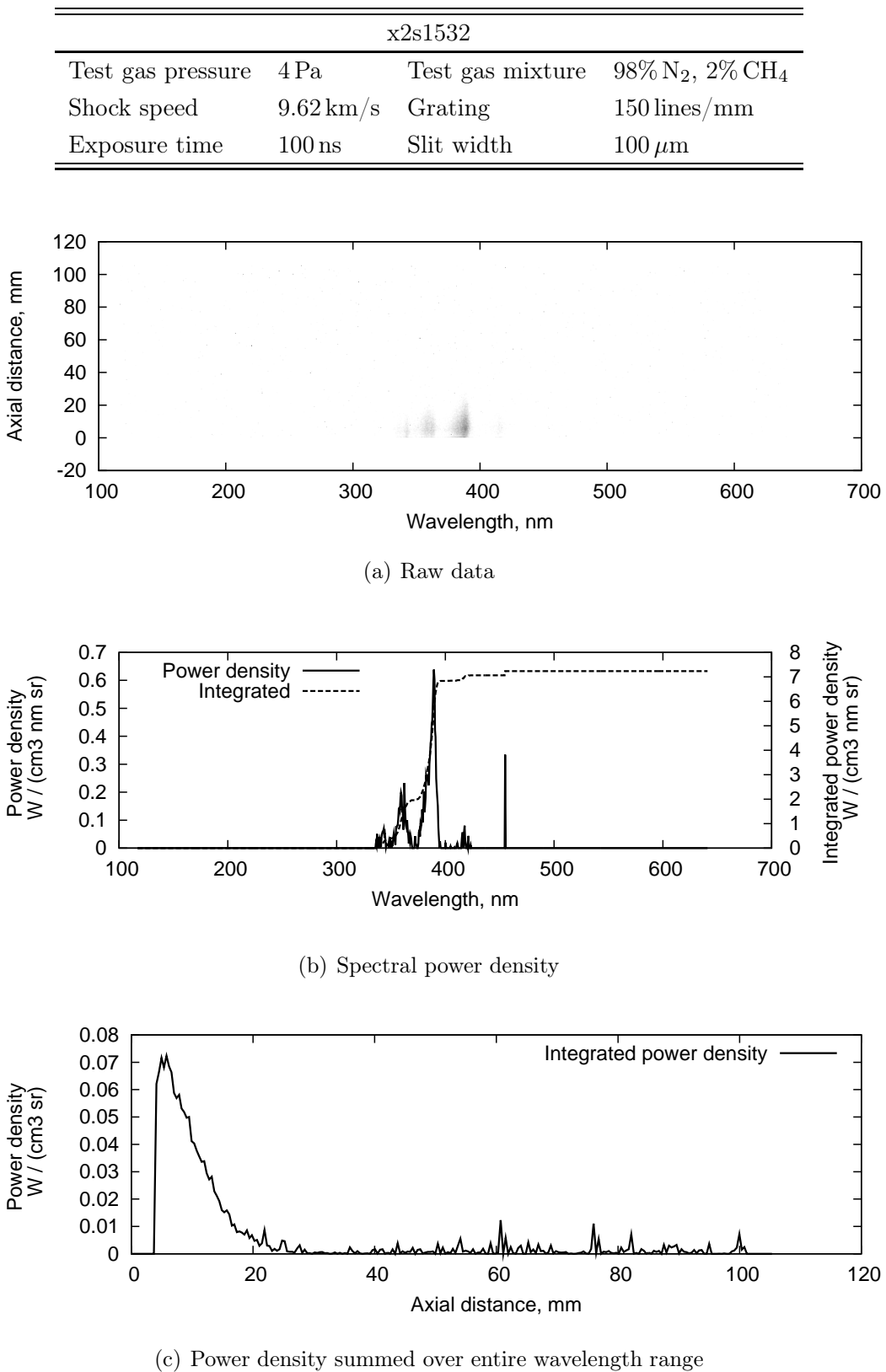


Figure F.42 : *Raw and calibrated data for x2s1532.*

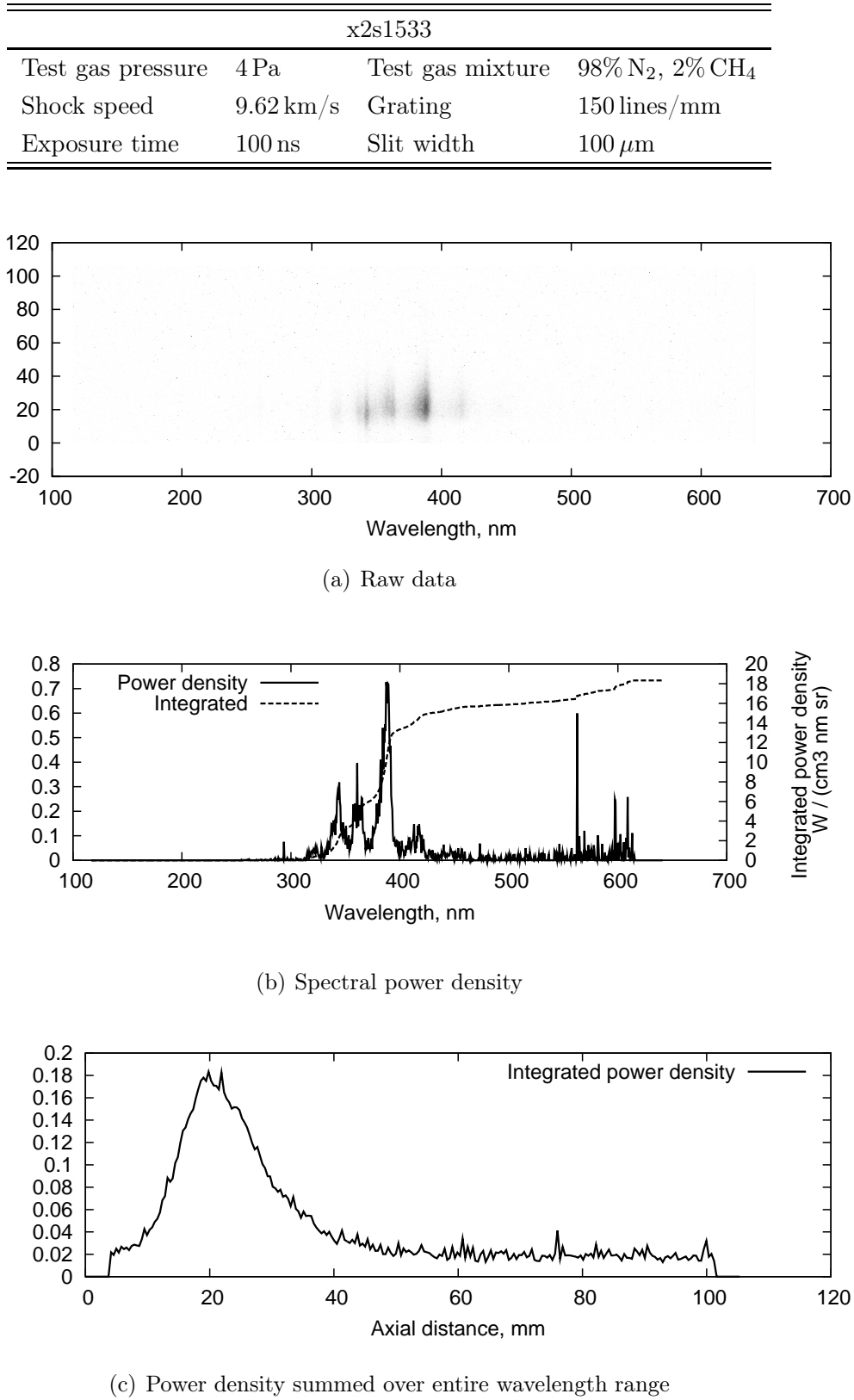
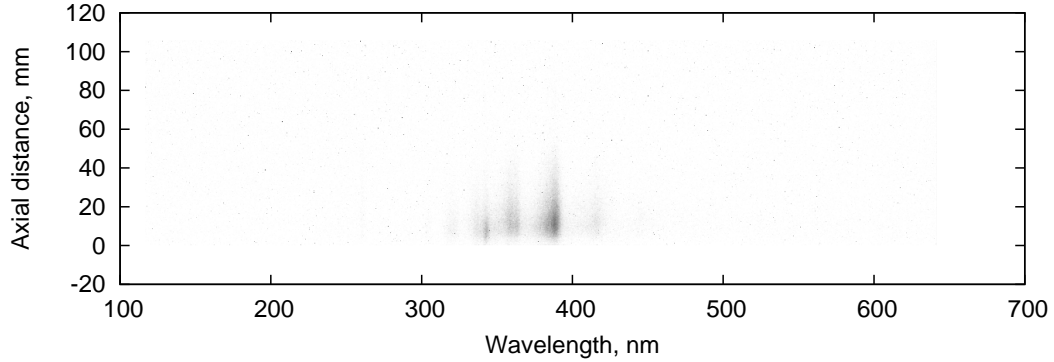
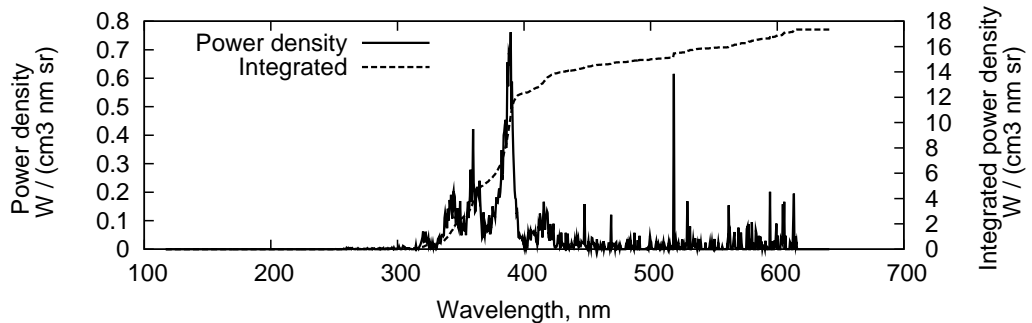


Figure F.43 : *Raw and calibrated data for x2s1533.*

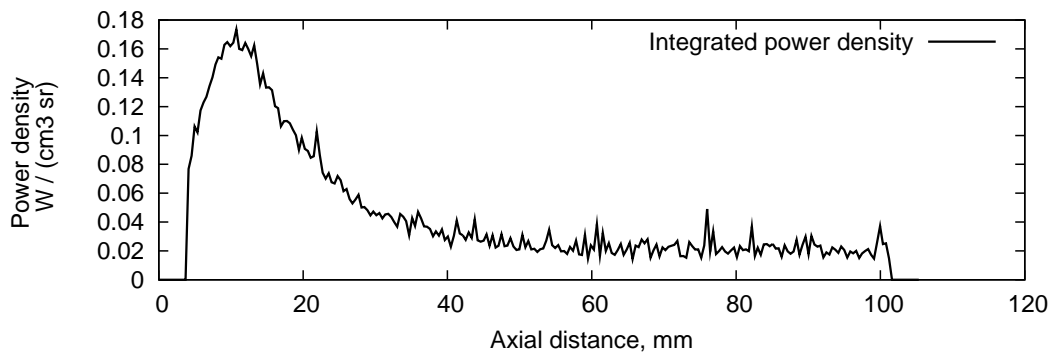
x2s1534			
Test gas pressure	4 Pa	Test gas mixture	98% N ₂ , 2% CH ₄
Shock speed	9.80 km/s	Grating	150 lines/mm
Exposure time	100 ns	Slit width	100 μm



(a) Raw data



(b) Spectral power density



(c) Power density summed over entire wavelength range

Figure F.44 : Raw and calibrated data for x2s1534.

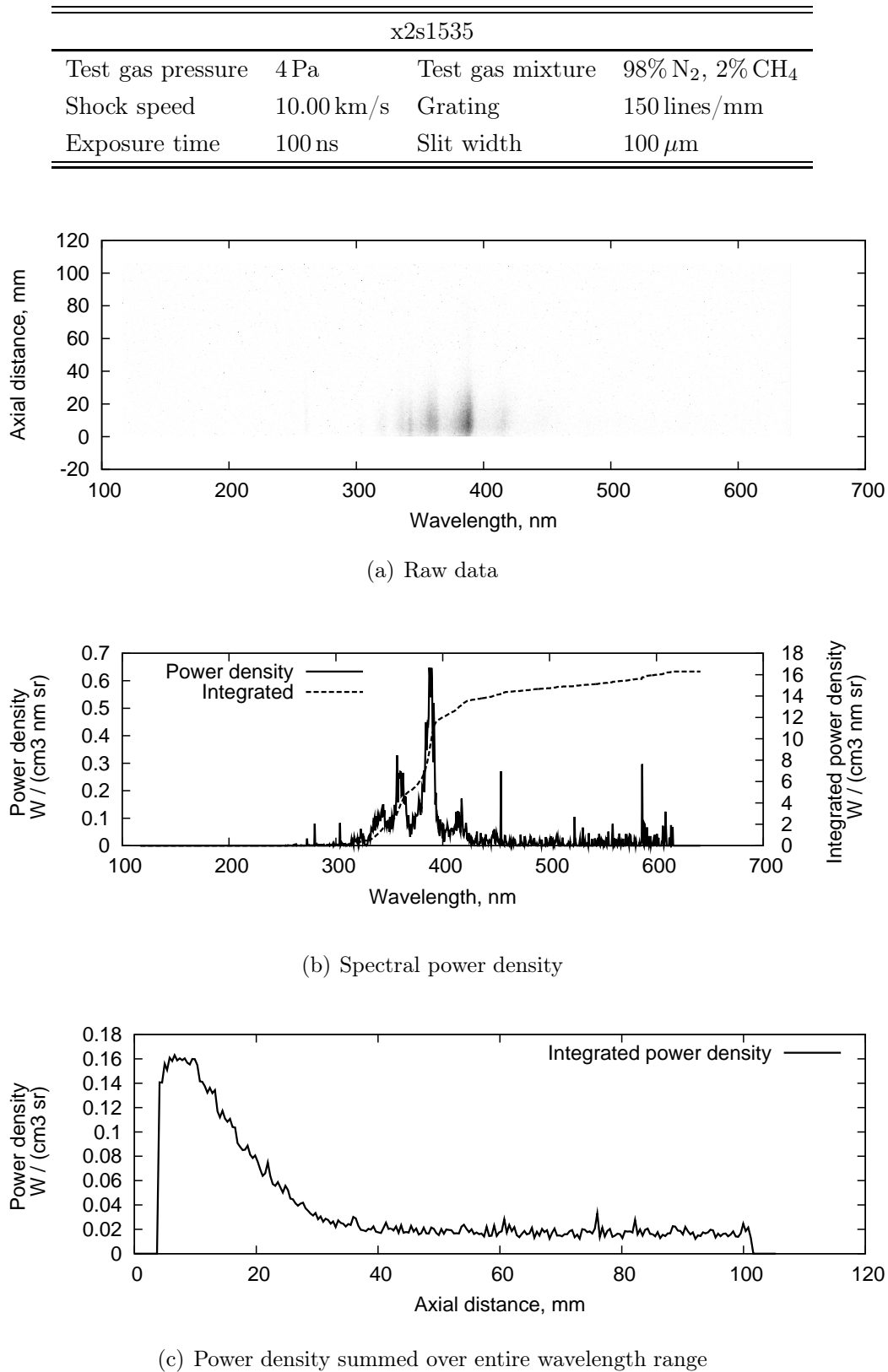


Figure F.45 : *Raw and calibrated data for x2s1535.*

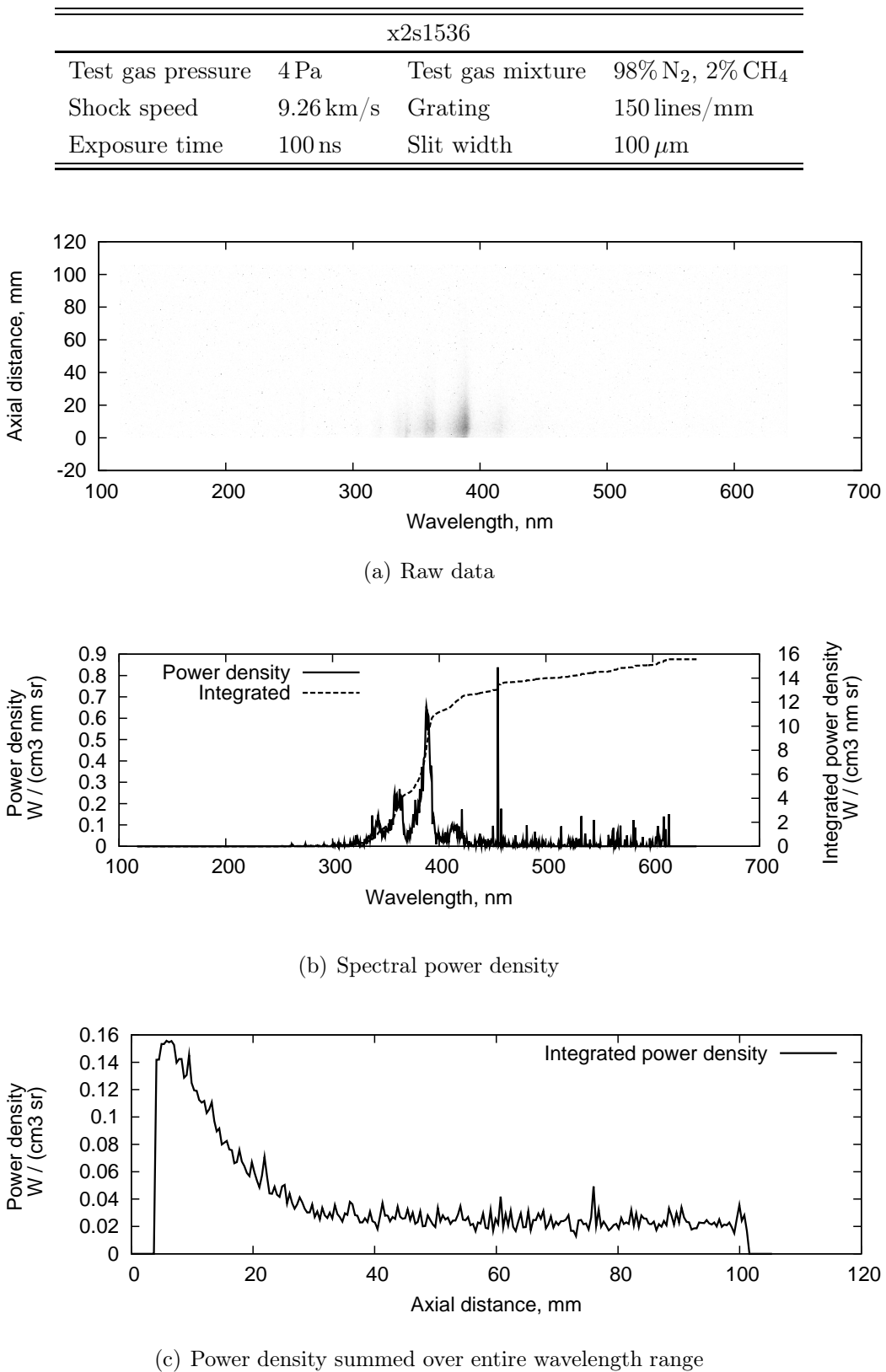
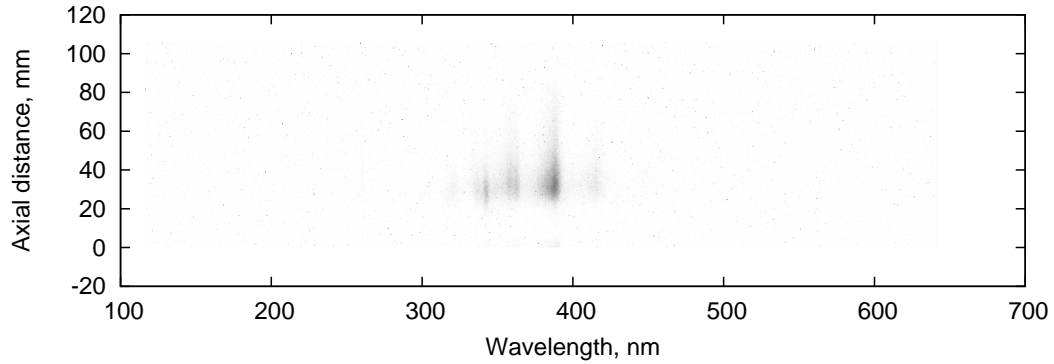
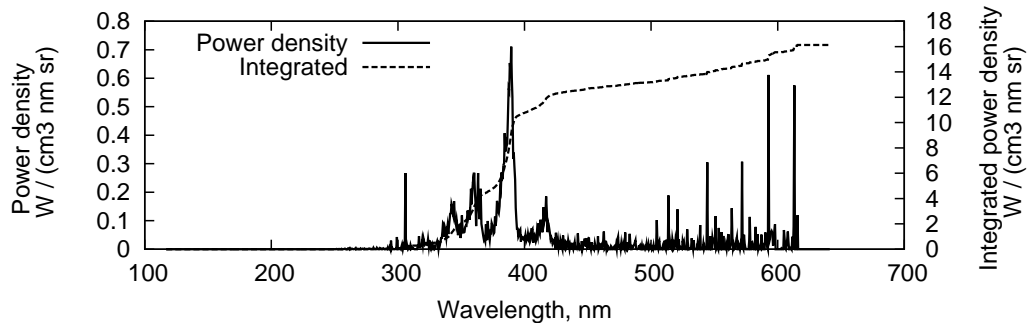


Figure F.46 : *Raw and calibrated data for x2s1536.*

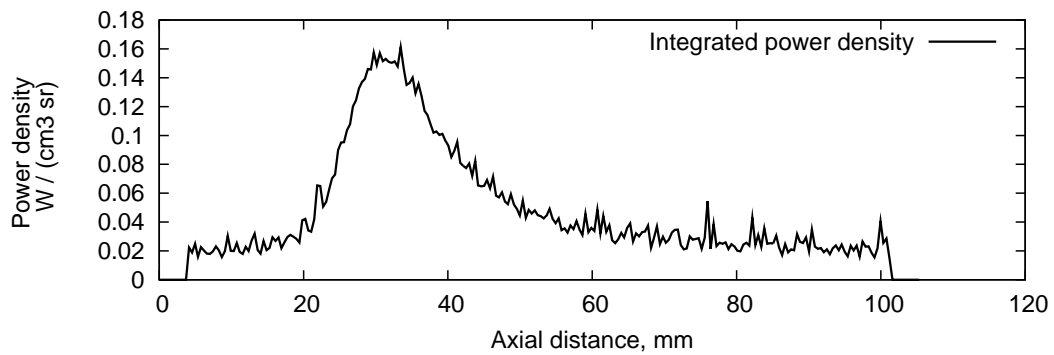
x2s1538			
Test gas pressure	4 Pa	Test gas mixture	98% N ₂ , 2% CH ₄
Shock speed	9.43 km/s	Grating	150 lines/mm
Exposure time	100 ns	Slit width	100 μ m



(a) Raw data



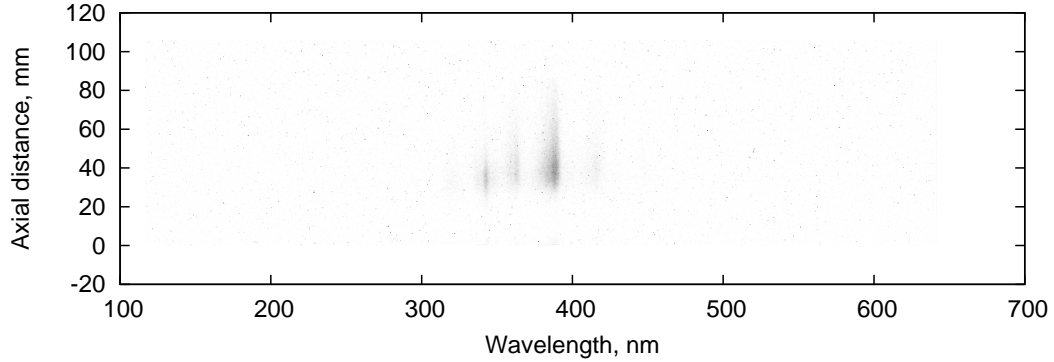
(b) Spectral power density



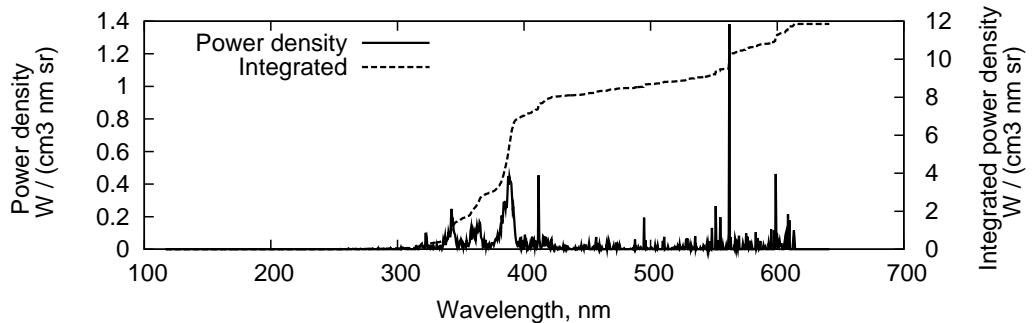
(c) Power density summed over entire wavelength range

Figure F.47 : Raw and calibrated data for x2s1538.

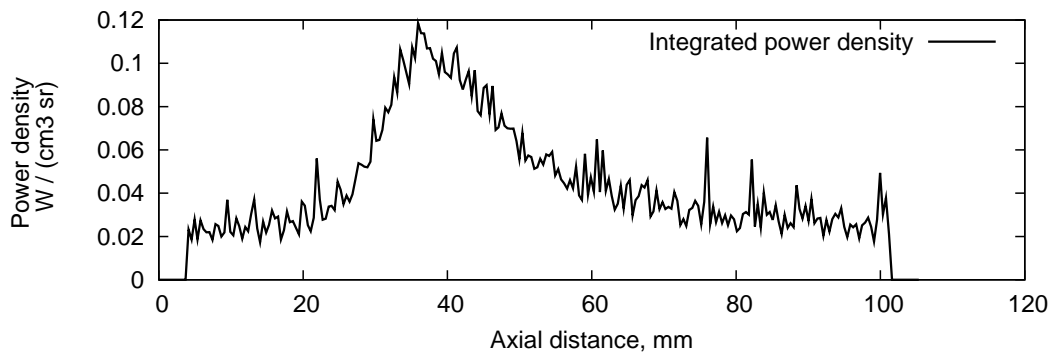
x2s1539			
Test gas pressure	4 Pa	Test gas mixture	98% N ₂ , 2% CH ₄
Shock speed	7.81 km/s	Grating	150 lines/mm
Exposure time	100 ns	Slit width	100 μ m



(a) Raw data



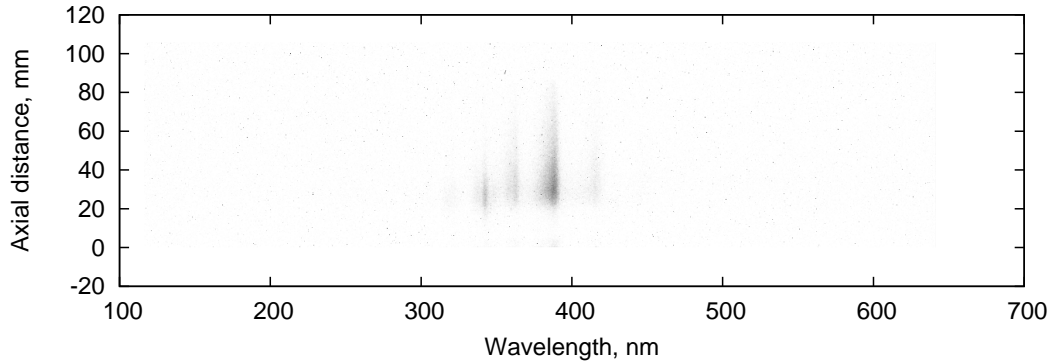
(b) Spectral power density



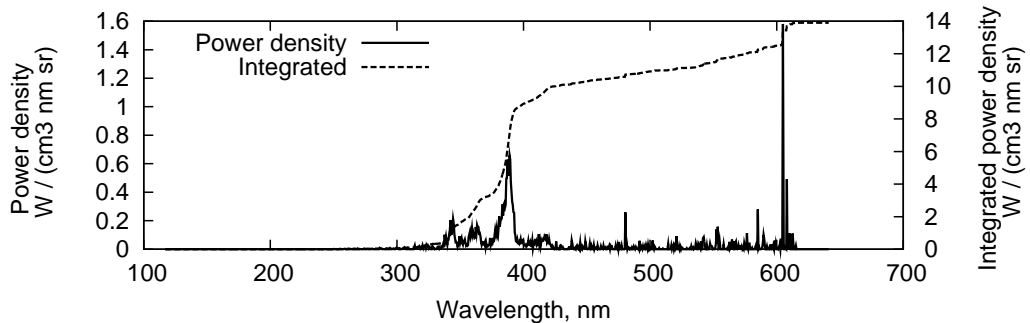
(c) Power density summed over entire wavelength range

Figure F.48 : *Raw and calibrated data for x2s1539.*

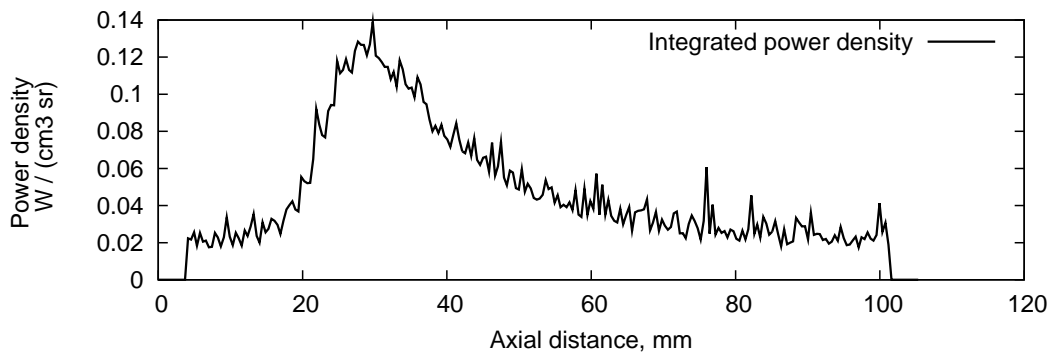
x2s1540			
Test gas pressure	4 Pa	Test gas mixture	98% N ₂ , 2% CH ₄
Shock speed	7.94 km/s	Grating	150 lines/mm
Exposure time	100 ns	Slit width	100 μ m



(a) Raw data



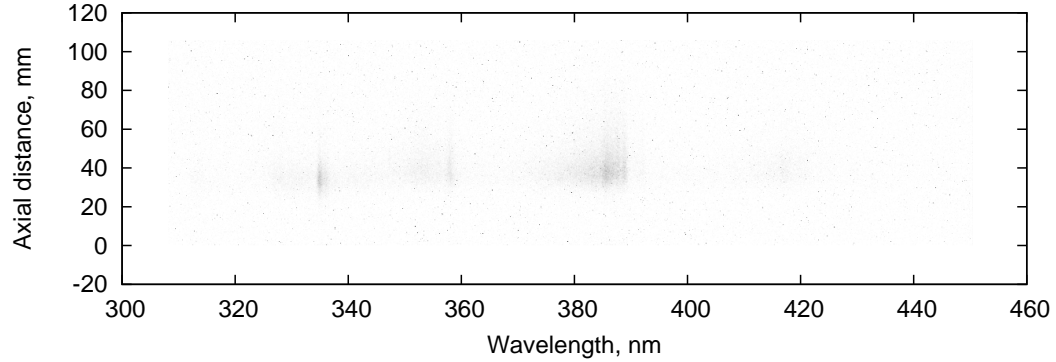
(b) Spectral power density



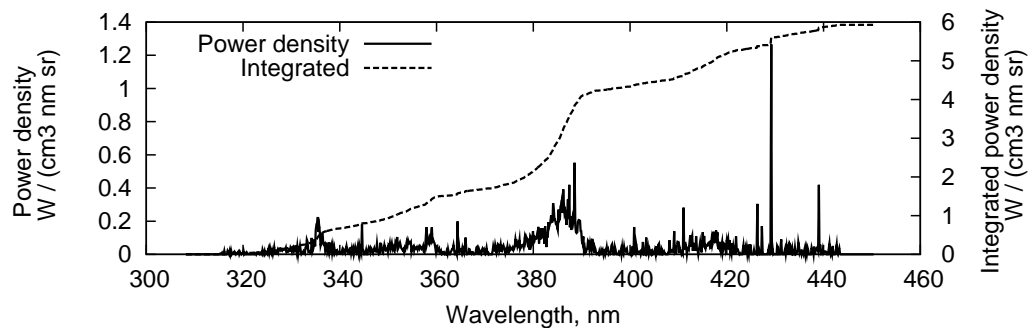
(c) Power density summed over entire wavelength range

Figure F.49 : *Raw and calibrated data for x2s1540.*

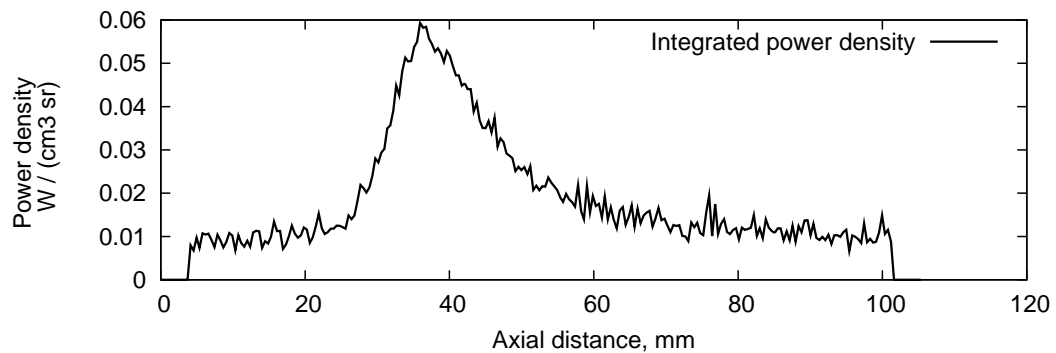
x2s1541			
Test gas pressure	4 Pa	Test gas mixture	98% N ₂ , 2% CH ₄
Shock speed	9.09 km/s	Grating	600 lines/mm
Exposure time	100 ns	Slit width	100 μ m



(a) Raw data



(b) Spectral power density

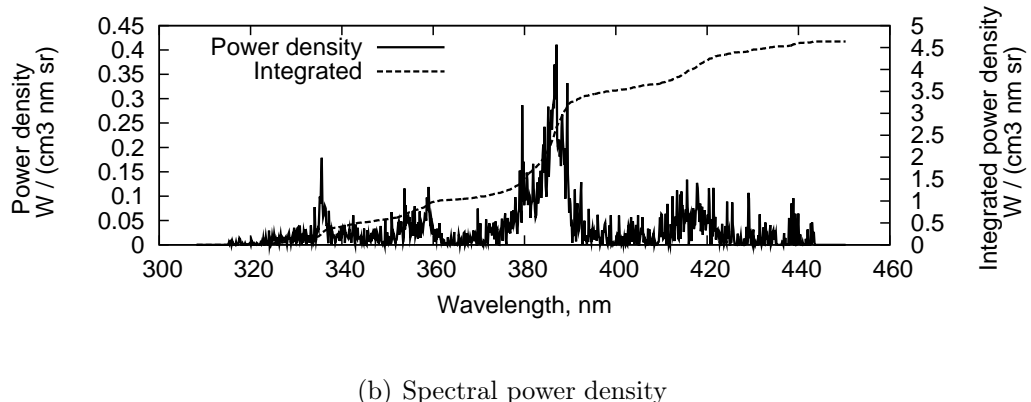
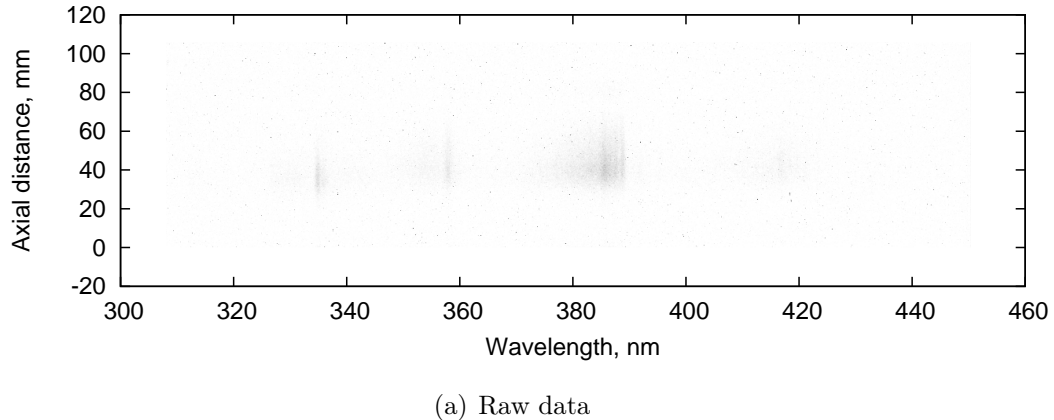


(c) Power density summed over entire wavelength range

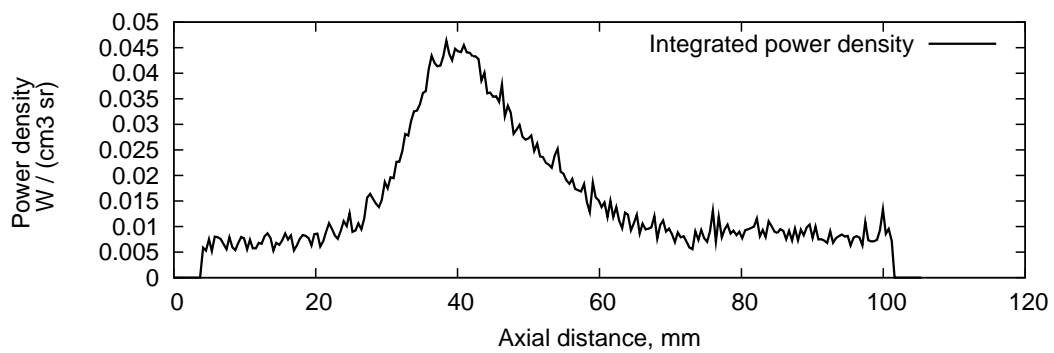
Figure F.50 : *Raw and calibrated data for x2s1541.*

APPENDIX F

x2s1542			
Test gas pressure	4 Pa	Test gas mixture	98% N ₂ , 2% CH ₄
Shock speed	7.81 km/s	Grating	600 lines/mm
Exposure time	100 ns	Slit width	100 μ m



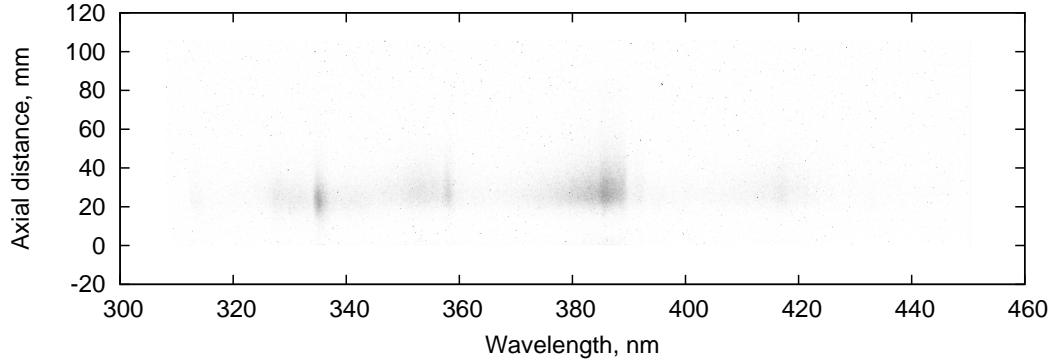
(b) Spectral power density



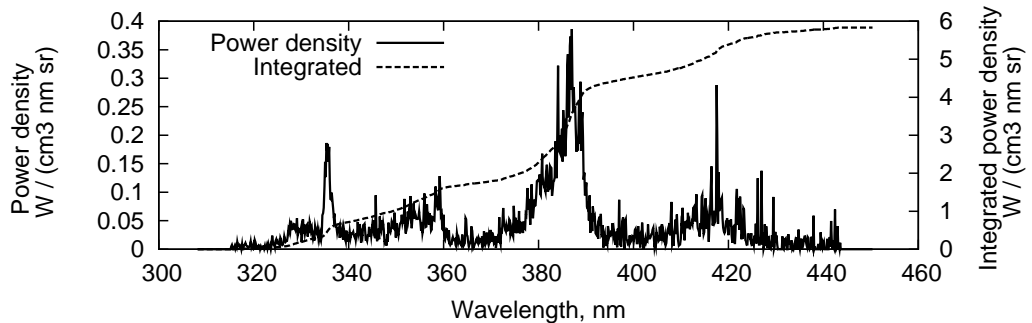
(c) Power density summed over entire wavelength range

Figure F.51 : *Raw and calibrated data for x2s1542.*

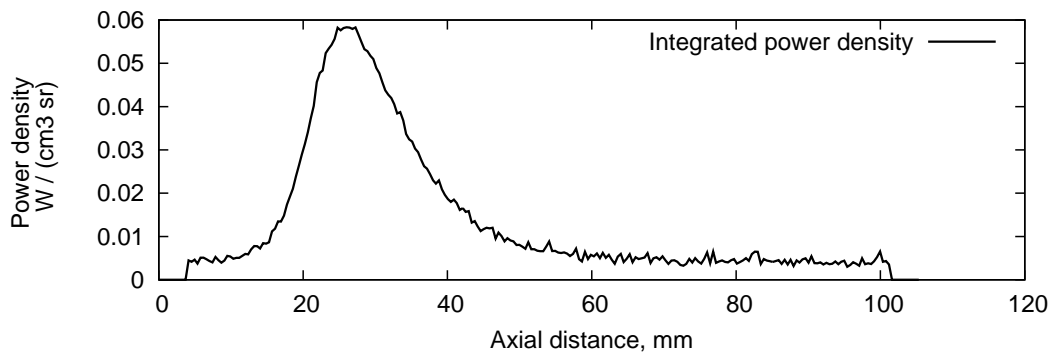
x2s1543			
Test gas pressure	4 Pa	Test gas mixture	98% N ₂ , 2% CH ₄
Shock speed	9.62 km/s	Grating	600 lines/mm
Exposure time	100 ns	Slit width	100 μ m



(a) Raw data



(b) Spectral power density



(c) Power density summed over entire wavelength range

Figure F.52 : *Raw and calibrated data for x2s1543.*

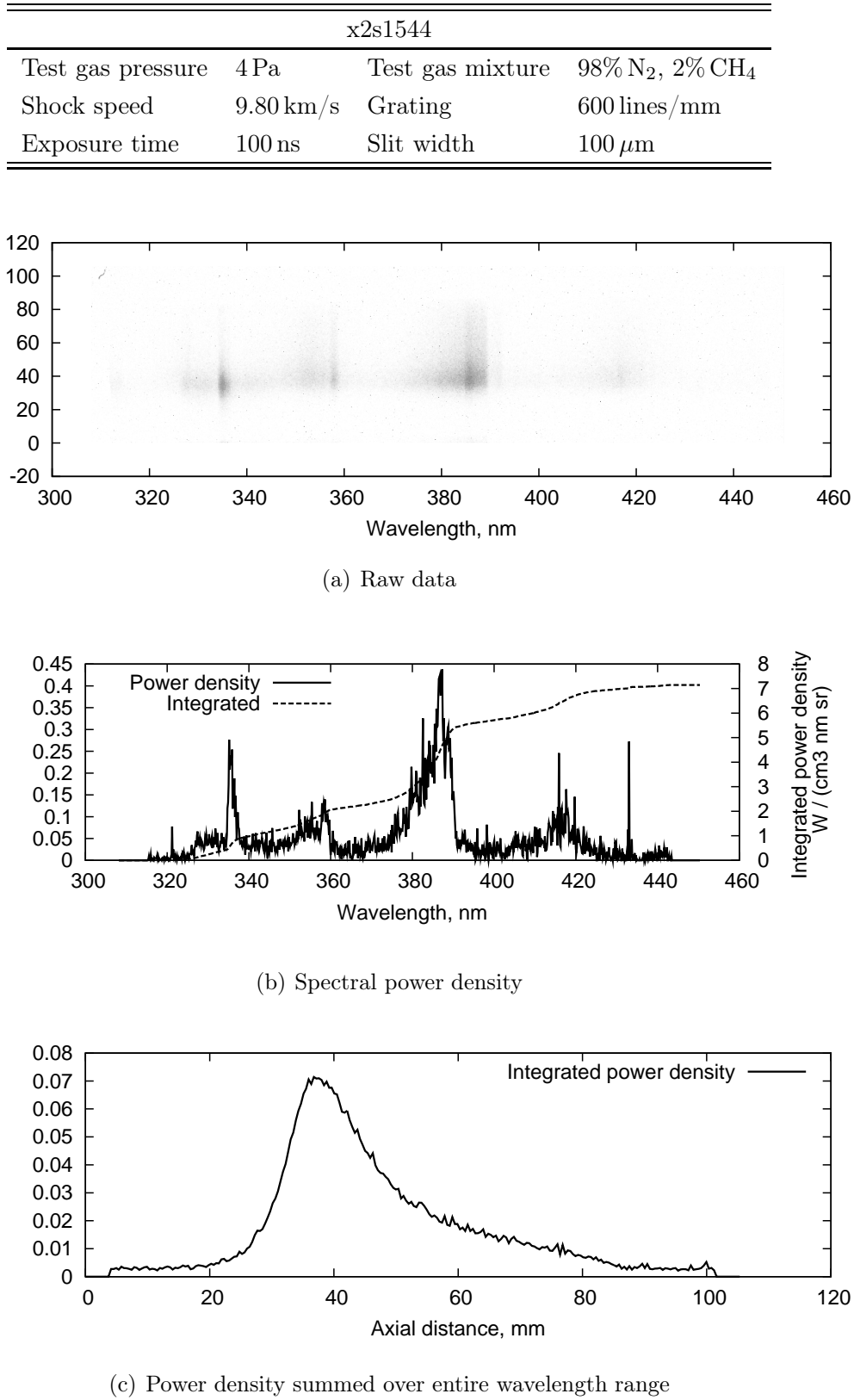
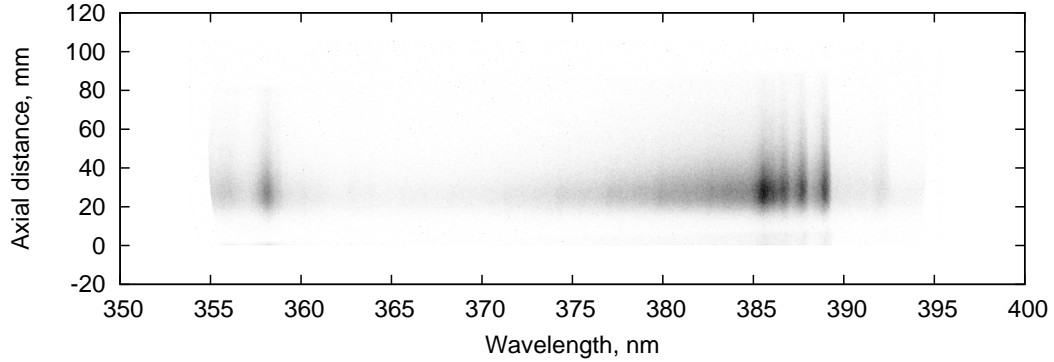
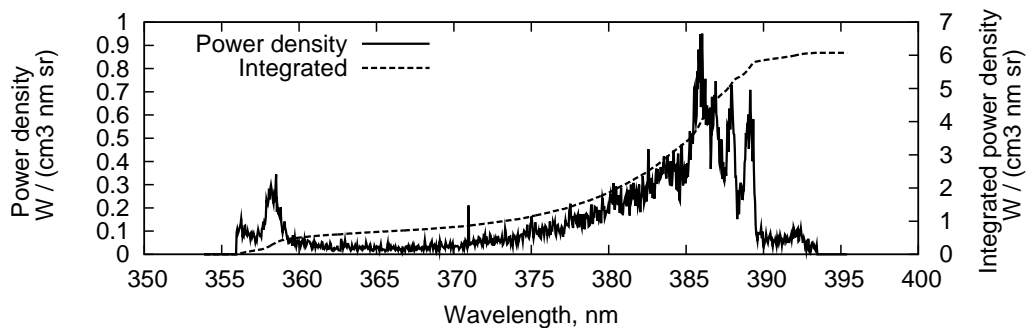


Figure F.53 : *Raw and calibrated data for x2s1544.*

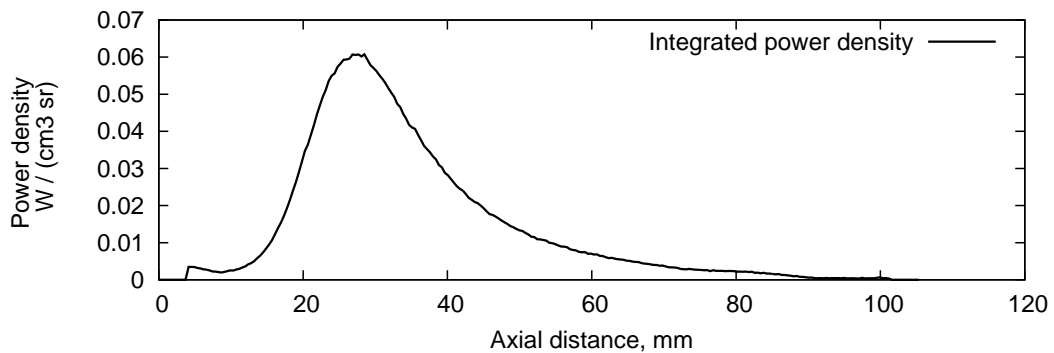
x2s1545			
Test gas pressure	4 Pa	Test gas mixture	98% N ₂ , 2% CH ₄
Shock speed	8.77 km/s	Grating	1800 lines/mm
Exposure time	1000 ns	Slit width	200 μ m



(a) Raw data



(b) Spectral power density

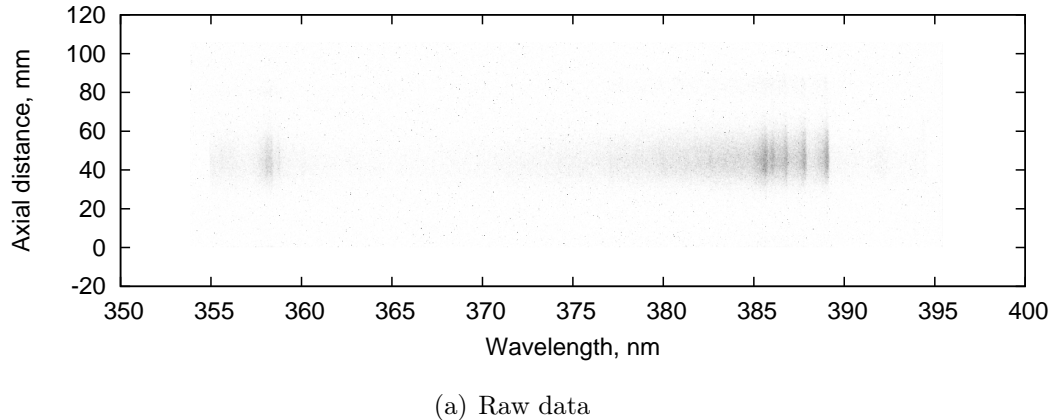


(c) Power density summed over entire wavelength range

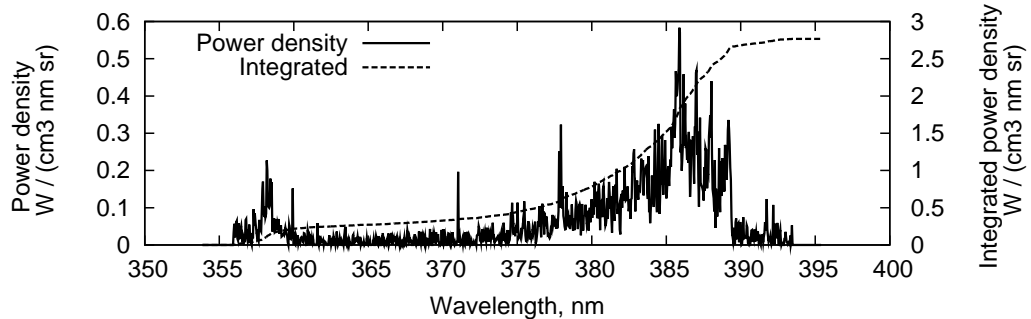
Figure F.54 : Raw and calibrated data for x2s1545.

APPENDIX F

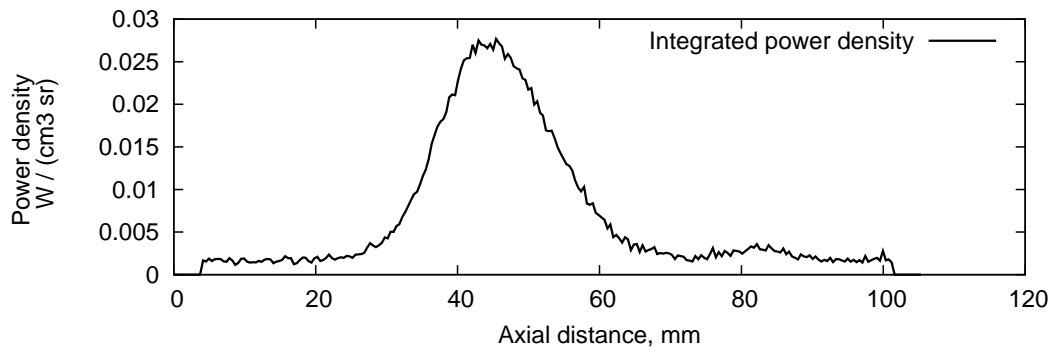
x2s1546			
Test gas pressure	4 Pa	Test gas mixture	98% N ₂ , 2% CH ₄
Shock speed	7.69 km/s	Grating	1800 lines/mm
Exposure time	1000 ns	Slit width	50 μ m



(a) Raw data



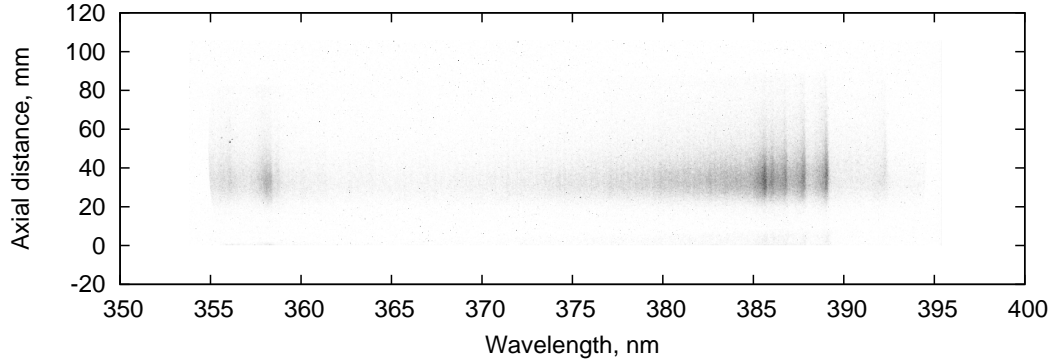
(b) Spectral power density



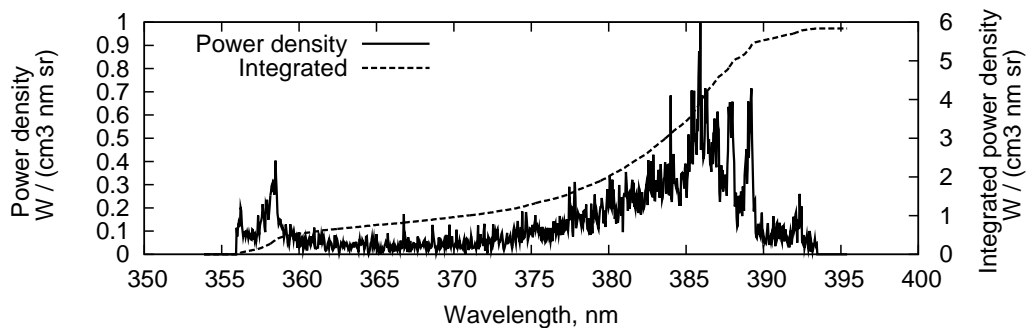
(c) Power density summed over entire wavelength range

Figure F.55 : *Raw and calibrated data for x2s1546.*

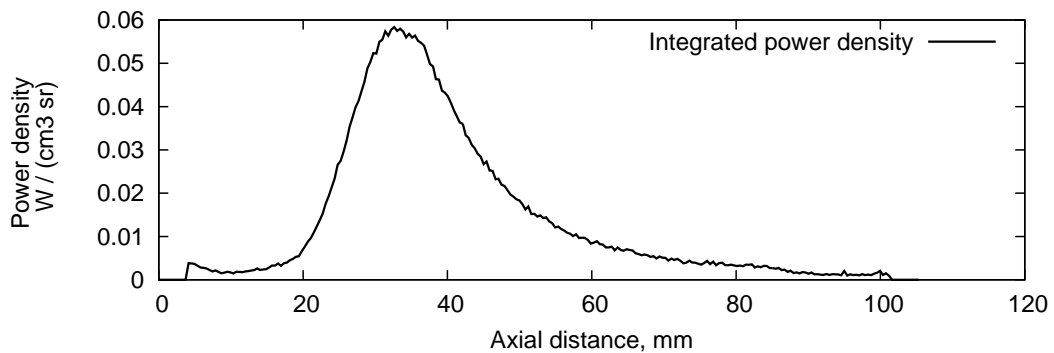
x2s1547			
Test gas pressure	4 Pa	Test gas mixture	98% N ₂ , 2% CH ₄
Shock speed	9.80 km/s	Grating	1800 lines/mm
Exposure time	1000 ns	Slit width	50 μ m



(a) Raw data



(b) Spectral power density



(c) Power density summed over entire wavelength range

Figure F.56 : *Raw and calibrated data for x2s1547.*

